Development of Self Organising Size-Limited Liposomal Clusters Using Asymmetric Janus-Textured Liposomes and DNA-Amphiphiles

Thomas Jacob Wild

Submitted in accordance with the requirements for the degree of
Doctor of Philosophy

The University of Leeds
School of Chemistry

March 2017

The candidate confirms that the work submitted is his own and that appropriate credit has been given where reference has been made to the work of others.

Acknowledgements

This thesis has only been completed to appease the two most imposing and loving women in my life.

The first being my mum, Patricia Wild.

She is someone I will *always* remember as the bravest, most caring and selfless person that I have had the privilege of sharing my journey with.

A close second is Ruth Diskin.

My rock, my confidant, my soul mate and ma moo.

I would also like to thank both Ivona Petrache & James Warren (in no other order than alphabetical, although in Ivona's thesis my name featured after James's with no explanation why) for being two people I could always depend on, both in the lab and in the pub.

I would also like to make a belated thank you to the late Julie Fisher, for seeing me as more than just a lab coat.

Ph.D defined:

Prescribed heavy Dejection.

Product of high Dreams.

Abstract

Current technologies focus on the use of single drug delivery carriers delivering a single drug species, or multiple species, in a compromisingly loaded or damaged state. Here we aim to develop controlled liposome (vesicle) clusters as potential multi-drug carriers for applications in nanomedicine. Specifically; applications include but are not limited to, combinational therapeutics and for the simultaneous delivery of prodrug and complementary activating enzyme. To this end, we are utilising a platform where different liposomes can be connected through DNA linkers, in hope to deliver multiple species in close proximity whilst keeping the individual cargos separate.

Liposome clusters can be formed using complementary lipid-DNA conjugates integrated into a vesicle's surface. To ensure strong directional liposome bridging, a patch of localised DNA allows the assembly of size-limited clusters through the directionality of the adhesive interactions. Studies have localised DNA through phase coexistence, mixing saturated (DPPC) and unsaturated (DOPC) lipids with cholesterol, forming l_o patches of saturated lipid surrounded by a l_d phase of unsaturated lipids. However, these studies displayed poor saturated lipid-DNA partitioning to the l_o ordered patches, allowing a lack of specificity in directional interactions between functionalised domains. To enhance saturated lipid-DNA l_o partitioning, 10 mole percent (mol%) cardiolipin (CL) was added. CL increases the free energy required for a saturated lipid to insert into the l_d phase, increasing DNA partition coefficient to the l_o phase by an order of magnitude. Here, a new four component phase diagram incorporating 10 mol% CL was plotted using liposomes with diameters of ~100 nm, an appropriate particle magnitude required for cellular uptake. Förster Resonance Energy Transfer (FRET) was implemented to map out the four component phase diagram as vesicle size was below optical microscopy limits. Results showed similar phase topology to the analogous three component diagram with the addition of potential l_o-H_{II} phase coexistence.

Using the new phase diagram in conjunction with lipid-DNA conjugates, dynamic light scattering (DLS) displayed size limited tethered clusters <200 nm in diameter could be achieved. This Indicated 10 mol% CL and phase diagram position limits the average number of tethered vesicles to single figures. Moreover, DNA-lipid bridging stability was examined using van't Hoff analysis, where aggregates were shown to be stable at homeostatic temperature, pH and salt concentration. Furthermore, through the implementation of DNA i-motifs, small clusters were shown to be able to disassemble at pH 3, forming ~single vesicles, and to reassemble when the pH was raised to pH 7.4.

Contents

Table of figures

Table of tables

Abbreviations

A	adenine
BP	base pair
C	cytosine
CCD	charge-coupled device
chol	cholesterol
chol-DNA	cholesterol DNA conjugate
CL	cardiolipin
CMC	critical micelle concentration
CPP	critical packing parameter
CPS	counts per second
CTC's	circulating tumour cells
DLPC	1,2-dilauroyl-sn-glycero-3-phosphocholine
DLS	dynamic light scattering
DMPE	1,2-dimyristoyl-sn-glycero-3-phosphorylethanolamine
DNA	deoxyribonucleic acid
DNA_{ds}	double stranded DNA
DNA_{ss}	single stranded DNA
DOPC	1,2-dioleoyl-sn-glycero-3-phosphocholine
DOPE	1,2-dioleoyl-sn-glycero-3-phosphoethanolamine
DOX	doxorubicin
DPPC	1,2-dipalmitoyl-sn-glycero-3-phosphocholine
DSC	differential scanning calorimetry
DSPC	distearoylphosphatidylcholine
FCCS	fluorescence cross-correlation spectroscopy
EPR	enhanced permeability and retention
FRET	fluorescence resonance energy transfer

G	guanine
GNP	gold nanoparticle
GUV	giant unilamellar vesicle
HEPES	4-(2-hydroxyethyl)-1-piperazineethanesulfonic acid
H_{II}	inverted micelles
HOMO	highest occupied molecular orbital
HPLC	high performance liquid chromatography
l_d	liquid disordered
l_{gel}	liquid gel
l_o	liquid ordered
LUMO	lowest unoccupied molecular orbital
mers	oligomers
MRI	magnetic resonance imaging
NBD PE	1,2-dipalmitoyl-sn-glycero-3-phosphoethanolamine-N-(7-nitro-2-1,3-benzoxadiazol-4-yl)
ND	nanodisc
NMR	nuclear magnetic resonance spectroscopy
NP	nanoparticle
PAN	1-(2-pyridylazo)-2-naphthol
PD	silicon photodiodes
PEG	propylene glycol
PMT	photomultiplier tube
POPC	1-palmitoyl-2-oleoyl-sn-glycero-3-phosphocholine
Q-dots	quantum dots
Rhod PE	1,2-dioleoyl-sn-glycero-3-phosphoethanolamine-N-(lissamine rhodamine B sulfonyl)
R_o	Förster radius
RSE	rapid solvent extraction
SP-FRET	steady-state probe-partitioning florescence resonance energy transfer

T	thymine
T1	tie line position 1
T2	tie line position 2
T3	tie line position 3
TLC	thin layer chromatography
T_m	DNA melting temperature
UV	ultraviolet
UV-vis	ultraviolet-visible
ΔH	enthalpy change
ΔS	entropy change
λ_{max}	excitation wavelength

Chapter 1

Introduction

Nanotechnology is a term used to describe developments of materials that are within a size range of 1 nm to a few hundred nanometres. The broad magnitude of nanoparticle (NP) size results in nanoparticles (NPs) scaling from small atomic clusters, to large complex self-organising molecular systems such as nanodiscs, liposomes, viral based nanoparticles, polymersomes, carbon nanotubes, bucky balls and dendrimers [1]. Nanotechnology and its bottom up design approach allows for fine tuning and enhancement of a materials' electrical, magnetic, mechanical, and optical properties. With these enrichments, nanoparticles are at the forefront of new innovative science, helping give rise to the large scale multidisciplinary research that occurs today. Through this interdisciplinary research, new innovative products are being produced across industry: carbon nanotubes are being woven to replace steel for lighter, stronger and corrosion free car chassis parts [2]; nanoparticle doped coatings gave rise to smart materials including switchable privacy glass windows; e-readers and pollution removing paint to name but a few [3], [4]. However, it is within medical research, specifically nanoparticle drug delivery systems, where this project focuses.

With over 350 thousand people in the UK in 2014 being diagnosed with cancer and over 150 thousand deaths in 2014 due to cancer, large organisations of researchers are looking towards developing more effective treatments [5]. In this space, drug delivery will play a vital role in forming new cures in place of ineffective palliative care treatments [6]. For example, lung cancer alone shows there is a high demand for new technology, with 12% of all lung cancer patients' only have the option of palliative chemotherapy [7]. On its own palliative chemotherapy is a treatment for the short term prolonging of life and minimisation of symptoms not a cure [6]. Through proceeding with treatment, the chemotherapy agents preferentially destroy the cancerous tissues but this is in competition between healthy cells. Palliative treatment therefore leads to a significant loss of quality of life through inducing nausea, vomiting, fatigue, mouth sores, hair loss and an increase in the chance of infection [5]. It is then evident that drug delivery must play a key role in providing more effective treatments in tackling disease while ensuring a better quality of life.

Nano-drug delivery carriers offer many benefits to both the patient and drug species. Principally they enhance the therapeutic index of cargo drug while protecting the patient from unintended interactions leading to side effects; thereby lowering drug toxicity [8]. Nanomedicine can control the bio-distribution and protect against reticuloendothelial system removal [9], [10]. Additionally, nanomaterials have two routes open for a targeted drug delivery. Firstly, passive targeting can be achieved through taking advantage of the enhanced permeability and retention (EPR) effect [11]. Secondly, the addition of targeting ligands on the material's surface offers an active target cell approach. Interestingly, in order to enhance the EPR effect and the circulation half-life of nanomaterials, a "stealth" coating can be applied. Regardless of method, once targeted a

nanomaterial can deliver its cargo through various mechanisms. Two such routes include; diffusion from the nanomaterials into the cell or a triggered rapid release from an external stimuli e.g. temperature or pH [12].

From this brief synopsis it can be seen multiple approaches and methods are offered by the scientific community for dealing with drug delivery. The specific strategies however are dependent upon the individual drug species, as each drug has a preferred administration route and environment in which it is stable. Current nanocarriers have therefore been reviewed here to give an insight into the breadth and advancement of drug delivering nanocarriers.

1.1 Nanocarrier drug delivery materials

In short, the employment of drug delivering nanocarriers is to transport locally high concentrations of drug species to a target area, to induce a therapeutic effect while minimising exposure to non-target areas. Other benefits from using carriers can come from tuned parameters for targeted stimulated responsiveness. Whatever the intended extra effects, carriers can be categorised into two factions; solid and soft nanoparticles.

1.1.1 Solid nanoparticles

Many examples of solid nanoparticles are demonstrated in literature, including silver, silica and gold nanoparticles and quantum dots (Q-dots). Silver nanoparticles are commonly incorporated within plasters and on computer keyboards, where both applications take advantage of silver NPs antimicrobial properties [13], [14]. However the effect of silver NPs entering the environment are in much debate with regard to their long-lasting toxic effects [15]. Mesoporous silica on the other hand, has been widely adopted into the field of drug delivery, where silica offers chemical stability, a reasonable biocompatibility and capacity to undergo surface modification [16]. That being said there are issues with silica phosphorus reactivity and resulting haemolysis leading to a promotion in melanoma growth [17], [18]. Moving forward, similar silica NP advantages apply to Q-dots. In addition though, Q-dots have a major benefit of being able to replace fluorescent dyes as contrast agents [19]. When imaged Q-dots are brighter and less susceptible to photobleaching than standard indicators, while also providing a route to deliver photothermal therapy to a patient [19]. While there are many advantages to using Q-dots, the inorganic semiconductor is cytotoxic, limiting their biological use [20].

For the purpose of this review, a more in-depth appraisal has been made of gold nanoparticles (GNPs), with their selection being due to their use in the clinic today [21]. Depending on their application gold nanoparticles can be tagged with ligands and/or can be formed into many different shapes, the most obvious being a sphere. Spherical nanoparticles offer a straightforward synthesis with diameters ranging between 2-100 nm [22].

To functionalise a GNP, ligands are attached through a thiol group. An example of this attachment can be seen through the addition of paclitaxel; a mitotic inhibitor which prevents mitosis (cell division) in chemotherapy [23]. Once attached the ligand is biologically inactive, therefore at the target site it must be again detached from the particle in order to be activated. To detach the ligands intracellular glutathione has been discussed to partially displace any thiol groups, thereby removing the original ligand [24]. Furthermore, gold-thio nanoparticles are widely used in gene delivery [22], whereby DNA is modified with a thiol group. In summary Figure 1.1 displays a scheme illustrating thiol attachment ligand types and GNP shapes.

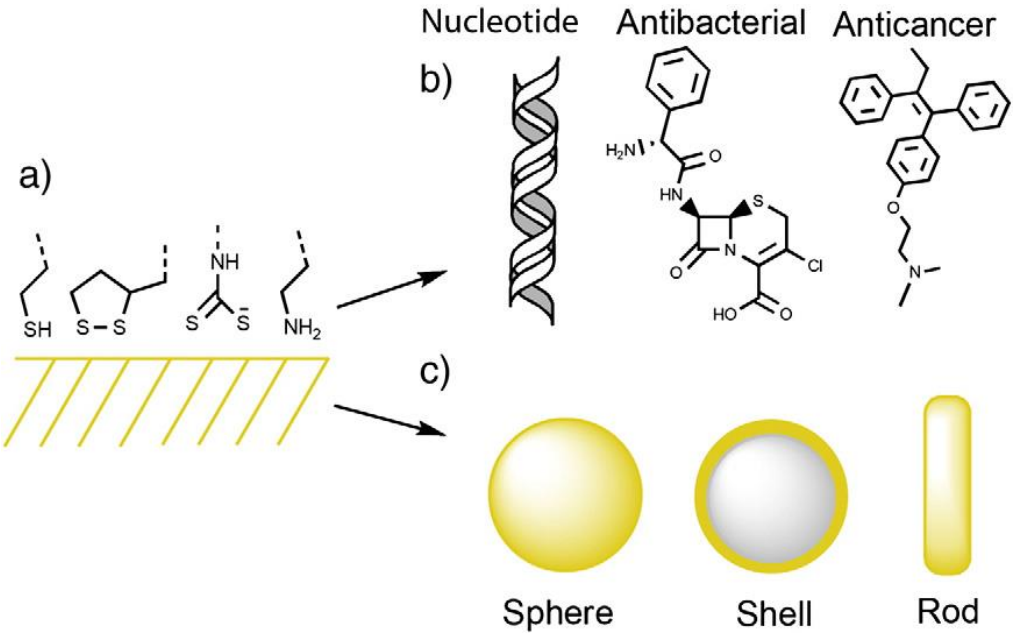

Figure 1.1 – Three gold nanoparticle structures with three representative types of therapeutic drugs with possible thiol attachment routes [22].

Additionally, gold nanoparticles have also been developed to interact with an applied outside electromagnetic radiation source, which can be used to induce localised heating. This property is unavailable to larger diameter nanoparticles (10-100 nm), whose surface area to volume ratio is smaller than that of the small diameter nanoparticles (5 nm) [22]. The surface to volume ratio plays an integral part in the wavelength of light absorbed due to the level of surface plasmon available. Larger spherical gold nanoparticles only absorb between 520-550 nm in the visible region, to which biological tissue is opaque [22]. Smaller nanoparticles, nanorods and shells have developed to have strong surface plasmon resonance. These materials have been shown to absorb radiation within the near infrared region (800-1200 nm), enabling deeper tissue penetration, making GNPs such as these ideal candidates to be used within photothermal cancer therapy [22], [25].

Unfortunately, solid gold nanoparticles are not without their disadvantages. Not all drugs species can be modified with thiol attachment group(s) without loss of functionality of the therapeutic.

While GNPs can provide localised drug delivery, the ligands are not localised to any specific side of the NP, and therefore cannot be linked with another NP in a directional manner. This is not to say there are no examples of solid NPs having localised functionalities, an example to the contrary would be silica NPs in combination with Pickering emulsions and microfluidic devices [26]. However these silica NPs are more commonly found within electronic e-readers rather than in medical applications [27].

Furthermore, when functionalised GNPs are used in patient treatment the ligands themselves are not protected from their environment, thereby making it possible for the exposed drugs to be degraded. Additionally the attachment thiols themselves are in much debate in literature with regard to their toxicity [28]. However, a broader issue associated with the use of GNPs is their environmental impact. Once excreted they could expose their toxic effects to plants and animals, which in turn could enable them to enter the food chain [29].

1.1.2 Soft nanoparticles

Soft NPs are often made from self-organising organic molecular building blocks gathering together to form complexes of ordered and thermodynamically stable structures, held together through non-covalent interactions. For example, lipids and polymers self-assemble in liposomes and polymersomes respectively; and through their own individual complexity they build a richer catalogue of nanoparticles that are available for use within drug delivery. The self-assembly of these building blocks is made possible through an enthalpic energy cost being balanced by an entropic energy gain, driven by the hydrophobic effect of amphiphilic molecules [30], [31]. The hydrophobic effect is driven through a hydrophobic molecule disrupting water's three-dimensional hydrogen bonding network. At the surface at, for example a lipid chain, water forms a solvation shell which limits the translational and rotational entropy of the water molecules, making for an unfavourable interaction in terms of free energy. Through lipids self-assembling however, this interface between the hydrophobic region and water is minimised and so reduces the disruptive effect of the lipid.

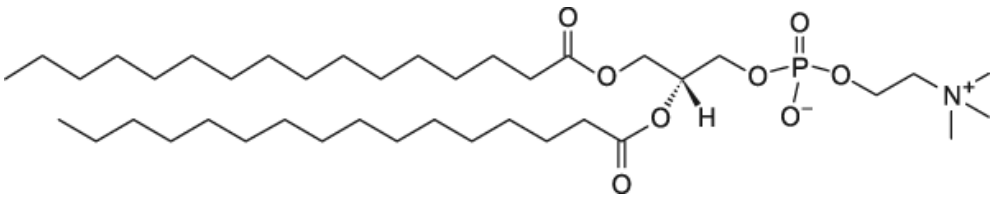

Figure 1.2 – 1,2-dipalmitoyl-sn-glycero-3-phosphocholine (DPPC) lipid with two 16 carbon long lipid chains/tails and a phosphocholine hydrophobic head group [32].

With an extensive library of lipids varying in both shape and size polymorphism is observed, with the end self-assembled structure dependent upon lipid(s) used. There are four main categoriesof lipids that are characterised through their molecular geometry [33]. To predict what structures lipids form during self-assembly, a Critical Packing Parameter (CPP) can be calculated from the geometric parameters of the individual lipids, this is outlined in Equation 1.1.

Equation 1.1 $$CPP = \frac{v}{l_c a_0}$$ **[34]**

Where v is the volume of the hydrophilic head group, l_c is the critical length of the hydrophobic tail (fully extended) and a_0 is the area of the hydrophilic head group. The results from Equation 1.1 can be compared to tabulated data to predict what lipid structures are formed.

CPP	Lipid "Shape"	Self-Assembled Structure
<1/3	Cone	Micelles
1/3–1/2	Truncated Cone	Extended Micelles (Rods)
~1	Cylinder	Planar bilayers
>1	Inverted Cone / Wedge	Inverted micelles (H_{II}) and cubic phases

Table 1.1 – Critical packing parameter influencing the formed self-assembled structure [34].

The resulting arrangements within Table 1.1 can be rationalised through considering packing space. Cone shaped lipids with large polar head groups and smaller hydrophobic tails form spherical micelles. The small volume of the tails allows the tails to pack together tightly, complementing the larger space required for the bulky head groups to pack together. Extended micelles form when the volume of the surfactant's hydrocarbon region is increased, distorting the packing arrangement which prevents the formation of a typical spherical micelle [33]. Further increasing the volume of the hydrocarbon region through additional chains/tails allows the formation of bilayers. Lipids are commonly found taking on a "cylindrical shape" where upon self-assembly the lipids arrange themselves to be perpendicular to the plane of the bilayer [33]. The final lipid shape that will be considered in this review has a small cross-sectional head group in comparison with its tails; leading to the head groups being at the trailing end of the cone shape. As a result these lipids pack in an inverted micelle formation, where the head groups pack into the core of the micelle, leaving the bulky tail groups exposed to the water [33]. In response to

this packing, the HII phase forms a bulk phase to minimise water contact. It is worth noting environmental triggers can enable polymophorism, for example, a trigger could include changing the charge on a lipids head group [35].

1.1.2.1 Polymersomes

Block copolymers can be used to make a synthetic fluid polymer membrane. Amphiphilic block copolymers consist of one long chain of polymer with sections of contrasting hydrophobicity. When the chains are placed within an aqueous environment they may self-assemble to form hollow spheres with an internal aqueous compartment, termed polymersomes [36]. The aqueous core can be used to store therapeutic molecules which contrasts with hard NPs. This incorporated internal storage shields the contents from the external environment which could lead to the denaturing or inhibition of a therapeutic. Polymersomes have thick 10 - 50 nm membranes which are attributed to the high molecular weight of the initial building blocks [37]. The thick membrane of a polymersome offers great stability, mechanical strength and long cargo retention times. Analogous to solid nanoparticles, polymersomes can be surface functionalised for drug delivery to provoke therapeutic effects. Modification is possible through the addition of a motif to the polymer chain. A cartoon displayed within Figure 1.3 exhibits some conceivable multiblock polymer compositions and the resulting hypothetical assembled configurations.

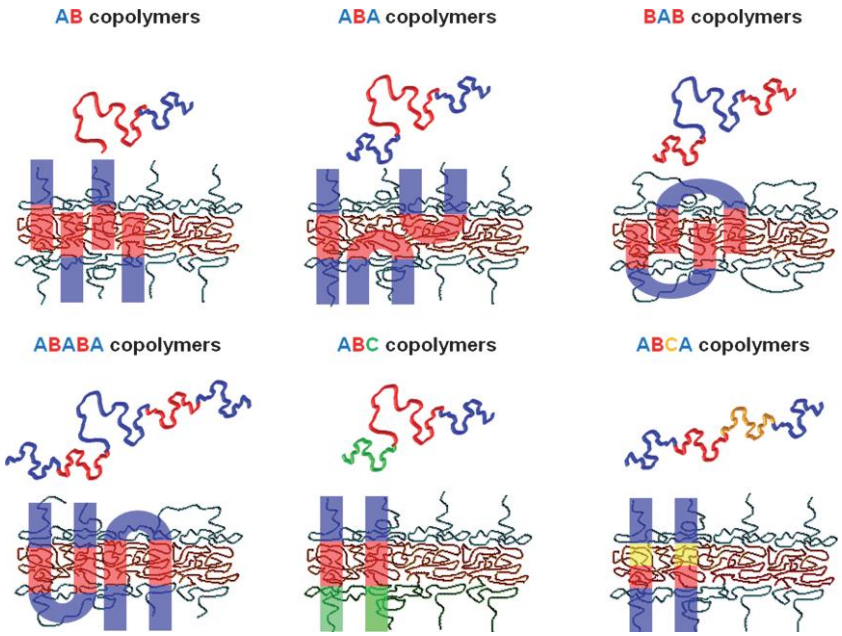

Figure 1.3 – Polymersomes membrane conformations where the initial building block of the polymersomes becomes more complicated. The complexity of the copolymer from diblock, triblock to more theoretically possible multiblock co-polymers in membrane assemblies has been illustrated [38].

From the cartoon in Figure 1.3 it can be seen that it could be possible to tune the polymersome to have contrasting internal and external surface areas. It is likely that, to produce structures such as these, large functional groups would have to be used to encourage partitioning to the outside of the polymersome, where steric hindrance would be significantly reduced opposed to internal partitioning. What is clear from this cartoon, is that polymersome structures offer more in the way of tuneable parameters which the hard NP could not. The higher degree of structural freedom afforded to the polymersomes aids the ability to produce particles more specifically adept to targeting and delivering therapeutics for/to an individual disease. For example through adding a monoclonal antibody to polymer chains, the subsequent polymersomes have been able to cross the blood brain barrier, to deliver therapeutic peptides [38].

Additionally soft polymersomes offer an easier and safer route to the preparation of NP than gold, removing the need to use powerful reducing agents [22]. Moreover, polymersomes are quickly prepared with respect to GNPs, where GNPs can take weeks to form. Regrettably, polymersomes are still not without their flaws; namely, biocompatibility and slow diffusion rates of the polymer [36]. The slow phase separation impedes heterogeneous surface formation to ~a month, limiting polymersome's capacity to form directionally linked materials [36].

1.1.2.2 Micelles

Therapeutic delivering micelles can be formed using polymers, lipids and surfactants alike. Once assembled into micelles, the hydrophobic core offers a better environment for partitioning of low water soluble drugs than the aqueous core of a polymersome or liposome. Micelles are therefore capable of transporting hydrophobic species in hydrophilic conditions, making them distinctive from other the NP drug carriers discussed so far.

A micelle's suitability for the transport of hydrophobic species is nevertheless a blessing and a curse. While there is a demand for the delivery of a wealth of lower water solubility therapeutics, there is a larger demand for the safe delivery of more biologically suitable hydrophilic drugs. Again, there are also further issues regarding the biocompatibility of the polymers used and the circulation time of the NP. To address the latter the NP would need to be doped with a stealthing agent such as propylene glycol (PEG), which would extend the NP circulation time by impeding immune system detection [39]. Nevertheless, a more sophisticated drug delivery unit analogousto a micelle in terms of hydrophobic therapeutic delivery, has been developed. These new delivery units are called nadenanodiscs (ND).

1.1.2.3 Nanodiscs

A ND is made from a sandwich of lipids that are wrapped in a protein “belt”; where the belt reduces the hydrophobic line tension at the ND boundary. The protein is derived from a high density lipoprotein Apolipoprotein [40]. Apolipoprotein derivatives function as membrane scaffold proteins that have a high affinity towards lipids, with common examples including MSP1D1 and MSP1D1-deltaH5 [41]. The protein length determines the size of the final NP where its length is the circumference of the stabilising belt [41]. While both NDs and micelles have been discussed to carry hydrophobic species, the lipid bilayer inherent to NDs has been debated to resemble a biological membrane, affording greater stability to other therapeutic proteins being delivered [42].

NDs have similar issues to micelles through a somewhat limited hydrophilic drug delivery capacity. Additionally, the preparation of NDs is not trivial, requiring specialised skills to formulate a ND, where opposingly, micelles spontaneously form in water as long as the concentration is above the Critical Micelle Concentration (CMC).

1.1.2.4 Liposomes

Liposomes/vesicles are spherical shells built through the self-assembly of lipid building blocks, resulting in a lipid membrane encapsulating an aqueous core, similar to a polymersome. Scientists researching liposomes take inspiration from nature where amphiphilic lipids are seen in cellular membranes. Lipids present the cell with inherent valuable properties including the ability to be deformed by external forces and self-repair all while preventing leakage from the cell [43]. These powerful natural lipid membrane properties are therefore incorporated into liposomes, making vesicles ideal bio delivery tools. Due to these properties liposomes are at the forefront of novel biomedical encapsulation applications for the delivery of drugs, contrast reagents and catalysis [44].

Liposomes have distinct advantages over their therapeutic delivering NP equivalents. These advantages include; the delivery both hydrophobic and hydrophilic species through their hydrophobic centred bilayer and aqueous core respectively, with the additional benefit of being made of biological molecules, granting enhanced biocompatibility over block copolymers. Furthermore, the relatively fast diffusion of lipids over their polymer counterparts enables fast phase separation (discussed further in section 1.2 page 11). Through phase separation it has been shown that a liposome’s functionalised surface can be localised to form a heterogeneous Janus particle. This permits Janus liposomes, with the aid of a molecular linker, to form binary size limited liposome A bound to liposome B clusters. In contrast, without phase separation polymersomes when tagged with an appropriate molecular linker, would bind together to form a

large mass of aggregated polymersomes. In summary Janus liposomes offer new potential routes to faster and more effective treatments in the field of multiple drug delivery.

1.1.3 Multiple nanocarriers

Four new treatment routes can be explored through the possibility of simultaneous transportation and delivery of therapeutic species, these include; prodrug, combinational and theranostic delivery. Also, simultaneous transportation offers new routes into targeted delivery where links between liposomal carriers can be disturbed in the presence of an intended stimulus.

Currently, DaunoXome, Doxil, ONCO-TCS and DepoCyt are typical liposomal therapies on the market, however, these systems all encapsulate one drug species per product and these are daunorubicin, doxorubicin, vincristine and cytarabine respectively [45]. In order to further enhance the potency of these approved treatments, combinational therapies were developed. Agrawal et al. encapsulated both 6-mercaptopurine and daunorubicin into the same vesicles to provide a more effective treatment of leukaemia [46]. In the study it was found that the two mechanistically different drugs offered a higher cytotoxicity against Jurkat and Hut 76 T-cell lymphoma when coupled together in the same vesicle, than either drug applied singularly [46]. This in turn suggests that a cocktail of the two drugs has the potential to provide a higher therapeutic efficiency. Unfortunately it was found that 6-mercaptopurine has a poor 1.5% loading efficiency and therefore that specific treatment was described as being unsuitable for use [46], [47]. Although it was unsuitable, this study showed the idea of combinational delivery of multiple drugs not being something new to the world of nano carriers. Where this project seeks to lead on from the work presented by Agrawal et al. is to form separate AB tethered dimer carriers, where separation of drugs would offer the potential for better therapeutic tailoring. Tethered vesicles would remove the need to add two drugs to the same liposome. In turn vesicles would have a higher maximum loading efficiency, as each vesicle can be engineered to suit its cargo's requirements. A further effect of separating out the loading of therapeutics over multiple liposomes is the prevention of cross reactions between species.

The ability to prevent cross reactions and tune therapeutic loadings is key to the advancement of theranostic treatments. Rapid detection of disease is often paramount, especially when fast action will strongly influence the effectiveness of a treatment and the resulting outcome. Theranostic treatments bridge the gap between detection and prescription through delivering diagnostic imaging agents/biosensors, with the corresponding therapeutics. A key change and benefit to using the technique, is that there would be drastically reduced lag time which would ultimately increase survival rates [48], [49].

As an example of a hard theranostic material, hybrid gold-iron NPs are currently being used to detect and remove tumour cells that have been shed into the vascular system from a primary site; which if left unchecked leads to metastasis. The Circulating Tumour Cells (CTC's) are tagged using a S6 aptamer, which are themselves attached to the gold coated $Fe_3O_{4\,(s)}$ NP using a thiol

coupling group [50]. The tagged CTC's could then be imaged through the fluorescently labelled aptamer. The hybrid NP then presents the user with two functionalities, separation and ablation. The iron oxide is magnetically sensitive and so in the presence of a magnetic field the CTC's can be isolated or imaged through magnetic resonance imaging (MRI) instruments, allowing early stage CTC detection [51], [52]. A further benefit of the NP is the gold coating, whilst already contributing an attachment route for the aptamer, gold is able to induce localised heating through the absorbance of infrared radiation. The induced localised heating then selectively ablates the CTC through the gold [50]. However, this specific treatment still has the disadvantages of solid NPs discussed in section 1.1.2 page 4, which are not present when using vesicles.

Where tethered liposomes show further potential over their hard NP counterparts is in the delivery of prodrugs. Prodrugs are the therapeutic equivalent to a fibre glass application kit. The resin (pharmacologically inactive therapeutic) and the activating agent are transported and packaged separately until the point of application. Current prodrug treatments require *in vivo* enzymatic and or chemical transformation before the parent inactive drug can exert its therapeutic effect [53]. Tethered liposomes can offer an alternate approach where the parent drug and activator are kept separate whilst being delivered. Upon being supplied to the target the activator and therapeutic would combine leading to treatment. Through tethering the carriers together there will be an increased probability of delivering both species simultaneously to the same cell, inducing the wanted pharmaceutical effect.

In summary, vesicles present a favourable solution to forming size limited clusters required for combinational, theranostic and prodrug delivery treatments. The driving force behind a vesicles' diversity and pharmaceutical usefulness, in regards to the outlined treatments, rests in lipid phase behaviour.

1.2 Liposome phase behaviour

Liposomes/vesicles have been shown to form multiple phases dependent upon the lipids from which they are made and temperature they are at. Homogenous vesicles are usually described as being in a liquid disordered (l_d) or more solid gel (l_{gel}) phase [54]. As a rule of thumb, a vesicle's phase is dictated by the saturation of the lipid carbon chains. In other words, saturated chains closely pack together forming a more solid phase than unsaturated lipids [54]. The combination of saturated and unsaturated lipids within vesicles can lead to the formation of rafts/domains. A domain within a liposome is the heterogeneous arrangement of lipids on the surface of a vesicle, which is a result of phase separation [55]. Essentially, comparable lipids concentrate together so that lipids with saturated and unsaturated tails separate from one another to form separate patches.

It is widely known that mixtures of lipids can form l_d, liquid ordered (l_o) and many l_{gel} phases, with mixtures of phases being able to coexist. It is important to note the phase of the membrane significantly impacts the structural properties of the vesicle [56]. A liquid gel phase is more solid

than a liquid disordered phase, where l_{gel} phase vesicles have a distorted spherical morphology and both a slower lipid diffusion rate and cargo release rate. When phases coexist the size of each coexisting phase ranges typically from nanometres to micrometres, with size being dependent upon lipid type, quantity and the preparation method of the liposome [57]. Each lipid type has an individual transition temperature, bending modulus and length [58]; with lipid transition temperatures being largely reliant on the length of the hydrophobic tail, level of saturation within the tail and the type of head group [59]. The mixing of dissimilar lipids in a vesicle introduces a higher interfacial energy cost than having a vesicle made up of one lipid type, leading to separation.

When below the transition temperature, lipid mixtures no longer have enough thermal energy to overcome the interfacial energy cost required to maintain a homogeneous structure. This promotes the lowest melting lipids to de-mix and coalesce together once they come into contact with one another, through Brownian motion. Through coalescence, small domains of the lowest melting lipid form in competition with an entropic energy cost [60]. Each formed domain has an associated line tension (an energy per unit length of boundary) that exists at the edge of the domain [61]. Multiple small domains have a greater interface than a large domain, therefore to reduce the interfacial tension across the multiple domains they further coalesce together [61], [62].

1.2.1 Binary systems

For binary lipid systems, phase diagrams define a liposome's local lipid concentration and morphology with respect to temperature. Phase diagrams in combination with the Gibbs phase rule, Equation 1.2, give a prediction of the degrees of freedom when phases coexist for a stated number of components.

Equation 1.2 - $\boldsymbol{F = C + 2 - P}$ **[63]**

Where F is the number of degrees of freedom available for number of P coexisting phases, C is the number of components. The phase rule however cannot give any information about the amount/size of each phase present. To do this the lever rule must be applied. To examine the lever rule more closely a lipid phase diagram has been displayed in Figure 1.4.

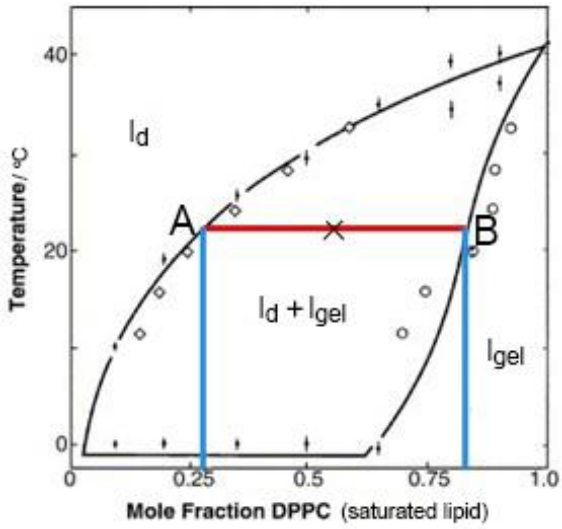

Figure 1.4 – A modified example of a binary phase diagram for DPPC:DLPC liposomes. Circles represent differential scanning calorimetry (DSC) gathered data and diamonds display Fluorescence Resonance Energy Transfer (FRET) data. The solid line displays the phase boundaries [64].

The graph in Figure 1.4 shows the x-axis representing the mole fraction of DPPC, in other words it describes the fraction of saturated lipid. At high concentrations of DPPC and at low temperatures, it would be expected the lipids would be in an l_{gel} phase due to the liposome mainly consisting of saturated lipids below the lipid melting temperature. Alternatively, at low concentrations of DPPC and at a high temperature it would be expected that the liposomes would be in an l_d phase due to the increase in unsaturated lipids. In between the pure ordered gel phase and pure liquid phase there exists a region where a liposome's surface will have the properties of both i.e. the membrane has become phase separated. In this region, the fraction of lipids in the gel phase and fraction in the liquid phase can be calculated through the lever rule.

In Figure 1.4 a binary phase separated liposome has been recorded through point "x". It is important to note when calculating the mole fraction of each phase that the temperature and mole fraction of DPPC remains constant. A horizontal isotherm/tie line running through point x parallel to the x-axis has been drawn (red line Figure 1.4). When the red line intersects the phase boundaries (solid black lines) two perpendicular lines (blue) of l_d and l_{gel} can be drawn down to the x-axis. It is through these three points, A, B and X that the mole fraction of each phase can be calculated using Equation 1.3 and Equation 1.4.

Equation 1.3 - $$mole\ fraction\ of\ l_d\ phase = \frac{B-\times}{B-A}$$ **[63]**

Equation 1.4 - $mole\ fraction\ of\ l_{gel}\ phase = \frac{\times - \mathbf{A}}{\mathbf{B} - \mathbf{A}}$ **[63]**

Using the knowledge gained from binary lipid mixtures enables ternary phase systems, more relevant to the project, to be further discussed.

1.2.2 Ternary systems

The addition of cholesterol to binary lipid systems affects the packing arrangement of lipids, thereby strongly changing a liposome's properties, making cholesterol of high interest within the literature. When cholesterol is applied to a lipid membrane it will preferentially enter the close packed highly ordered gel phase, disrupting the close packing arrangement [65]. Cholesterol's rigid fused ring structure cannot pack as tightly as saturated lipids increasing the lipid diffusion coefficient and membrane mechanical flexibility [65]. In contrast, cholesterol within l_d domains aids the membrane to become more rigid through restricting chain conformations [66]. In other words, cholesterol limits the degrees of freedom in chain confirmations in the l_d phase. By reducing the degrees of freedom the lipid tails can adopt, cholesterol decreases the lateral diffusion coefficient of the unsaturated lipids and increase mechanical rigidity of the liposome; making the liposome less deformable [65]. The addition of cholesterol to the binary phase diagram enables the possibility of the liposome's surface to become liquid ordered (l_o), rather than just being gel or liquid disordered. Cholesterol addition is therefore favourable when designing heterogeneous, drug delivering liposomes, where cholesterol maintains the flexible fluid shell while making the liposomes less leaky. Cholesterol further benefits this project by driving the l_d-l_o phase separation required to form Janus vesicles. However, in order to make controlled heterogeneous liposomes when a third component is added to the binary system, a new phase diagram with updated tie lines is required.

1.2.2.1 Ternary phase diagrams

Lipid ternary phase diagrams have been plotted and updated using complementary techniques in an effort to achieve more accurate data with which to construct the phase diagram [67], [68]. The most researched phase diagram consists of liposomes being made from DOPC:DPPC:cholesterol components. The initial attraction for using PC lipids within research is that they are found naturally in biological cell membranes [69]. Specifically, DPPC was selected because it already had a wealth of literature describing its behaviour within bilayers. Furthermore, unsaturated DOPC was selected due to it having the same head group as its saturated lipid

counterpart, thus nulling the potential effect of a different head group on phase separation [68]. By varying the ratios of lipid as previously discussed for binary systems, and using suitable fluorescent dyes, the separate lipid domains were viewed via confocal fluorescent microscopy as shown within Figure 1.5.

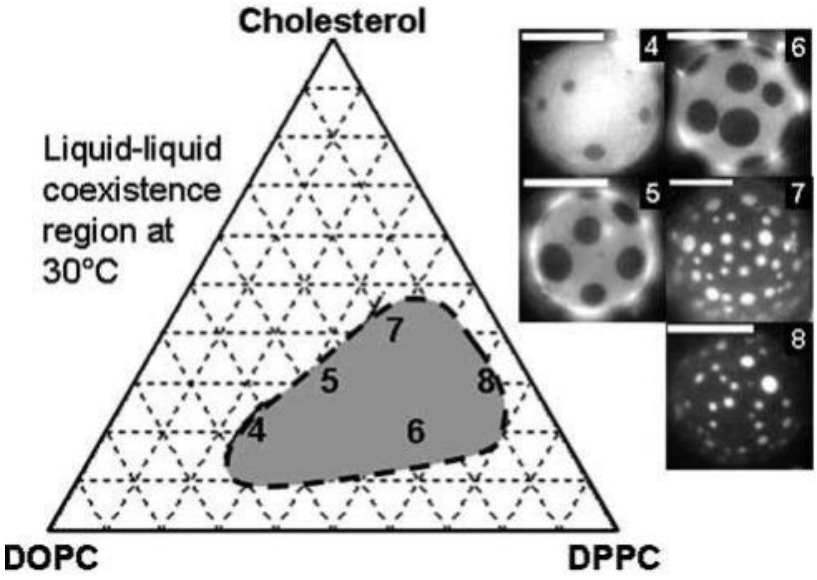

Figure 1.5 – An early ternary phase diagram for giant vesicles of DOPC:DPPC:Cholesterol at 30 °C. The microscopy images display bright l_d DOPC rich domains, distinguished through Texas Red dipalmitoyl-phosphatidylethanolamine (TR DPPE) partitioning. Scale bars represent 20 µm [68].

From Figure 1.5 it can be seen that the apexes of the triangle represent 1 mole fraction of that specific lipid and the dashed lines display 10% change in lipid mole fraction. The shaded area on the phase diagram outlines the l_d and saturated lipid phase coexistence region, which was mapped through monitoring TR DPPE dye phase separation in the confocal images. Even though the dye has saturated carbon chains, TR DPPE has been shown to preferentially partition to the l_d phase. This counterintuitive partitioning, is due to the bulky labelling fluorophore disturbing the l_o phase packing lipids around it, leading to TR DPPE partitioning into the l_d phase [70]. That note a side, experiments such as these formed the basis to monitor phase separation reversibility. These confocal images display both the melting and formation of lipid domains [71].

While giant unilamellar vesicles (GUVs) are useful in characterising vesicle structures on a micro scale, it is perhaps not appropriate to extrapolate the data to the nanoscale due to the increased effect of curvature on the membrane. With potential changes to the phase diagram induced by making nano vesicles, a new phase diagram using the same components but on the nanoscale would be required to model nano phase separated vesicles.

Phase diagrams where liposomes are on the nanoscale have been developed using quantitative Florescence Resonance Energy Transfer (FRET) techniques rather than using confocal fluorescence microscopy. Steady-state Probe-partitioning Florescence Resonance Energy Transfer (SP-FRET) also exploits probe partitioning between phases as seen in confocal fluorescence studies [72]. The basic principles behind SP-FRET can be best understood when discussed alongside Figure 1.6.

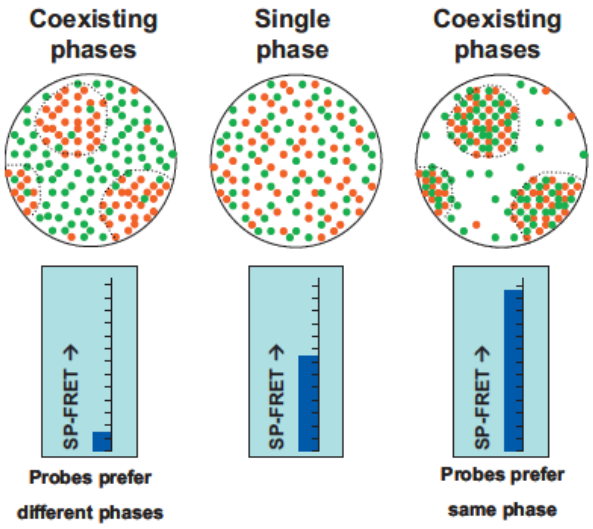

Figure 1.6 – SP-FRET fluorescent probe partitioning: green being the donor probes and red the acceptor probes [72].

Figure 1.6 displays that there are three possible SP-FRET signals that can be produced depending on the dye and probes partitioning preferences. In a single phase system where no domains have formed, probes are homogenously distributed across the surface of the liposome. When domains form, membrane probes can partition in one of two ways; either they can coexist in the same domain, or separate out among the saturated lipid and l_d phases depending on the probe type. To model phases and phase changes, FRET signals are recorded where a change in the FRET signal is due to the change in distance between the probes. This technique is limited to measuring small distances, where the largest accurately measured distance ~10 nm, limiting the domain sizes that can be measured [73].

Using FRET a fully mapped updated nano-version of the ternary phase diagram of DOPC:DPPC:cholesterol was suggested [67].

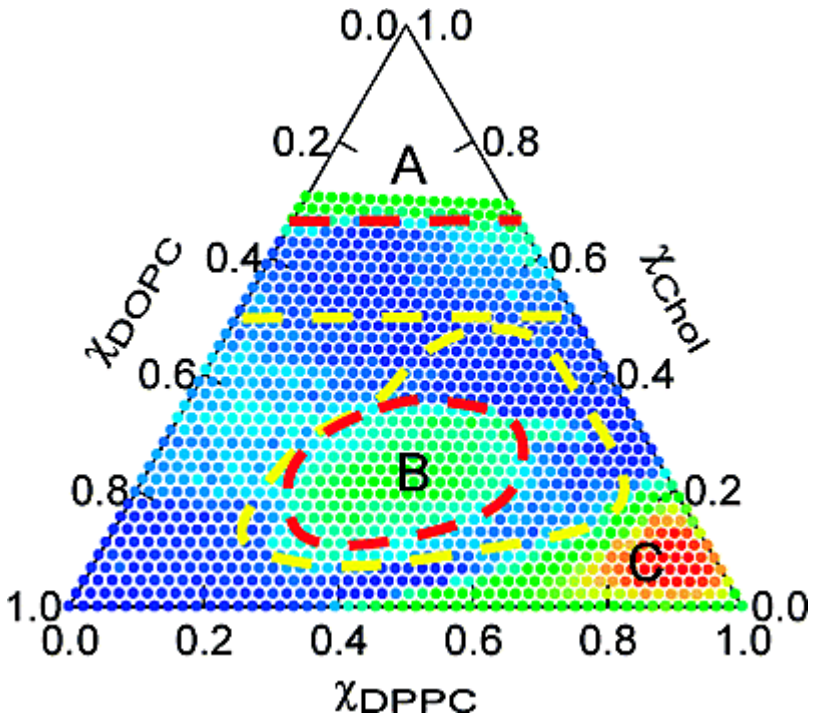

Figure 1.7 – The suggested later phase diagram of liposomes composed of DOPC:DPPC:cholesterol by J.T. Buboltz et al. Yellow dashed line in region B displays the previous l_o and l_d phase boundary presented for the same liposome systems by S.Keller et al. Region A displays the boundary at which cholesterol crystallises in the membrane, and region C displays the compositions where the membrane is in a l_{gel} phase. This phase diagram was conducted from data collected at 25 °C [67].

The phase diagram for nano vesicles presented by J.T. Buboltz et al. does potentially show a difference between the nano and giant liposome model systems. However, this could also be rationalised as a discrepancy between the analytical phase boundary detection techniques. Regardless of this the authors argue that the difference between zone B and the previous l_d-l_o phase model by S.Keller et al. is through the preparation of their samples by Rapid Solvent Extraction (RSE) [67]. RSE relies upon rapid drying under vacuum and immediate hydration, rather than slower electro-cell vesicle preparation [67].

This review concludes that the two ternary phase diagrams cannot be compared for two reasons: The liposomes used by S.Keller et al. in phase boundary experiments are giant unilamellar vesicles (GUVs), with diameters in the range of 10-50 µm. Whereas in RSE prepared liposomes diameters are not quoted, but it can be assumed that they are on the nanoscale. Secondly the temperatures at which the phase diagrams have been recorded at are different. S.Keller et.al. quotes a phase diagram at 30 °C and J.T.Buboltz et.al. quotes a phase diagram at 25 °C. As previously discussed an increase in temperature promotes lipids into the l_d phase making l_o domains smaller in size [74]. Furthermore, the GUVs have more membrane material which drives

faster nucleation of domains where in small vesicles nucleation will be slower. Therefore preparation time could be key in determining whether domains form for particular compositions.

This review will limit itself to the study of three component DPPC:DOPC:cholesterol lipid systems, due to the components being relevant to this project, and this project only adding a fourth lipid component, cardiolipin (CL), at a low constant 10 mol%. At this low percentage, it was assumed that any significant phase behavioural changes would be avoided (see section 1.4.1 page 27). It is of note however that a four component lipid system has been mapped by G. W. Feigenson et al. using a mixture of distearoylphosphatidylcholine:dioleoylphosphatidylcholine:1-palmitoyl,-2-oleoylphosphatidylcholine:cholesterol (DSPC/DOPC/POPC/cholesterol) lipids [75].

1.2.2.2 Tie lines

Similarly to binary lipid systems, tie lines in three component phase diagrams are used to calculate how much of a liposomes surface is phase separated. Unlike a binary system l_d-l_o tie lines do not run parallel to the x-axis, instead moving from the three phase triangle to the critical point, where the three phase tringle must exist to comply with phase diagram thermodynamics. To determine the tie lines of a ternary lipid phase diagram a number of techniques have been used including x-ray scattering and nuclear magnetic resonance (NMR) techniques [76], [77], [78]. The methods behind each technique will not be considered here. However, both NMR and x-ray spectroscopy have shown good agreement to the direction of the guide tie lines shown Figure 1.8.

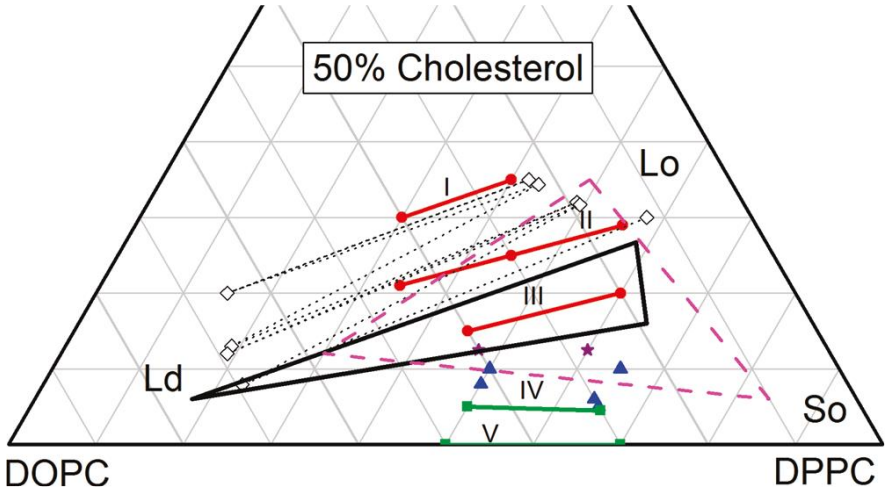

Figure 1.8 – Ternary phase diagram displaying tie lines moving across the DOPC/DPPC axis at 15 °C. The fine dotted lines with open diamonds display the NMR data collected by S.L Veatch et.al. the diamonds signifying the l_d and the l_o phase boundary [78]. The black triangle displays a suspected three phase region where l_d, l_o and the l_{gel} (So) coexist [78]. The red lines and circles display the data gathered through the x-ray study [76]. All other lines can be ignored for the purpose of this review.

The overall direction of the tie line is of high importance; however, the exact angle is not required when building heterogeneous liposomes. The requisite for an utmost accurate angle not being necessary can be best described in conjunction with Figure 1.9.

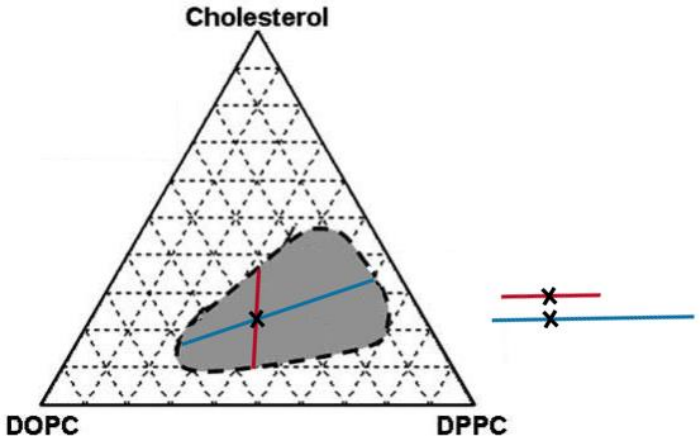

Figure 1.9 – A modified S. Keller phase diagram with an incorrectly drawn tie line (red) and the experimentally determined tie line (blue).

Through use of the lever rule in combination with the tie lines present within Figure 1.9, the blue line will predict that sample x will have a smaller liquid ordered domain than would be predicted with the red tie line. This example displays that without correctly mapped and oriented tie lines, vesicle structures would be difficult to predict. Moving across to the right of the experimentally measured blue tie line enables phase separation to be controlled in a manner similar to the cartoon in Figure 1.10.

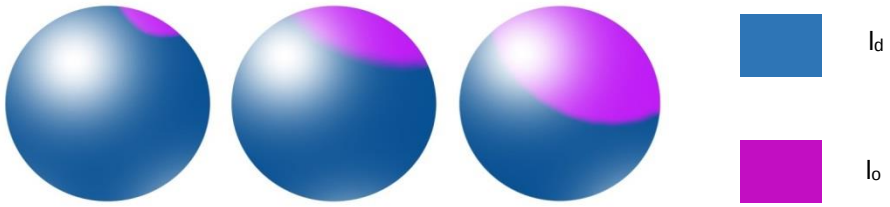

Figure 1.10 – Three Janus liposomes with increasing concentrations of saturated lipid across the experimentally measured (blue) tie line presented in Figure 1.9 when vesicles are left to equilibrate.

1.2.2.3 Measuring domain Size

Rather than using the lever rule to approximate potential domain sizes, different techniques have been implemented to measure them, with methods being dependent upon vesicle size and the suspected domain sizes. Lipid-fluorescent dyes coupled with confocal fluorescence microscopy, enabled images of >micrometre sized vesicles to be taken. The resulting images permit a scale bar to be used as a ruler to measure domain size. However, care has to be taken when interpreting these domain size measurements, due to the lack of consideration towards membrane curvature. These intrinsic inaccuracies can be accounted for though corrections being applied in image analysis. Criticisms aside, the raw measured data will give a good approximation to the respective domain size. Nevertheless, confocal fluorescence microscopy is limited with respect to the size of liposome it can image, due to its inherent use of light. The Abbe diffraction limit (d) (Equation 1.5) prevents the resolution of <~200 nm structures [79].

Equation 1.5 - $$d = \frac{\lambda}{2nsin\,\theta}$$ **[79]**

This limit is dependent on the numerical aperture of the lens (2nsinθ) and the wavelength of light entering the microscope. The numerical aperture is calculated from aperture angle and the

refractive index of the imaging medium [79]. A larger angle and refractive index leads to a greater numerical aperture, granting a better resolution. In addition, smaller wavelengths of light contribute to a better resolution through greater refraction. With a microscope's average numerical aperture being 0.2-1.4 the maximum resolution of 520 nm beam of light is ~370-260 nm [79]. Therefore nanometre sized domains on nano sized vesicles cannot be imaged using visible light microscopy as the vesicles are under the maximum resolution [80]. Phase separation on vesicles with nanometre diameters, required for cellular uptake, necessitates the application of other techniques.

Nanometre domain size measurements have been carried out for binary systems using a FRET based method, where the fluorescent tags phase separate in the l_d and l_{gel} phases [80]. More in line with this project's aims, the same techniques were used to investigate DOPC:DPPC:cholesterol liposomes [80], [81].

Initially the FRET based model for calculating domain sizes considers that there are two FRET pathways; either energy can be transferred across the bilayer in the same monolayer or transversely through the bilayer. Due to the large separation between the probes through (perpendicular to the membrane plane) the bilayer, FRET will be more predominant parallel across the membrane. As a result, low fluorescence is recorded from inter-monolayer FRET, outputting significantly less acceptor fluorescence intensity. This is in accordance with FRET's Förster radius (R_o) dependence (discussed in section 2.1.3.1 page 45). The resulting FRET efficiencies therefore describe lateral probe partitioning. Through phase separation saturated and unsaturated lipid probes de-mix, raising inter probe separation, reducing FRET efficiency. From FRET efficiency an average probe separation was calculated [80], leading to the formation of an extended DOPC:DPPC:cholesterol phase diagram [81].

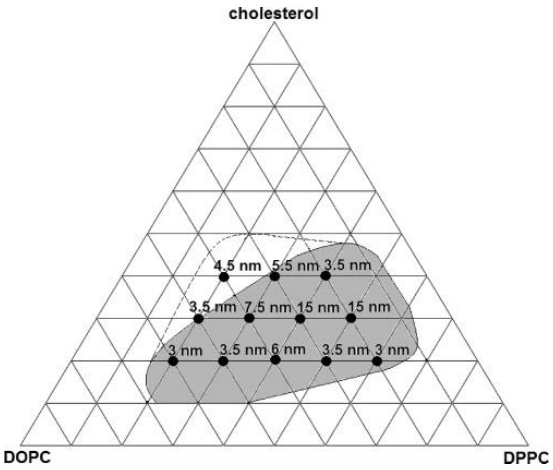

Figure 1.11 – DOPC:DPPC:cholesterol ternary phase diagram with l_d-l_o phase region fitted with suggested domain sizes (shaded area). The dashed line represents the suggested extension of the two phase l_d-l_o region, when the domain size model was applied [81].

The authors acknowledge that there is a major limiting factor of the model outlined. Through the inverse sixth power relationship in FRET calculations, the model can only consider domains 0.5-10 nm in diameter. When domains are in the range of 10 nm the model calculates equivalent energy transfer profiles. Even with this addressed, the authors plot domains >10 nm, which are high in error due to the loss in resolution at large distances [81]. It is of note that no definitive calculated errors are quoted. Furthermore it is debated the model cannot distinguish one domain size from another for large domains [80]. Finally it is discussed that the model assumes the smallest domains are always saturated l_o domains; this assumption limits the models wide potential use, preventing the ability of calculating l_d nanometre domain diameters [80].

Once vesicle surface heterogeneity had been achieved and demonstrated it was desirable to functionalise a vesicles surface to generate a Janus particle. However homogeneous vesicle functionalisation will first be discussed.

1.3 Homogeneous DNA functionalised liposomes

Research investigating DNA integration into both hard and soft colloidal systems has been examined for new gene therapy treatments, and more pertinently to this project, DNA connected colloidal superstructures [82]. In regards to this project, both hard and soft colloids have been shown to hybridise together, with the complementary DNA strands present on opposing particles [43]. In both cases the use of DNA offers many advantages namely; high specificity through the ATGC base pair coding for programmable assembly of aggregates and a programmable reversible aggregation, dependent upon surrounding conditions (discussed in section 1.5 page 38) [43]. It is of note that there are further benefits of using vesicles over their hard counterparts beyond their intrinsic biocompatibility; specifically, vesicles are structurally deformable. The inherent deformability affords the lipid membrane flexibility, reducing the strain on the helical DNA bridges, thereby providing an enthalpic gain over rigid particles [83] . While not directly linked with this project, DNA has also been shown to aid the fusion of vesicles [84]. Hard colloidal particles cannot mimic this behaviour, preventing the ability to tailor small scale reactions through vesicle cargo mixing. DNA vesicle integration consequently has a richer diversity of techniques and potential products over the hard colloidal alternative. Moving forward this review will only consider vesicles and DNA mediated cluster formation.

DNA directed lipid clusters have many applications beyond the realm of drug delivery. A substantial area of interest lays in mimicking biology's ability to compartmentalise cellular chemistry on micrometre and sub-micrometre length scales, using multi step reactors. These self-assembled reactor clusters would grant control over chemical processes, allowing for the maintenance of small quantities of active compounds at high concentrations [85], [86]. Furthermore, multi-step reactions in chemically incompatible environments (e.g. acidic and alkaline pH, or oxidising and reducing environments) could be achieved as the reactants move through each localised compartment [86].

The first experiments documenting tethered vesicle superstructures used homogenous liposome compositions in combination with commercially available cholesterol DNA (chol-DNA) lipids [43]. Upon vesicle formulation chol-DNA was applied, enabling the cholesterol moiety to anchor itself within the hydrophobic part of the bilayer, resulting in the DNA strands being randomly distributed out from the surface of the liposome. Figure 1.12 demonstrates when complementary cholesterol DNA is applied to separately prepared liposomes and then mixed, the DNA hybridises linking the two different liposomes together [43].

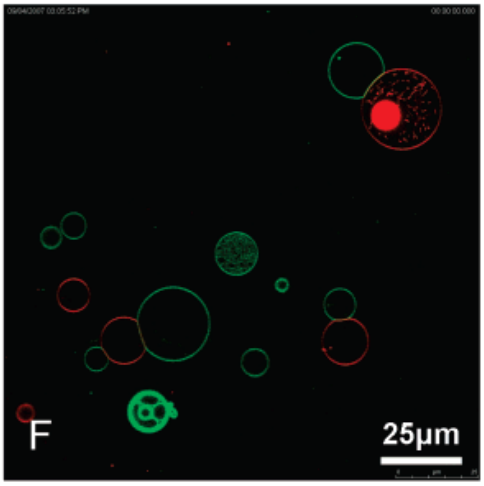

Figure 1.12 – An equator confocal microscopy image of two different populations of POPC liposomes tagged with complementary DNA (chol-DNA 10 mers) hybridised together. The colours (red and green) represent the different liposome types using a 5.0 ×10^{-3} ssDNA/lipid in a 38 mM Na^{+} solution [43].

To image the hybridised vesicles the groups of liposomes were tagged with two different fluorescent probes: 1,2-dipalmitoyl-*sn*-phosphoethanolamine-*N*-[lissamine rhodamine B sulfonyl] (Rh DPPE (red)) and Oregon Green 1,2-dihexadecanoyl-dn-glycero-3-phosphoethanolamine (Oregon Green 488 (green)) in conjunction with confocal microscopy.

To enhance the hybridisation seen in Figure 1.12 between vesicles, further similar experiments were imaged. Figure 1.13 displays the resulting level of hybridisation between vesicles when the DNA loading was decreased and salt concentration was increased from 5.0 ×10-3 ssDNA and 38 mM Na^{+} to 1.3 ×10-3 ssDNA and 47 mM Na^{+} respectively.

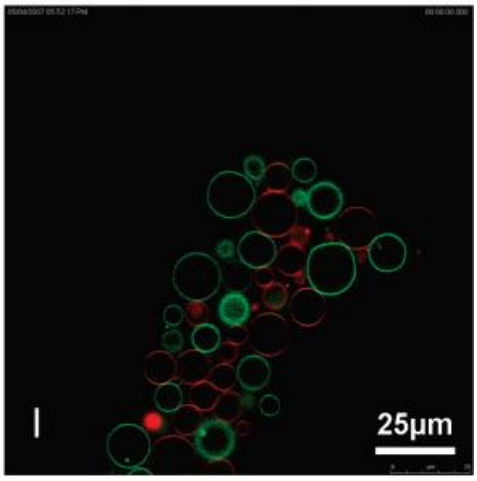

Figure 1.13 - An equator confocal microscopy image of two different populations of POPC liposomes tagged with complementary DNA (chol-DNA 10 mers) hybridising together. The colours (red and green) representing the different liposome types in a 1.3 ×10^{-3} ssDNA/lipid, 47 mM Na+ solution [43].

Even though the number of DNA strands was dropped, Figure 1.13 shows that salt shielding the negative phosphate back bone of the DNA has a profound effect on increasing levels of hybridisation.

While showing promise in terms of cluster size controllability, the data presented in Figure 1.12 and Figure 1.13 display a lack of specificity, where red and green liposomes are shown to be homogenously aggregating. This mono-aggregation should not be possible when considering the inherent DNA specific coding. To accommodate this observation the authors recognise that the cholesterol anchor and with it DNA linker, must be exchanging between liposomes [43]. The swapping mechanism was also discussed to be potentially enhanced by sucrose being present within the buffer, where cyclic sugar based molecules have been demonstrated to extract cholesterol from membranes [87]. Sucrose's structure is partially non polar (~25% of its surface) [87]; and therefore sucrose molecules could potentially cluster around non polar cholesterol, reducing the free energy difference between being anchored in the hydrophobic part of the bilayer and the aqueous solution [43].

1.4 Heterogeneous DNA functionalised liposomes

1.4.1 Cholesterol DNA conjugates

Being able to understand and control phase separation over a liposomes surface, grants the ability to localise functionality to a particular hemisphere of a vesicle. In the literature, phase

separation selectivity has been exploited to localise DNA conjugates to form Janus particles with “sticky” patches of DNA. Through using complementary DNA sequences, directional bridges between liposomes enable the formation of size limited clusters.

To overcome the previous cholesterol membrane switching issue, two new DNA vesicle bridging techniques were devised: The first utilised two cholesterol moieties with partially matching DNA sequences in the same liposome which hybridise together. The partial hybridisation still enables one longer sequence to heterogeneously bind together with a complementary vesicle [88]. The second method involved one DNA sequence being attached to two cholesterol moieties, thereby again doubling the anchorage to the bilayer through an increase in cholesterol lipid interactions [88]. The three methods discussed so far can be summarised in Figure 1.14.

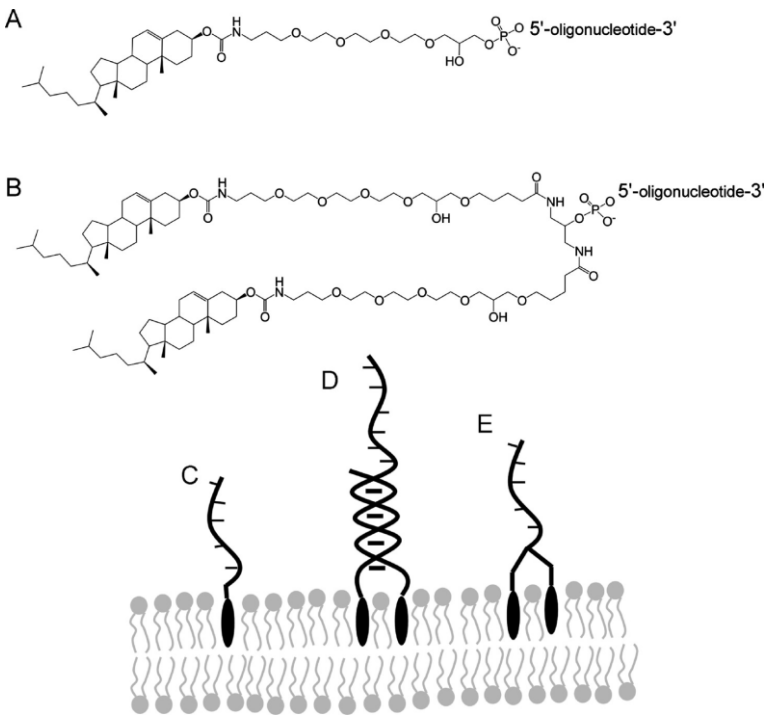

Figure 1.14 – DNA-cholesterol membrane binding methods. A displays cholesterol bound to a single DNA bridging group and C displays its cartoon representation when inserted into the membrane. B and E display the structure and a cartoon representation of two cholesterol moieties attached to DNA inserting into the membrane. Finally D shows a cartoon of two cholesterols both with a DNA sequence capable of binding together, with one sequence being longer than the other to allow for heterogeneous liposome bonding [88].

In l_d-l_{gel} phase separated vesicles, the partitioning of the chol-DNA was monitored using complementary DNA fluorescent dye conjugates. Subsequent DNA hybridisation enabled the detection of cholesterol DNA partitioning when combined with confocal fluorescent microscopy. Literature discusses that both the single and double cholesterol anchors predominantly partition

to the l_d phase when the liposomes contain 1,2-dilauroyl-sn-glycero-3-phosphocholine: 1,2-dimyristoyl-sn-glycero-3-phosphorylethanolamine (DLPC:DMPE) lipids in a one to one ratio. This result was rationalised through impurities within lipid bilayers always entering the most disordered phase, due to a high free energy cost of entering a highly ordered saturated gel phase [88]. In other words, it is rare for molecular additives to have a lower free energy cost when inserting into phases with a higher molecular ordering [88]. This behaviour contrasts with untagged cholesterol partitioning, whereby, cholesterol would normally enter a more saturated lipid domain. To understand this behaviour the cholesterol umbrella model must be discussed. Briefly, this model suggests cholesterol's small polar headgroup is insufficient in size to shield its large hydrophobic body from water. Fortunately when cholesterol is in a bilayer, neighbouring lipids manoeuvre their hydrophilic head groups towards cholesterol's hydroxyl group, which in turn covers the exposed hydrophobic body of cholesterol [89]. Specially in regards to cholesterol partitioning, a lipids ability to minimise cholesterol's water exposure is linked with the level of saturation in the lipid tail. Unsaturated lipids have less degrees of freedom and understandably, pack poorly with cholesterol, when compared to their saturated counterparts, resulting in poor coverage of cholesterol. Thus, untagged cholesterol preferentially partitions in domains rich with saturated chains, over those with mono- or polyunsaturated chains [89]. Furthermore, the need for the stabilising umbrella effect is likely minimised when cholesterol's small hydroxyl group is used to attach the bulky hydrophilic DNA moiety.

In ternary lipid systems, confocal images displayed the level of cholesterol DNA partitioning to be dependent upon whether a single cholesterol moiety or the bi-cholesterol DNA conjugates were applied. For the latter, the double anchored DNA cholesterols partitioned preferentially to l_o domains. Through the fluorescence intensities of labelled DNA, it was calculated that the concentration of double anchored DNA in the l_o phases was double that of the l_d phase [88]. For single cholesterol DNA conjugates there was a 10-20% preference of cholesterol entering the l_o phase [88]. This observation was rationalised through DOPC in the l_d phase having unsaturated carbon bonds, increasing the difficulty of cholesterol entering the domain. The rigid structure of cholesterol has a reduced number of degrees of freedom in the l_d phase over the l_o phase [90]. Explicitly, this is an entropic based argument where cholesterol has limited degrees of freedom or n conformations within the l_d phase, and qn possible conformations with q >1 in the saturated lipid region [88]. Similarly, the double anchored cholesterol DNA's partitioning can also be explained using the method described, with the addition of the assumption that conformational freedom between the two cholesterols is not coupled. The adapted model describes the first cholesterol entering the l_d bilayer in n configurations, with the second cholesterol also having n configurations. The cholesterol anchors can therefore enter the l_d domain in n^2 configurations. When applying the same logic to the l_o domain the cholesterols can enter the bilayer in q^2n^2 configurations [88].

Putting cholesterol partitioning theory aside, through being able to coordinate and enrich a l_o domain with DNA using the two cholesterol anchors, a heterogeneous liposome is converted to a Janus particle. The localisation of DNA affords the user the potential to build AB tethered vesicle structures rather than forming large uncontrolled aggregates as previously outlined. However,

though using a cholesterol membrane anchor, a significant proportion of DNA still partitions to the l_d phase of the membrane, removing the binary specificity required for controlled size limited aggregation [88].

To influence a stronger partitioning of the cholesterol DNA conjugates, a membrane composition in the centre of the DOPC:DPPC:cholesterol l_d-l_o coexisting phase was adapted to include the highly unsaturated lipid, CL. It was hoped that CL would mprove DNA partitioning to a specific phase and thus a create a more definitive binary Janus liposome. In these experiments 10 mol% unsaturated DOPC was replaced with CL. In essence, a lipid with two unsaturated symmetric acyl chains was exchanged for a lipid with four highly unsaturated symmetric acyl chains as outlined in Figure 1.15.

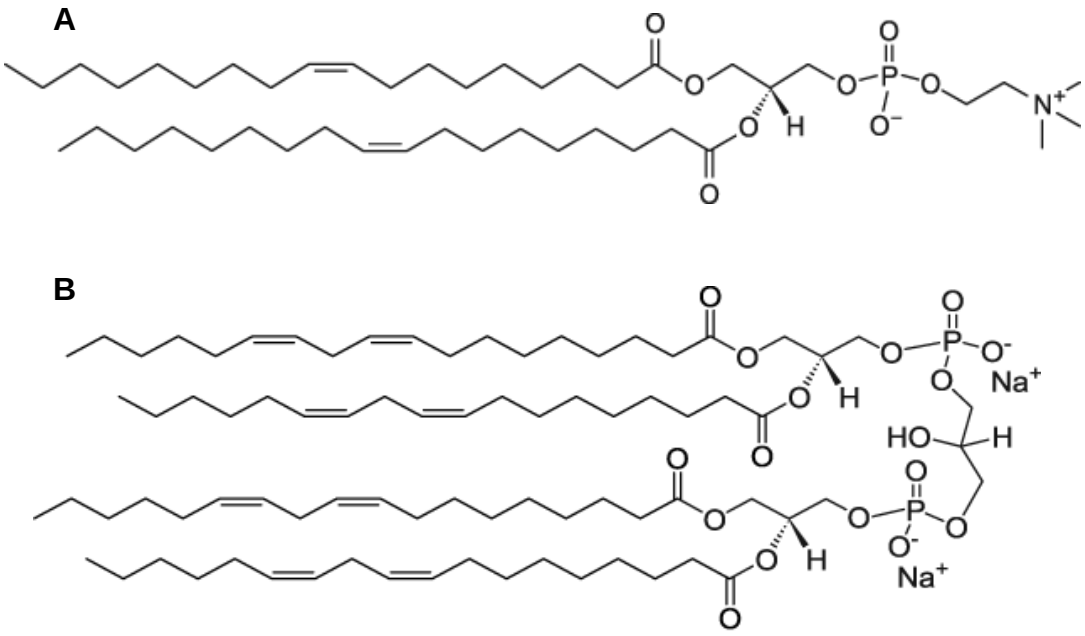

Figure 1.15 – A comparison of unsaturated lipid chemical structures: A – 1,2-dioleoyl-sn-glycero-3-phosphocholine (DOPC). B - cardiolipin.

Due to CL's highly unsaturated nature it strongly resides within the l_d phase, influencing both lipid and cholesterol partitioning [91]. CL inclusion is thought to increase lateral packing stress of lipids within the bilayer. In other words, the increased stress generated through CL inclusion creates a localised negative curvature force within the membrane [91]. It was hypothesised that the increased lateral stress in the hydrophobic region of the bilayer, may lead to an increase the cholesterol DNA free energy cost of packing into the l_d phase. As a result CL would enhance the partition of cholesterol DNA conjugates into the l_o domain, promoting directional DNA bridging between vesicles [91].

When implementing CL inclusion experimental data displayed that the exchange of 10 mol% DOPC with CL had a significant effect on the partitioning of both single and double cholesterol anchors. Preference towards l_o domain partitioning was increased by a factor of three for single

anchored DNAs [91]. Additionally double anchored chol-DNA was shown to provide superior l_o partitioning, displaying an order of magnitude difference between the l_d and l_o phases [91]. However, introducing CL to the phase diagram creates a four component system rather than three component one. In order to minimise changes in DOPC:DPPC:cholesterol phase behaviour, CL content was maintained at 10 mol%. This nevertheless is an estimate and CLs addition to the phase diagram would ideally need to be mapped, this in turn could allow selectivity in vesicle composition to drive separation. Rather than exploring this avenue to vesicle binding, the authors examined replacing cholesterol conjugates with lipid-DNA based conjugates to gain greater DNA partitioning control.

1.4.2 Lipid-DNA conjugates

It was initially hypothesised that DNA tagged lipids (lipid-DNA) would provide an opportunity to create an improved Janus liposome. The lipid moiety was suspected to be able to grant stronger bilayer interactions than cholesterol, increasing DNA anchorage to the bilayer, preventing DNA liposome swapping. Furthermore, the lipid acyl chain would also potentially offer a more robust DNA partitioning to the l_o phase, than seen in cholesterol mediated anchorage. However, DNA tagged lipids were not commercially available; consequently lipid-DNA had to be formed using a phosphoramidite approach undertaken in house. This process was broken up into a two-step synthesis, the schematic of which is displayed within Figure 1.16.

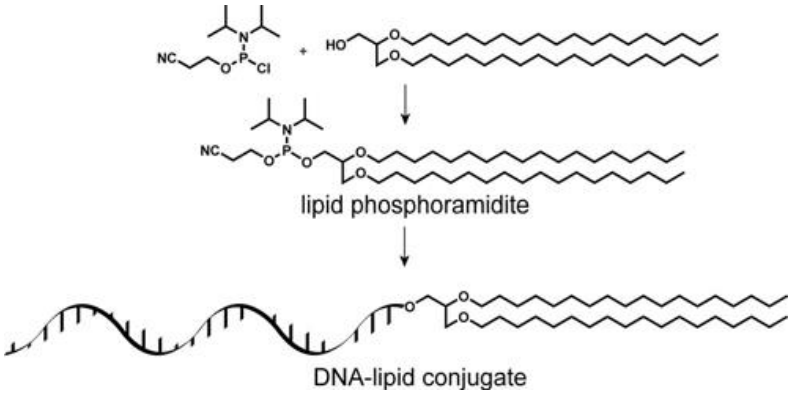

Figure 1.16 – Reaction scheme for creating a DNA tagged saturated lipid using the phosphoramidite approach [84].

The preparation of lipid-DNA involved a functional group substitution whereby the chlorine in 2-cyanoethyl N, N-diisopropylchlorophosphoramidite was removed and the “lipid tail” of 1,2-O-dioctadecyl-rac-glycerol was attached, forming a lipid phosphoramidite. The lipid

phosphoramidite was then dissolved in dichloromethane and attached as the “last base” to the DNA oligomer, generating the lipid-DNA conjugate [84].

Initial data from the inclusion of lipid-DNA conjugates within DOPC:DPPC:Cholesterol membranes, displayed a significant two to three times higher partitioning into the l_o phase over the l_d domains [91]. Additionally, the incorporation of 10 mol% CL into DOPC:DPPC:cholesterol vesicles, strongly influenced the partitioning of lipid-DNA conjugates. Using confocal fluorescence microscopy coupled with DNA fluorescence tagging, the Janus surface of the CL containing liposomes was imaged, whilst also enabling the relative fluorescence intensities to be plotted.

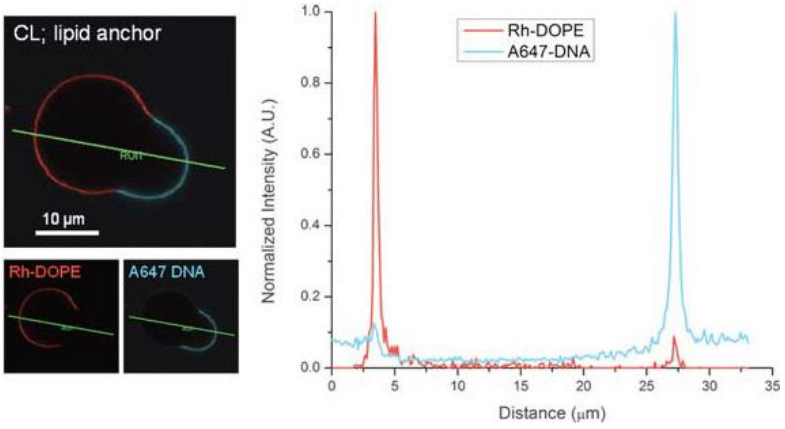

Figure 1.17 – An example of a confocal image of a DOPC:CL:DPPC:cholesterol liposome sliced through its equator. The green line represents an example of an intensity profile drawn through the coexisting phases. The red Rh-DOPE fluorescent dye displays the l_d phase and the blue A647-DNA conjugate dye displays the DNA functionalised surface of the Janus particle in the l_o phase [91].

From the fluorescence intensities (an example of which is plotted in Figure 1.17) it was inferred that the addition of CL had resulted in an order of magnitude increase in lipid-DNA partitioning to the l_o phase, over the ternary mixture of DOPC:DPPC:cholesterol [91]. Lipid-DNA conjugates in conjunction with CL provided a route to form improved directional size limited clusters, where work discussed previously using cholesterol-DNA conjugates had failed or had been shown to be not as affective [43].

Further samples combining CL addition with lipid-DNA were made and imaged through fluorescent microscopy. These new samples demonstrated the abundance of interactions size limited clusters can form when DNA is effectively localised to individual vesicles and domains.

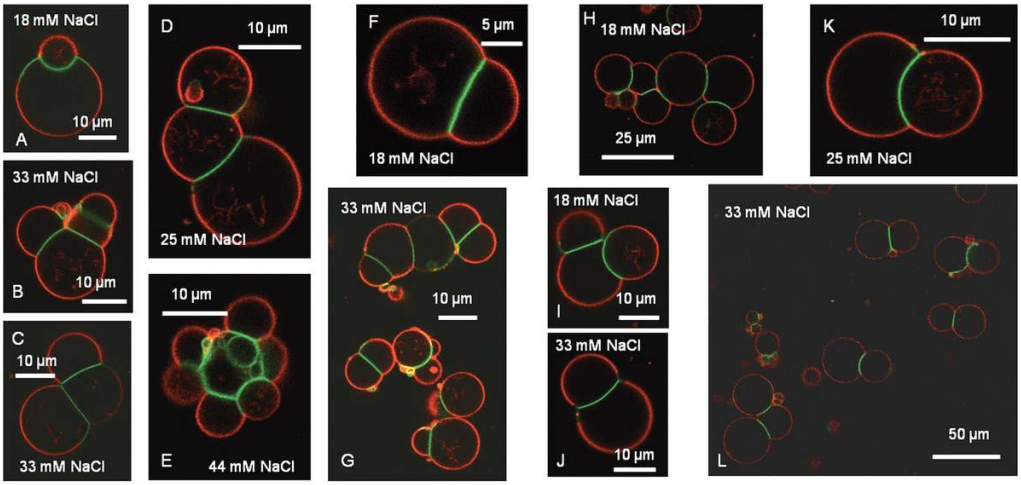

Figure 1.18 – Janus liposomes adhering together through complementary DNA hybridization with varying salt concentrations shown through confocal fluorescent microscopy images. The red fluorescent dye (Rh-DOPE) depicts the l_d phase and green fluorescent dye (NBD-DPPE) displays l_o regions functionalised with DNA [91].

Other than displaying the benefit of CL and lipid-DNA addition, Figure 1.18 illustrates evidence for a further advantageous effect between DNA adhesion plaques that helps promote size limited cluster formation. Due lipids forming soft deformable membranes, adhesion plaques of DNA can be flattened and misshapen. This membrane malleability results in the DNA plaques flattening together, encouraging DNA hybridisation initially limited by liposome curvature. Furthermore, flat adhesion plaques lead to only the l_d phase, with very dilute lipid-DNA present, being on the exposed periphery of the cluster; limiting any further hybridisation with other vesicles [91].

Once directional DNA bridges between vesicles were successfully formed and imaged, a loose model for DNA vesicle adhesion was created to account for the differences in the number of hybridised vesicles in Figure 1.18. The model takes into consideration both the strength of the DNA hybridisation between strands; which considers salt concentration and temperature, and the surface concentration of DNA/receptors within the phase [91].

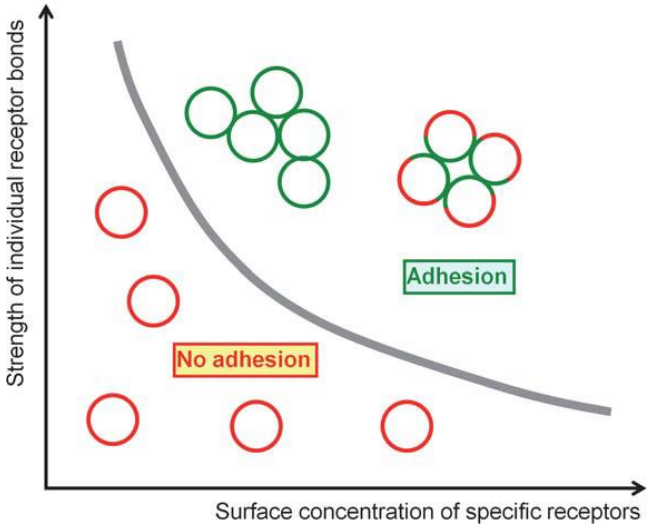

Figure 1.19 – Model displaying how surface concentration of DNA/receptors affects nanoparticle adhesion against the strength of e.g. DNA bonds [91].

Through interpreting the model, it can be seen that lots of short/weak bonding DNA sequences on the surface of the liposome would be required for liposome adhesion. Alternatively, few very long strongly hybridised DNA sequences would also result in liposome binding. The model also displays that in low salt concentrations, hybridisation and aggregation will be poor. The model therefore predicts that external stimuli can control both DNA hybridisation and dissociation, subsequently governing any liposome aggregation. Through DNA's switchable and reversible nature, a switchable device tailored towards therapeutic drug delivery is conceivable. In an effort to make this device a reality, work studying the dissociation of DNA-liposome clusters is imperative.

1.4.3 Dehybridisation of DNA

Liposomes tethered together through DNA have been demonstrated to reversibly aggregate and disassemble through a change in temperature as shown within Figure 1.20.

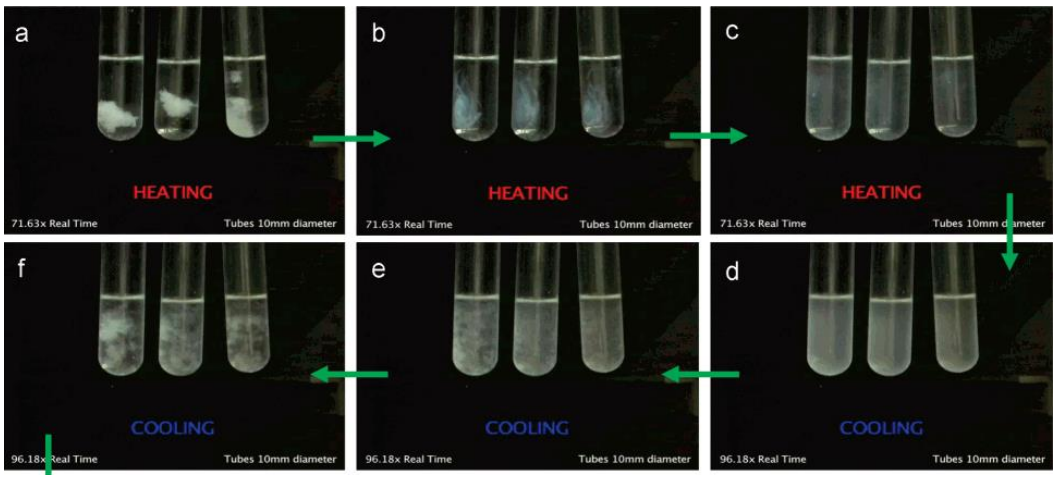

Figure 1.20 – Screenshots taken from a video of thermally driven assembly and disassemblyof DNA bridged liposome clusters [43].

Initially at cooler temperatures the vesicles shown within Figure 1.20 cluster together, forming a white flocculate that scatters incident light (a). Through heating DNA begins to dehybridise causing vesicles to break away from the initial large cluster (b). Additional heating then drives further dispersion of vesicles from the initial plaque (c). During the cooling cycle the opposite trend is recorded where liposomes bind together to form visible flocculates (d-f).

To melt DNA, the thermal energy of the solution needs to be greater than that of the hydrogen bonds between the ATGC base pairs connecting the strands together. To weaken this hydrogen bonding and lower the melting temperature of the DNA (T_m), salt concentration can be decreased. DNA has base pairs connected to sugars which in turn are all connect through a negatively charged phosphate backbone. The weak hydrogen bonding base pair recognition system of DNA is only possible with sufficient positive salt ions, screening the negative phosphate charge. To ensure DNA tethered vesicles with intended biological use are stable at 37 ^{o}C it is appropriate to measure/calculate DNA melting temperatures.

This review will now consider a few approaches to calculating and measuring T_m of DNA. Classically when calculating T_m two equations can be used: the first being the Wallace rule.

Equation 1.6 - $$\boldsymbol{T_m = 2(\#A + \#T) + 4(\#C + \#G)}$$ **[92]**

Where T_m is the melting temperature of DNA in degrees Celsius #A #T #C #G are the respective numbers of base pairs in the DNA sequence. The Wallace rule has limited potential use, it is discussed that it is best applied when calculating sequences 14-20 base pairs long in a sodium chloride solution equal to 1 mol dm^{-3}, [93], [94]. Furthermore the Wallace rule in its simplicity

does not consider DNA concentration, changes in salt concentration or any nearest neighbour interactions, therefore making it inaccurate and inappropriate to use. A more accurate method for calculating the T_m involves an equation termed the nearest neighbour empirical formula (Equation 1.7) [95]. Its improvement over the Wallace rule is due to both the sequence of base pairs and the environmental salt concentration being taken into consideration.

Equation 1.7 $$T_m = (1000\Delta H)/A + \Delta S + Rln(C/4) - 273.15 + 16.6\,log[Na+] \quad \textbf{[95]}$$

ΔH is the sum of nearest neighbour enthalpic interactions; A is a small constant to correct for helical initiations; ΔS is the sum of nearest neighbour enthalpic interactions (where ΔH and ΔS are found tabulated in data books); R is the molar gas constant; C is the concentration of the oligo and $[Na^+]$ is the concentration of salt (sodium ions) [93].

However, for complex DNA-liposome tethering it is more appropriate to use an experimentally driven method to measure the T_m of DNA rather than calculate it. Through experimentally measuring T_m, potential liposome effects that could change the melting temperature are recorded, leading to better modelling of vesicle aggregate systems. Additionally through measuring the T_m both ΔH and ΔS can be more accurately calculated as a function of concentration [96].

DNA is widely known for having distinct ultraviolet (UV) absorption peaks at 260 and 280 nm, where the ratio of the absorbance's at these wavelengths is used to determine DNA purity [97]. Absorbance at the UV range has been discussed to be due to π to π* electronic transitions of the base pairs. These transitions are only available when the DNA is in its free form; once hybridised DNA absorbance is significantly reduced [98]. In line with this, heating and cooling cycles of DNA have shown to exhibit a UV absorbance sigmoidal transition curve. Transition curves were smoothed and the upper and lower baselines were normalised to f=0 and f=1 were f is the fraction of unbound bases [96]. The centre of the curve where f= 0.5 represents the T_m of the DNA. To extract the T_m the first derivative was taken and plotted with the peak maximum being the T_m. A similar experimental procedure can be implemented to calculate T_m of DNA liposome aggregations but at 320 nm with melting curves being attributed to scattering [96].

To extract entropy and enthalpy data, a series of van't Hoff plots for DNA tethered vesicles was produced through raising the concentration of DNA/vesicle. Such plots have been outlined in Figure 1.21.

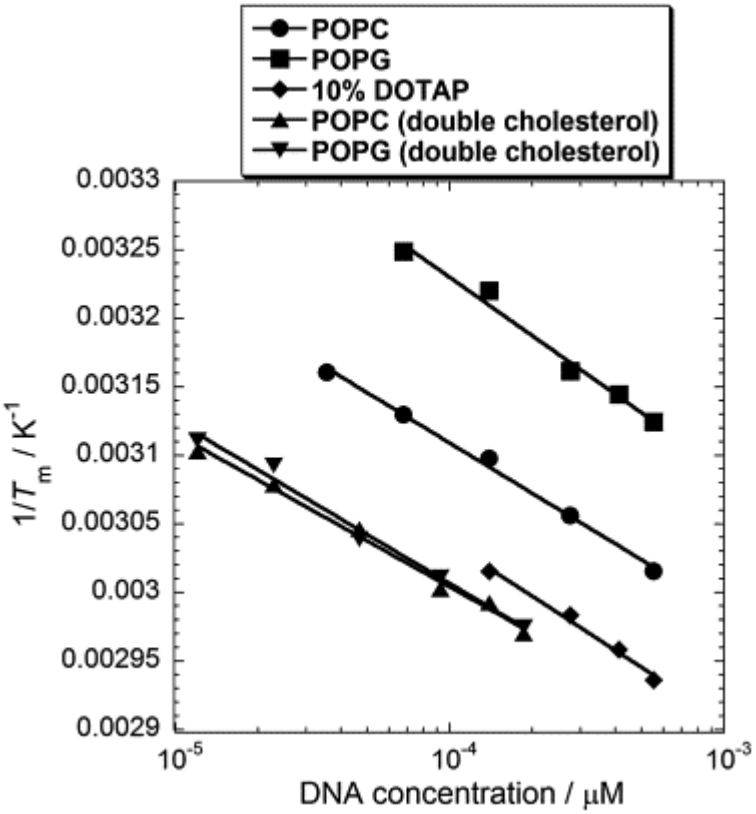

Figure 1.21 – An example of van't Hoff plots for the melting data of non-Janus DNA bridged POPC, POPG vesicles, implementing cholesterol DNA conjugates. The graph shows DNA concentration on the vesicle surface plotted against inverse temperature.

Diverting from the main narrative of this review, it would appear that there is a mistake on the graph presented in Figure 1.21. Specifically, the DNA concentrations plotted would not be feasible if the x axis label is to be believed. Nevertheless, a derivation of the traditional van't Hoff equation for modelling DNA hybridisation was made by the authors, describing the effect of liposome intermembrane forces on DNA melting [96]. The van't Hoff equation and its liposome derivative are shown in Equation 1.8 and Equation 1.9 respectively.

Equation 1.8 - $$T_m = \frac{\Delta H^0}{\Delta S^0 + k_B ln(C_T/4)}$$ **[98], [99]**

Equation 1.9 - $$T_m = \frac{\Delta H^0 + U^F}{\Delta S^0 + k_B ln(C_T/4)}$$ **[96]**

Where ΔH and ΔS are the enthalpy and entropy change per molecule between single and double strands of DNA, K_B is the Boltzman constant, C_T is the total concentration of DNA strands and U^F is the work done by intermembrane forces [96]. In conjunction with the van't Hoff plot and Equation 1.9, the gradient and intercept are $R/(\Delta H + U^F)$ and $\Delta S/\Delta H$ respectively, enabling ΔH and ΔS to be calculated where R is the molar gas constant. The model developed to estimate U^F displayed that intermembrane forces do play an important roll for short DNA sequences, with longer sequences reducing the effect of intermembrane pressures [96]. Thirty BP sequences were shown to be adequate in providing tethering without significant intermembrane forces. The authors further discuss that intermembrane forces are not just unique to liposomes but also significant to other NPs tethered using DNA [96].

Lipid-DNA conjugates have so far been shown to have melting temperatures dependent upon DNA length, salt concentration, nearest neighbour interactions and the attached NP. This review will now examine how modified DNA sequences can make for programmable dehybridisation.

1.5 DNA i-Motifs

In nature DNA extensively exists in its B-form double helix state, but it is well researched that DNA can form other secondary structures including; three way junctions, triplexes and quadruplexes [100], [101]. i-motifs are an example of a C-quadruplex, where cytosine-rich DNA sequences intercalate (i) together to form a self-hybridising strand of DNA [102]. A cartoon of regular B-form DNA attached to C-quadruplex DNA has been shown in Figure 1.22.

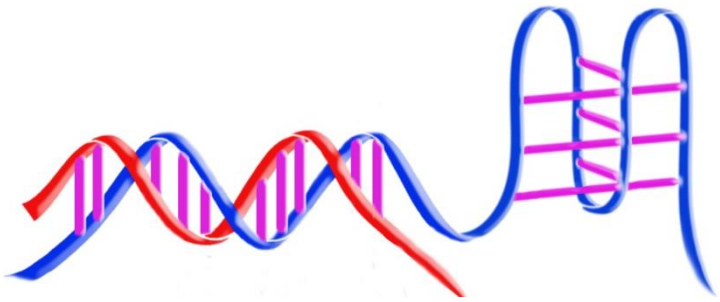

Figure 1.22 – A cartoon of the Watson-Crick duplex structure and the C-quadruplex intercalated DNA structure.

DNA i-motif sequences are responsive to pH's in acidic conditions, the added protons afford cytosine to become hemiprotonated at the N3 position (Figure 1.23), forming cytosine–cytosine hydrogen bonded base pairs. The resulting hybridisation produces stronger intra-strand BP interactions over inter-strand cytosine-guanine bonding [102]. The preference of C-rich DNA to intercalate with itself in acidic conditions dehybridises Watson-Crick duplex DNA, creating a switch.

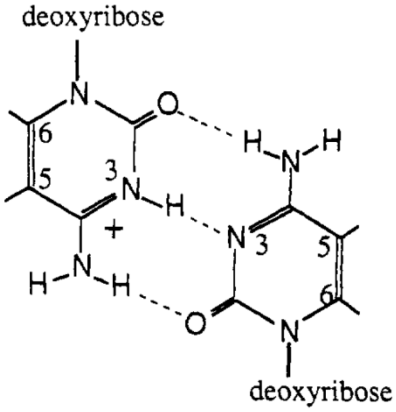

Figure 1.23 – Hemiprotonated DNA cytosine–cytosine hydrogen bonding in acid conditions [103].

An i-motif structure can form as two variants which are dependent upon the positioning of the outermost cytosine–cytosine bonding base pair [104]. The position of the base pair more specifically relates to whether the cytosine is in a 3' or the 5' site in the DNA [105]. Resulting structures from cytosine's 3' and 5' positioning were determined through NMR and are shown in Figure 1.24. Figure 1.24 also shows wide and narrow grooves still being present in the hybridised molecule, where the small groves are thought to be a major stabilising factor enabling CH···O hydrogen bonding.

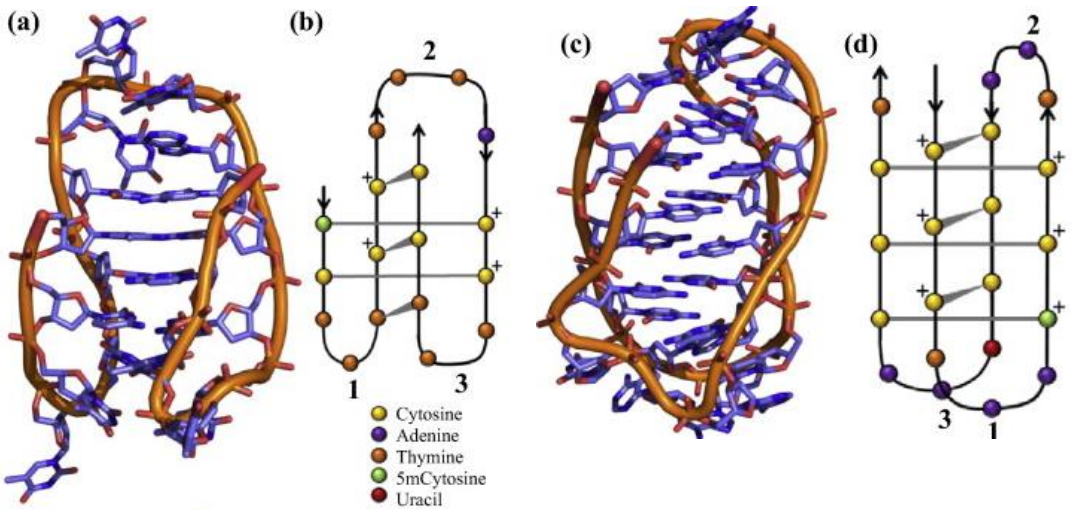

Figure 1.24 – (a) An NMR determined structure for an example 3' based cytosine system, (b) a schematic diagram for an example 3' based cytosine system, (c) an NMR determined structure for an example 5' based cytosine system, and (d) a schematic diagram for an example 5' based cytosine system [106].

The pH sensitivity of i-motif formation is spread from pH's 7 to 3, where the exact pH is dictated by the surrounding conditions and the addition of stabilising and destabilising features in the DNA sequence [106]. i-motifs still have phosphorus and sugar backbones making them susceptible to salt conditions as seen for the Watson-Crick duplex. Low salt concentration results in limited shielding of the negative phosphate groups, introducing intrarepulsion of DNA preventing intrahybridisation. Furthermore, guanine or thymine insertion into the cytosine sequence makes DNA i-motif formation unfavourable, through reducing the stabilising hemiprotonated cytosine–cytosine hydrogen bonding [105].

Previous studies have attached i-motif sequences to GNPs, via a thiol attachment, in an effort to develop a targeted drug release mechanism in cancer therapy. At homeostatic pH (~7.4) i-motifs form duplexes, however when in a low pH environment, for example, in close proximity to diseased tumour tissue or in an intracellular endosomal/lysosomal compartment, it is hoped the i-motif will present a triggered response. Using a complementary hybridised sequence with doxorubicin, a model anticancer drug, was stably intercalated into the duplex [107]. Upon reducing the pH down to ~5.1, cytosines became hemiprotonated promoting intrahybridisation and DNA dissociation, subsequently releasing doxorubicin [107]. This mechanism is displayed in Figure 1.25.

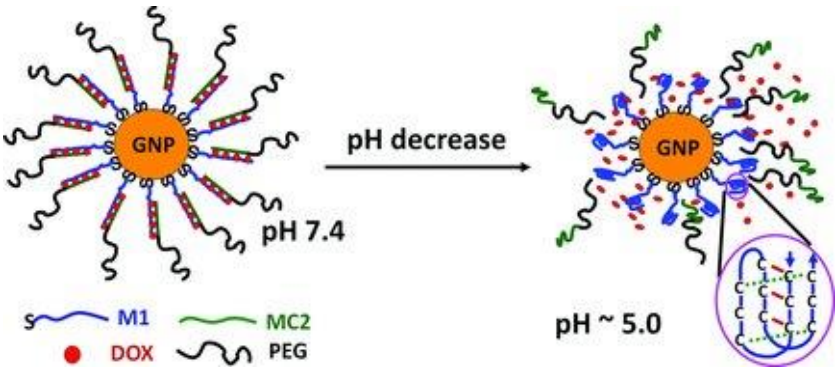

Figure 1.25 – Cartoon displaying the pH controlled loading and release of doxorubicin (DOX). At normal physiological pH (7.4), DOX is intercalated in the DNA duplex which is in turn attached via a thiol group to the GNP. In an acidic environment (pH < 5.1), DNA dissociates releasing DOX. Inset showing the formation of an i-motif [107].

Through exploiting the i-motif pH switching mechanism, as demonstrated by D. Zhou et al., a biologically relevant triggered release could be implemented in vesicle therapeutic nanocarrier design. Once incorporated into NP flocculates, i-motifs could promote the destabilisation of NP bridges for a triggered response. In other words, lipid-DNA i-motifs can be tailored towards a targeted delivery technique, whereby a flocculation of NPs can be broken up in the presence of an acidic site; for example within tumours [108]. Furthermore, by using lipids instead of GNPs and thiol attachment groups, there is a higher degree of control in regards to in transit therapeutic protection and therapeutic loading. Additionally, the employment of lipid based drug delivery technology ensures the benefits previously discussed in section 1.1.2 page 4.

1.6 Aims

Three themes run through the papers reviewed here. The first demonstrates the potential of liposomes as therapeutic nanocarriers over their hard and soft counterparts. The second illustrates DNA being used as a responsive tether to directionally link dimer AB liposomes together, rather than form uncontrolled clustering. And finally, DNA i-motif incorporation was discussed in reference to yielding a potential triggered vesicle dissociation mechanism.

These three topics were directed towards the overarching project goal of developing directionally linked Janus DNA connected vesicle clusters, to form the basis of a new therapeutic drug delivery platform. It is hoped that this platform will be then be taken forward and tailored towards “real world” treatments. However, to produce the initial drug delivery platform four key stages need to be fulfilled in this project:

1. Map a four component phase diagram of DOPC:DPPC:cholesterol:CL using 100 nm diameter liposomes where cardiolipin is set at 10 mol%.
2. Incorporate lipid-DNA into vesicles and measure hybridised vesicle flocculate melting temperatures, ensuring platform stability and DNA suitability.
3. Examine resulting size limited DNA hybridised vesicle flocculate size through DLS, in conjunction with the newly plotted phase diagram.
4. Integrate lipid-DNA i-motifs within vesicles and measure a pH triggered response.

Chapter 2

Experimental procedures

This chapter examines the instrumentation, materials and methods used/carried out throughout this project. Additionally, a brief scientific introduction is given to each instrument used.

2.1 Instrumentation and theory

2.1.1 Thermocouple

A type K thermocouple was implemented to ensure the temperature of key stages in vesicle preparation was maintained above the highest lipid melting temperature. Furthermore, a thermocouple monitored the temperature within the fluorometer when conducting FRET experiments. Within a K type device alumel and chromel alloys are fused together, where: alumel is 95 % nickel, 2 % manganese, 2 % alluminium, 1 % silicon and chromel is 90 % nickel 10 % chromium [109]. Due to the Seebeck effect, when the fused junction between the dissimilar metals is heated a temperature gradient is formed across the wires. This temperature increase allows the movement of charge carriers to diffuse from the heated junction to the cold second junction [63]. The voltage difference generated was then applied to a calibration table [110]. The gradient between the two junctions is dependent upon the temperature of both junctions, therefore the reference junction was held at the calibration reference temperature of 0 ^{o}C, achieved through using an ice bath.

2.1.2 Ultraviolet-Visible (UV-vis) spectroscopy

When conducting the phosphorus assay to determine phosphorus content of samples, and DNA thermal-melt experiments, UV-visible spectroscopy was applied to measure the change in light absorbance.

Light absorbance is due to electron excitation from the highest occupied molecular orbital (HOMO) to the lowest unoccupied molecular orbital (LUMO). This band gap between the HOMO and LUMO has an associated energy and a resulting associated excitation wavelength (λ_{max}). Raising analyte concentration promotes the number of HOMO to LUMO excitations, increasing light absorbance. When calculating absorbance a reference is measured at the same wavelength, matching the solvent and cuvette type, to account for any absorbance that was not due to the

analyte [111]. The reference and sample signals can then be used to calculate the analyte's absorbance.

Equation 2.1 - $A = Log \frac{I_0}{I}$ **[111]**

Where l_o is the reference signal and I is the sample signal both measured in watts (W) and A is absorbance, a unit less parameter. Once absorbance has been calculated the Beer-Lambert law can be applied to calculate the concentration of analyte.

Equation 2.2 - $A = \varepsilon lc$ **[111]**

Where ε ($M^{-1}cm^{-1}$) is the molar extinction coefficient, a proportionality constant which allows different spectra to be compared. l is the path length of the cuvette (cm) and c is the concentration of analyte ($moldm^{-3}$) [111].

In order to measure the change in light absorbance a UV-visible spectrometer requires a light source, which is dependent upon the wavelength of light required. Wavelengths that are in the UV range require a deuterium bulb, where as to generate wavelengths that are within the visible region a tungsten bulb is required [111]. Both bulbs generate a spectrum of wavelengths, which are broken into individual wavelengths through a monochromator [111]. The selected wavelength passes through the sample, where some of the light is absorbed, to the detector. The detector is commonly a photomultiplier tube (PMT) [111]. The basic instrument layout has been described in Figure 2.1.

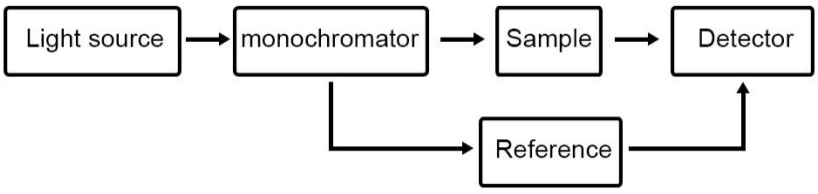

Figure 2.1 – A schematic diagram displaying the major components of a UV-vis spectrometer. Black arrows representing the pathway of light to the detector.

2.1.3 Fluorescence spectroscopy

Fluorescence spectroscopy was used in Förster Resonance Energy Transfer (FRET) experiments and was integral in the detection of nano-size vesicle phase behaviour.

Fluorescence is achieved by electromagnetic radiation being absorbed, through electrons being electronically excited, and then subsequently relaxing. The process of excitation and relaxation is best described when coupled with the Jablonski diagram presented within Figure 2.2.

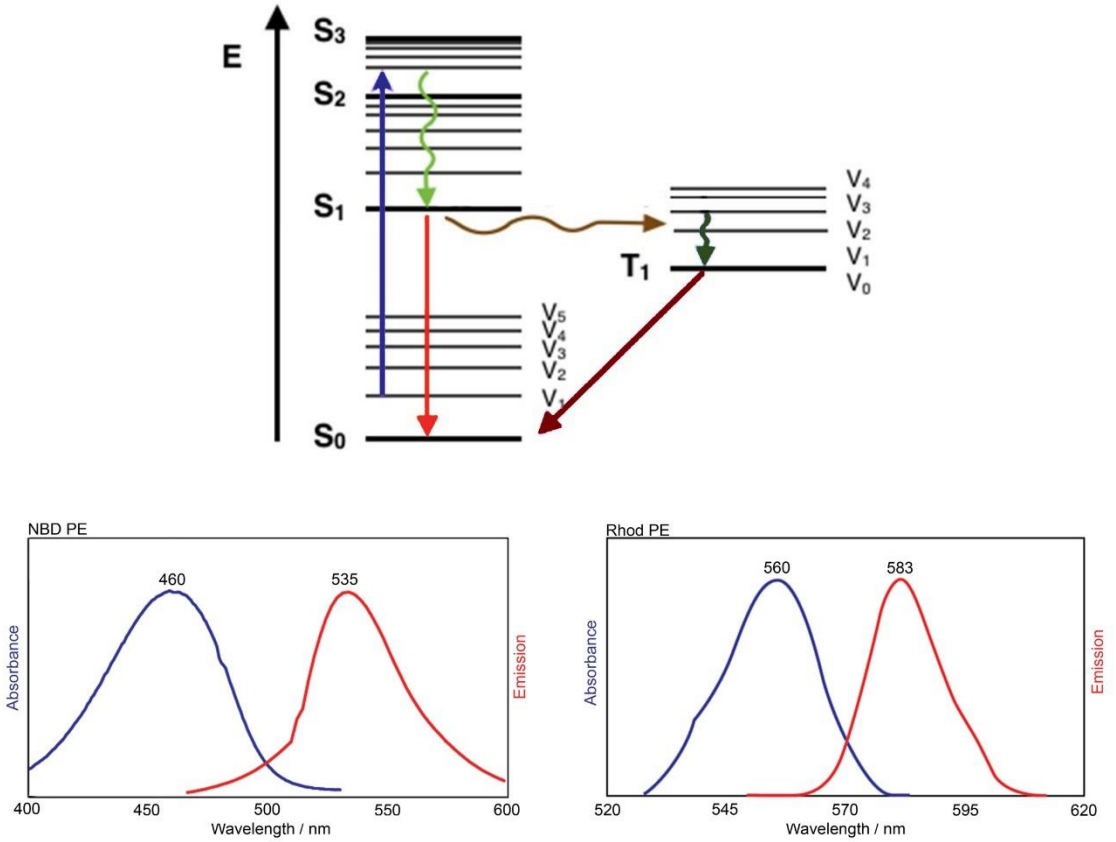

Figure 2.2 – Top: Jablonski diagram, where E is energy with S_1, S_2, S_3 and T_1 being electronic energy levels. Between the electronic energy levels V_1, V_2 V_3 etc. represent the vibrational energy levels. Arrows display energy pathways where: blue; photon absorbance, green; internal conversion, red; fluorescence emission; brown-intersystem crossing, dark green; vibrational relaxation, dark red; phosphorescence [112]. Bottom: Normalised absorbance and emission spectra for 1,2-dipalmitoyl-sn-glycero-3-phosphoethanolamine-N-(7-nitro-2-1,3-benzoxadiazol-4-yl) (NBD PE, FRET donor) and 1,2-dioleoyl-sn-glycero-3-phosphoethanolamine-N-(lissamine rhodamine B sulfonyl) (Rhod PE, FRET acceptor) at a concentration of 1 µg/ml in Chloroform respectively [113], [114].

From the Jablonski diagram it can be seen that the first transition is the excitation of an electron from the electronic ground state, to an electronic excited state (blue arrow). This transition is achieved through an incident photon of light being greater in energy than the energy gap between the ground and excited states [112]. The blue line in the spectra for NBD PE and Rhod PE in Figure 2.2 displays experimental data for the absorbance of this energy. Once excited the electron will then relax back to its ground state through various pathways: The Jablonski diagram displays that the molecule will initially relax through non-radiative intramolecular and intermolecular kinetic

movement, an example of this relaxation is represented by the dark green arrow [112]. The next option for relaxation is fluorescence; a drop from the energetically higher excited electronic state to the ground electronic state, releasing a photon shown by the red arrow. This released photon is lower in energy than the incident beam due to energy being previously lost through vibrational pathways [111]. The red line in the experimentally determined spectra in Figure 2.2, displays the lower energy fluorescent light being emitted. When excitation occurs above the HOMO, the possibility of vibrational and electronic energy levels overlapping increases. As a result of the states overlapping, internal conversion can take place, where electrons drop down electronic energy levels, through a vibrational mechanism, rather than a fluorescence mechanism. Internal conversion can be seen in the Jablonski diagram between the electronic energy levels S_3 and S_2, highlighted by the green arrow [111].

A less common relaxation route is also available when dissipating energy; named intersystem crossing (brown arrow). Intersystem crossing occurs when an electron changes its spin state from an excited single state to an excited triplet state [111]. In the excited triplet state molecules can undergo vibrational relaxation. However, only when the triple state reverts back to its singlet state can the electron electronically drop back to the ground state, whereby it emits a photon via phosphorescence (dark red arrow) [111]. Phosphorescence is a less common route of relaxation than fluorescence, and is a much slower process, due to the route involving a forbidden energy state transition [111].

To initiate fluorescence an incident beam of light needs to be generated. This is achieved through two commonly used light sources; a low pressure mercury lamp and xenon arc lamp, both providing a spectrum of wavelengths across the visible and ultra violet range [111]. Figure 2.3 displays the light passing through the instrument. Initially light hits the monochromator that selects the wavelength of UV-vis radiation desired for excitation. The wavelength enters the sample which excites the fluorescent analyte. The collection monochromator enables fluorescence intensity to be plotted against emission wavelength, where the 90^{o} positioning to the excitation beam significantly reduces incident photons being detected. Light detection is achieved through either; PMT's or silicon photodiodes (PD). Both detectors yield units of counts per second (CPS), describing how many photons strike the detector every second [111].

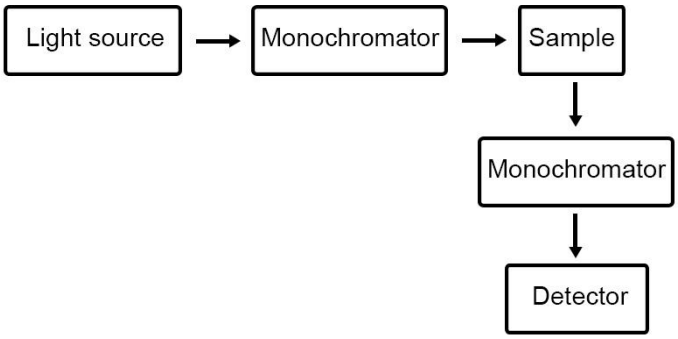

Figure 2.3 – Schematic diagram displaying the major components of a fluorometer. Black arrows representing the pathway of light to the detector [115].

2.1.3.1 Förster Resonance Energy Transfer (FRET)

FRET is an acronym for Förster Resonance Energy Transfer. FRET commonly involves using two compatible fluorescent dyes simultaneously in the same sample; deemed donor and acceptor. In order for FRET to occur spectral overlap between the two dyes must exist, whereby the emission of the donor dye must overlap with absorbance of the acceptor dye by ~30% [77]. When the donor dye is excited, rather than fluorescing, it passes on its energy through a non-radiative resonance process, electronically exciting the acceptor dye [73]. Through electronic relaxation electrons will re-enter their ground states releasing photons [73]. The emitted photons will be lower in energy than the initial resonance excitation and the initial incident beam of light due to energy loss through vibrational mechanisms, producing a red shift. The energy transfer process can be best understood when again considering a Jablonski diagram.

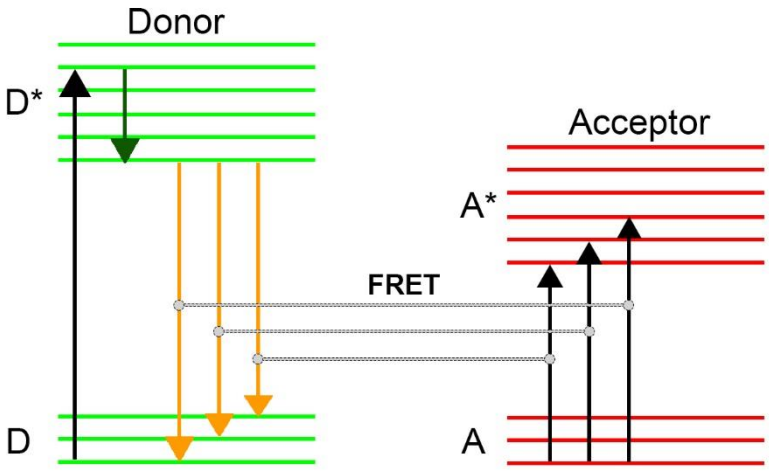

Figure 2.4 - Jablonski diagram displaying FRET, where D, A and D* and A* are the donor, acceptor ground states and electronically excited states respectively. Black arrows represent excitation transitions, the green arrow represents non-radiative relaxation, orange arrows display electron donor relaxation and grey lines define resonance energy transfer [116], [117].

From Figure 2.4 it can be seen that the acceptor and donor ground and excited states are of the same magnitude of energy. The band gap between the ground and excited states for the donor and acceptor also overlap in energy; this overlap is necessary in order for FRET to occur. The overlap between dyes, combined with the energetically lower excitation bands in the acceptor, according to resonance to excite the electrons from the ground state of the acceptor into an excited state [118].

While the energy overlap between probes is vital for energy transfer, probe separation also plays a significant role. The further the dyes are from one another the lower the probability of exciting an acceptor decreases in an inverse power of six relationship as described in Equation 2.3.

Equation 2.3 - $$E = \frac{(R_o/r)^6}{1+(R_o/r)^6}$$ **[73]**

Where E is energy transfer efficiency, r is the distance between the two dyes and R_o is the Förster distance, which is defined as the distance where energy transfer is 50% efficient. R_o is calculated through Equation 2.4.

Equation 2.4 - $$R_o = 9.78\times10^3(n^{-4}\times f_d\times k^2\times J)^{1/6}$$ **[80]**

Where n is the refractive index of the solution, f_d is the fluorescence quantum yield of the donor dye when the acceptor is not present, k^2 is the dipole angular orientation of each dye, and J is the spectral overlap integral (discussed in section 3.1.1 page 67) [80].

The distance dependence of probe FRET efficiency can be used as a useful tool to monitor probe separation. To calculate probe separation using Equation 2.3, the FRET efficiency (E) of a sample must be experimentally determined in conjunction with Equation 2.5.

Equation 2.5 - $$E = 1 - \frac{D_{DA}}{D_D}$$

Where D_{DA} is the maximum donor fluorescence intensity when both donor and acceptor dyes are present in the sample, and D_D is the maximum donor fluorescence intensity when only the donor dye is present within a sample. From Equation 2.3 and Equation 2.4 only nano-scale separation, typically between 1-10 nm [119], allows for detectable resonance energy transfer. Subsequently, separating the dyes further than 10 nm limits energy transfer yielding high experimental error. Other methods of quantifying FRET include calculating a FRET ratio.

Equation 2.6 - $$FRET\ ratio = \frac{A_{DA}}{D_{DA}}$$

Where A_{DA} represents maximum acceptor fluorescence intensity when both donor and acceptor dyes are present in the sample. The ratio between the donor and acceptor intensities does not directly measure E but exists as a relative measure of FRET. Because of this the FRET ratio should only be used for qualitative purposes or for monitoring relative changes in the FRET efficiency.

Additional FRET based experiments where the acceptor does not fluoresce but quenches the donor are documented but these will not be discussed here [119].

2.1.3.2 Confocal fluorescence microscopy

To confirm FRET analysis, images of vesicles were taken using confocal fluorescence microscopy. The foundation of fluorescence imaging involves the same fluorescence principles discussed in section 2.1.3 page 42. However, to produce a fluorescence image the excitation beam requires focusing. To focus the beam, lens' are implemented similarly to an epifluorescence instrument. However, confocal microscopy utilises additional confocal pinholes and a laser to

remove unfocused light, producing focused, crisp images. The schematic diagram of the workings of a confocal fluorescent microscope have been illustrated in Figure 2.5.

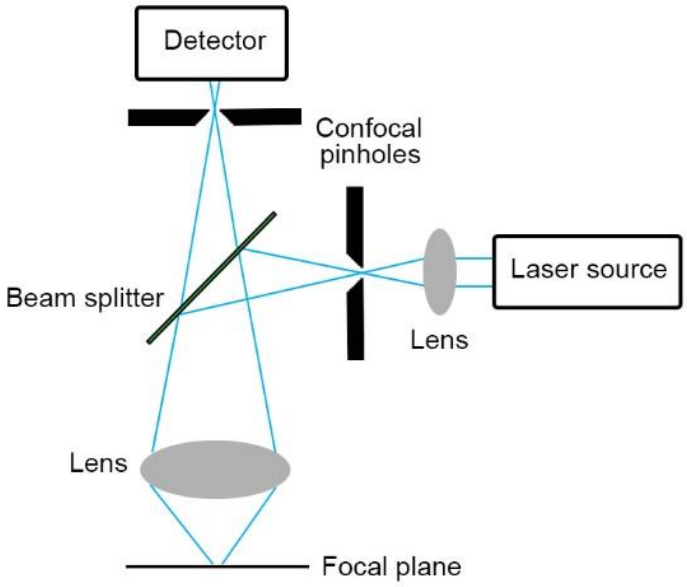

Figure 2.5 – Schematic diagram displaying the major components of a confocal fluorescence microscope. Blue lines show the pathway of light to the sample and back to the detector.

To produce an image, the laser source must be paired with the fluorescent dye's λ_{max} for reasons outlined in FRET detection. Furthermore, in order to detect the fluorescent light a charge-coupled device (CCD) is commonly used.

2.1.4 Dynamic Light Scattering (DLS)

Dynamic Light Scattering (DLS) was used to measure the hydrodynamic radius of individual vesicles and vesicle aggregates. Fundamentally, DLS involves the measurement of the diffusion coefficient of the particle of interest. When the diffusion coefficient is applied to the Stokes Einstein equation the hydrodynamic radius can be calculated.

Equation 2.7 - $$r = \frac{kT}{6\pi\eta D}$$ **[120]**

r is the hydrodynamic radius, η is the viscosity of the sample, T is temperature, k is the Boltzmann constant and D the diffusion coefficient. To define the diffusion coefficients of particles in solution, the instrument measures scattered light in time intervals, tracking particle movement in Brownian

motion. Under Brownian motion larger particles move at slower rates than smaller particles, owing to solvent molecule bombardment in random thermal motion. DLS therefore measures scattering intensity of light off of these particles over time. The application of an auto correlation function (Equation 2.8) extracts the time dependence of the scattering signal in the presence of noise.

Equation 2.8 - $$G^{(2)}(\tau) = \frac{\langle I(t)I(t+\tau)\rangle}{\langle I(t)\rangle^2}$$ **[121]**

Where G(τ) is the auto correlation function with respect to scattering intensity, I is intensity of scattered light, t is time and τ is delay time. Through increasing τ, signal is raised above random noise. By plotting the auto correlation function against time, a decay curve is produced, which is modelled through Equation 2.9.

Equation 2.9 - $$G^{(2)}(\tau) = B + A\sum e^{(-2q^2D\tau)}$$ **[121]**

Equation 2.9 provides a platform where the diffusion coefficient (D) can be calculated. B is the baseline at infinite time, A is the intercept and q is the scattering vector calculated using Equation 2.10.

Equation 2.10 - $$q = (4\pi\, n/\lambda_o)\, sin(\theta/2)$$ **[121]**

Where λ_o is laser wavelength and θ is the detection angle.

A schematic of a DLS instrument is presented in Figure 2.6 displaying the detector at a >90° angle to the sample. Common angles being either at 90° for right angle detection and 173° for back angle detection, where back angle offers a preferred choice for smaller nano-sized particles [122]. The instrument is also commonly equipped with a He-Ne laser at 633 nm and a PMT detector [121].

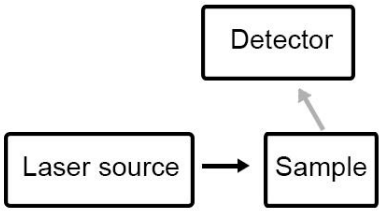

Figure 2.6 - Schematic diagram displaying the major components of a DLS instrument. The black arrow represents the pathway of incident light and the grey arrow represents scattered light to the detector [121].

2.1.5 High Performance Liquid Chromatography (HPLC)

Reverse phase High Performance Liquid Chromatography (HPLC) was applied in analysis of potential lipid-DNA degradation. HPLC separates analytes upon their polarity, specifically through the analytes interactions with the column and solvent. Reverse phase denotes the column is packed with, typically silica, beads treated with a hydrophobic coating. Through the addition of using a polar solvent, polar molecules will have little interaction with the column and will be quickly eluted. Moreover, a hydrophobic molecule will be retained by the column through favourable hydrophobic interactions to the packing material. The high pressure applied to the solvent enables the elution of the hydrophobic molecule but at a much slower rate to the hydrophilic molecule. After elution molecules were identified through in-line UV detection.

2.2 Materials

2.2.1 Lipids

1,2-dioleoyl-sn-glycero-3-phosphocholine (DOPC), 1,2-dipalmitoyl-sn-glycero-3-phosphocholine (DPPC), bovine (heart) cardiolipin (CL), cholesterol (ovine wool) powder, 1,2-dioleoyl-sn-glycero-3-phosphoethanolamine-N-(lissamine rhodamine B sulfonyl) (Rhod PE, FRET acceptor) and 1,2-dipalmitoyl-sn-glycero-3-phosphoethanolamine-N-(7-nitro-2-1,3-benzoxadiazol-4-yl) (NBD PE, FRET donor) were purchased from Avanti Polar Lipids, lipid structures have been displayed in Figure 2.7.

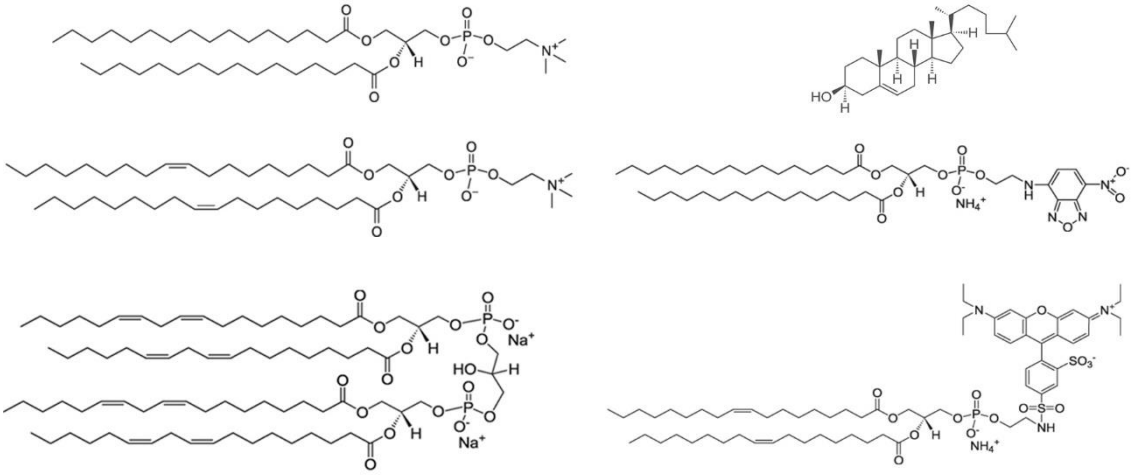

Figure 2.7 – Lipid structures, where: Top left - DPPC, top right - cholesterol, central left – DOPC, central right –NBD PE, bottom left – CL, bottom right – rhod PE.

Additionally, 16 carbon chain long saturated 1,2-O-dioctadecylrac-glycerol lipid-DNA conjugates were purchased from ATDBio. The DNA sequences were:

1. lipid-5′-TTT ACA GAC TAC C-3′
2. lipid-5′-TTT GGT AGT CTG T-3′
3. lipid-5’-TTT TTT TTT CCC TAA CCC TAA CCC TAA CCC-3‘
4. lipid-5’-TTT TTT GGG TTA TGG TTA GGA TTA GTG-3’

All other reagents, including analytical grade reagents, were purchased from Sigma-Aldrich and Fisher Scientific.

2.2.2 Solution preparation

2.2.2.1 Nano-sized liposome preparation

0.259 M cholesterol solution was made using 0.05 g of powdered cholesterol which was dissolved within 5 ml of chloroform. 1 l HEPES buffer was made from 125 mM NaCl, 10 mM 4-(2-hydroxyethyl)-1-piperazineethanesulfonic acid (HEPES) titrated against 260 mM $NaOH_{(aq)}$ until a pH of 7.4 was achieved.

2.2.2.2 Phosphorus assay

8.9 N $H_2SO_{4\,(aq)}$ was prepared through the slow addition of 123.5 ml of H_2SO_4 to 376.5 ml of deionised water. A stirrer bar was used ensuring the acid was evenly dispersed through the solution and that the heat was evenly distributed. 10% ascorbic acid solution was prepared by dissolving 2.5 g of ascorbic acid in 25 ml of deionised water, which was then well mixed. 2.5% ammonium molybdate (VI) tetrahydrate solution was prepared by dissolving 0.625 g of ammonium molybdate (VI) tetrahydrate in 25 ml of deionised water which was then well mixed.

2.2.2.3 Giant unilamellar vesicle (GUV) preparation

A 300 mM sucrose solution was made through dissolving 2.565 g of sucrose into 25 ml of deionised water. A 1% albumin from bovine serum was made through dissolving 0.5 g of albumin into 50 ml of deionised water.

2.3 Methods

2.3.1 Nano-sized liposome preparation

To prepare vesicles, lipids in chloroform were pipetted using Hamilton gastight syringes in volumes that reflected their mol% for that particular sample in the phase diagram. Molar ratios between lipids were calculated where 100% was equal to 3.5×10^{-6} moles. The lipid samples were deposited into glass sample tubes, which were then dried under a 1×10^{-3} torr vacuum, equipped with a liquid nitrogen trap overnight. 0.5 ml HEPES buffer at 50 ^{o}C was added to the dried lipid and vortexed until all visible dried lipid was dissolved. Freeze thaw was then performed, freezing the sample in liquid nitrogen and thawing the sample in a water bath at 50 ^{o}C, until the sample reached above 41 ^{o}C, ensuring all lipids were homogeneously distributed across the liposomes. Freeze thaw was repeated five times per sample. Liposomes were then extruded through an Avanti Polar Lipids Extruder 11 times using 100 nm Whatman nuclepore Track-Etch Membrane filter and four Whatman drain disks. The extruder and Hamilton syringes were maintained at 50 ^{o}C at all times to ensure all lipids were homogeneously distributed.

2.3.2 Giant Unilamellar Vesicle (GUV) preparation

50 µl of 1 mM lipid was deposited drop wise onto two platinum wires within an electro chamber. The electro-chamber was then dried under vacuum alongside 1% bovine serum albumin coated glass slides for two hours. The electro chamber was sealed using the dried glass slides in

conjunction with rubber gaskets and then filled with 50 ^{o}C 10% sucrose solution. Maintaining the 50 ^{o}C temperature, 1 V was applied at 10 Hz for 40 minutes. The frequency was then dropped to 3 Hz for 15 minutes, then 1 Hz for 7 minutes and finally 0.5 Hz for 7 minutes, before extraction.

2.3.3 FRET analysis

Using the lipid concentration calculated from the phosphorus assay experiments, samples containing ~50 µM of lipid were prepared, ensuring that the samples were suitably dilute for FRET analysis. This ensured minimal inner filtering effects due to scattering from high concentrations, while still recording a strong signal from the sample.

All FRET experiments were conducted using a Fluoromax-3 fluorometer. To monitor phase behaviour, the fluorometer's sample holder was heated to six different temperatures; 18, 20, 25, 30, 40 and 50 ^{o}C using a heated water bath connected to the sample chamber. To monitor the sample holder's temperature a thermocouple device was placed within a cuvette filled with water. Before analysis samples were stored in sealed containers in a heated water bath, at the appropriate temperature for analysis for a minimum of 30 minutes. Before analysis samples were taken out of the water bath and emptied into an appropriate fluorescence cuvette. The cuvettes were then placed within the fluorimeters sample holder, which was left for a further 10 minutes to thermally equilibrate. In the analysis the excitation beam was set to 460 nm for direct donor (NBD PE) excitation, with the excitation band width maintained at 5 nm [122]. The emission spectra were recorded between 490–650 nm with an emission band width of 5 nm and an integration time of 0.1 s. The emission maxima for NDB PE and rhod PE used in FRET ratio and efficiency calculations were 530 nm and 587 nm respectively.

2.3.4 Phosphorus assay

A phosphorus assay experiment was conducted to calculate the total concentration of phosphorus within a liposome sample. With lipids having ~one phosphorus atom per lipid molecule it is possible to determine a guide number of lipids within a sample (cholesterol has no phosphorous atom and CL has two). To calculate an unknown phosphorus concentration, a standard phosphorus solution was used to create a calibration of 0 µmoles, 0.0325 µmoles, 0.065 µmoles, 0.114 µmoles, 0.163 µmoles and 0.228 µmoles. 0.45 ml of 8.9 N $H_2SO_{4\,(aq)}$ was added to the calibration samples and unknown samples. Each test tube was then heated above 200 ^{o}C using a hot plate and an aluminium block for 25 minutes to perform acid digestion. The test tubes were removed and cooled before adding 150 µl of H_2O_2. The test tubes were then placed back into the heated block for a further 30 minutes. Once cooled to an ambient temperature, 3.9 ml of deionised water was added to each test tube along with 0.5 ml ammonium molybdate (VI) tetrahydrate solution and 0.5 ml of ascorbic acid solution. Each test tube was then vortexed to ensure complete mixing before placing in a water bath at 100 ^{o}C for 7 minutes. The calibration and unknown

samples were cooled before UV-visible spectroscopic analysis. Absorbance was measured at 820 nm on an Agilent Cary 100 UV-vis spectrophotometer. Using the absorbance vs. moles calibration, a guide lipid concentration of the unknown samples could be calculated.

2.3.5 Confocal fluorescence microscopy

25 µl of the prepared GUV sample was pipetted onto a bovine serum albumin treated slide along with 75 µl of HEPES buffer. To image the samples a Zeiss LSM700 inverted confocal fluorescent microscope was used with a 488 nm laser at 10mW, in conjunction with a 555 nm laser at 10 mW for NBD PE and rhod PE excitement respectively. Images were produced with a Plan-Apochromat SF25 lens capable of 63x magnification under oil with a numerical aperture of 1.4. The resulting images were processed using Adobe Photoshop CS6 for brightness and contrast adjustment.

2.3.6 UV DNA thermal-melt analysis

1 ml of 1 x10^{-3} M lipid nano vesicle samples were prepared through the extrusion method and left at room temperature for 30 minutes. After this time, the sample was separated in 0.5 ml aliquots. Opposing thawed aliquots of complementary 2 x10^{-5} M lipid-DNA conjugates in pH 7.4 HEPES buffer were then pipetted into the 0.5 ml vesicle samples at an equimolar concentration. For example, sequence 1 was placed into one of the 0.5 ml vesicle samples and sequence 2 was placed in the other 0.5 ml vesicle sample. DNA loadings varied from 10, 25, 50, 75, 100, 150, 200 and 250 DNA strands per vesicle, which was calculated using Equation 2.11.

Equation 2.11 $$\boldsymbol{DNA\ loading} = \left(\frac{\boldsymbol{total\ lipid\ conc.} \times N_A}{\mathbf{100000}}\right) \times \boldsymbol{wanted\ number\ of\ DNA\ strands}$$

Where N_A is Avogadro's number and there are ~10^5 lipids per 100 nm vesicle [123]. Once the DNA was pipetted into the vesicle aliquots, they were then left a further 30 minutes at room temperature for the lipid-DNA to integrate into the vesicles' membrane. Complementary DNA doped vesicles were then mixed at a one to one ratio in termers of vesicle concentration and lipid-DNA concentration, making a 1 ml 1x10^{-3} M sample. These sample were then given a final 20 minutes at room temperature to hybridise together. An Agilent Cary 100 UV-vis spectrophotometer was used in thermal analysis, where the wavelength was set at 260 nm. To Complete thermal analysis temperature ramps were between 15-75 ^oC at a rate of 0.4 $^oC\ min^{-1}$ were conducted, with measurements being taken every 0.1 ^oC. Before analysis samples were initially heated to and maintained at 75 ^oC for 10 minutes. Sample temperature was monitored using the on-board thermocouple rather than using the heating block temperature, yielding more accurate DNA T_m. Melting curves were smoothed and a first derivative was applied to the data.

Subsequent DNA T_m calculations were made using Origin Pro 9.1 and the Gaussian peak fitting model. During pH examination pH was raised and lowered using aliquots of 1.2 M $HCl_{(aq)}$ and $NaOH_{(aq)}$ in accordance with a HEPES pH calibration. Acid/base was added once complementary vesicles were mixed and left to stand for 30 minutes. Once the pH adjustment component was added samples were left for 20 minutes.

2.3.7 Dynamic Light Scattering (DLS) of vesicle aggregates

Sample preparation was carried out as described for UV DNA Thermal-melt analysis in section 2.3.6 page 53, with the addition of leaving the sample at 4 ^oC overnight before analysis. DLS was performed using a Malvern Zetasizer Nano ZS where samples were left to thermally equilibrate in the instrument for 20 minutes before examination. Aliquots of acid/base were again added in accordance with a HEPES pH calibration. pH responsive experiments were allowed to equilibrate for a minimum of 30 minutes upon the addition of acid/base, preceding measurement.

2.3.8 High Performance Liquid Chromatography (HPLC)

For lipid-DNA separation and detection, an Agilent 1290 series HPLC instrument was used in conjunction with an inline Agilent 1290 UV detector, Agilent 1290 autosampler, Agilent 1260 infinity binary pump and a phenomenex hyperclone C18 250 x 4.6mm 5 µm particle packed column. To elute lipid-DNA a solvent gradient was applied, as shown in Table 2.1, under a 1.0 ml min^{-1} flow rate.

Time / min	A%	B%
0	100	0
25	90	10
30	55	45
45	0	100

Table 2.1 – Solvent gradient applied during HPLC analysis of lipid-DNA conjugates with A representing 0.1% ammonium acetate (wt/v in water) and B representing acetonitrile.

2.3.9 Lipid-DNA preparation

To prepare the lipid-DNA, the phosphoramidite method used by S. G. Boxer et al. was applied with some deviations in purification technique [84], [124], [125]. 0.5 g of 1,2-O-dioctadecylrac-

glycerol (0.83 mmol) and 0.32 ml diisopropylethylamine (1.8 mmol) were dissolved in 10 ml anhydrous dichloromethane at 0 °C under a nitrogen atmosphere. 0.25 g 2-cyanoethyl N, N-diisopropylchlorophosphoramidite (1.3 mmol) was added dropwise to the reaction, with constant stirring at 0 °C for 15 min, then at room temperature for 2 h. The crude product solution was washed with a saturated solution of sodium bicarbonate and saturated solution of $NaCl_{(aq)}$ to dry the reaction mixture. The solvent was removed under vacuum. Purification by silica gel chromatography was then attempted using a 90:9:1 hexanes:ethyl acetate:trimethylamine mixture. Structures were confirmed through ^{1}H, ^{31}P NMR and mass spectrometry.

The attachment of DNA to the lipid-phosphoramidite was done as a service using ultra-mild protecting reagents by Dr Iain Manfield in the Astbury biomolecular interactions facility.

2.3.10 Critical Micelle Concentration (CMC) measurement

The method adopted to analyse the CMC was that laid out by Stef A. J. van der Meulen et al. Whereby the method implements the use of 1-(2-pyridylazo)-2-naphthol (PAN) [126], a water insoluble inorganic dye [127]. Upon increasing surfactant concentration above the CMC micelles form, enabling PAN to partition into the hydrophobic rich domains, leading to an increase in absorbance at 470 nm [126]. 20 µl PAN suspension (0.2 mg ml^{-1} dissolved in hexane), was added to 450 µl DNA-lipid samples in HEPES buffer, the concentration of the samples were made across the estimated CMC range of the lipid-DNA. Samples were then vortexed and the hexane was left to evaporate for 30 minutes. The absorbance of each sample was then measured at 470 nm.

2.4 Synthesis

DNA is often synthesised through an automated phosphoramidite approach, where each base is sequentially added to the next, with the starting base being attached to a solid glass bead [128]. To produce lipid-DNA, the lipid tail conjugate must be added as the final “base” in the synthesis. While the lipid tail is not a base, the addition of a phosphoramidite functional group enables it to follow the same synthesis route used for building a DNA strand. A summary of the lipid-DNA synthesis can be seen in the cartoon displayed in Figure 2.8.

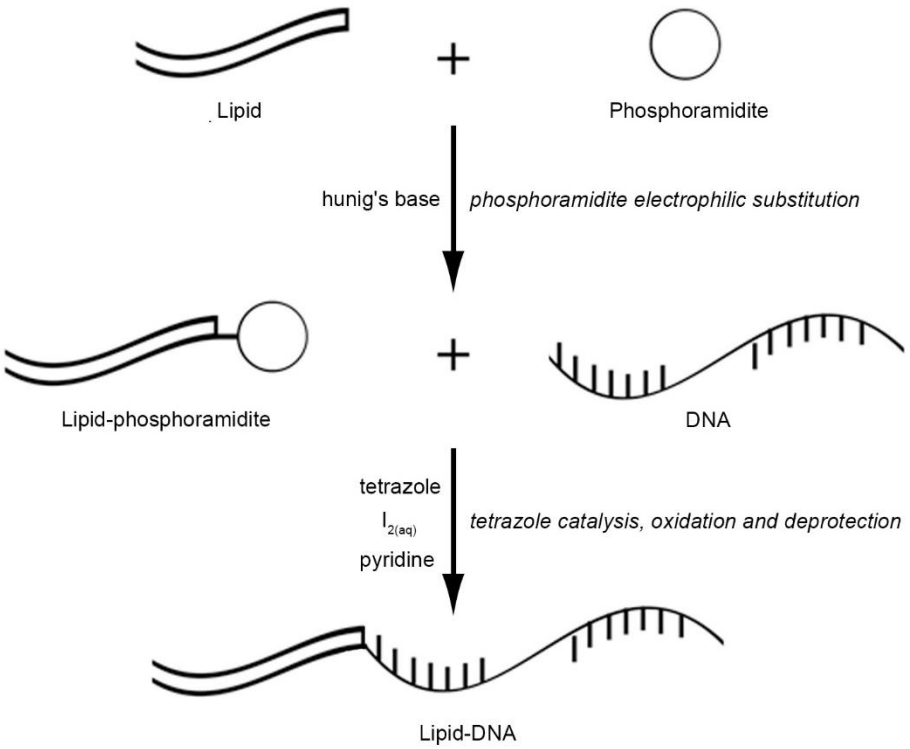

Figure 2.8 - Schematic diagram of DNA-lipid conjugate synthesis via a lipid-phsphoamidite intermediate.

2.4.1 Lipid-phosphoramidite synthesis

The initial stage of the synthesis was to produce the lipid-phosphoramidite intermediate. This was carried out by flowing the method laid out by S. Boxer et al. where the reaction mechanism can be seen in Figure 2.9.

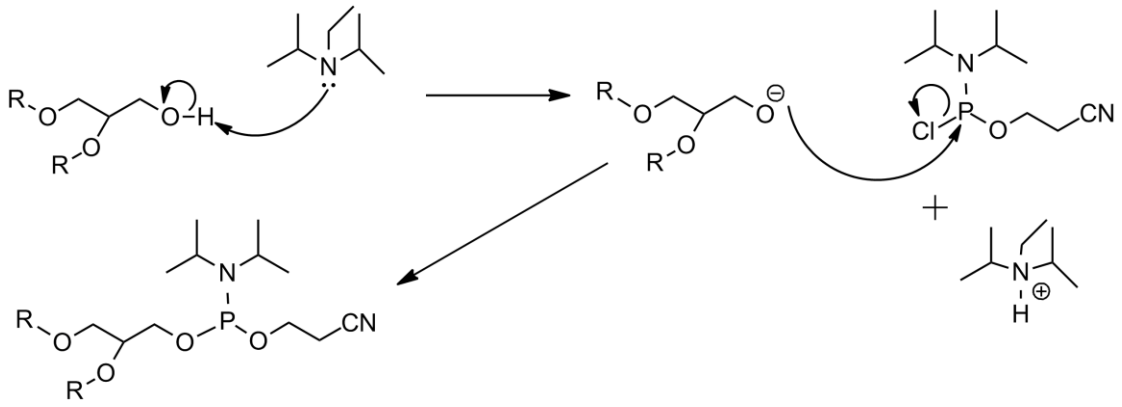

Figure 2.9 – Reaction mechanism dispaying the formation of the lipid-phosphoramidite intermediate required for lipid-DNA synthesis. R represents an 18 carbon long alkyl chain [128].

The reaction mechanism in Figure 2.9 displays hunig's base acting as a nucleophile to the hydroxyl group. This activates the “lipid tail” enabling it to perform nucleophile substitution with the chlorine on the phosphoramidite. When carrying out the experiment, reaction progress was monitored via Thin Layer Chromatography (TLC) and after two hours the reaction was stopped. Once the mixture had been dried, and the solvent removed, the products were ready for purification on a silica column. However, it was found that the purification step using a silica gel column, coupled with the mobile phase of hexane:elthylacetate:triethylamine (90:9:1), was ineffective. The separation only eluted an unwanted derivative of the lipid phosphoramidite product, with a mass of 744.7 $gmol^{-1}$ and 766.7 $gmol^{-1}$ with sodium addition from electrospray ionisation (Figure 2.10), not the intended 797 $gmol^{-1}$ lipid-phosphoramidite intermediate.

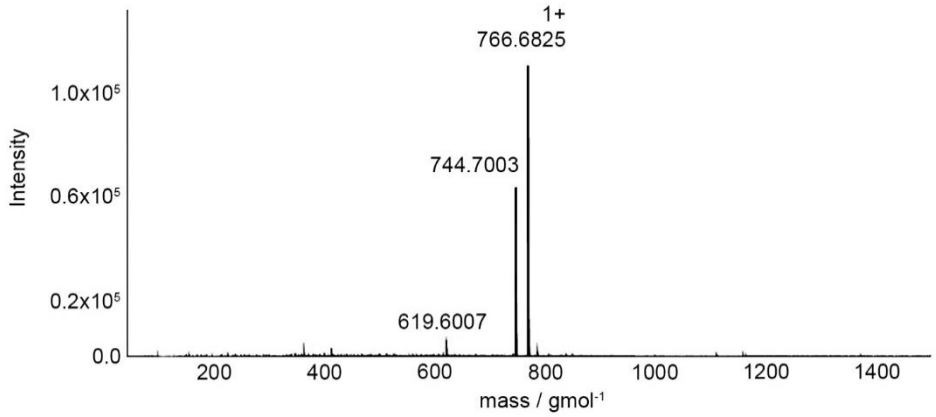

Figure 2.10 – Mass spectra of the purified lipid-phosphoramidite.

From the data presented within Figure 2.10 it was assumed that the lipid-phosphoramidite was stuck to the silica. Solvent parameters were therefore examined using TLC to drive more successful separation (data not shown). Conversely, the original solvent parameters were found to be optimal to drive an effective separation between products and reactants via TLC. To analyse whether the lipid-phosphoramidite was indeed being formed, the crude product was examined via mass spectrometry.

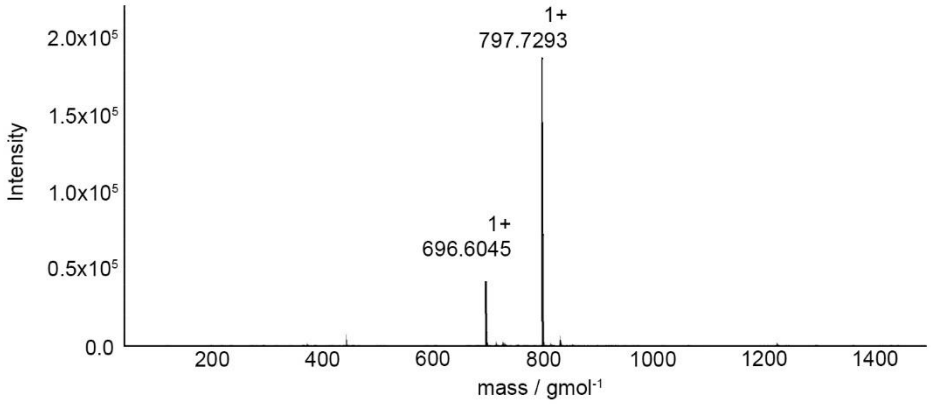

Figure 2.11 - Mass spectra of the crude lipid-phosphoramidite.

The mass spectrometry data shown in Figure 2.11 exhibits the crude product having an abundance of the wanted lipid-phosphoramidite, with the addition of some impurities. However, these impurities are not seen in the “purified” sample in Figure 2.10, indicating that during purification a reaction may be taking place. Interestingly between the wanted lipid-phosphoramidite shown in Figure 2.11 and one of the impurities found in the Figure 2.10 there is a 53 $gmol^{-1}$ mass disparity, telling of an arguable acrylonitrile (CH_2CHCN) removal. The removal of the protecting leaving group has been outlined in Figure 2.12

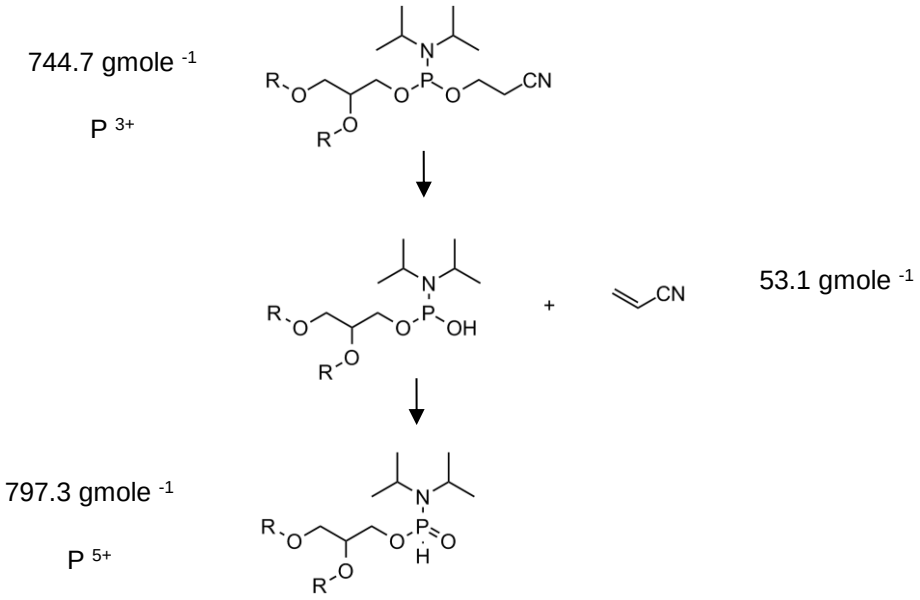

Figure 2.12 - Suggested pathway for lipid-phosphoramidite degradation through the removal of CH_2CHCN and consequential change in phosphorus oxidation state.

Additionally, the reaction pathway outlines that there is a change in the phosphorus oxidation state from P^{3+} to P^{5+}. To detect this change in oxidation state and support an argument for acrylonitrile removal, phosphorus NMR was conducted.

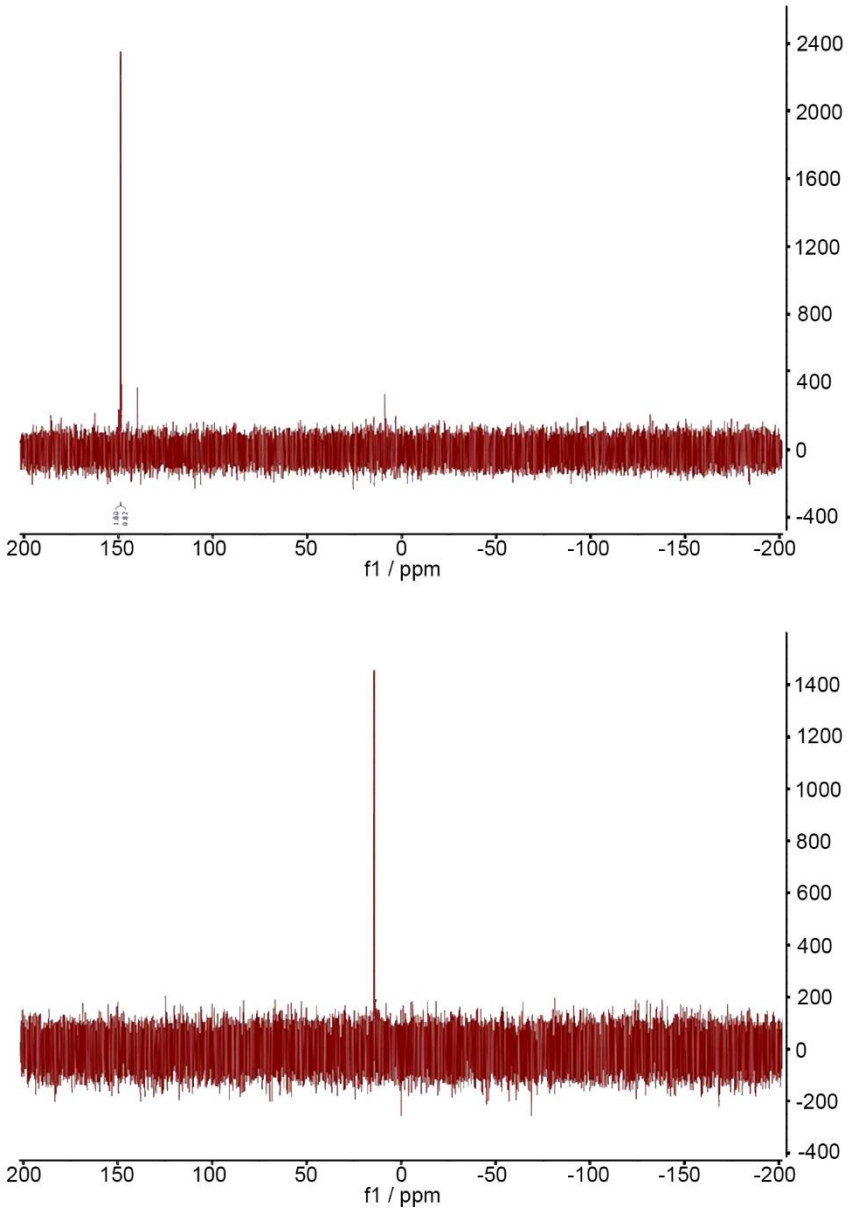

Figure 2.13 - Phosphorus NMR data for the crude and purified lipid-phosphoramidite intermediate: Top – the crude lipid-phosphoramidite (~150 ppm). Bottom – the oxidised phosphoramidite intermediate (~15 ppm).

The phosphorus NMR data displays a peak position shift from ~150 ppm to ~15 ppm. These peak positions indicate the presence of phosphorous 3^+ and 5^+ containing compounds respectively [129]. Further evidence for the phosphorous oxidation state change from 3^+ to 5^+ can be found in the proton NMR spectra shown in Figure 2.14.

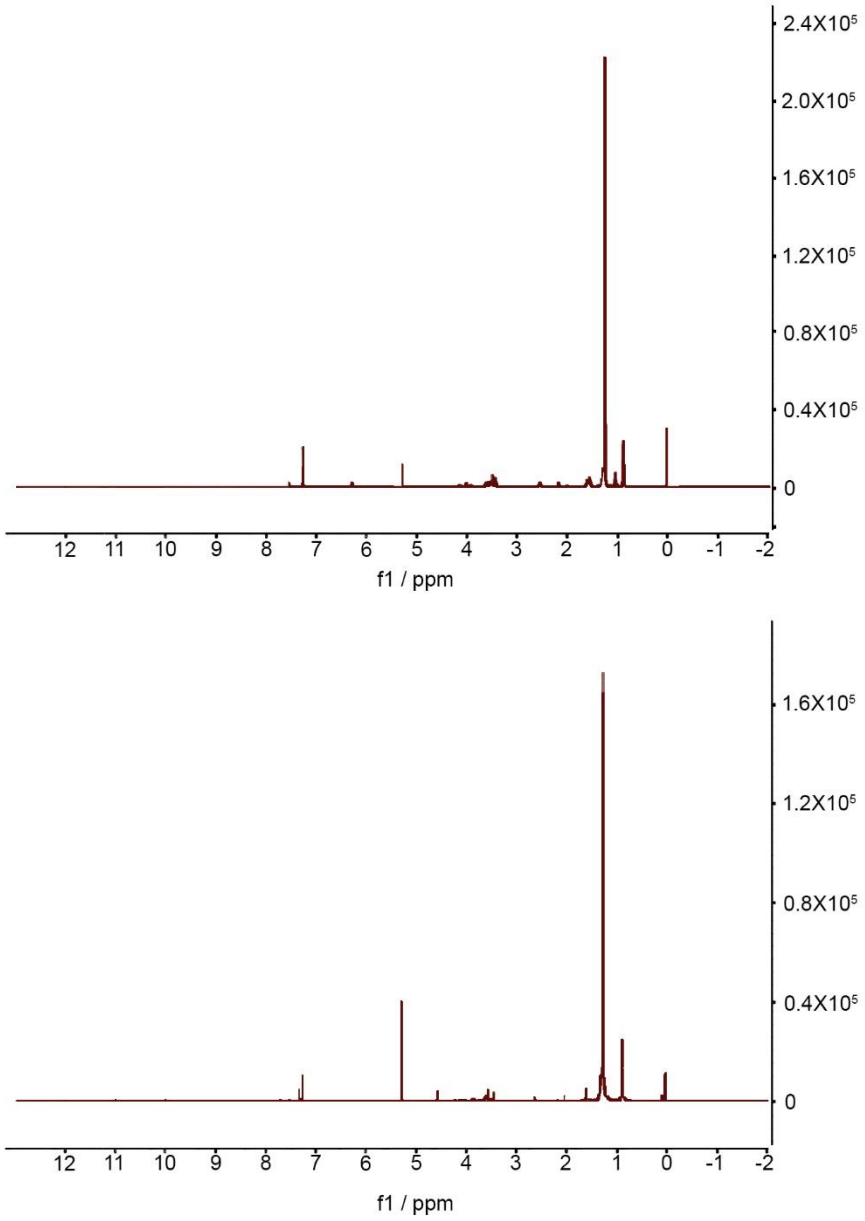

Figure 2.14 - Proton NMR data for lipid-phosphoramidite derivates. Top - crude 3+ lipid-phosphoramidite intermediate. Bottom – oxidised 5+ lipid phosphoramidite intermediate.

Through phosphorus 5^+ having a spin state of ½ it can couple with the newly attached proton shown in Figure 2.12 [130]. The hydrogen–phosphorous splitting at ~5.4 ppm found in the purified product is significantly reduced in the crude lipid-phosphoramidite 3^+ sample. This indicates that there is a much lower oxidised phosphorus 5^+ content in the crude product.

In conclusion it was hypothesised that TLC displayed good separation through the purification being over a short time scale. The larger column used for purification takes longer to run, and so the lipid phosphoramidite has a longer time frame in which to oxidise, forming the 5^+ complex. Vanderlick et al. used a similar method to prepare the lipid phosphoramidite, however they did

not use a purification step and placed the crude product onto the DNA synthesiser. In light of this, moving forward crude product was not purified and was placed directly into the DNA synthesiser.

2.4.2 Lipid-DNA conjugation

To generate lipid-DNA conjugates, a lipid-phosphoramidite “base” was added as the “last base” to the DNA sequences via phosphoramidite chemistry. This would be achieved through a tetrazole catalyst reaction, where the mechanism has been outlined below in Figure 2.15.

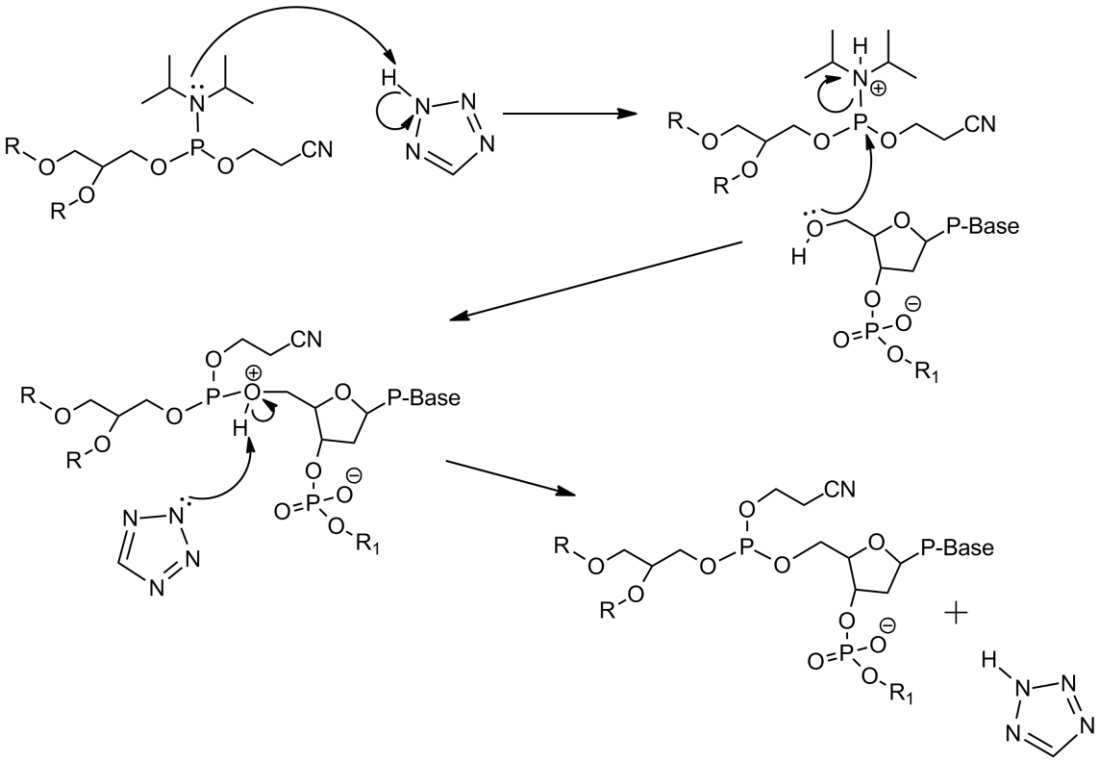

Figure 2.15 – “Last base” phosphoramidite attachment of the lipid tail to the DNA sequence through tetrazole cytolysis [128]. R and R_1 represent the 18 carbon long alkyl chain and the rest of the DNA sequence respectively and P-Base is a protected base pair.

Upon lipid tail DNA conjugation further work up was required to oxidise the phosphorus from a 3^+ state to a more stable 5^+ state.

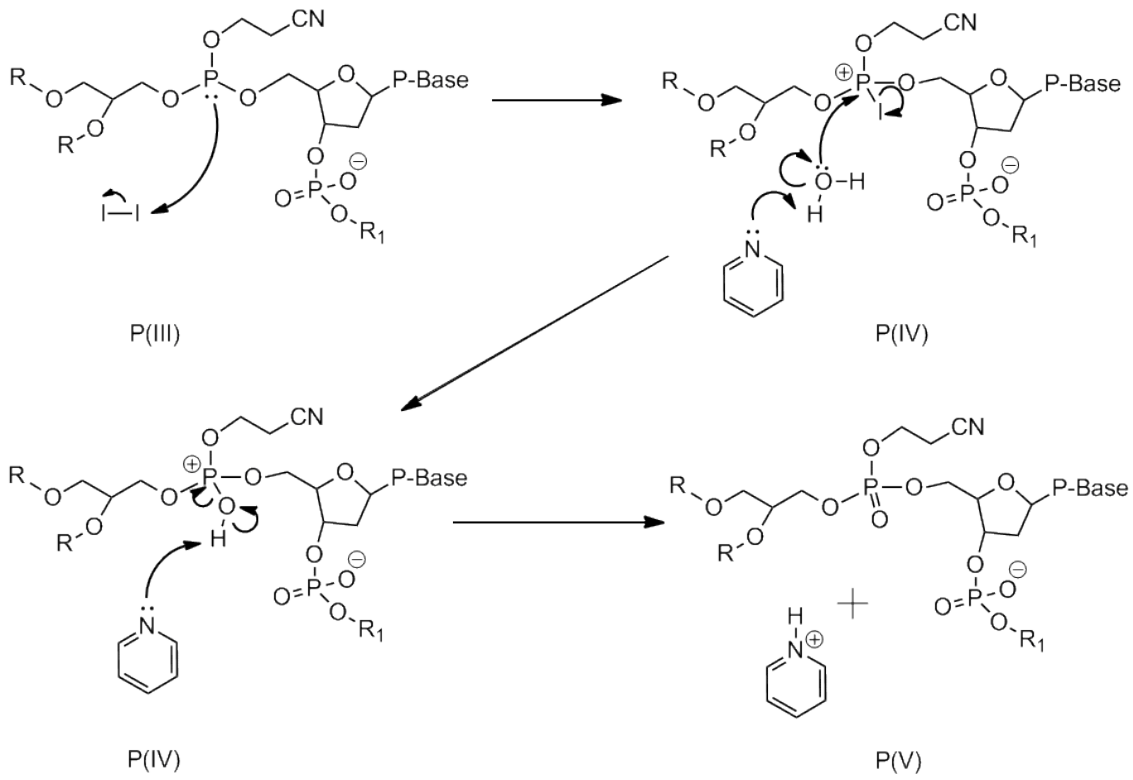

Figure 2.16 - Oxidation of the phosphorus from 3+ to 5+ [128]. R and R1 represent the 18 carbon long alkyl chain and the rest of the DNA sequence respectively and P-Base is a protected base pair.

The oxidation initially requires the addition of iodine to produce phosphorus 4^+. Iodine, a good leaving group, provides a point of access for a hydroxyl substitution; initiated through the addition of pyridine. The use of pyridine in excess will further drive phosphorus from its 4^+ oxidation state to the desired 5^+ state. Finally, protection group removal is achieved through the addition of warmed ammonia [128].

However, in this instance using the method outlined above lipid-DNA was not successfully yielded. Through mass spectrometry it was observed that only DNA was synthesised for each sequence, data shown within Figure 2.17.

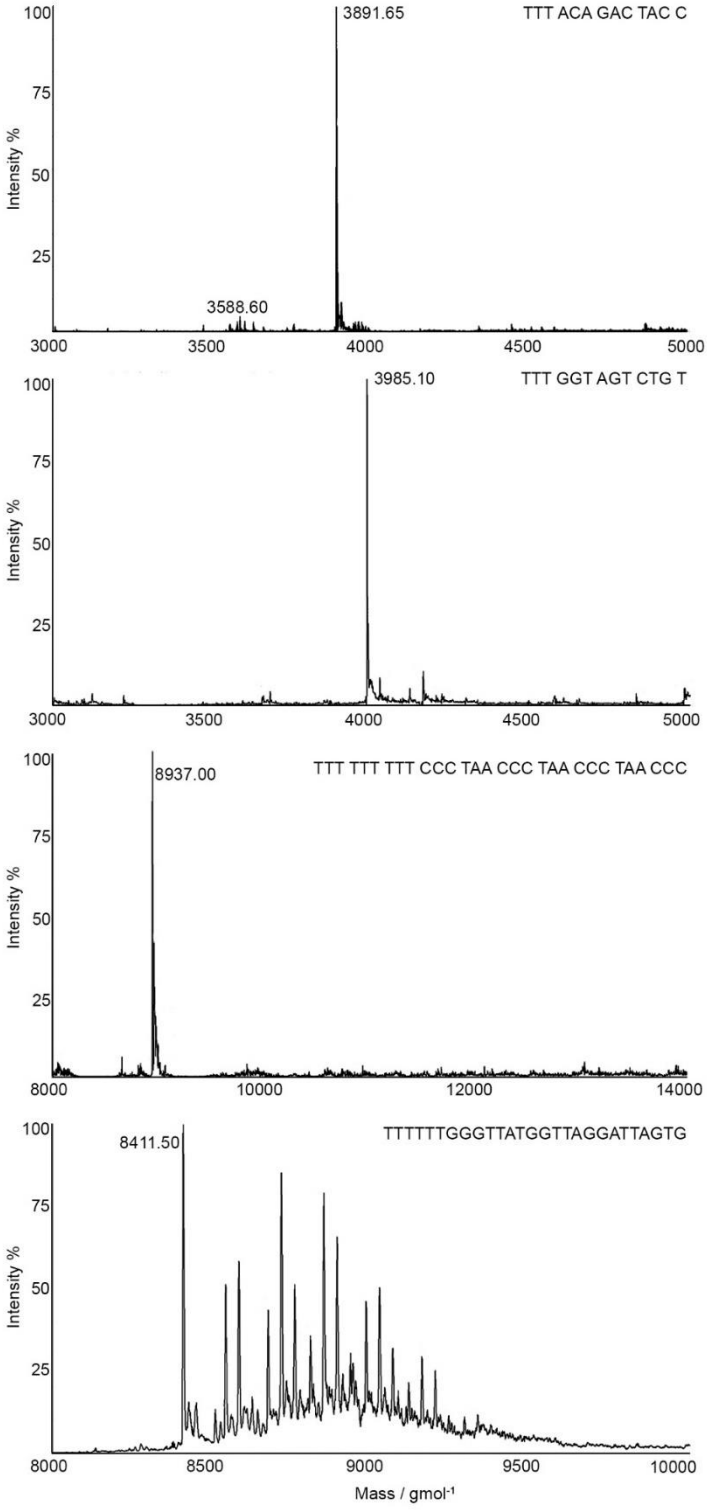

Figure 2.17 – Mass spectrometry data indicating the presence of just the DNA sequences opposed to the desired lipid-DNA conjugates. Graphs are presented in DNA sequence order, where the first graph at the top is for DNA sequence 1.

With respect to Figure 2.17, the measured masses are comparable to the calculated masses of the DNA sequences alone without the conjugated lipid tail. The calculated masses for each of the

DNA sequences are 3893.60, 3986.63, 8937.84 and 8412.47 $gmol^{-1}$ for sequences 1, 2, 3 and 4 respectively.

Due to the DNA synthesis and subsequent lipid-phosphoramidite attachment being run as a service by Dr Iain Manfield in the Astbury biomolecular interactions facility, it was difficult to speculate the cause of lack of success. Speculatively, the fault may lie in the difficulty met when dissolving the lipid-phosphoramidite, and/or the lipid-DNA may have been lost in salt removal column after synthesis. Due to the extended lead time in preparing the lipid-DNA it was considered to be more time effective and more in line with the overall project goals to purchase the material required.

Chapter 3

Phase boundary mapping of four component nano vesicles via Förster resonance energy transfer (FRET)

To build a Janus liposome capable of forming a controllable, directional, size limited cluster; understanding and regulating vesicle lipid composition is key. From the introductory review, it was shown that the addition of 10 mol% cardiolipin (CL), significantly influences trace saturated DNA-lipid bridging conjugate partitioning to the l_o phase, by an order of magnitude. This in turn aided the formation of size limited vesicle clusters. In this chapter, we aim to fully examine the influence 10 mol% CL has on the previously established three component DPPC:DOPC:cholesterol phase diagram, in the hope of producing a tuneable and adaptable drug delivery platform.

Taking inspiration from previous studies examining the formation and measurement of lipid phase separation by S. Keller et al. and S. Veatch et al., this worked focused on producing a nano vesicle four component phase diagram. Specifically, we examined the phase diagram of DOPC:DPPC:cholesterol:CL where CL concentration is maintained at 10 mol%, outlined in Figure 3.1. Through limiting the CL content, it is hoped unwanted higher order and more complex four component phase behaviour is avoided, while exploiting the aided DNA-lipid partitioning to the l_o phase.

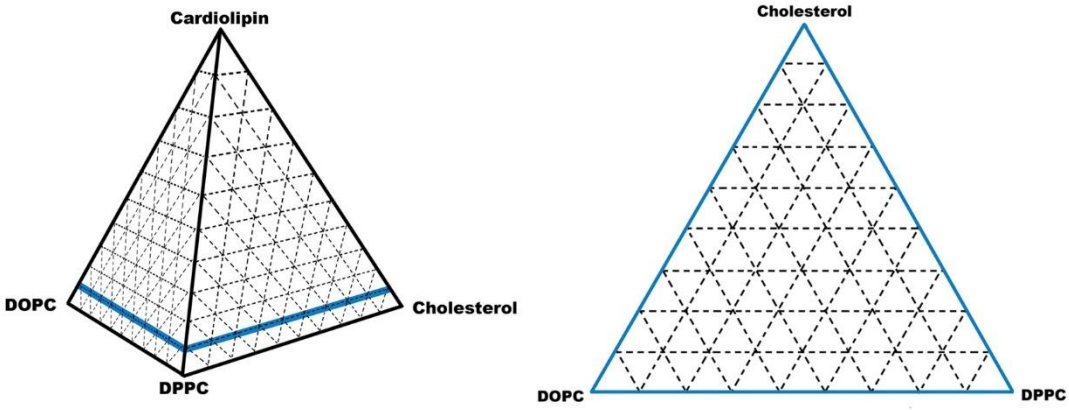

Figure 3.1 – Left: the four component DPPC:DOPD:cholesterol:CL phase diagram with the blue line representing the 10 mol% CL slice. Right: The "three" component phase diagram slice where vertices represent 90 mol% where CL is maintained at 10 mol%

With similar phase diagrams already documented both on a nano and micro scale, our new four component phase diagram could be plotted using a previously used vesicle mapping technique [72]. Here Förster resonance energy transfer (FRET) was chosen to map the DOPC:DPPC:cholesterol:CL phase diagram slice.

3.1 FRET and phase detection

3.1.1 Fluorescent dyes

In order to obtain FRET data, the lipid conjugated fluorescent dyes, 1,2-dioleoyl-*sn*-glycero-3-phosphoethanolamine-N-(lissamine rhodamine B sulfonyl) (rhod PE) and 1,2-dipalmitoyl-*sn*-glycero-3-phosphoethanolamine-N-(7-nitro-2-1,3-benzoxadiazol-4-yl) (NBD PE) were used. The selected lipid dyes have two distinct properties required to measure phase separation via FRET analysis.

1. Good spectral overlap of fluorescent probes.
2. Different phase partitioning preferences due to the unsaturated and saturated lipid tails of rhod PE and NBD PE respectively.

These points are considered in turn. To carry out FRET analysis the two fluorescent probes have to have a minimum of 30% spectral overlap between a donor's emission and acceptor's excitation peaks. The spectral crossover between the two probes used in this analysis are shown within Figure 3.2.

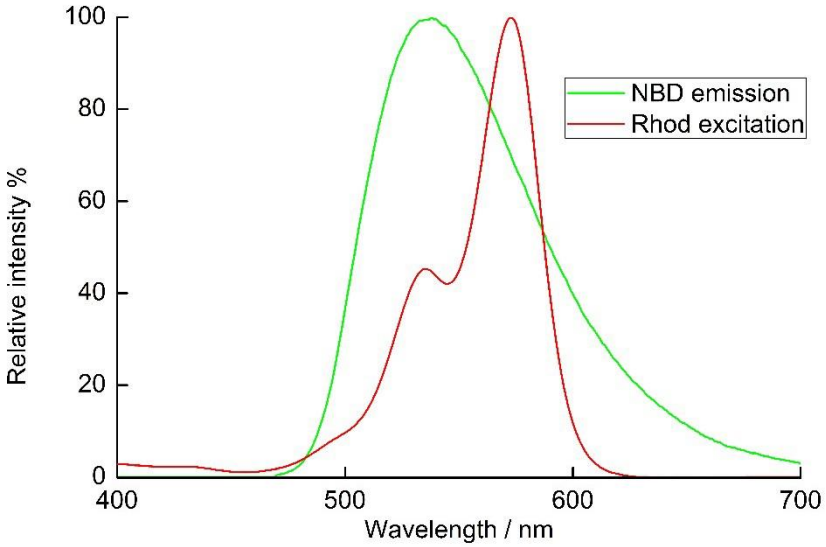

Figure 3.2 – Spectral overlap between FRET donor NBD PE and rhod PE probes used in the phase boundary mapping of nano vesicles [131].

Secondly, to detect membrane phase heterogeneity through FRET; rhod PE and NBD PE have unsaturated and saturated lipid tails,driving probe partitioning to the l_d and l_o phases present respectively. Through phase co-existence and subsequent probe separation into local discrete domains, average donor/acceptor probe separation is enhanced. The increase in probe separation prevents effective resonant energy transfer between probes. The resulting reduction in donor fluorescence quenching leads to a promotion of donor fluorescence intensity and a reduction in acceptor intensity. Through this mechanism, a qualitative technique was developed. Initially, homogenous membranes have homogenously mixed fluorescent dyes and good energy transfer between donor and acceptor probes. Upon membrane l_d-l_o phase separation, inter rhod PE and NBD PE distances will rise significantly, reducing acceptor fluorescence intensity. Furthermore, in instances of l_d-l_{gel} phase separation there will be a significant reduction in probe separation from the homogeneous vesicle. This increased level of FRET is through NBD PE's preferential partitioning into the l_d phase in this case [132].

3.1.2 Phase detection

Using published phase diagrams for DOPC:DPPC:cholesterol vesicles as a guide, three initial phase representatives were chosen for the new four component phase diagram containing 10 mol% CL. These three samples were chosen to examine whether FRET's energy transfer dependence on distance, was suitable for being able to detect the difference between l_d, l_d-l_o coexistence and l_{gel} phases, enabling phase boundaries to be recorded on the phase diagram. These initial samples had composition probe concentrations maintained at 0.2 mol%/probe. From the raw fluorescence data, FRET efficiencies and ratios were calculated using Equation 2.5 and Equation 2.6 and processed to give a FRET profile with respect to temperature. Both FRET efficiency and ratio, Equation 2.5 and Equation 2.6 respectively, are commonly used experimentally. Where the ratio gives a relative measure of energy transfer and the efficiency can give a more detailed account of the percentage of energy transferred from the donor to acceptor dye. Here both were examined to assess which was most suitable in vesicle samples.

The first of the three phase representative samples examined was in a suspected l_d phase region of the phase diagram. The result from the FRET based phase detection technique is outlined in Figure 3.3.

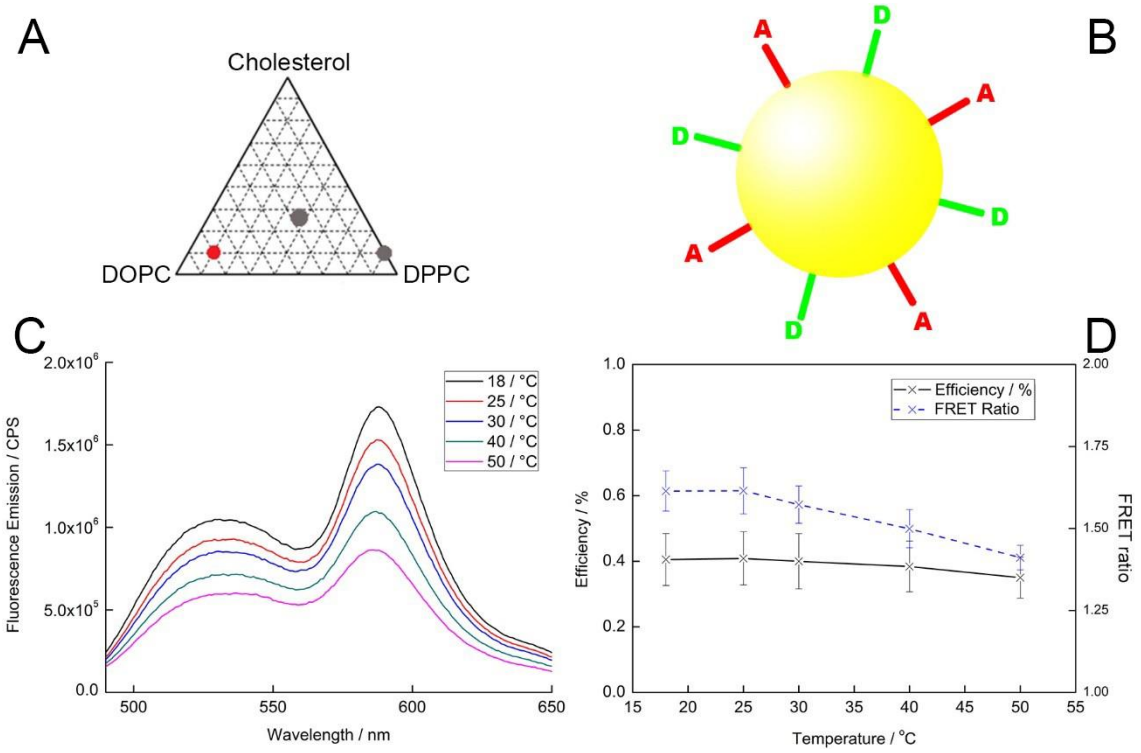

Figure 3.3 – A: Phase diagram displaying sample composition DOPC:70%, DPPC:10%, cholesterol:10% CL:10% in red, sample doped with NBD PE: 0.2% and rhod PE:0.2%. B: Cartoon of interpreted data where donor (D) and acceptor (A) lipid dyes are homogenously mixed across the vesicle's surface. C: Example of raw fluorescence data initially excited at 460 nm with emission maxima for D at 535 nm and A at 587 nm. D: Calculated FRET ratios and efficiencies plotted against temperature.

For the suspected homogeneous l_d phase raw fluorescence data, there is a high acceptor peak and low donor peak relative to one another, irrespective of temperature. This profile indicates consistent good energy transfer from the donor to the acceptor. This data are consistent with the hypothesis of a single phase being present with limited probe separation and homogeneous lipid mixing. The decrease present in the overall fluorescence signal, for both the acceptor and donor peak intensities with respect to rising temperature, is likely due to a quenching effect. There are two main types of fluorescence quenching; dynamic and static.

1. Dynamic quenching refers to three mechanisms: FRET which has previously been discussed, Dexter electron transfer and exciplex formation. Dexter electron transfer/enhanced thermal collisional energy transfer occurs when an excited dye collides with a dye species with overlapping molecular orbitals [133]. An exciplex is a short lived excited state dimer complex formed from an excited dye and an unexcited molecule.
2. Static quenching is the process where complexes are formed before excitation occurs, contrasting with the formation of exciplexs.

The most probable mechanism causing the quenching seen in this data is through dynamic collisional quenching. Heating increases diffusion rates of the lipids, increasing the frequency of molecular collisions allowing energy to be lost through a non-radiative pathway, therefore decreasing the fluorescent signal [111].

With regard to whether the FRET ratio or efficiency displays the better FRET temperature profile, no significant changes are present within the data, making it difficult to assess which method is better. The efficiency did show to be more constant with temperature, however, the FRET ratio exhibited a smaller uncertainty in respect of the specific data series.

The next sample chosen was a previously reported phase separating composition [91]. Using this as a reference sample the FRET based technique's effectiveness to detect phase co-existence was analysed.

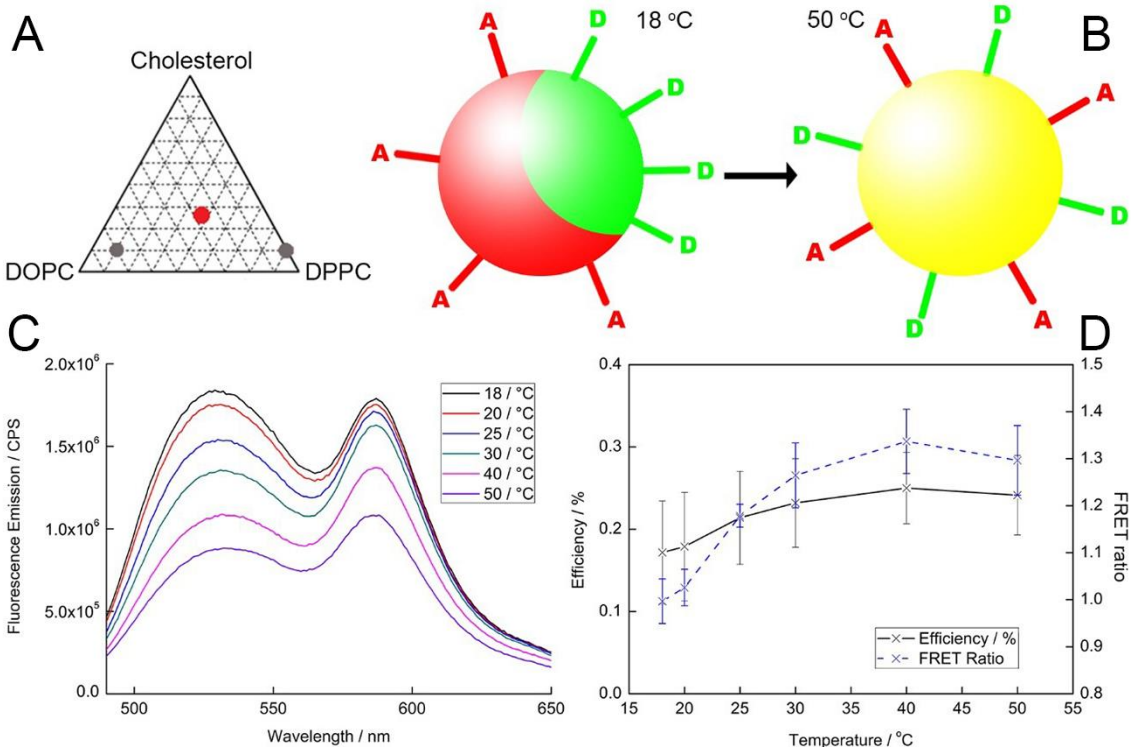

Figure 3.4 - A: Phase diagram displaying sample composition DOPC:27.5%, DPPC:37.5%, Cholesterol:25% CL:10%in red, sample doped with NBD PE:0.2% and rhod PE:0.2%. B: Cartoon of interpreted data where donor (D) and acceptor (A) lipid dyes partition into separate l_o and l_d coexisting domains respectively at low temperatures, leading to homogenous mixing across the vesicle's surface at 50 °C. C: Example of raw fluorescence data initially excited at 460 nm with emission maxima for D at 535 nm and A at 587 nm. D: Calculated FRET ratios and efficiencies plotted against temperature.

The suspected l_d-l_o phase coexisting liposomes show a different FRET regime to what was previously reported for the suspected homogeneous l_d phase. Here at low temperatures the raw fluorescence spectra display a donor peak larger in intensity than the acceptor peak, contrastingthat seen for the suspected single phase l_d system. Through heating the suspected l_d-l_o samples, similar peak intensities to the reported l_d phase are displayed, with the FRET ratio at 50 ^oC being comparable to that shown for the l_d samples. It is clear that heating the samples changes lipid phase behaviour from exhibiting a poor FRET regime, where NBD PE and rhod PE probes are heterogeneously separated through preferential phase partitioning at low temperatures, to an effective FRET regime at higher temperatures. At a temperature above the T_m for the highest melting lipid (DPPC 41 ^oC), lipids form a homogenous vesicle surface [134]. In other words, as the temperature is raised, lipids begin to diffuse out of their respective domains as the thermal energy rises, forming a homogenous membrane. Subsequently the donor probes are mixed with the acceptor probes, allowing for good energy transfer as seen for the l_d phase sample. Upon forming an l_d surface, the donor intensity peak decreases and the acceptor peak increases due to the probes becoming closer together, enabling energy to be transferred through resonance.

Upon examining the FRET ratios and efficiency data presented, using the ratio is much clearer with error bars significantly smaller than the efficiency errors. This in turn demonstrates and implies vesicles moving from a l_d-l_o phase coexisting state, to a l_d phase upon heating.

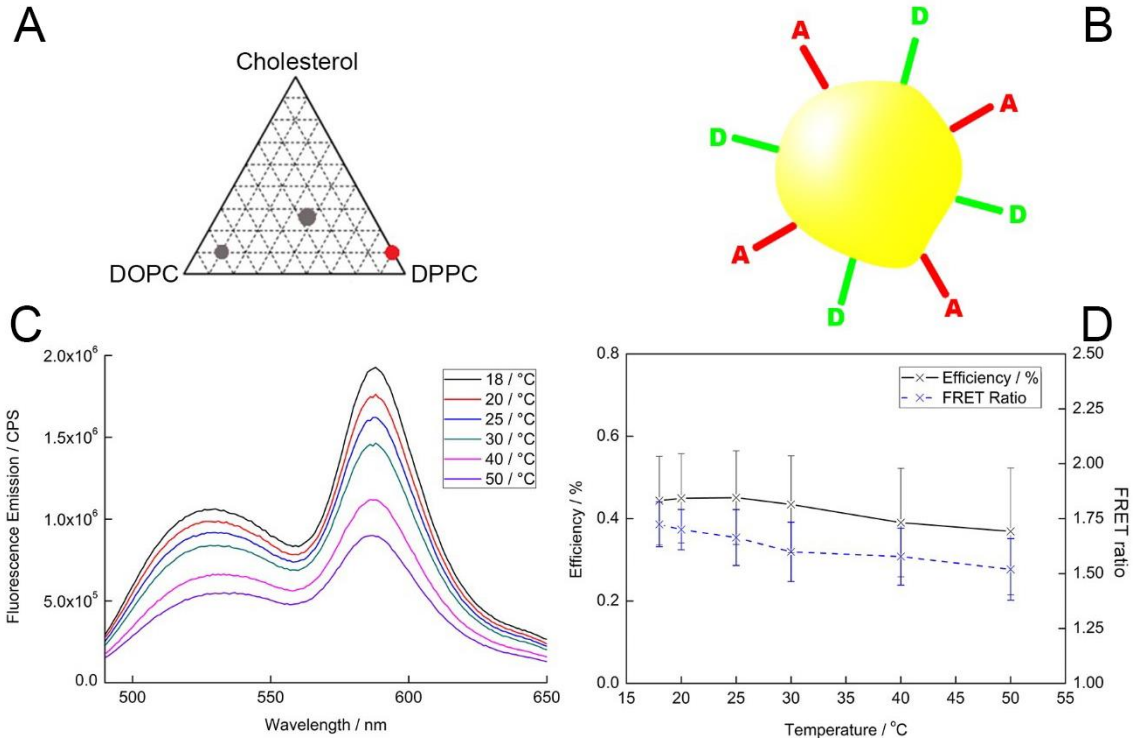

Figure 3.5 - A: Phase diagram displaying sample composition of DOPC:0%, DPPC:80%, Cholesterol:10% CL:10%in red, sample doped with NBD PE:0.2% and rhod PE:0.2%. B: Cartoon of interpreted data displaying donor (D) and acceptor (A) lipid dyes homogenously mixed across the vesicle's surface, where the vesicle is no longer a smooth sphere but rather a gel like distorted sphere. C: Example of raw fluorescence data initially excited at 460 nm with emission maxima for D at 535 nm and A at 587 nm. D: Calculated FRET ratios and efficiencies plotted against temperature.

The suspected single l_{gel} phase data displays a similarly high and consistent energy transfer across the temperatures measured, as seen in the l_d phase representatives. However, the l_{gel} samples displayed a higher fluorescence profile, suggesting that complementary FRET probes are closer in proximity to one another than in l_d phase representative samples. Overall from the FRET profile, it would appear that liposomes are always in a single phase, where it would be expected under heating that they transition from a single l_{gel} phase to single l_d phase.

Once again it was confirmed, through the data presented within Figure 3.5, that the FRET ratio offers a better means of processing FRET data than efficiency. Throughout the three phase representative samples, the FRET ratio temperature profile was able to distinguish between the three different phases more clearly than a FRET efficiency profile. The downfall of calculating FRET efficiency here is that it requires two samples; one with just donor dye in vesicles and a second with both donor and acceptor dyes. The need for two samples escalates experimental uncertainty when calculating FRET, resulting in a significant decrease in data accuracy. Where on the other hand, taking the ratio reduces uncertainty as it compensates for slight sample to

sample total lipid concentration deviations. A further disadvantage of calculating FRET efficiency, is that the need for two samples significantly lengthens experimental procedures, both in terms of the formation of samples and the analysis of samples.

However, neither data processing technique accounts for direct acceptor fluorescence instigated through donor excitation. Therefore, new experiments were conducted to gather a background measurement for all three samples, where acceptor fluorescence could be adjusted through Equation 3.1 and Equation 3.2.

Equation 3.1 - $$\boldsymbol{Attenuated\ Ratio} = \frac{(\boldsymbol{A_{DA}} - \boldsymbol{A_A})}{\boldsymbol{D_{DA}}}$$

Equation 3.2 - $$\boldsymbol{Attenuated\ Efficiency} = \mathbf{1} - \frac{(\boldsymbol{D_{DA}} - \boldsymbol{A_A})}{\boldsymbol{D_D}}$$

Where; A_A is the maximum acceptor fluorescence intensity when only acceptor dye is present within a vesicle, D_{DA} is the maximum donor fluorescence intensity when both donor and acceptor dyes are present a vesicle, D_D is the maximum donor fluorescence intensity when only the donor dye is present within a vesicle, and A_{DA} represents maximum acceptor fluorescence intensity when both donor and acceptor dyes are present in a vesicle.

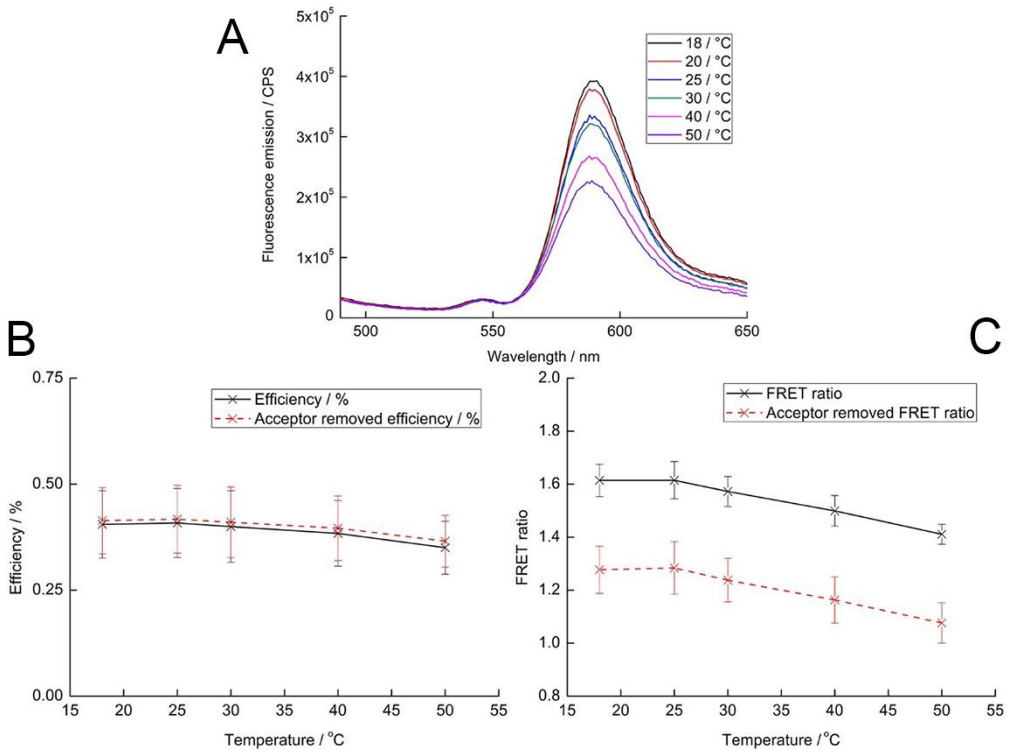

Figure 3.6 – l_d phase representative with a composition of DOPC:70%, DPPC:10%, Cholesterol:10% CL:10% A: Example of raw fluorescence acceptor data when excited at 430 nm doped with 0.2% rhod PE. B: Graph to compare FRET efficiency with FRET efficiency with non-resonant fluorescence removed. C: Graph to compare FRET ratios with FRET ratios with non-resonant fluorescence removed.

The initial raw fluorescence graph in Figure 3.6 displays rhod PE is excited through the dye's wide Gaussian excitation peak distribution. This subsequent fluorescence emission from rhod PE attributes to the fluorescence seen when both dyes are present in FRET experiments. Through subtracting the non-resonance induced fluorescence, measured in Figure 3.6, an attenuated efficiency and ratio was calculated. For the attenuated l_d phase efficiency, there was little improvement in the presented data. Contrastingly the FRET ratio had a significant systematic drop coupled with a rise in error.

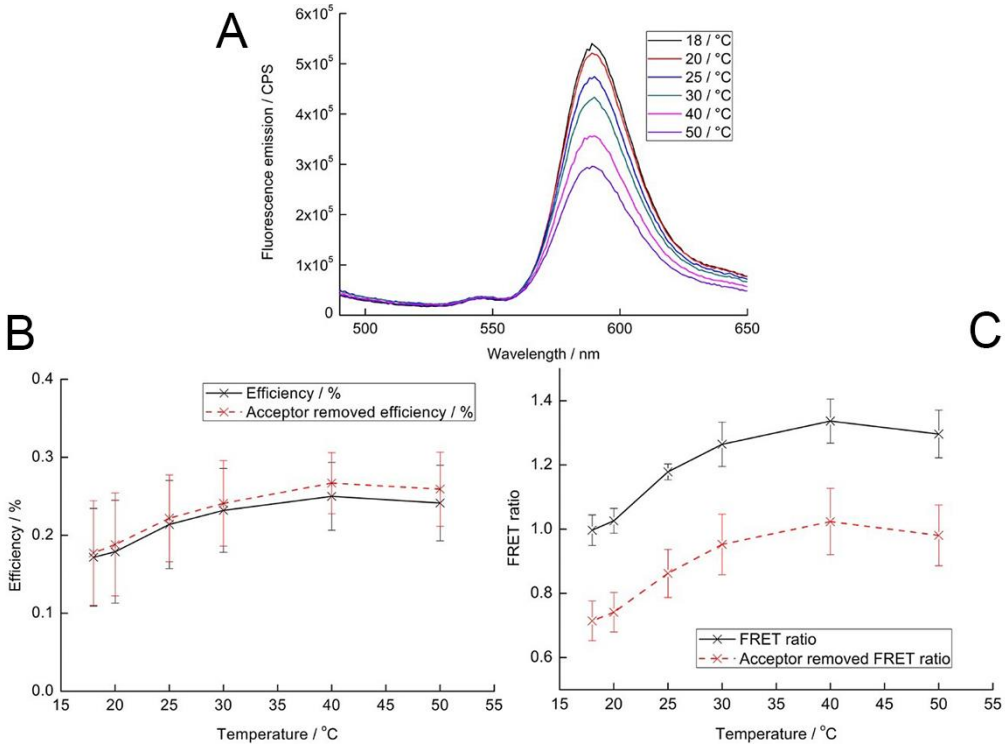

Figure 3.7 - l_d-l_o phase coexistence phase representative with a composition of DOPC:27.5%, DPPC:37.5%, Cholesterol:25% CL:10% A: Example of raw fluorescence acceptor data when excited at 430 nm doped with 0.2% rhod PE. B: Graph to compare FRET efficiency with FRET efficiency with non-resonant fluorescence removed. C: Graph to compare FRET ratios with FRET ratios with non-resonant fluorescence removed.

A similar trend occurs in Figure 3.7, as displayed for Figure 3.6, whereby attenuated FRET efficiency shows little in the way of change, and the FRET ratio displays an overall drop draped in higher experimental uncertainty.

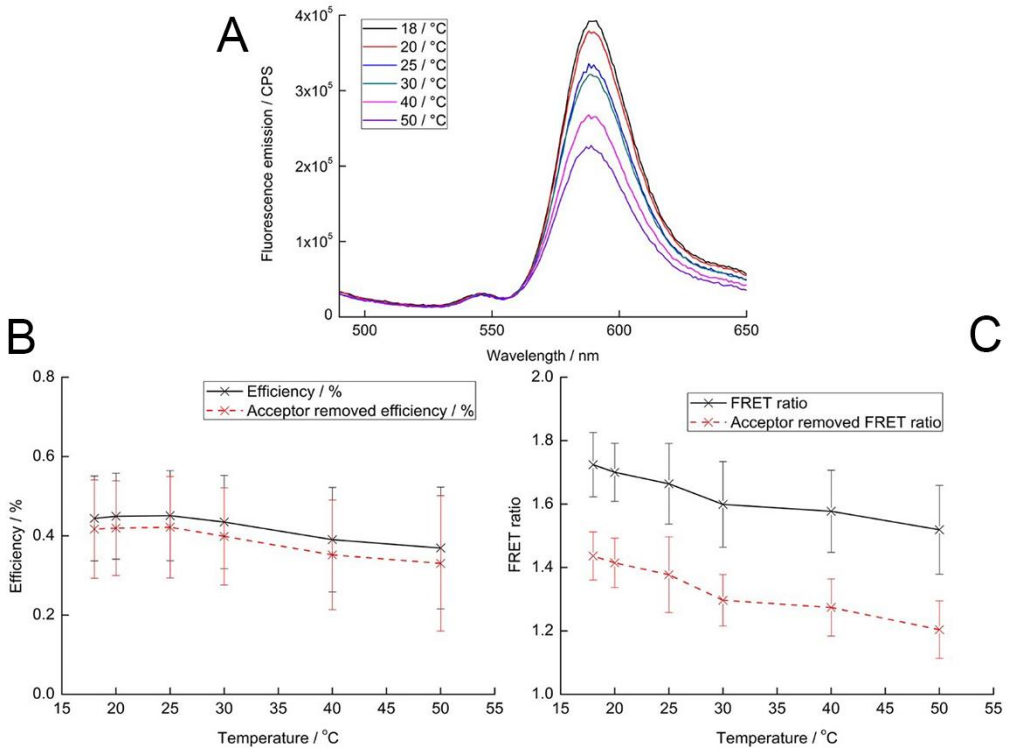

Figure 3.8 - l_{gel} phase representative with a composition DOPC:0%, DPPC:80%, Cholesterol:10% CL:10% A: Example of raw fluorescence acceptor data when excited at 430 nm doped with 0.2% rhod PE. B: Graph to compare FRET efficiency with FRET efficiency with non-resonant fluorescence removed. C: Graph to compare FRET ratios with FRET ratios with non-resonant fluorescence removed.

The final experiment, in regard to plotting attenuated FRET shown in Figure 3.8, displays the same trends seen for both FRET efficiency and ratio, already discussed. From Figure 3.6, Figure 3.7 and Figure 3.8 it is clear that accounting for direct rhod PE excitation does not lead to more distinguishable trends but invokes the opposite. This is a result of more experimental uncertainty being added through the need for further samples to be made and measured.

In summary, the most accurate technique to analyse the raw FRET data was to take the FRET ratio. Through only requiring one sample the ratio is overall lowest in uncertainty, and to maintain low uncertainty, direct acceptor excitation was not removed during future data processing.

3.1.3 Fluorescent probe concentration

3.1.3.1 Calculating probe separation

To ensure that the probes are at an appropriate concentration to detect phase transitions and phase boundaries, probe separation (r) was calculated for a 100 nm diameter l_d liposome. The first part of calculating r was to know the number of lipids on the surface of the liposome. To do this some assumptions were made:

- The diameter of the liposomes did not vary.
- There was no inter-liposome probe quenching.
- Only the surface monolayer of the vesicle was considered.
- All lipids had the same 0.71 nm^2 head group area [135].

Equation 3.3 - $$N_{surface\ total} = \frac{4\pi \times \left(\frac{d}{2}\right)^2}{a}$$

Where $N_{surface\ total}$ is the total number of lipids in the surface monolayer of the liposome, d is the liposome diameter and a is the surface area of a lipid. Assuming liposome diameter is 100 nm $N_{surface\ total}$ = 44247 lipids. 0.2 mole% of the lipids in the liposome surface are FRET acceptor probes and 0.2 mole% are FRET donor probes; therefore, the number of FRET probes within the monolayer is 177. Taking the ratio between the number of FRET probes against $N_{surface\ total}$ reveals there are 500 lipids per FRET pair. Assuming the FRET pair will be in a disk of 500 lipids, the maximum separation can be known once lipid disk diameter is calculated from its area. When calculating disk radius some assumptions again have to be made.

- There is only one acceptor probe and one donor probe per 500 lipids.
- Membrane curvature effects are insignificant.
- No other effects but the donor in question effect acceptor excitation.
- The liposome surface monolayer is in an l_d phase.
- There are no non-FRET quenching effects.

Equation 3.4 - $$r = \sqrt{\frac{N_{disk} \times a}{\pi}}$$

r is the radius of the lipid disk, N_{disk} is the number of lipids in the disk, which in this example is 500. From the calculation the 500 lipid disk was calculated to have a radius of 10.6 nm. In the 500

lipid disk the FRET pair are randomly separated by distance x. To calculate average probe distribution within the disk Equation 3.5 was used.

Equation 3.5 - $$x = \frac{r}{\sqrt{2}}$$

From Equation 3.5 average probe separation for 0.2% NBD PE and 0.2% rhod PE for 100 nm vesicles was calculated to be 7.5 nm. This separation is on the larger side of recommended FRET analysis limits of 10 nm [73]. However, the collected FRET data for the three phase representatives still displays an ability to depict the necessary information, to differentiate the phases. To compare this theoretical value of probe separation, an experimentally determined value was calculated using Equation 3.6.

Equation 3.6 - $$x^6 = \frac{{R_o}^6}{Efficiency} - {R_o}^6$$ **[136]**

Where x is the probe separation distance and R_o for NBD PE and rhod PE was found to be 5.2 nm [137]. Through Equation 3.6 and using the experimentally determined l_d 18 ^oC efficiency (0.401 from Figure 3.3), the experimental inter probe separation was calculated to be 5.5 ± 0.7 nm which is more representative of the 5.2 nm R_o for NBD PE and rhod PE. The disparity in the theoretical and experimental probe separation is likely due to three large assumptions made when making the theoretical calculation. Firstly, only the exterior monolayer was considered, removing any potential interactions across the lower dielectric oily lipid tail interface. Secondly, this analysis only reflects two probes, removing the complexity of mapping many probes. And thirdly, the model does not consider membrane curvature.

3.1.3.2 Raising probe concentration

Low probe concentrations are vital when mapping out the new phase diagram. If the concentration of the probe is too high they will become a major component of the phase diagram, which could lead to complex phase behaviour. High probe concentrations could potentially lead to the wanted four component phase diagram not being mapped but rather a six component diagram. Conversely if the probe concentrations are too low, high noise to signal data will be recorded. To ensure that probe concentrations are optimum to detect phase boundaries, where FRET signals may be less clear, probe concentrations were raised from 0.2-0.6 mol% for the previously shown l_d-l_o phase coexisting sample (DOPC:27.5, CL:10, DPPC:37.5, cholesterol:25).

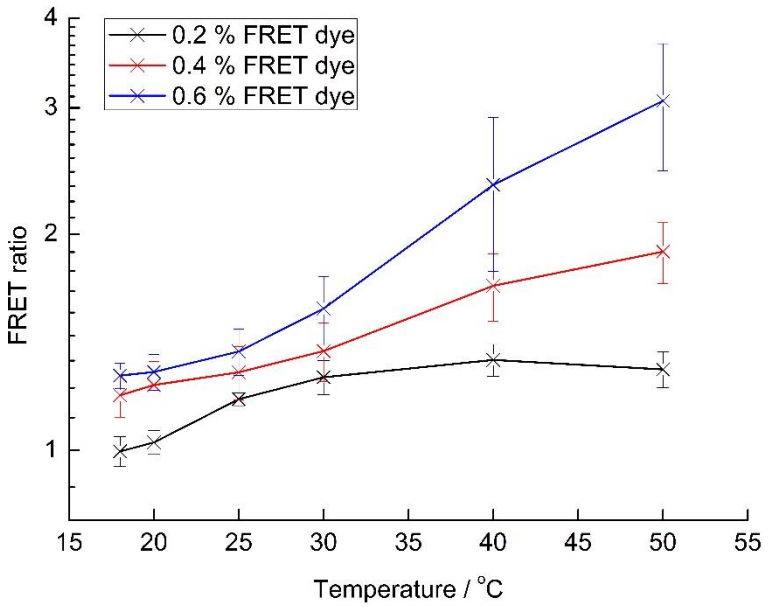

Figure 3.9 - Comparison of FRET ratios when the concentration of FRET probes is raised from 0.2-0.6 mol% in the l_d-l_o phase coexisting DOPC:27.5, CL:10, DPPC:37.5, cholesterol:25 sample.

Figure 3.9 exhibits higher probe concentrations leading to larger FRET ratios, while still displaying the FRET change, attributed to l_d-l_o phase coexistence melting at high temperatures. However, using higher concentrations of fluorescent probes has shown to be problematic. Whereby the experimental uncertainty has drastically increased, preventing data trends from being readily observed.

Furthermore, issues have been reported in the literature when using these probes in higher concentrations. Specifically, NBD has been discussed to self-quench when in high concentration through a static mechanism [133].This is a potential issue at low temperatures, where the donor probe partitions preferentially to the l_o domain, driving locally high concentrations of NBD. This is of major concern especially when domain sizes are small, raising the probability of self-quenching. Through self-quenching NBD would not be able to transfer energy through resonance to the acceptor, limiting the donor and acceptor fluorescence peak intensity. In the case of rhod PE, literature has shown that higher concentrations of the trace probe in solution and in model membranes, leads to a decrease in fluorescence emission [138]. In solution, quenching is driven through to the formation of aggregates. Conversely, within a l_d membrane, the reduced fluorescence is through an increase in the probability of dyes dynamically self-quenching, i.e. they collided together while in an excited state [138].

In conclusion, the experimental work illustrates that using lower concentrations of FRET probes (0.2 mol%) minimises error in calculating FRET, while still allowing the l_d, l_{gel} and l_d-l_o phases to be distinguished from one another. Lower concentrations also aid in minimising potential self-

quenching effects associated with NBD PE and rhod PE. Moving forward, all experiments used a concentration of 0.2 mol% for each fluorescence probe.

3.2 Phase boundary mapping

3.2.1 A coarse grain approach

With the NBD PE/rhod PE based FRET technique displaying the ability to effectively gather data to allow reliable interpretation of phase behaviour, coarse grain mapping of the four component phase diagram was initiated. Through coarse grain mapping and theoretical knowledge of allowed thermodynamic phase diagram topologies, a detailed phase diagram can be constructed while minimizing sample selection and analysis lead time. This is opposed to the previous work in mapping phase diagrams, whereby small changes in composition were made and analysed with no regard to composition error and sample preparation time [67].

Coarse grain experimental design relies upon taking samples across the phase diagram that are significantly removed from one another, to gain a general overview of the phase diagram. This general overview will display rough locations of the different phases. In order to find specific phase boundaries new samples were taken half way between the points of the two phases. This process was repeated until there was 5 mol% composition discrepancy between the two phases. 5 mol % was used as the experimental cut off, due to 3 mol% sample preparation error. Figure 3.10 displays an early example of coarse grain mapping and resulting FRET data.

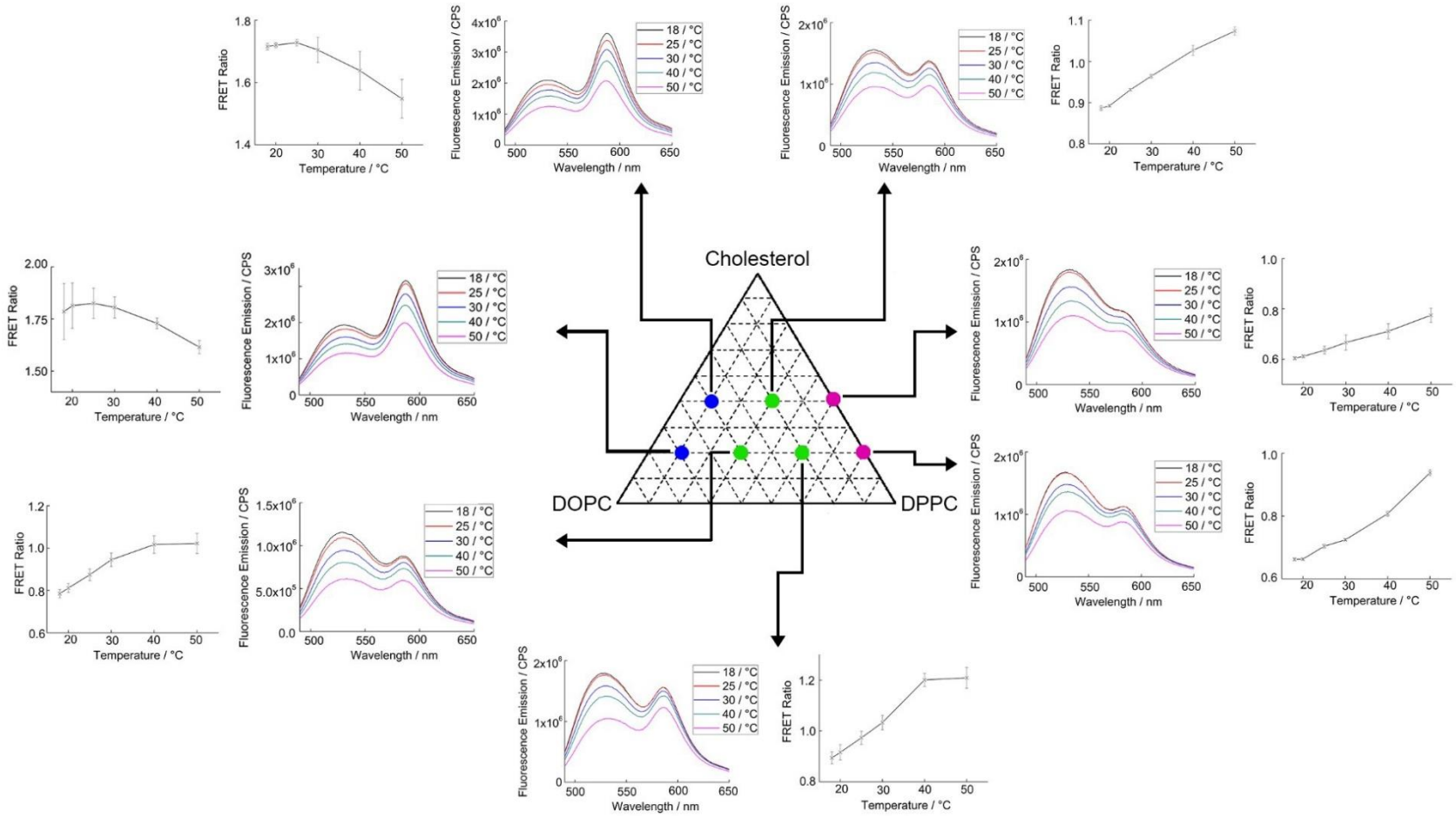

Figure 3.10 – Example of coarse grain mapping over the DOPC:DPPC:Cholesterol:CL phase diagram where CL was maintained at 10 mol%. The phase diagram has been annotated with raw fluorescence and processed FRET data. Blue samples display suspected l_d phase behaviour, green samples display suspected l_d-l_o phase behaviour and purple displays suspected l_o-H_{II} phase coexistence.

To develop the beginnings of the mapped phase diagram as shown in Figure 3.10; the FRET melting profiles and raw fluorescence graphs gathered from previously recorded phase representatives, were used to categorise new samples into FRET/phase behaviour styles. The FRET temperature profiles for samples in a suspected l_d phase, always have a FRET ratio above one despite raising the temperature. Suspected phase l_d-l_o co-existence regions, have FRET ratios that increase with temperature, where, at low temperatures (~20 ^oC) the FRET ratio is below 1 and upon heating (~50 ^oC) the ratio is higher than one. These designated categories have been labelled on the phase diagram shown in Figure 3.10 using colour. Blue has been used to express samples with implied l_d phase behaviour and green to display suspected l_d-l_o phase co-existence at low temperatures.

Purple on the other hand, has been used to denote previously unseen phase behaviour. It was anticipated from the previously recorded analogous three component phase diagrams, that the purple region of the phase diagram in Figure 3.10 would display l_o phase behaviour, attributed to the high cholesterol saturated lipid composition. Therefore, it was anticipated that these samples would have high FRET ratios similar to those recorded for the l_d phase. However, the samples high in saturated lipid content are unique in that they always maintain a FRET ratio below one, irrespective of temperature. To determine the cause of the phase diagram disparity from the addition of 10 mol% CL, further FRET investigation was conducted.

3.2.1.1 l_o-H_{II} phase coexistence

From the early coarse grain mapping of the phase diagram, samples that contained 0 mol% DOPC produced fluorescence spectra and FRET temperature profiles unlike those produced for the phase representatives. Figure 3.10 displays samples with 0 mol% DOPC having low acceptor fluorescence, which when heated does not rise above the donor fluorescence as seen for l_d-l_o phase coexisting FRET samples. The addition of CL as a fourth component opens up the potential for a four phase triangular pyramid, yielding possible H_{II} phase formation at high CL concentrations (see Table 1.1) [139]. In other words, rather than centre of the phase diagram having three phase coexistence, as shown in Figure 1.8, the extra lipid component, CL, could be adding to its complexity, which has been speculatively outlined in Figure 3.11.The extra vertices offered by this potentially new four phase triangular pyramid, affords the possibility for new phase co-existence regions.

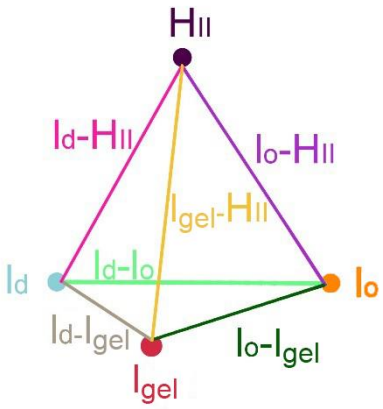

Figure 3.11 – Cartoon of the four phase triangular pyramid when CL is added as a fourth component and is no longer set at 10 mol%. The cartoon displays the potential phases associated with each of the edges and vertices. The 3 phase co-existence regions have not been recorded for image clarity.

It was anticipated that 10 mol% CL would be low enough in concentration to cause minimal disturbance to the previously recorded three component phase diagram, and limit the potential for additional unwanted phase coexistence beyond what is necessary for Janus vesicle cluster building. However, this early coarse gain mapping indicates that this may not be the case. To further explore the potential of phase I_o-H_{II} coexistence and map the size of this region, coarse grain mapping was continued along the 0 mol% DOPC axis where CL concentration is maintained at 10 mol%.

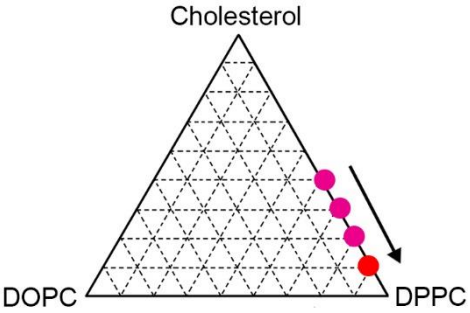

Cholesterol mole%	DPPC mole%	FRET ratio at 18 °C	Error	FRET ratio at 50 °C	Error
40	50	0.604	0.006	0.775	0.028
30	60	0.608	0.004	0.815	0.018
20	70	0.662	0.004	0.938	0.008
10	80	1.724	0.102	1.519	0.14

Figure 3.12 – Top: DOPC:DPPC:Cholesterol: phase diagram where CL is maintained at 10 mol% displaying sample selection with colour denoting phase behaviour. Purple references suspected l_o-H_{II} phase behaviour and red the l_{gel} phase. Bottom: Table displaying sample composition and calculated FRET ratios at 18 and 50 °C.

Through coarse grain mapping the 0 mol% DOPC axis displays a trend where FRET ratio rises slowly with a decreasing mol% of cholesterol, as seen in Figure 3.12, until crossing into the l_{gel} phase at 10 mol% cholesterol. This indicated phase behaviour change along the 0% DOPC axis was perhaps linked with cholesterol concentration. To validate the hypothesis that unsuspected FRET results were related to the addition of CL, rather than a failing of the FRET analytical technique, a comparison of samples, where 30% cholesterol was maintained alongside 10 mol% unsaturated lipid, were examined via FRET.

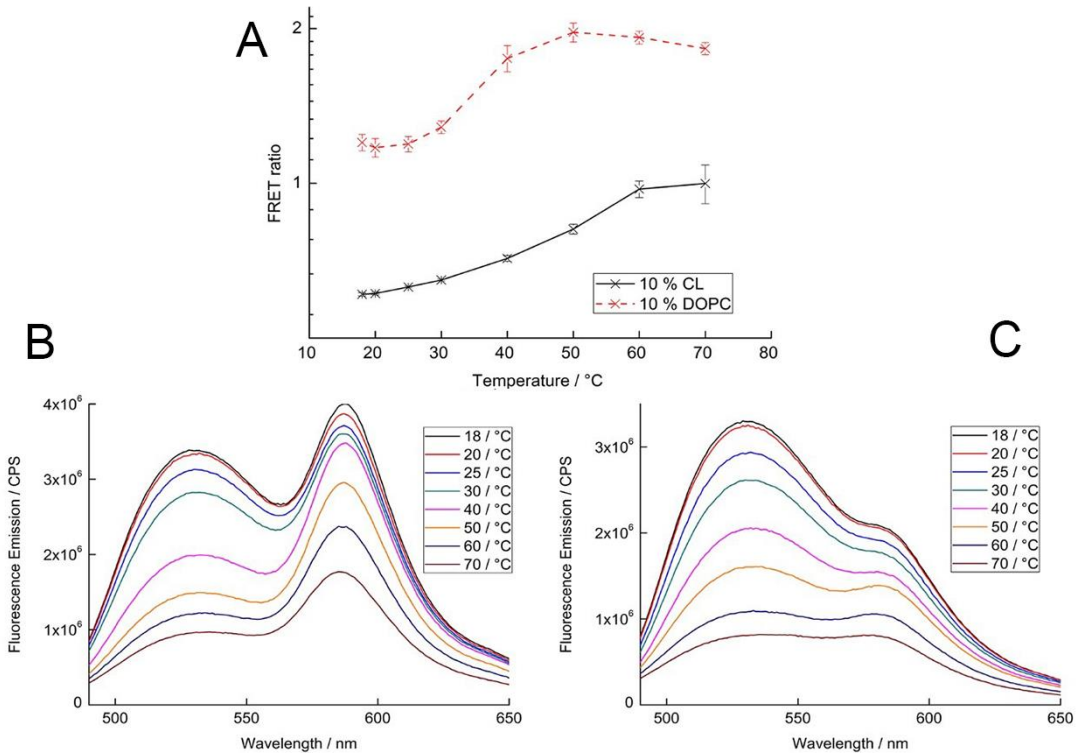

Figure 3.13 – A: comparison of FRET ratios from samples where the unsaturated component was changed from 10 mol% CL to DOPC. DPPC and cholesterol were maintained at 60 and 30 mol% respectively. B: raw fluorescence data for DOPC:DPPC:cholesterol at concentrations of 10:60:30 mol% respectively. C: raw fluorescence data for CL:DPPC:cholesterol at concentrations of 10:60:30 mol% respectively

Figure 3.13 displays that the swapping of 10 mol% CL with the alternate DOPC leads to drastically different FRET data. Fluorescence results for the DOPC system, fell in line with published data by S. Keller et al; indicating that FRET does provide a solid platform to map out phase behaviour in this low DOPC environment. The unexpected results must consequently be significant in displaying unusual phase behaviour.

A plausible explanation for the low FRET values, attributed to low DOPC mol%, could be due to CL's polymorphism, whereby CL can form bilayers or hexagonal (H_{II}) phase arrangements. Furthermore literature discusses that CL in its polymorphism can swap between phases by nulling the head group's negative charge, specifically through the addition of calcium ions (Ca^{+2}) [140]. CL is a lipid that is physically cone shaped with a small polar head group and four large di-unsaturated hydrophobic tails. However CL's negative net charge, gained from two acidic protons; one with a pk_a of 1.05-2.8 the second being 7.5-9.5 [141], provides a repulsive force, creating a cylindrical shaped molecule in terms of packing arrangement. Through removing the negative

charge (shown within Figure 3.14) with sodium, there will be no head group repulsion; and the overall shape of the molecule will be a cone.

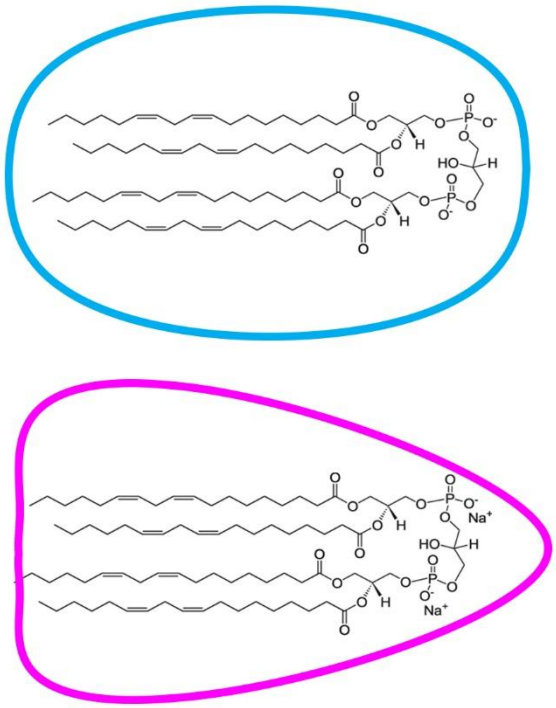

Figure 3.14 – The polymorphism cardiolipin: Top - net 2^- charge results in cylindrical packing arrangement; outlined by the blue cylinder. Right – cardiolipin neutralised through sodium addition generates an inverted cone shape, with the purple cone displaying the new preferred packing arrangement.

Upon forming a cone shape where head groups are smaller than their respective hydrophobic tail groups, which is achieved when CL is neutralised, H_{II} packing is preferential. 1,2-dioleoyl-sn-glycero-3-phosphoethanolamine (DOPE) is an analogous lipid to CL, with the ability to form H_{II} phases and the potential to form “lipidic particles” (I_o-H_{II} coexistence) [142]. DOPE has been discussed to enter a I_o-H_{II} phase coexisting state, as an intermediate between planar bilayers and inverted micelles. Specifically of interest DOPE has shown to display I_o-H_{II} phase coexistence through increasing the cholesterol concentration to 33 mol% [142]. The authors argue that cholesterol stabilises the hydrophobic tails by inserting itself into the free spaces formed once the membrane starts to invert [142].

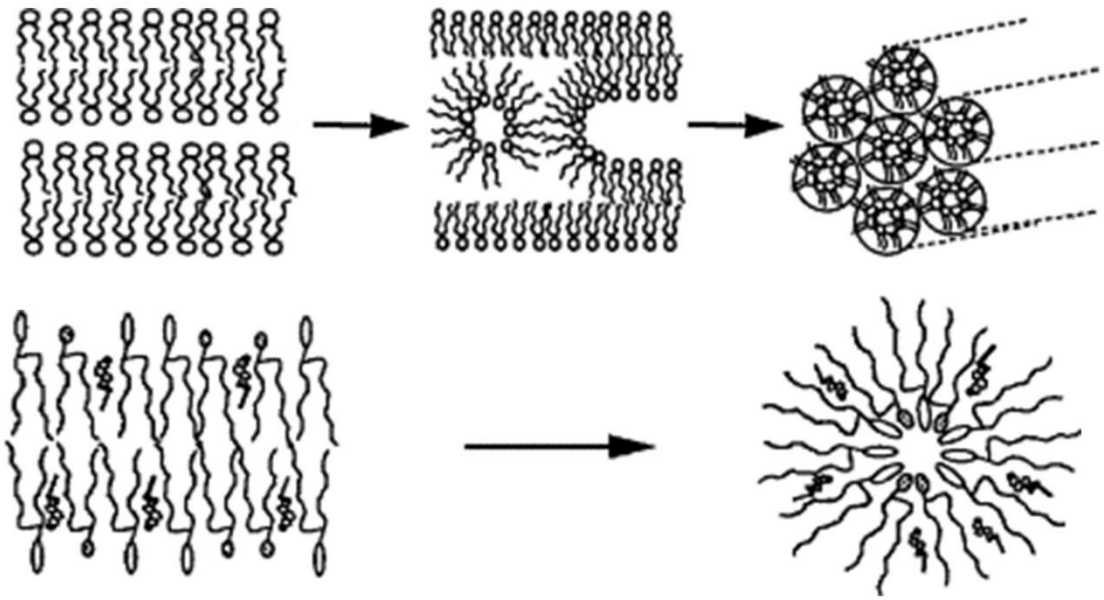

Figure 3.15 – Suggested cartoon model for "lipidic" particle/I_o-H_{II} phase coexistence: Top - Cartoon displaying formation route of the H_{II} phase from a bilayer via I_o-H_{II} phase coexistence intermediate. Bottom – Cartoon displaying the role of cholesterol stabilising H_{II} phase formation [142].

Literature therefore indicates that cholesterol may play an important role in polymorphic lipids being able to swap their packing arrangements. This model potentially agrees with data presented here for CL, whereby FRET signal is reduced with rising cholesterol for samples with limited DOPC. In other words, rising cholesterol may encourage I_o-H_{II} phase coexistence. Furthermore, CL has four times the number of unsaturated bonds than that offered by DOPE, potentially proposing an explanation as to why inverted phase behaviour is apparent for CL at lower cholesterol concentrations (<33 mol%) as previously reported for DOPE [142].

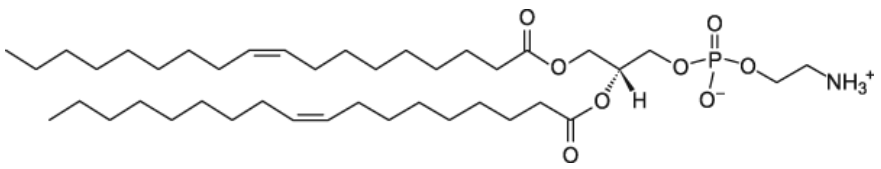

Figure 3.16 – 1,2-dioleoyl-sn-glycero-3-phosphoethanolamine (DOPE).

To confirm and gain a fuller understand of the potential I_o-H_{II} phase coexistence, further investigation using complementary techniques was required, as discussed in section 3.2.2 page 93. However, for the purpose of phase boundary mapping FRET still offered a viable, sensitive approach to detect dissimilar lipid phases. Specifically, FRET was still able to provide a

method to define phase boundaries, even across this unexpected phase region. Finally, in regard to potential l_o-H_{II} coexistence, while the full mapping of the phase diagram is of interest, it should be recognised that the spirit of the project is directed towards mapping out the l_d-l_o phase co-existence region, for practical uses within size limited Janus drug delivery systems.

3.2.2 FRET interpretations

Continuing with the coarse grain FRET analytical technique, three phase diagrams of the four component DPPC, DOPC and cholesterol across a 10 mol% CL slice were produced. Originally lipid composition was plotted against FRET ratio at 20 °C, yielding a 3D FRET ratio plot of the phase diagram which is displayed in Figure 3.17. This plot shows the four main areas of interest l_d, l_d-l_o, l_{gel} l_o-H_{II} phases, each represented by blue, green, red, and purple respectively. Similarly, a phase diagram at 50 °C was produced from the FRET data. At this raised temperature, the l_d-l_o phase coexistence region had melted increasing the FRET ratios. However, these 3D FRET ratio graphs poorly define phase boundaries and only partially display the phase diagram, making them difficult to interpret. Through returning to using FRET data and phase representatives as a qualitative technique, a clear, experimentally determined, phase diagram was plotted (Figure 3.17).

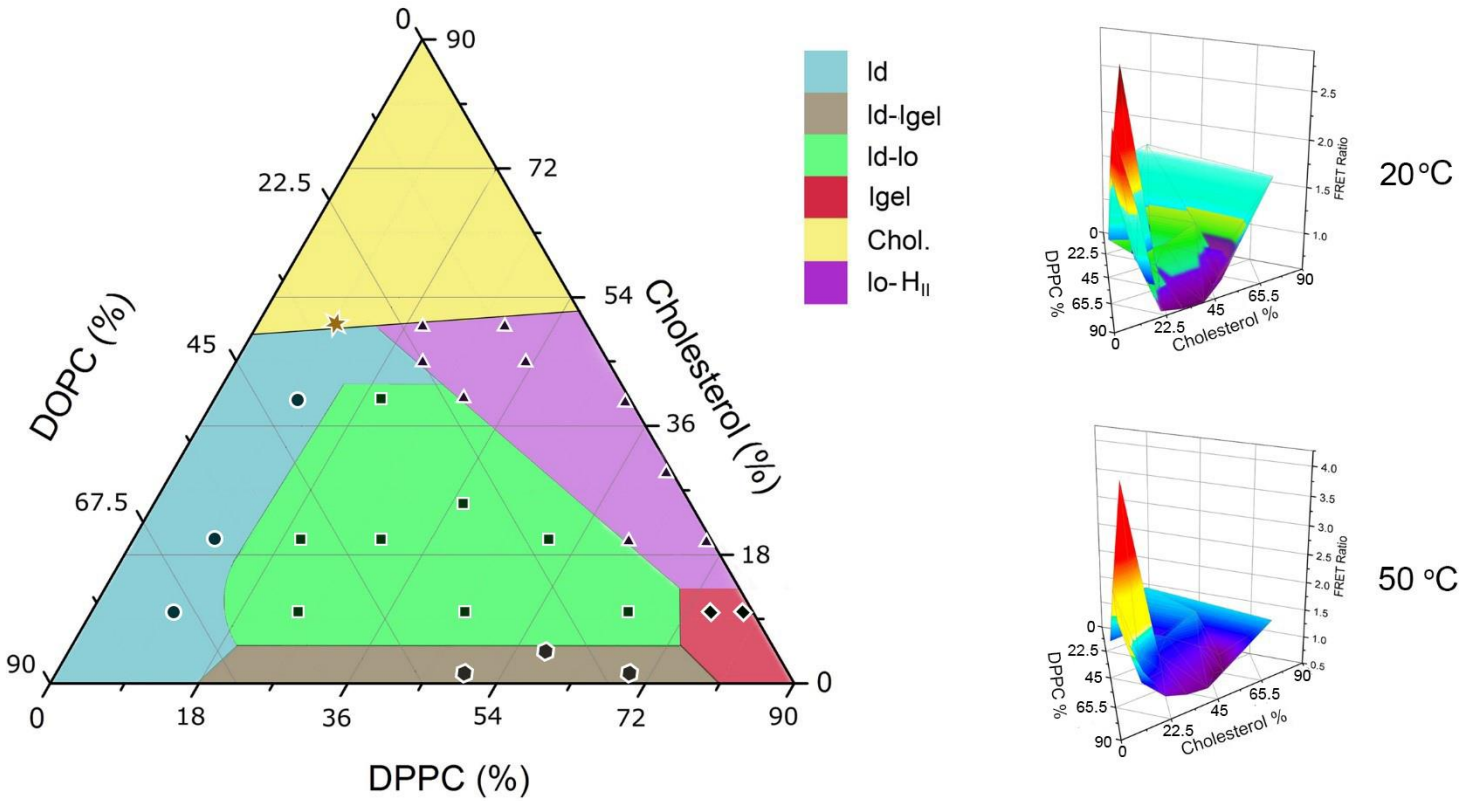

Figure 3.17 – Left: Experimentally determined 2D DPPC, DOPC, cholesterol phase diagram with CL set at 10 mol% at 20 °C, dots representing samples taken. Top Right: raw FRET ratio data plotted on a DPPC, DOPC, cholesterol phase diagram with CL set at 10 mol% at 20 °C creating a 3D representation of the phase diagram. Bottom Right: raw FRET ratio data plotted on a DPPC, DOPC, cholesterol phase diagram with CL set at 10 mol% at 50 °C.

The 2D experimentally determined phase diagram was drawn through further FRET interpretations and the visualisation of the formation of cholesterol crystals. The latter was readily observed, Figure 3.18, with the crystal phase boundary beginning at ~50 mol%.

Figure 3.18 – Cholesterol crystalsformed at a composition of DOPC 30% DPPC 10% cholesterol 50% CL10% with NBD PE and rhod PE both being maintained at 0.2 mol% respectively. The photograph displays three repeats with crystals being present.

The formation of crystals produces vesicles with reduced and unknown cholesterol levels in their membranes, rendering them unsuitable for further development. Continued mapping above 50 mol% cholesterol was not carried out due to project focus being about the l_d-l_o phase coexistence region. Previous published phase diagrams for DPPC:DOPC:cholesterol states that above 50 mol% cholesterol no further phase changes occur [67].

In regards to the other interpreted phases, the l_{gel} phase was shown to be homogeneous through not presenting any melting transitions as seen for suspected l_o-l_d co-existing samples. While a lack of a transition does not directly link it with being a l_{gel} phase, the lack of unsaturated lipid and wealth of saturated lipid indicate a l_{gel} phase being present. Finally, where cholesterol is ≤0%, melting transitions are still observed similar to l_o-l_d co-existing samples, indicating the melting of saturated lipid domains. However, this result is accountable to l_d and l_{gel} phase separation, rather than l_d and l_o phase separation as previously shown by J.T. Buboltz et al. in the analogous DPPC:DOPPC:cholesterol phase diagram [67].

The phase diagram presented in Figure 3.17 only marks phase boundaries from the interpretation of FRET data. However, not all phases have been recorded that are known to be present. For example, while the three phase triangle for DOPC:DPPC:cholesterol is not always recorded, its location has been noted to calculate tie line positions, see Figure 1.8 [67], [76], [78]. The experimental data gathered through course grain mapping confirms that the three phase triangle has not significantly changed its position though CL incorporation, but has so far been ignored in

Figure 3.17. The next iteration of the phase diagram’s design was to evolve it to comply with phase diagram theory, where theory disclosed details that FRET/coarse grain mapping could not determine.

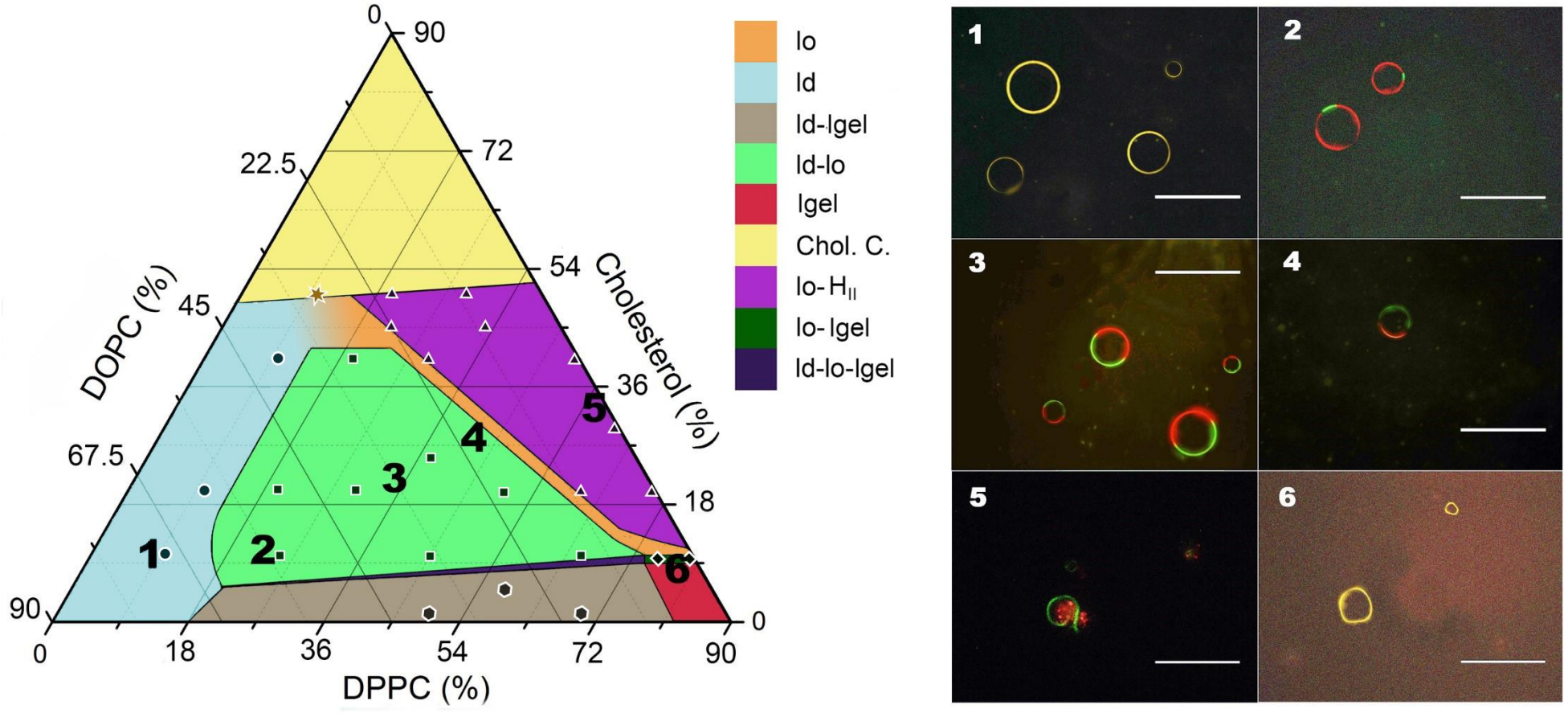

Figure 3.19 – The corrected experimentally determined DPPC, DOPC, cholesterol phase diagram with CL set at 10 mol% at 20 °C, dots represent samples taken. Numbered fluorescence microscopy images display phase behaviour of lipids in GUV samples. All images were produced in conjunction with 0.2 mol% NBD PE and rhod PE fluorescent dyes respectively Scale bar represents 20 μm.

The phase diagram present in Figure 3.19 has the addition putative phases. The first of these is a three phase triangle displaying three phase co-existence. From the top right hand corner of the three phase triangle will exist a pure l_o phase. This phase will be small and has no strict phase boundary with the l_d phase, therefore on the diagram no strict distinction between the l_d and l_o phases has been made and is represented through a colour gradient. The l_o phase must exist between the l_d-l_o and l_o-H_{II} phases to comply with the law of adjoining phases [139], where two phase coexisting regions must be separated by a single phase region. The final addition to the experimentally determined phase diagram was the small l_o-l_{gel} phase coexisting region. This will be a very small region due to the small size of the three phase triangle's edge and positioning between the two other phases. While all these additions are important to produce a comprehensive phase diagram, the experimentally interpreted diagram in Figure 3.17 would suffice to produce Janus nano vesicles.

The four component phase diagram slice was intentionally plotted using nano-sized vesicles using FRET in order to accurately map phase boundaries, rather than interpreting phase behaviour from giant vesicles. However, to confirm FRET data were being interpreted correctly, GUVs were prepared and imaged to visualise the suspected phase behaviour, as well as the unusual l_o-H_{II} phase behaviour as hypothesised in section 3.2.1.1 page 86. Figure 3.19 displays compositions of GUV samples taken across the phase diagram and resulting imaged structures. Images were gained through confocal fluorescence microscopy, once again taking advantage of NBD PE and rhod PE phase partitioning preferences. Sample 1 is in the single l_d phase part of the phase diagram which is displayed in the homogeneous surface shown in the microscopy fluorescence image. Samples 2, 3 and 4 are in the direction of the l_d-l_o phase tie line taken from the DOPC:DPPC:cholesterol phase diagram. It was assumed from the overall similar topology of the phase diagram 10 mol% CL would not invoke a large change in the overall direction of the three component l_d-l_o tie line, making it suitable for use as a pseudo tie line for the four component lipid system. Through interpreting this pseudo tie line, it was expected that the area of green NBD PE would increase with DPPC percentage and conversely the area of red, rhod PE, would diminish. Confocal images confirm that positioning on the pseudo tie line does affect the proportion of each coexisting phase and the potential size of functionalisable area. Sample 5 appears to have a l_o-H_{II} phase coexisting membrane, denoted by the NBD partitioning studded with very bright rhod PE groupings. These observations fall in line with the models previously presented whereby both l_o phase and H_{II} phase are cohabiting the same vesicle. Here it is inferred that NBD PE enters the saturated l_o domain across the surface of the vesicle and rhod PE partitions to the unsaturated H_{II} phase. This hypothesis has been illustrated in the cartoon model depicted in Figure 3.20.

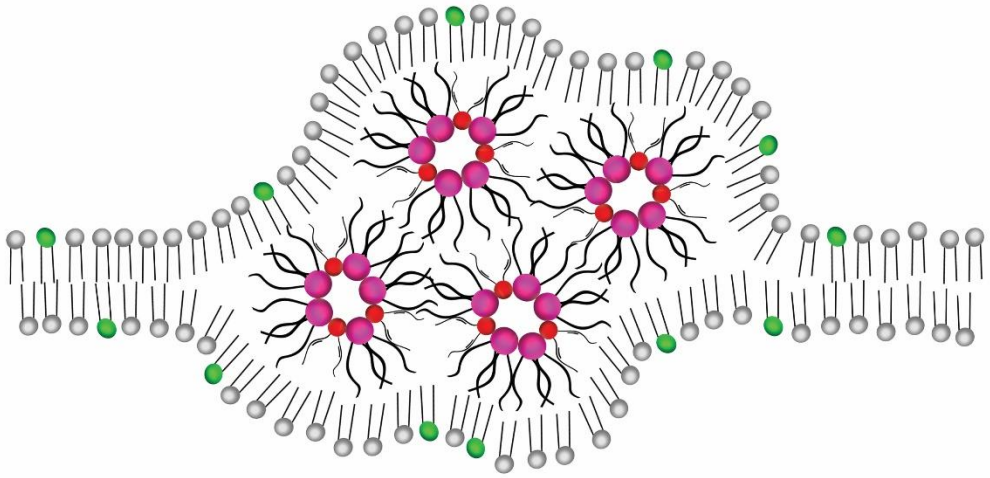

Figure 3.20 - Cartoon of the suggested model for l_o-H_{II} phase coexistence. DPPC, CL, NBD PE and rhod PE are represented through the grey, purple, green and red headed lipids respectively. Cholesterol has been removed from the cartoon for drawing clarity.

The model displays how the highly hydrophobic H_{II} phase is encompassed and stabilised through the surrounding l_o phase. This behaviour would go some way to explain NBD doped saturated membrane surrounding pockets of red rhod PE doped inverted micelles, inferred from the confocal image.

Finally, the last fluorescence confocal image for sample 6, displayed in Figure 3.19, exhibits a deformed structure similar to those present in literature.

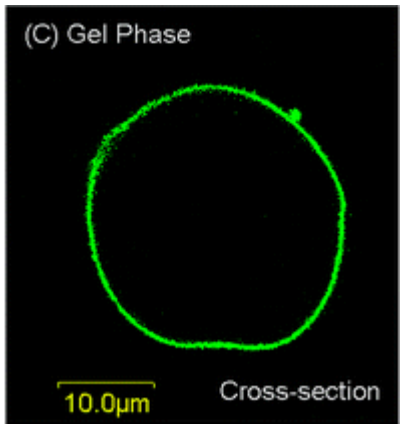

Figure 3.21 – Confocal fluorescence microscopy image of a DPPC vesicle in a l_{gel} phase labelled with Bodipy-PC [143].

The literature image in Figure 3.21 and the phase representative image of sample 6 in Figure 3.19, display very similar morphological characteristics. Both structures are shown to have similar rigid non-spherical morphologies due to the tight packing of saturated lipids. The similarity therefore gives confidence to the interpretation of sample 6 being in a l_{gel} phase.

3.3 Summary

Using FRET, nano-size vesicle phase behaviour has been mapped at 20 ^{o}C to produce a four component phase diagram of DOPC, DPPC, cholesterol and CL, where CL is fixed at 10 mol%. The phase behaviour and subsequent phase boundaries have been monitored through the measurement and interpretation of raw fluorescence data and FRET ratio temperature profiles, spanning 18-50 ^{o}C. Multiple methods were scrutinised to develop the best FRET data processing procedure, with the FRET ratio providing the best route to minimise uncertainty. While examining phase behaviour unexpected l_o-H_{II} phase coexistence was observed, where l_o-H_{II} phase coexistence has been rationalised to be connected to cholesterol concentration. This connection has previously been shown in literature with analogous DOPE. All phases were confirmed through complementary confocal fluorescence microscopy images of GUV samples.

Chapter 4

Thermal examination of lipid-DNA conjugates incorporated into vesicles

To form controlled vesicle dimers a DNA “glue” needed to be incorporated into the previously established heterogeneous liposome surface. To provide the “sticky” patch on the vesicle’s surface, lipid-DNA was integrated into vesicles. The purchased lipid-DNA consisted of two 16 carbon length saturated lipid tails attached to previously designed DNA sequences, constructed via phosphoramidite chemistry. The basic structure of a lipid-DNA molecule has been drawn in Figure 4.1.

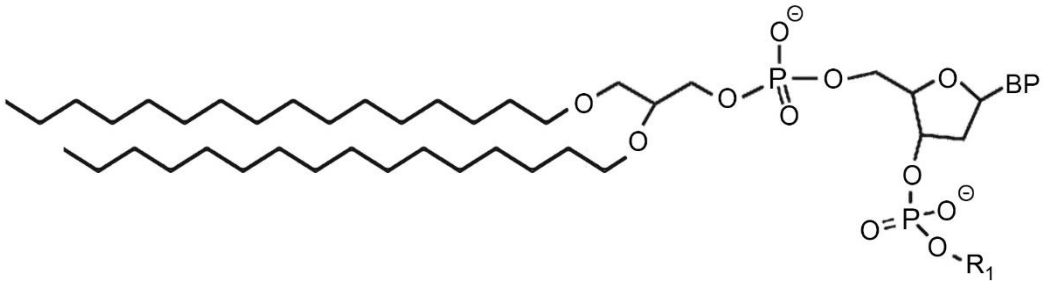

Figure 4.1 – Lipid structure of lipid-DNA conjugates. R_1 denotes the DNA rest of the oligonucleotide and BP represents the first BP attached to the lipid tail.

Expanding on the lipid-DNA structural template outlined in Figure 4.1, the complete four sequences purchased were:

1. lipid-5′-TTT ACA GAC TAC C-3′
2. lipid-5′-TTT GGT AGT CTG T-3′
3. lipid-5’-TTT TTT TTT CCC TAA CCC TAA CCC TAA CCC-3‘
4. lipid-5’-TTT TTT GGG TTA TGG TTA GGA TTA GTG-3’

The first two short 13 base pair (BP) long sequences are fully complementary to one another with the exception of the three thymine (T) spacers. These spacers ensure there is a gap between the vesicle

surface and the incoming binding DNA of ~1 nm, thereby reducing membrane surface effects on hybridisation. Sequences 3 and 4 are 30 mer and 27 mer BP long sequences respectively, and have been designed to provide pH sensitivity as i-motif sequences. Each strand has thymine spacer groups and three BP mismatches. These mismatches lower the binding free energy of the hybridised duplex aiding inter strand dehybridisation and intra molecular i-motif folding at low pH. The three mismatches between the two i-motif sequences have been displayed in Figure 4.2.

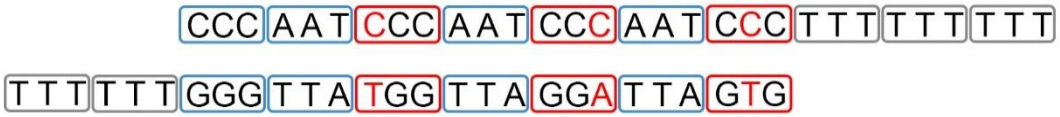

Figure 4.2 – i-motif DNA sequences aligned as they would be in vesicle hybridisation. Blue boxes display three complementary BPs and red denotes a mismatching base pair. Top: sequence 3. Bottom: sequence 4.

Through the incorporation of i-motif sequences into the Janus vesicles a pH sensitive switchable device could be produced. The resulting switchable device would greatly improve the scope of this Janus vesicle sized limited cluster drug delivery platform, into a realm of stimuli responsive applications.

4.1 Lipid-DNA self-assembly

Before incorporating the lipid-DNA into vesicles, the Critical Micelle Concentration (CMC) was measured. Through measuring the CMC and comparing results with literature, the lipid tail and DNA would be shown to be conjugated together. Furthermore, the CMC would give a working concentration to be below in future experiments, giving a twofold benefit. Firstly, micelle formation would lower the concentration of free lipid-DNA and membrane integrated lipid-DNA. Secondly, it ensures lipid-DNA micelles do not significantly interfere in later dynamic light scattering experiments. To measure the CMC of the DNA-lipids 1-(2-pyridylazo)-2-naphthol (PAN) [126], a water insoluble organic dye [127], was dissolved in hexane and added to DNA-lipid solutions. Upon increasing surfactant concentration above the CMC micelles form, which enabled PAN to partition into the hydrophobic rich domains, increasing absorbance at 470 nm [126].

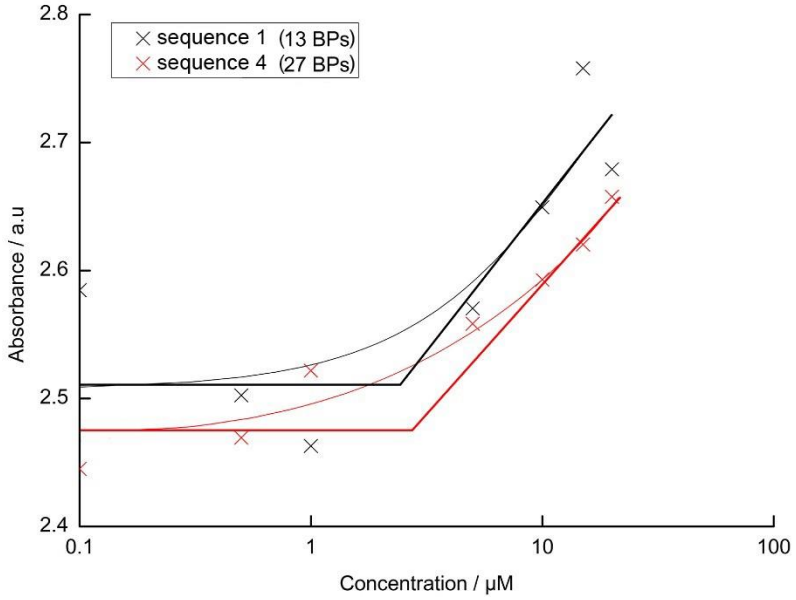

Figure 4.3 - Detecting the CMC for lipid-DNA using UV-vis spectroscopy. Wavelength was set to 470 nm. Solid straight lines display the vertices at which the CMC values were measured. Curved lines are a guide for the eye.

From the data presented in Figure 4.3 a CMC was obtained for both sequences. The 13 base pair sequence was calculated to have a CMC of 6.4 mM and the 27 base pair sequence was calculated to have a CMC of 7.3 mM. These values are in the range of those presented by Stef A. J. van der Meulen et al., indicating that the lipid and DNA are conjugated together and ready for liposome incorporation. However, no clear distinction can be made to argue that the length of the DNA sequence affects the CMC, due to a lack of repeats and associated large uncertainty. No repeats were performed due to the high volume of sample required by this analytical method. Likewise Stef A. J. van der Meulen et al. did not display error bars on their data, suggesting that sample volume may have also been a limitation for them [126].

4.2 Ultraviolet absorption spectroscopy and calculating the melting temperature of lipid-DNA

Experiments were conducted to determine the appropriate loading of lipid-DNA per vesicle. To do this the melting temperature of integrated lipid-DNA (T_m) was measured through ultraviolet absorption spectroscopy, where two wavelengths could be used to measure the T_m. The first at 260 nm displays UV DNA absorption where the BPs in single stranded DNA (DNA_{ss}) are able to perform electronic $\pi - \pi^*$ transitions, which are quenched once hybridised to form double stranded DNA (DNA_{ds}) [96]. The second wavelength is 320 nm where turbidity changes are recorded. In other words, when

vesicles hybridise together the resulting clusters become larger than the incident light, and therefore scatters light more effectively than single vesicles [96]. Specifically, at low temperatures vesicles are hybridised together (high turbidity), and upon the DNA melting, the turbidity drops as more single vesicles are formed [96]. These turbidity changes in vesicle samples likely also swamp the π transitions seen at 260 nm. However, both experiments record a sigmoidal DNA transition curve, where half way up the curve is the point at which half of the DNA is hybridised to its complementary strand, signifying the melting temperature of the DNA.

Furthermore, using the experimentally determined T_m a van't Hoff derived thermodynamic model can be applied, allowing the changes in entropy and enthalpy to be calculated.

4.2.1 pH non-responsive lipid-DNA vesicle incorporation

4.2.1.1 pH 7.4

This thesis has so far primarily focused on heterogeneous mixtures of lipids to investigate phase separation. However, to assess DNA T_m and lipid-DNA suitability, homogeneous vesicles of 1-palmitoyl-2-oleoyl-sn-glycero-3-phosphocholine (POPC) were loaded with lipid-DNA. Through using a homogeneous vesicle, only DNA interactions between vesicles will be measured when the vesicles are heated/cooled. Measurements on heterogenous vesicles would be subject to the effects of both DNA melting and cooling, combined with the melting and condensing of l_o patches in phase coexisting vesicles.

Six loadings were initially chosen from 10 DNA strands per vesicle to 250/vesicle to examine the effect of DNA loading on T_m. DNA loadings in vesicles were kept at equimolar concentrations. For example, vesicles doped with 10 DNA stands/vesicle of sequence 1 were mixed with vesicles doped with 10 DNA strands/vesicle of sequence 2. To complete the sample for UV analysis, the 0.5 ml aliquot of vesicles doped with sequence 1 was mixed with the 0.5 ml aliquot containing vesicles doped with sequence 2, to make up a total volume of 1 ml. Lipid concentrations were maintained at $1x10^{-3}$ M and lipid-DNA loading were calculated using Equation 2.11.

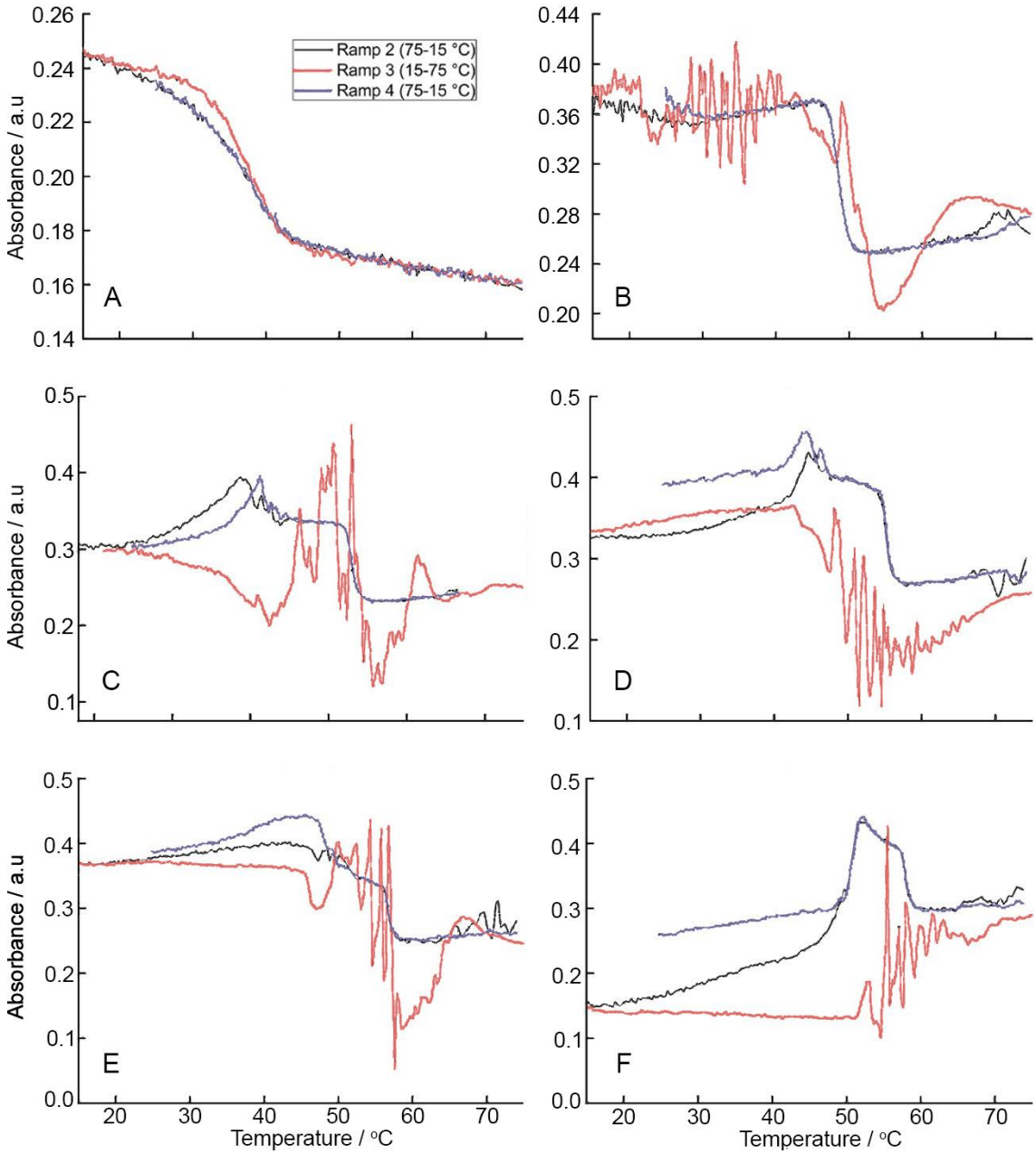

Figure 4.4 – Thermal-melt data of hybridised DNA loaded vesicles temperature controlled at a ramp rate of 0.5 °C min^{-1} with absorbance taken every 10 seconds. A and B are loadings of 10 and 50 lipid-DNA/vesicle respectively; C and D are loadings of 100 and 150 lipid-DNA/vesicle respectively, and finally; E and F are loadings of 200 and 250 lipid-DNA/vesicle respectively.

The data in Figure 4.4 displays that above a DNA concentration of 10 DNA/vesicle heating ramps lead to sharp uncontrolled transitions. Contrastingly cooling cycles gave more reliable sigmoidal curves. Furthermore, higher DNA loading affords more hybridisation between vesicles and therefore

yields higher temperature stability. These larger flocculates of vesicles formed a sediment at the bottom of the cuvette, leading to unpredictable absorption at lower temperatures for higher DNA concentrations.

To calculate the T_m of samples the melting ramps were discounted as they yielded unrepresentative results. Once removed, first derivatives were calculated from the cooling ramps in Figure 4.4. The cooling ramp first derivatives were then taken and plotted against temperature as shown in Figure 4.5. The data in Figure 4.5 displays temperature ramps for single samples, not separate sample repeats.

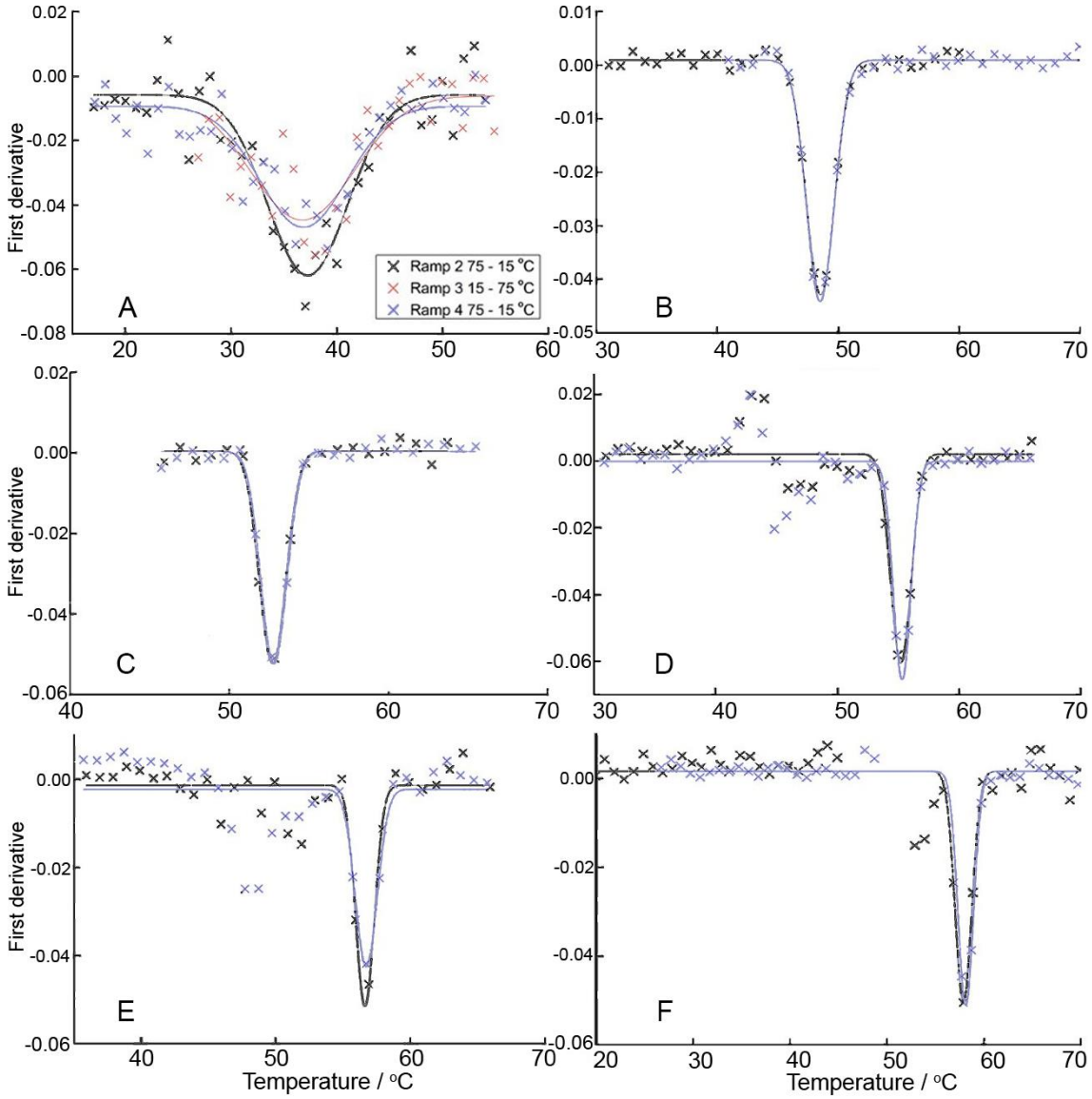

Figure 4.5 – First derivative plots of thermal-melt data of hybridised DNA loaded vesicles, temperature cycled at 0.5 °C min^{-1} with absorbance taken every 10 seconds. To the data a Gaussian peak fitting was applied in Origin Pro 9.1. A and B are loadings of 10 and 50 lipid-DNA/vesicle respectively; C and D are loadings of 100 and 150 lipid-DNA/vesicle respectively, and finally; E and F are loadings of 200 and 250 lipid-DNA/vesicle respectively.

Using the first derivative plots in Figure 4.5, the DNA T_m could be obtained from the peak maxima, for POPC vesicles doped with increasing concentrations of pH non-responsive DNA. These T_m data were accumulated and plotted in Figure 4.6.

DNA strands / vesicle	Average T_m / ^oC	error / ^oC
10	36.95	0.27
50	48.52	0.03
100	52.94	0.07
150	55.25	0.08
200	56.67	0.06
250	58.01	0.17

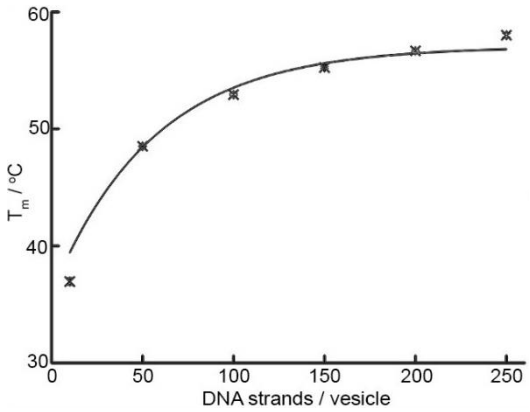

Figure 4.6 – Left: table to show average T_m of DNA calculated from first derivative plots presented in Figure 4.5. Right: graph to show how rising lipid-DNA loading per vesicle increases T_m of vesicle aggregates, line to guide the eye.

The rise in T_m with increased DNA concentration is driven through a higher number of DNA strands favouring duplex formation. The preference towards duplex formation is a consequence of constructive base stacking interactions [144]. Base stacking interactions are an amalgamation of attractive Van der Waals dispersive forces, dipole induced dipole and induced-dipole-induced dipole interactions across the flat π BP system. As the DNA concentration increases there is a considerable energetic gain leading to a higher T_m.

The data within Figure 4.6 clearly demonstrate that a DNA loading of 10 DNA/vesicle dehybridises at ~37 ^{o}C (body temperature). As a consequence of being at 37 ^{o}C, there would be a high population of single vesicles and subsequently low population of aggregated vesicles. This in turn would limit a 10 DNA/vesicle concentration in reaching this project's specific aims. Positively, 50-250 DNA/vesicle loadings present T_m considerably higher than body temperature. The high narrow melting temperature transitions for 50-250 DNA/vesicle loadings, have no overlap around 37 ^{o}C. This ensures that only a very small population of tethered vesicles would dehybridise in and above (~5 ^{o}C) normal body temperatures.

4.2.1.2 pH 5

To gain a greater picture of vesicle cluster stability, the 13 BP sequences were thermally examined at pH 5, a physiologically relevant pH in late endosome/lysosome encapsulation [145]. Moving forward additional samples using DNA at concentration of 25 and 75/vesicle were measured as

previous data displayed large increases in T_m, specifically within the range of 10 to 50 and 50 to 100 DNA/vesicle loadings, ~10 ^oC and ~5 ^oC respectively at pH 7.4.

DNA strands / vesicle	Average T_m / ^oC	error / ^oC
10	33.72	0.33
25	40.80	0.19
50	47.46	0.08
75	48.67	0.02
100	51.30	0.09
150	54.11	0.07
200	55.42	0.04
250	55.67	0.01

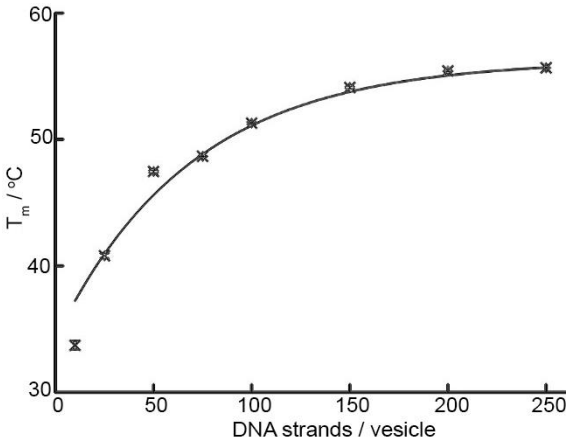

Figure 4.7 - Left: table to show average T_m of DNA calculated from first derivative plots for samples held at pH 5. Right: graph to show how rising lipid-DNA loading per vesicle increases T_m of DNA in the sample, line to guide the eye.

Data in Figure 4.7 display a rise in DNA instability gained by being at pH 5. The T_m of vesicle aggregates with loadings of 25 lipid-DNA/vesicle were still stable significantly above body temperature. However, reducing the pH from 7.4 to 5 resulted in a small drop in T_m across all loadings in the order of ~2 ^oC, suggesting that a lower pH does somewhat destabilise DNA binding between vesicles. To examine whether the difference in T_m at pH 7.4 and 5 is systematic with concentration, a plot of the difference between T_m of pH 7.4 and 5 was produced.

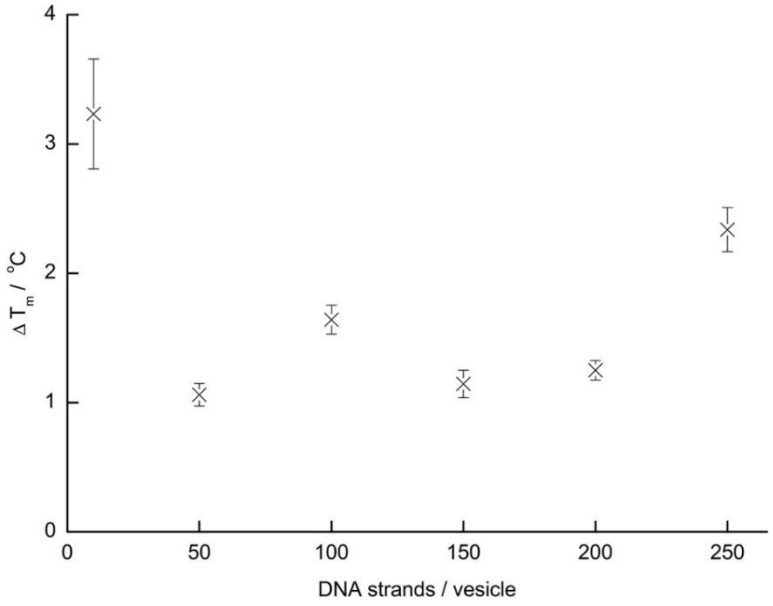

Figure 4.8 – The plotted difference between T_m for DNA loadings at pH 7.4 and 5 .

Figure 4.8 displays there is no systematic T_m change in regards to DNA concentration between pH 7.4 and 5, across all DNA loadings examined. While there is an overall reduction in stability at pH 5, it is insufficient for significant DNA to dehybridise in late endosome/lysosome encapsulation.

4.2.1.3 Thermodynamic data extrapolation

With the calculation of average T_m for DNA mediated hybridised vesicle samples, it was possible to construct a van't Hoff plot. Through this plot entropy and enthalpy changes of the lipid-DNA melting could be calculated to further characterise the system.

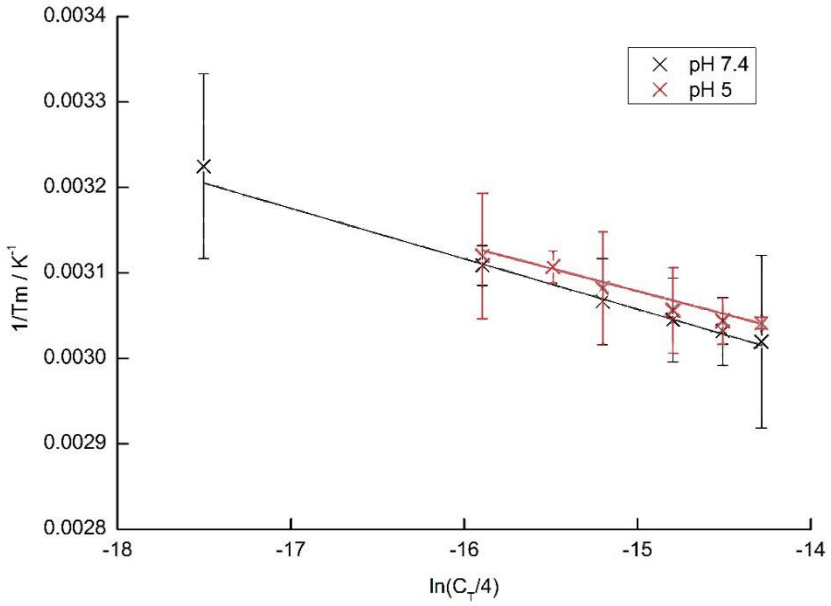

Figure 4.9 - van't Hoff plot of data presented in Figure 4.6 and Figure 4.7 for lipid-DNA loaded into POPC vesicles.

At pH 5, 10 and 25 DNA/vesicle loadings gave nonlinear results (data not shown in Figure 4.9) as required for van't Hoff thermodynamic modelling. The disparity from the trend is likely due to sample preparation errors, when pipetting small volumes of DNA-lipid, and lack of repeats. It is worth noting that previous analogous experiments by other groups did not run repeats, therefore do not show error bars [96]. This is likely due to a limited lipid-DNA supply.

In conjunction with the van't Hoff derived thermodynamic model presented in Equation 1.8, the gradient and intercept in Figure 4.9 are equal to $R/\Delta H$ and $\Delta S/\Delta H$ respectively. ΔH and ΔS were extracted from Figure 4.9 and are shown in Table 4.1.

pH	ΔH / kJ mol^{-1}	error / kJmol^{-1}	ΔS / J mol^{-1}	error / Jmol^{-1}
7.4	-129.37	1.26	-280.73	0.91
5	-120.62	1.91	-275.02	2.09

Table 4.1 – Thermodynamic data derived from the van't Hoff plot presented in Figure4.9 for the hybridisation of pH non-responsive lipid-DNA tethered POPC vesicles.

The thermodynamic energies shown in Table 4.1 display that pH does play a role in DNA binding strength, presenting that a reduction in pH decreases binding energy by ~8 $kJmol^{-1}$. Furthermore, the reduction in entropy mirrors the pH destabilisation argument through there being a smaller change in order of the system. These results are comparable with 10 BP cholesterol-DNA counterparts previously studied [96].

4.2.1.4 Vesicle stability vs salt concentration

Salt/sodium concentration is closely linked with DNA stability and the melting temperature of DNA. A reduction in salt has well documented negative effects on hybridisation, limiting the screening counter ions of the charged phosphate backbone of DNA. Without screening, there is a net negative repulsion between DNA strands and a drop in successful hybridisation. With this sensitivity to salt concentration the lipid-DNA linked clusters were again examined through UV thermal analysis.

To examine the effect of salt concentration on DNA vesicle tethering, two DNA loadings were chosen; 250 and 75 copies of 13 BP sequence DNA/vesicle respectively. These concentrations were chosen as they both showed reliable hybridisation irrespective of the tested pH. The salt concentrations examined were factors of the 120 mM salt concentration i.e 0, 0.5x, 1x, 2x, 5x and 10x. Furthermore, to accurately account for the salt concentration after the HEPES buffer was made to pH 7.4, the osmolality of each solution was measured.

NaCl Conc / mM	pH 7.4 75 DNA / Vesicle		pH 5 75 DNA / Vesicle		pH 7.4 250 DNA / Vesicle		pH 5 250 DNA / Vesicle	
	T_m / ^oC	error / ^oC	T_m / ^oC	error / ^oC	T_m / ^oC	error / ^oC	T_m / ^oC	error / ^oC
7.00	30.49	0.25	No hybridisation detected		39.58	2.21	No hybridisation detected	
67.67	51.27	0.11	37.68	0.36	55.08	0.16	49.14	0.24
126.50	-	-	48.67	0.02	58.09	0.18	55.67	0.01
252.50	56.62	0.08	55.84	0.10	62.70	0.69	61.91	0.28
693.33	58.40	1.09	56.69	0.12	64.57	0.19	65.66	0.61
1196.67	57.51	0.26	55.49	0.28	64.85	0.55	63.74	0.56

Table 4.2 – Calculated T_m of pH non-responsive DNA linked POPC vesicles with loading of 75 and 250 DNA/vesicle at pH 7.4 and 5.

From the DNA T_m data set presented within Table 4.2 a plot of the data was constructed, shown within Figure 4.10. To the data a decay exponential (y = A1*exp(-x/t1) + y0) was fitted in Origin Pro 9.1.

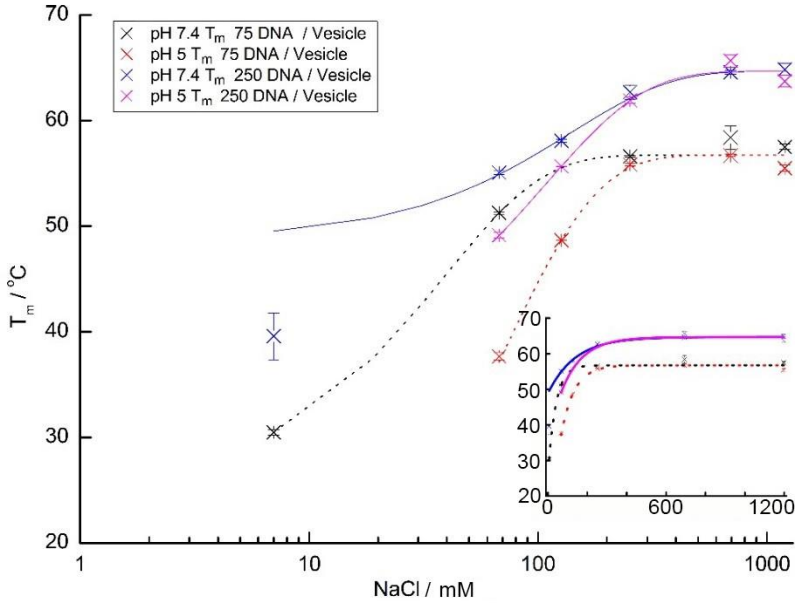

Figure 4.10 – log salt concentration against T_m for pH non-responsive DNA linked POPC vesicles with loading of 75 and 250 DNA strands/vesicle at pH 7.4 and 5. Insert displays the same data on a log temperature scale.

As expected sodium concentration was shown to play a vital role in modifying the T_m of hybridised vesicles. 250 mM sodium concentration further promoted negative screening and subsequently hybridisation, raising the T_m ~5 ^oC across all samples. Further increasing salt beyond a ~250 mM sodium concentration had no effect in raising the T_m, displaying that maximum screening for the 13 BP sequence is achieved after the addition of ~250 mM sodium. Furthermore, DNA sequences were shown to have a lower DNA T_m as sodium level decreased. The decrease in DNA melting temperature associated with lower salt also shows to be more significant for samples at pH 5 than pH 7.4, where low sodium (7 mM) and pH (5) prevented DNA hybridisation.

In summary, the 13 BP sequence has been shown to be effective in maintaining POPC cluster formations in relatively extreme pH, salt and temperature environments. However, in order to further develop the cluster forming drug delivery platform, the in house designed i-motif DNA sequences were substituted for the pH non-responsive sequence.

4.2.2 pH responsive lipid-DNA vesicle incorporation

4.2.2.1 pH 7.4 and 5

The same methodology used for the pH non-responsive sequences was carried out to analyse the i-motif counterparts. Initially, the DNA T_m of i-motif lipid-DNA doped POPC vesicles in HEPES buffer, at pH 7.4 and 5 at 125 mM sodium, was measured.

DNA strands / vesicle	pH 7.4		pH 5	
	T_m / ^oC	error / ^oC	T_m / ^oC	error / ^oC
10	No hybridisation detected		No hybridisation detected	
25				
50	40.38	0.13	40.32	0.42
75	40.69	0.04	41.00	0.27
100	42.48	0.05	41.32	0.22
150	45.25	0.03	42.74	0.07
200	47.37	0.02	49.43	0.08
250	48.11	0.02	49.95	0.07

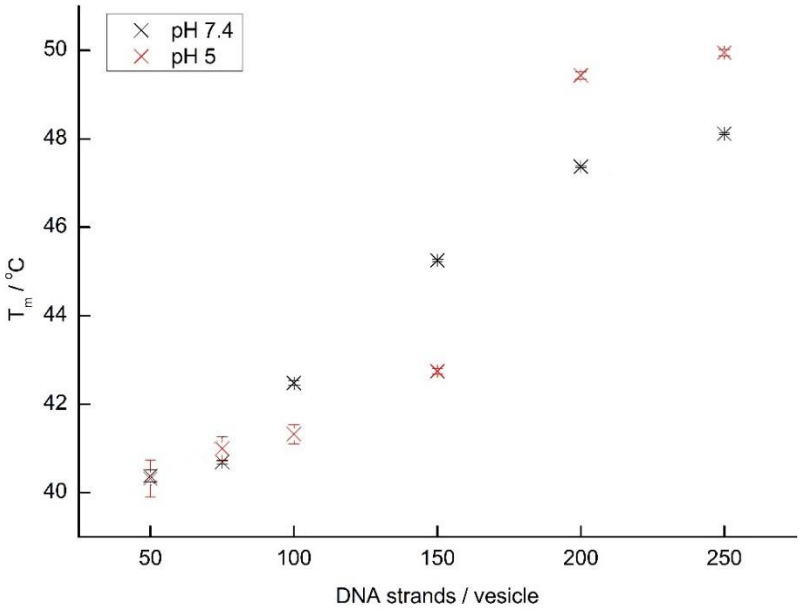

Figure 4.11 - Top: table to show average T_m of pH responsive DNA calculated from first derivative plots for samples held at pH 7.4 and 5. Bottom: graph to show how rising lipid-DNA loading per vesicle increases T_m of DNA in the sample.

The thermal-melt data presented here in Figure 4.11 displays a significant drop in T_m for the i-motif sequence, in comparison with the previously studied pH non-responsive sequence. This decrease is consistent across loadings and pH by ~10 ^oC. Unexpectedly, results show a discontinuous transition in T_m for 200 and 250 DNA/vesicle loadings at pH 5. While this is a small transition (~2 ^oC), future van't Hoff analysis will not use these data points. The rest of the DNA T_m data were converted and plotted in a van't Hoff plot.

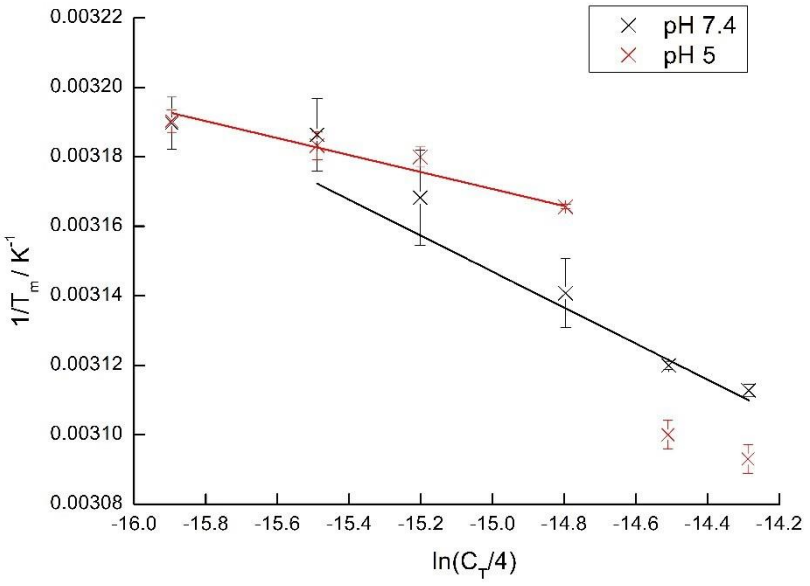

Figure 4.12 - van't Hoff plot of i-motif thermal-melt data presented in Figure 4.11 for lipid-DNA loaded into homogenous POPC vesicles.

Figure 4.12 shows T_m data for pH 5 to be unreliable, therefore it was not sensible to apply van't Hoff analysis to calculate thermodynamic values for this data. However, van't Hoff analysis was employed to extract thermodynamic values for pH 7.4.

pH	ΔH / kJ mol^{-1}	error / kJmol^{-1}	ΔS / J mol^{-1}	error / Jmol^{-1}
7.4	-134.02	26.16	-298.11	81.77

Table 4.3 - Thermodynamic data derived from the van't Hoff plot presented in Figure 4.12 for pH responsive lipid-DNA tethered POPC vesicles at pH 7.4.

Between the pH non-responsive and i-motif sequences, the longer i-motif at pH 7.4 has shown to have a higher change in enthalpy and entropy than the shorter, pH non-responsive sequence measured at pH 7.4. The larger enthalpy and entropy changes are due the larger number of BPs present per sequence on the i-motif.

4.2.2.2 Vesicle stability vs salt concentration

The DNA melting temperatures for the i-motif sequences have so far indicated that these sequences are able to maintain hybridisation between vesicles at pH 5, despite not being able to sensibly apply van't Hoff analysis. At pH 5 the DNA i-motif sequences were expected to display a significant reduction in DNA T_m. To encourage DNA dehybridisation, lipid-DNA doped POPC vesicles were made in the presence of low salt concentration buffer. Through reducing the DNA's sodium exposure, it was expected that electrostatic repulsion between phosphate backbones would disfavour duplex formation. To measure a change in DNA T_m in varying salt concentrations, the previous procedure used in Figure 4.10 was repeated for vesicles doped with 75 and 250 DNA/vesicle loadings.

NaCl conc / mM	pH 7.4 75 DNA / vesicle		pH 5 75 DNA / vesicle		pH 7.4 250 DNA / vesicle		pH 5 250 DNA / vesicle	
	T_m / °C	error / °C	T_m / °C	error / °C	T_m / °C	error / °C	T_m / °C	error / °C
7.00	28.97	0.17	No hybridisation detected		36.97	0.38	No hybridisation detected	
67.67	36.33	0.28			47.59	0.58		
126.50	39.86	0.36	40.99	0.40	48.14	0.31	50.18	0.44
252.50	47.67	0.31	49.35	0.58	54.43	0.53	51.43	0.73
693.33	50.70	0.57	51.98	0.32	58.18	0.36	56.05	1.32
1196.67	52.57	0.39	53.96	0.12	61.21	0.30	57.52	1.46

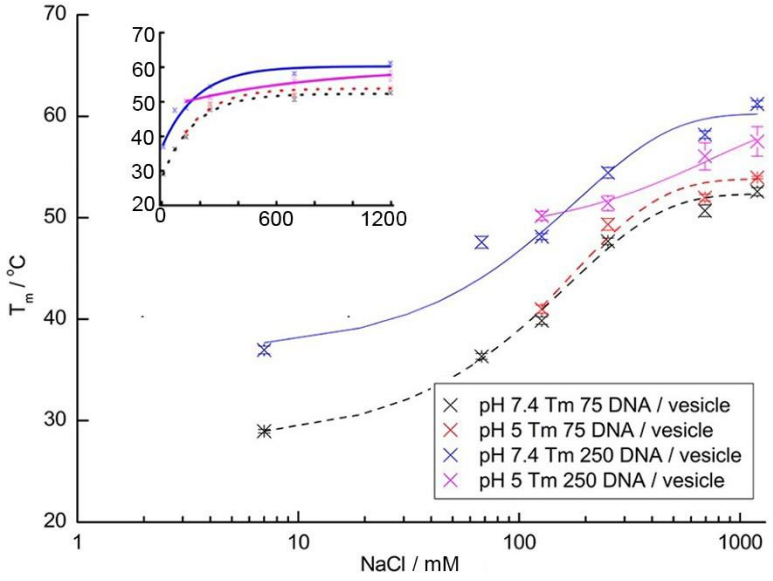

Figure 4.13 – Top: table to show calculated T_m of pH responsive DNA linked POPC vesicles with loadings of 75 and 250 DNA/vesicle at pH 7.4 and 5. Bottom: plot of measured log of salt concentration against T_m for DNA i-motif linked POPC vesicles, with loadings of 75 and 250 DNA/vesicle at pH 7.4 and 5, with a decay exponential applied. Insert displays the same data on log temperature scale.

Unexpectedly, Figure 4.13 displays 75 DNA/vesicle loading as having a higher thermal stability at pH 5 than pH 7.4, for salt concentrations greater than 126.5 mM. Conversely the opposite is true for 250 DNA/vesicle loading above 252.5 mM salt. However, while results are outside of the standard deviation, the first derivative data in Figure 4.14 displays that there is higher error in plotting a curve for samples at pH 5 than pH 7.4, through the increased data scatter.

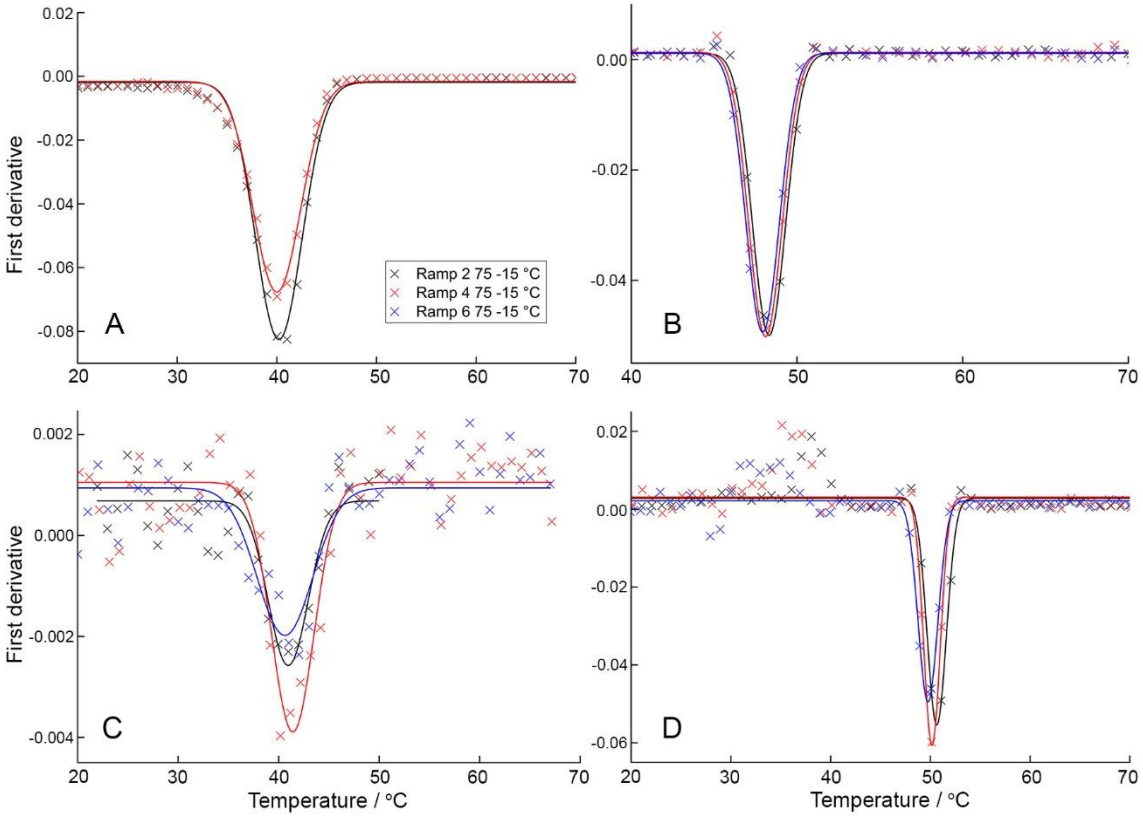

Figure 4.14 – First derivative plots of thermal-melt data of hybridised i-motif lipid-DNA loaded vesicles, the temperature was cycled at a ramp rate of 0.5 °C min $^{-1}$ with absorbance taken every 10 seconds. To the data a Gaussian peak fitting was applied in Origin Pro 9.1. A and B are loadings of 75 and 250 lipid-DNA/vesicle respectively at 126.5 mM salt and pH 7.4; C and D are loadings of 75 and 250 lipid-DNA/vesicle respectively at 126.5 mM salt and pH 5.

Nevertheless, across all salt concentrations in Figure 4.13 the i-motif sequence T_m is below that reported for the pH non-responsive sequence. Furthermore, samples at pH 5 at low salt concentrations (<126.50 mM) have been shown to have no measurable hybridisation, displaying the i-motif's sensitivity in forming a duplex in low pH and salt environment. Through this sensitivity and further DNA development, it could be possible that a triggered vesicle cluster release could be exhibited through reduced salt and i-motif lipid-DNA integration. However, this project will focus on using pH as a trigger for vesicle release.

4.3 A pH switchable device

i-motif DNA sequences form reversible inter and intra hybridised structures; using this technology it was hoped that a pH switchable vesicle cluster device could be produced. In this instance in the presence of a low pH, a dimer drug carrier would separate into its constituent single liposomes. Through increasing the pH back to its original higher pH, vesicles would reform into a dimer.

To measure this responsivity, POPC vesicles were once again separated into two aliquots and loaded with opposing complementary DNA sequences in equimolar concentrations using the previously outlined lipid-DNA series of 10 to 250 DNA/vesicle. Opposing aliquots of DNA doped vesicles were then recombined ensuring the DNA loadings were of the same concentration. This procedure was used for both the i-motif and non-responsive DNA. Initially samples were prepared and measured at pH 7.4 where UV data were captured across the usual temperature ramps. The pH was then dropped to pH 3 using 1.2 M $HCl_{(aq)}$. Once the pH was lowered UV thermal analysis was continued as previously detailed.

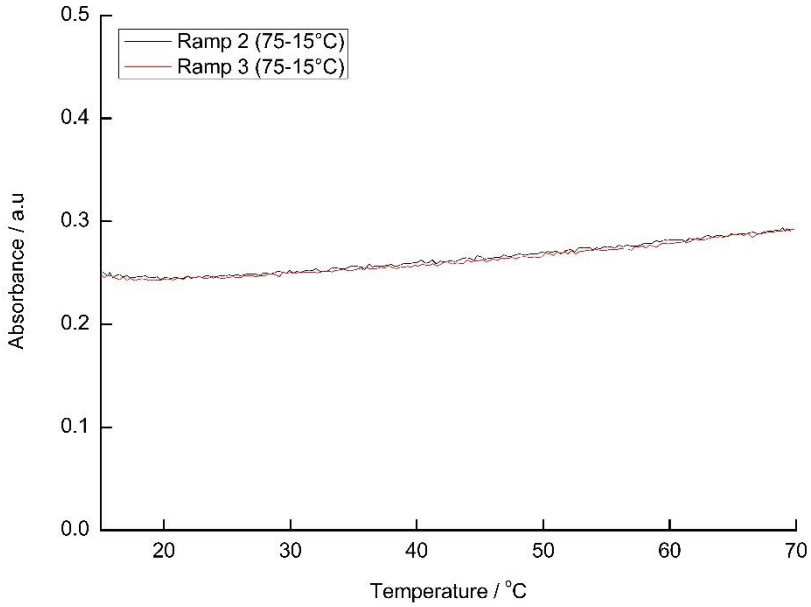

Figure 4.15 – A typical UV spectroscopy graph displaying no thermal-melt activity at pH 3. This behaviour is seen across all loadings irrespective of DNA sequence type at pH 3.

The UV data shown in Figure 4.15, displays that at pH 3 there are no features indicative of integrated lipid-DNA melting. Irrespective of loading or DNA sequence the sigmoidal melting curve was not

observed, demonstrating a lack of hybridisation between DNA and tethering between vesicles. The rising trend with temperature is likely due to thermal expansion of vesicles scattering more light. Upon collecting data at pH 3 aliquots of 1.2 M $NaOH_{(aq)}$ were added to the samples to raise the pH back to 7.4 and thermal melt scans were resumed.

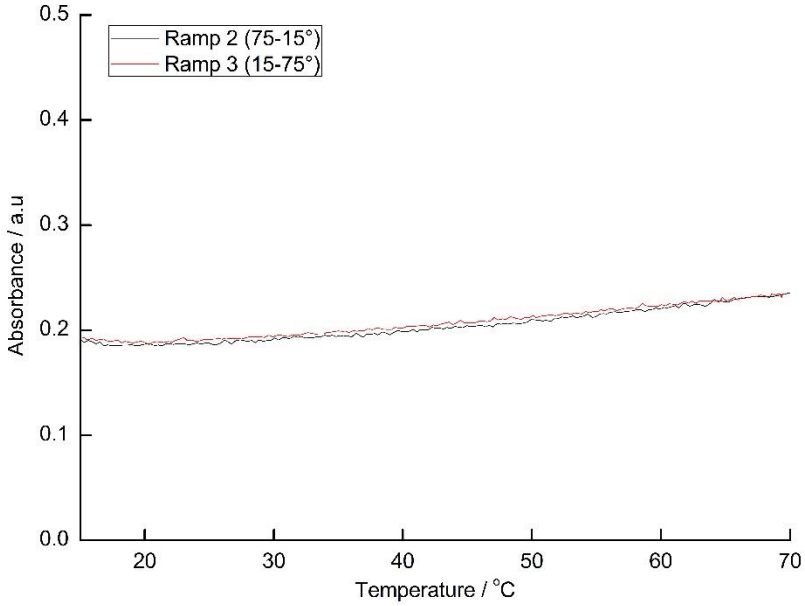

Figure 4.16 – A Typical UV spectroscopy graph displaying no thermal-melt activity at pH 7.4. This behaviour is seen across all loadings irrespective of DNA sequence type, after pH was risen back to pH 7.4.

Once the pH was raised back to 7.4, both sequences in all concentrations showed no signs of hybridisation; an example of this behaviour can be seen in Figure 4.16. The lack of hybridisation points to DNA being irreversibly damaged by the pH drop, preventing tethering. The likely route for this damage was thought to be through depurination. Whereby the glycosidic linkage to the G and A BPs is broken, liberating the BP from the DNA structure and leaving behind an apurinic site, as shown within Figure 4.17 [146].

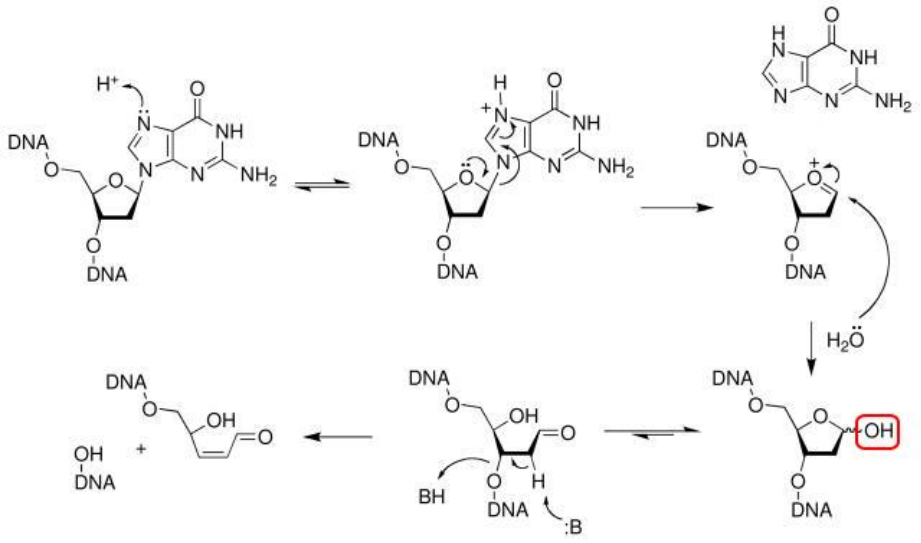

Figure 4.17 – The acid catalysed SN1 reaction mechanism for the depurination of guanine from DNA leaving behind an apurinic site (red box) [146], [147]. B represents the addition of base.

The depurination reaction mechanism in Figure 4.17 is shown to continue to progress to opening the sugar ring, which if base is further added leads to DNA sugar phosphate breakage. Specifically, after the formation of the apurinic site there exists an equilibrium mixture of the ring-closed acetal (99%) and the ring-opened aldehyde, which leads to DNA backbone breakage with the addition of base [147]. This may have happened in experiments presented here where the pH was initially dropped to pH 3 through the addition of hydrochloric acid.

Pyrimidine based cytosine and thymine groups undergo a slight variation of the depurination reaction mechanism. Instead T and C BPs undergo depyrimidination, a less common form of base loss. The preference towards A and G removal is rationalised through them having an easier removal route than T, and C [147].

4.3.1 HPLC of acid catalysed DNA break up

The hypothesis put forward, for a lack of pH switch ability, describes the DNA sequences succumbing to a thermally influenced acid catalysed degradation. High Performance Liquid Chromatography (HPLC) coupled with UV detection was therefore implemented to measure the potential retention time shifts due to DNA break down.

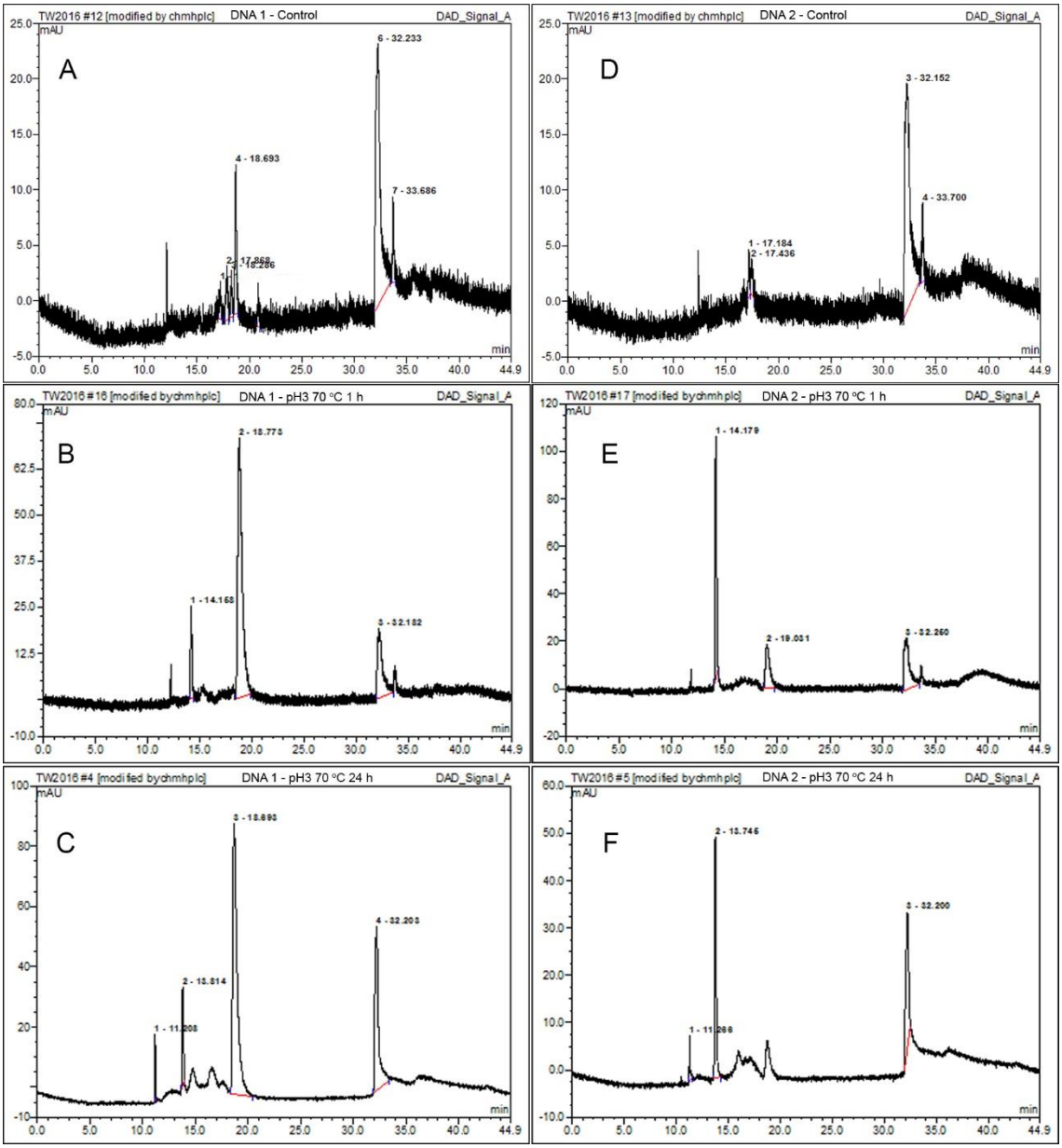

Figure 4.18 – HPLC data of pH non-responsive lipid-DNA . A: Control DNA sequence 1 (TTT ACA GAC TAC C). B: DNA sequence 1 at 70 °C for one hour at pH 3. C: DNA sequence 1 at 70 °C for 24 hours at pH 3. D: Control DNA sequence 2 (TTT GGT AGT CTG T). E: DNA sequence 2 at 70 °C for one hour at pH 3. F: DNA sequence 2 at 70 °C for 24 hours at pH 3. (HPLC conditions in section 2.3.8 page 54)

Initially Figure 4.18 outlines that extreme environmental conditions led to DNA instability. Across both pH non-responsive sequences UV absorption is low for all eluted compounds in the control samples.

The data displays lipid-DNA likely being resolved at ~32 minutes, with DNA that is not attached to the lipid tail being present at 19 minutes.

When the pH was dropped to pH 3 and the sample was left in a water bath at 70 ^{o}C for an hour, two distinct peaks were recorded at ~14.2 and ~18.8 minutes. As previously discussed, depurination is the loss of purine BPs from DNA and occurs at a faster rate than depyrimidination [147]. Therefore, it has been interpreted that the new peaks would be produced through the liberation of more hydrophilic G and A BPs from DNA and not T and C. Due to the two non-responsive sequences being fully complementary, chromatograms could be used to calibrate relative BP concentrations and identify the peaks to specific BPs. For example, sequence 1 is rich in adenine with 4 BPs per sequence, where sequence 2 is deficient in adenine with 1 per sequence. Therefore, in sequence 1 it is most likely that adenine is the largest peak after an hour at 70 ^{o}C at pH 3, with a retention time of 18.8 minutes. The peak resolved at 18.8 minutes in sequence 2 should therefore be a quarter in area of that reported for sequence 1, due to there being 75% less adenine in sequence 2. The data shown in Figure 4.18 reflects this hypothesis with the peak in sequence 1 having a peak area of 34.615 mAU*min and sequence 2 having a peak area of 8.469 mAU*min. A similar approach was used in an effort to verify that the peak with a retention time of 14.2 minutes was guanine. Where a recorded peak area ratio of 1:4 (3.956 and 15.817 mAU*min) reflected the DNA guanine base pair ratio of 1:4, for sequence 1 and sequence 2 respectively. Even if the hypothesis of depurination being more likely than depyrimidination is rejected, the peak areas in regards to T make little sense. T has a 1:~2 ratio with respect to sequence 1 and 2, and no peak area ratio fits that pattern. Additionally, the results displayed here were comparable to published HPLC elusion times for free BPs under similar solvent condition [148].

Continued 24 hour heating could possibly lead to further BP liberation, including T and C, but in these extreme conditions it is likely that BP breakdown is occurring alongside DNA backbone breakage, as seen in the reaction mechanism present within Figure 4.17. It is thought that these continued reactions go some way to explaining the rise in the number of peaks recorded through extended overnight heating.

A similar HPLC approach was used for examining the pH responsive i-motif sequences.

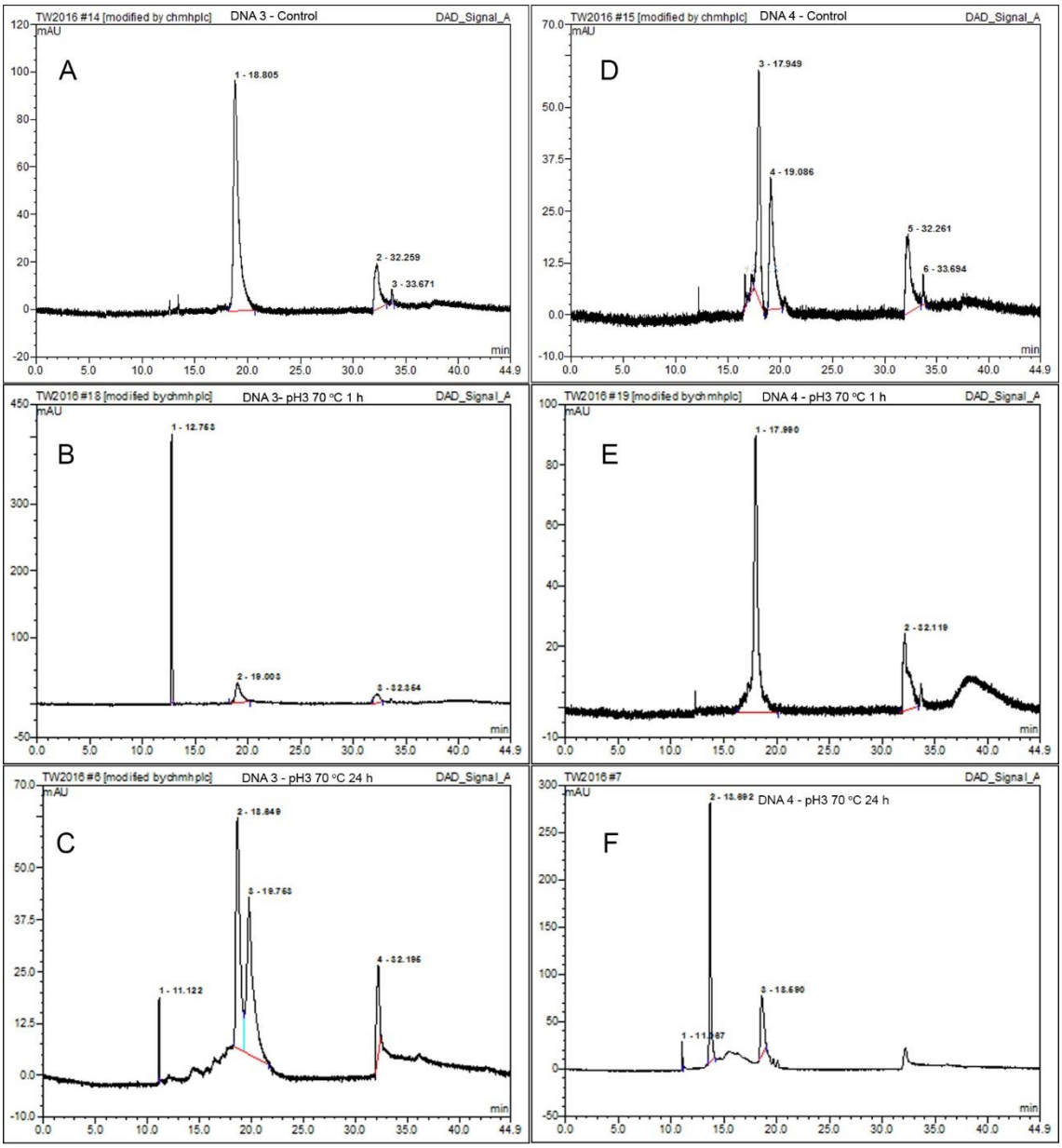

Figure 4.19 - HPLC data of pH responsive i-motif lipid-DNA. A: Control DNA sequence 3 (TTT TTT TTT CCC TAA CCC TAA CCC TAA CCC). B: DNA sequence 3 at 70 °C for one hour at pH 3. C: DNA sequence 3 at 70 °C for 24 hours at pH 3. D: Control DNA sequence 4 (TTT TTT GGG TTA TGG TTA GGA TTA GTG). E: DNA sequence 4 at 70 °C for one hour at pH 3. F: DNA sequence 4 at 70 °C for 24 hours at pH 3. (HPLC conditions in section 2.3.8 page 54)

Once again HPLC data displays evidence of DNA BP liberation as previously shown for the short fully complementary sequences after 24 hours of heating, indicated by peaks being present at ~18.8 minutes and ~14 minutes for BPs A and G respectively.

The data within Figure 4.19 display the controls having a larger peak separations than previously seen for the shorter DNA sequences. It has been rationalised that the lipid-DNA elutes at ~33 minutes and the larger peaks with shorter retention times are DNA sequences missing the hydrophobic lipid tail (free DNA). The rise in free DNA absorbance for sequences 3 and 4 in comparison with sequences 1 and 2 is thought to be due to DNA BP attachment efficiencies. When building DNA there is a coupling efficiency of 98.5% per BP, meaning for each BP attachment cycle 1.5% of the all the DNA strands are missing that particular cycle's BP. In the result of a BP not been added to a sequence, a capping step in the synthesis prevents the continuation further BP addition. Predictably, longer sequences have more BP addition cycles, resulting in consecutive losses of 1.5% DNA per BP. Through the i-motifs being ~15 BPs longer than the non-responsive sequences, there will be a conservative 20% drop in successfully lipid-DNA production [149]. However, sequence 4's control has two peaks in the DNA resolution area (~18 minutes and ~19 minutes), each thought to be denoting a DNA substructure. Sequence 4 has been previously discussed to have the ability to form guanine quadruplex [150]. A quadruplex is similar to the i-motif where intra-hybridisation occurs along a strand of DNA, but in place of C^{+}-C hydrogen bonding, G rich sequences can hybridise without the need for hemi-protonation [151].

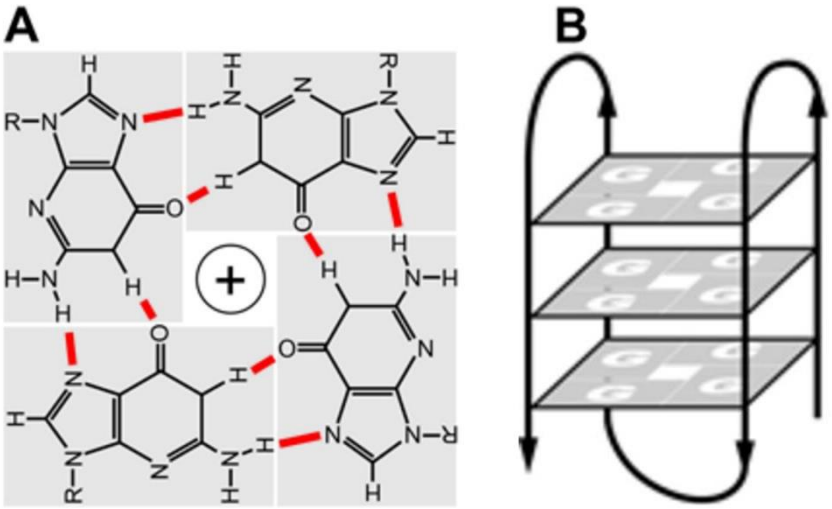

Figure 4.20 – A model of intra-hydrogen bonding of a guanine rich DNA forming a G quadruplex substructure of DNA [151]. A – cartoon displaying guanine base pair arrangement around a positively charged ion. B - cartoon displaying stacked hydrogen bonded guanine base pair layers.

Figure 4.20 displays that in a quadruplex the DNA contorts to form four hydrogen bonds between G BPs, rather than the usual three which is often aided by a metal centre such as potassium or sodium [151]. Intra-hybridised DNA would likely be separated from free DNA and in HPLC experiments, potentially giving rise to the two starting peaks in the HPLC sequence 4 control. However, literature displays that quadruplex formation and disassembly is complex with three intermediate structures [152], where the final quadraplex can either form a monomolecular, bimolecular or tetramolecular substructure [153]. Furthermore, literature demonstrates that these final quadraplex substructures have been separated via HPLC [153]. This highlights that more work needs to be done here to fully determine the peaks in HPLC data for the sequence 4 control and pH 3 70 ^{o}C heating study. Nevertheless, the change indicated by the 70 ^{o}C 24 hour pH 3 study in Figure 4.19 demonstrates there is some structural changes in the DNA that are likely contributing the lack of rehybridization when the pH is raised back to pH 7.4 (shown in Figure 4.16).

Figure 4.19 also shows a definitive peak shift from 19 minutes to 12.8 minutes for sequence 3 after being held at 70 ^{o}C for an hour at pH 3. This shift is likely due to minimal depurination when heated and the formation of the i-motif, which is promoted in the presence of a low pH environment and lower temperature during analysis. This change in DNA structure from unhybridised to intra-hybridised would likely result different elution times. In other words, when the DNA was held at 70 ^{o}C for an hour, any intra-strand hybridisation would likely melt as 70 ^{o}C is well above any pervious recorded T_m using sequence 3. At these high temperatures, the unhybridised DNA would expose BPs to potential depurination. However, over this short period of time, relative to the 24 hour heating, depurination would be minimal, enabling the prospect of the i-motif to form when the sample was cooled. Furthermore because of suspected i-motif formation, the reduced peak at 19 minutes could be attributed to residual non i-motif folded DNA. With regard to sequence 4 the addition of acid could remove intra-strand hybridisation through nitrogen/free-proton hydrogen bonding, resulting in the large now single peak seen after 18 minutes. It is important to note that no peaks at ~18.8 and ~14 minutes have been recorded after 1 hour of heating, indicative of no A and G BPs being removed via depurination.

However, HPLC analysis of samples heated for 24 hours display that sequences 3 and 4 may become susceptible to acid catalysed BP removal. Chromatograms for both sequences reveal a distinctive peak at ~18.7 minutes suggesting adenine removal. Interestingly, no peaks at ~14 minutes for sequence 3 are present, this coincides with the fact no G BPs are in DNA sequence 3. This data therefore adds significant weight behind the hypothesis that the peaks seen at ~14 minutes for other sequences after being heated 70 ^{o}C are guanine. Nevertheless, the reoccurrence of peaks at 14 and ~18.7 minutes seem to be linked with the data previously recoded from POPC lipid-DNA thermal-melt analysis.

In summary HPLC has been an effective tool in describing why pH switching was not observed through UV thermal-melt analysis. To monitor a potential pH switch a technique where temperature could be kept at a lower 25 ^{o}C would be beneficial.

4.4 Summary

The data gathered in this chapter describe how UV temperature ramping cycles can be used to measure vesicle bound lipid-DNA melting temperatures. Initially three experiments were run for two sets of complementary DNA sequences, a fully complementary short sequence and a pH responsive i-motif:

1. Measurement of T_m for lipid-DNA bound POPC vesicles, at physiological salt and pH, across 10-250 DNA strand loadings/vesicle.
2. Measurement of T_m to gauge stability in lower pH conditions
3. Measurement of T_m to examine the effect of sodium on vesicle binding

Through these experiments, it was found that DNA concentration plays a large role in the thermal properties of vesicle bridging, allowing van't Hoff plots to interpret thermodynamic properties of the system for both sets of sequences. Furthermore, it was found that the sequence dictates the T_m of hybridised vesicles, where the i-motif forming DNA had a lower T_m independent of loading. A reduction in pH from 7.4 to 5 gave a lower T_m across all DNA loadings. Salt concentrations below ~125 mM for the fully complementary sequences were found to lower DNA binding at pH 7.4, through reducing the screening of the negative charges on the phosphate backbone of samples. The same effect was not recoded for the i-motif sequences at pH 5 due to high error in the data.

Finally, the potential for a pH switchable tethered vesicle devise was investigated. However, it was found that using a UV temperature ramp based experimental method led to potential depurination of BPs from the DNA. If occurring the reduced number of BPs would prevent hybridisation when the pH was raised back to a physiological pH 7.4. HPLC data also so signs for confirming DNA depurination.

Moving forward, the lipid-DNA sequences examined here were coupled with the four-component phase diagram of DPPC:DOPC:cholesterol:CL. Through this integration, it was hoped that controlled size limited clusters could be formed.

Chapter 5

Measuring the size of vesicle clusters tethered together through lipid-DNA conjugates

Once controlled DOPC:DPPC:cholesterol:CL (where CL is set at 10 mol%) phase separation was achieved through the newly constructed phase diagram, and suitable DNA sequences were chosen; specific liposome compositions could be tuned to control average liposome aggregate size. Initially to investigate controlled aggregation two fundamental questions were explored.

1. Does the size of the l_o patch influence the average cluster size?
2. Does the concentration of DNA influence the average cluster size?

To address the former, the suspected "pseudo" tie line across the l_d-l_o phase coexistence region was used as a guide for sample selection. It must be emphasised that the real tie line for the four-component phase diagram would not be limited to the 10 mol% CL plane. However, it has been shown that moving across the pseudo tie line provides the ability to control membrane heterogeneity. Using this tie line, it was hoped the controllable l_o surface area would potentially lead to the control of average cluster size. With regard to the second question, the concentration of DNA was expected to change the number of hybridised vesicles in a cluster, dependent upon the position in the tie line. Three representative phase positions on the pseudo tie line were carried forward from Figure 3.19**,** where 2, 3 and 4 represent tie line positions T1, T2, T3.

5.1 Cluster formation and measurement

To examine whether DNA concentration influences Janus liposome clustering, 75 and 250 DNA strands/vesicle were chosen as representative of low and high concentrations respectively. Previous data displayed that concentrations below 75 DNA strands/vesicle provided unreliable turbidity detection for small hybridised clusters.

In order to monitor cluster size, Dynamic Light Scattering (DLS) was implemented. Through measuring the diffusion of the vesicles by Brownian motion and the use of the Stokes-Einstein equation, it is possible to determine liposome hydrodynamic diameters [154]. Smaller particles exhibit faster diffusion coefficients than larger particles therefore it is possible to determine the difference in hydrodynamic diameter and therefore cluster size. The hydrodynamic diameter is not the true

diameter of a particle's size but is an average diameter across the entirety of the sample and a particle's shape. The hydrodynamic diameter therefore assumes spherical particles. In the case of individual vesicles this does not raise an issue due to their already spherical shape. However, for tethered liposomes this does raise an issue that needs to be addressed in reference with Figure 5.1.

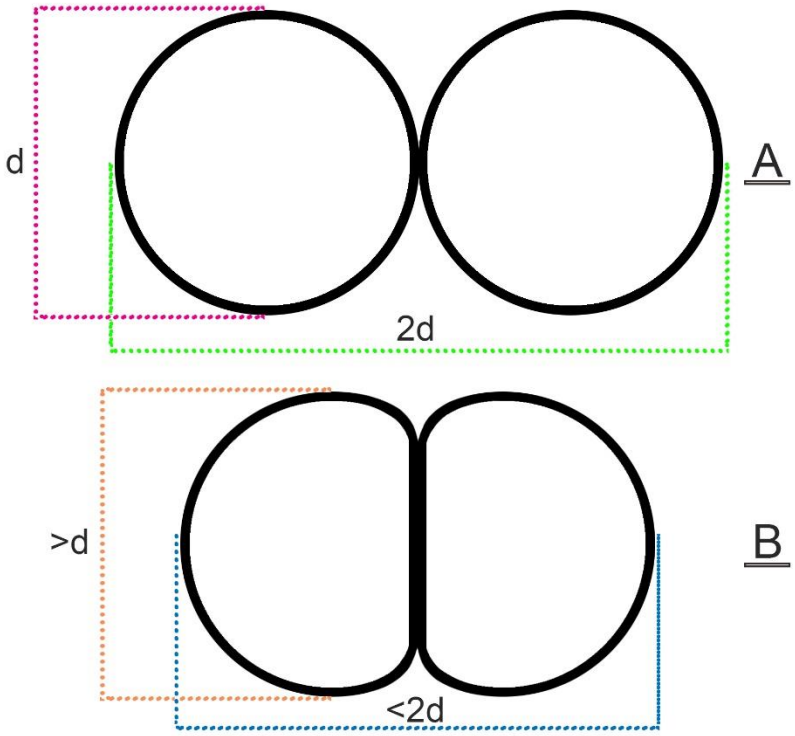

Figure 5.1 - A cartoon of vesicle cross sections to show models A and B; where A displays a false hypothesis of how DNA doped Janus vesicles hybridise together with a subsequently inaccurate hydrodynamic diameter. B displays a more accurate representation of how Janus DNA doped liposomes hybridise together with a deformed adhesion plaque and more accurate hydrodynamic diameter.

If liposomes were solid spheres they would link together as displayed in example A within Figure 5.1, where they would have a long aggregated vesicle length (2d) and a shorter vesicle width (d). Through using DLS to measure the aggregate's size, the hydrodynamic radius would be reported as the average between the aggregate's length and the aggregate's width, resulting in an inaccurate hydrodynamic diameter reading. However, previous work has shown that when liposomes are tethered using DNA they deform due to their soft membranes, forming a flat adhesion plaque [91]. In

this model (B) the cluster diameter is significantly less than 2d, resulting in a more overall spherical particle. Membrane flexibility therefore gives rise to more accurate DLS measurement of the clusters, raising the accuracy of the calculated hydrodynamic diameter of the tethered vesicles. Individual larger vesicle clusters may not form an overall spherical shape, but due to the random tethering in these clusters, throughout the sample, an average hydrodynamic diameter would be calculated which would be representative of the physical diameter.

Diameter recording via DLS enabled the volume of vesicles to be readily calculated. Using the calculated volume of a cluster and that of a single vesicle, a coarse number of vesicles within a tethered cluster could be interpreted with reference to Equation 5.1.

Equation 5.1 - $$\boldsymbol{Average\ number\ of\ tethered\ vesicles} = \frac{\boldsymbol{average\ volume\ of\ a\ cluster}}{\boldsymbol{average\ volume\ of\ a\ single\ vesicle}}$$

In Equation 5.1 large assumptions have been made when calculating the volume of the clusters. As discussed there is an error in the DLS calculated hydrodynamic diameter, where it is assumed that what is being measured is strictly spherical or a dense cluster rather than fractal aggregates. Furthermore, there is a space between vesicles taken up by the DNA bridge which through this calculation is incorporated into the vesicle volume. Additionally, it is also assumed that vesicle volumes are equivalent whether they are discrete or clustered. However, the calculated coarse number of vesicles, while carrying significant error, gave an insight to the levels of vesicle hybridisation in samples.

5.2 Phase diagram led cluster formation

5.2.1 pH non-responsive DNA mediated cluster assembly

To ensure that observed aggregation was due to tie line effects rather than unforeseen properties of a DNA sequence, the fully complementary 10 base pair (BP) pH “non-responsive” sequences were investigated to begin with.

5.2.1.1 Across tie line examination

To examine whether controlled DNA vesicle tethering was being observed, 100 nm diameter phase separated T1, T2 and T3 vesicles, loaded with 75 and 250 lipid-DNA/vesicle were examined via DLS. As disused for UV thermal melt analysis, the sample's vesicle population was separated into two, separately doped with the opposing complementary lipid-DNA conjugates and recombined to complete the sample. Additionally, a positive control experiment examining mass hybridisation when DNA is not localised via phase separation (hybridised DNA POPC) was prepared and run alongside a negative control experiment, where POPC vesicles were doped with only sequence 1 (unhybridised DNA POPC).

Composition	**75 DNA strands/vesicle**			**250 DNA strands/vesicle**		
	Average hydrodynamic diameter / nm	**PD**	**Error /nm**	**Average hydrodynamic diameter / nm**	**PD**	**Error /nm**
Hybridised DNA POPC	-	-	-	2554.56	0.53	97.00
T1	149.67	0.11	1.95	189.73	0.13	1.07
T2	166.20	0.20	5.80	181.03	0.11	0.59
T3	132.30	0.09	0.75	149.27	0.09	0.83
Unhybridised DNA POPC	119.90	0.05	1.47	123.53	0.31	1.14
	Average number of vesicles		**Error**	**Average number of vesicles**		**Error**
Hybridised POPC	-		-	9256.17		1027.28
T1	1.94		0.01	3.96		0.11
T2	2.66		0.26	3.44		0.06
T3	1.34		0.04	1.93		0.05

Table 5.1 – Average hydrodynamic diameter across the DPPC:DOPC:Cholesterol:CL (CL set at 10 mol%) l_d-l_o phase coexistence tie line with positive and negative POPC controls, with 75 and 250 non-responsive DNA loadings. Errors calculated using individual repeats. Readings were taken at 25 ^oC.

The data were then processed from Table 5.1 into line graphs, to clearly define how liposome composition changes vesicle aggregation.

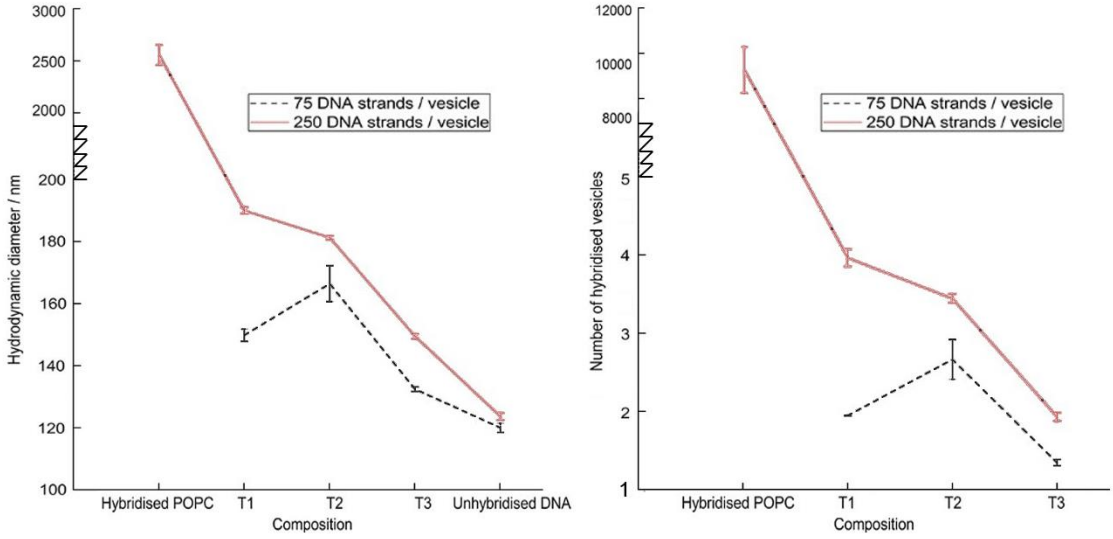

Figure 5.2 – Line graphs to show the data presented in Table 5.1. Left: average hydrodynamic diameter of clusters. Right: average number of vesicles. Readings were taken at 25 ºC.

The data presented within Figure 5.2 display that phase separation on the 250 non-responsive DNA loading has a dramatic effect on decreasing the hydrodynamic diameter of a single cluster. Specifically, phase separation has been shown to reduce cluster diameters by over an order of magnitude relative to homogenous POPC vesicle clusters. Furthermore, it can be seen that tie line position and DNA concentration influence the hydrodynamic diameter and consequently the number of tethered vesicles within a cluster. This significant drop in hybridisation enables the formation of clusters <200 nm, qualifying them to be large enough to take advantage of the EPR effect when administered in drug delivery. Furthermore, the chosen DNA concentrations per vesicle gave cluster sizes appropriate for designing small clusters of vesicles as desired; with T1 75 loading and T3 250 loading displaying particular promise in dimer formation.

At T1 there is a difference in cluster diameter between the two loadings. This can be explained through considering the partitioning of many DNA lipids into the small l_o domain. In the case of the 250 DNA loading, there may be a significant number of lipid-DNAs that begin to partition into the l_d phase as the small l_o domain becomes saturated with lipid-DNA. Furthermore, between the two phases a lipid-DNA partition coefficient will exist which describes the ratio of lipid-DNA present within each phase. While the lipid-DNA preferentially partitions into the saturated l_o domain, there will be some lipid-DNA that partitions to the l_d phase. Increasing lipid-DNA concentration will therefore

promote the number of DNA strands in the l_d phase available for l_d directed vesicle aggregation. Continuing with T1, the 75 DNA loading displays a significant decrease in hydrodynamic diameter. With over three times less DNA, the number of strands present with l_d phase is limited and the average cluster size is smaller by ~40 nm. Interestingly the T1 l_o patch size is shown to be sufficiently small enough to sterically block multiple liposomes from hybridising.

Tie line position 2 (T2) again has two rivalling effects, dependent upon lipid-DNA concentration. For the T2 250 loading there is a larger l_o domain than was present in T1, allowing more lipid-DNA to partition within it. This therefore reduces the number of lipid-DNAs in the l_d domain and subsequent tethered vesicles. Conversely there is a subtle rise in the hydrodynamic diameter for the 75 lipid-DNA loading from T1 to T2 by ~15 nm. This growth is suspected to be caused by the larger area on vesicles' surface granting enough room for more than one vesicle to bind. Additionally, the increase in saturated DPPC dilutes the lipid-DNA in the l_o domain. This reduces the number of available lipid-DNAs in close proximity for strong hybridisation, between a pair of A and B vesicles. The 250 lipid-DNA loading provides a "stickier" l_o patch than the 75 DNA/vesicle loading, resulting in superior l_o patch to patch tethering between a pair of 250 lipids-DNA doped vesicles. In other words, once two T2 250 lipid-DNA loaded vesicles collide, the close proximity of all the DNA strands enable the liposomes to "zip" tightly together. The T2 75 loading on the other hand does not have its DNA lipids in such close proximity to one another; therefore, it weakly hybridises to its counterpart, preventing the "zipping" action. Without fast and strong hybridisation between liposomes potential sites for further tethering with other liposomes are available in the l_o phase.

Finally, at T3, the hydrodynamic diameter drops significantly for both concentrations of lipid-DNA, where the 250 lipid-DNA loading can fully partition to the large l_o patch. Without random l_d phase hybridisation, a stable average AB dimer conformation is formed. With regard to the T3 75 lipid DNA/vesicle loading the DNA has become too dilute across the l_o domain, resulting in poor, unstable hybridisation between vesicles. Through this dilution, the zippering action is limited resulting in weak hybridisation between vesicles, decreasing the hydrodynamic diameter. A cartoon model of the discussed hybridisation conjecture across the tie line has been drawn in Figure 5.3.

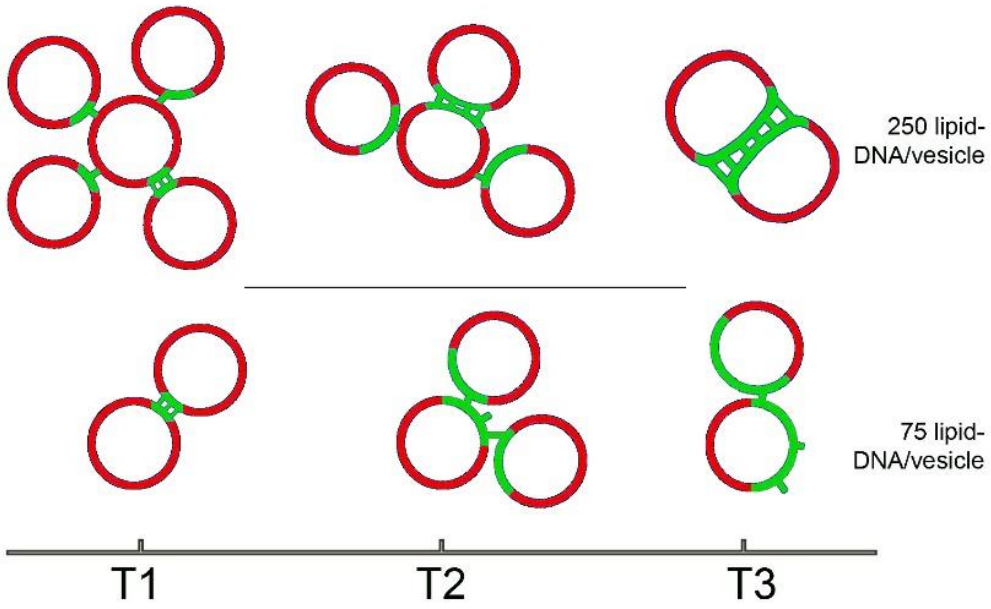

Figure 5.3 – A cartoon summary of vesicle hybridisation across the assumed DPPC:DOPC:Cholesterol:CL (CL set at 10 mol%) l_d-l_o phase coexistence tie line. Green represents the l_o phase and DNA hybridisation, red displays the l_d phase.

From the initial tie line aggregation data, samples could be selected to confirm dimer tethering through cryo-EM. To capture dimer formation a sample of T3 250 DNA/vesicle loading was chosen, frozen under liquid nitrogen and then imaged.

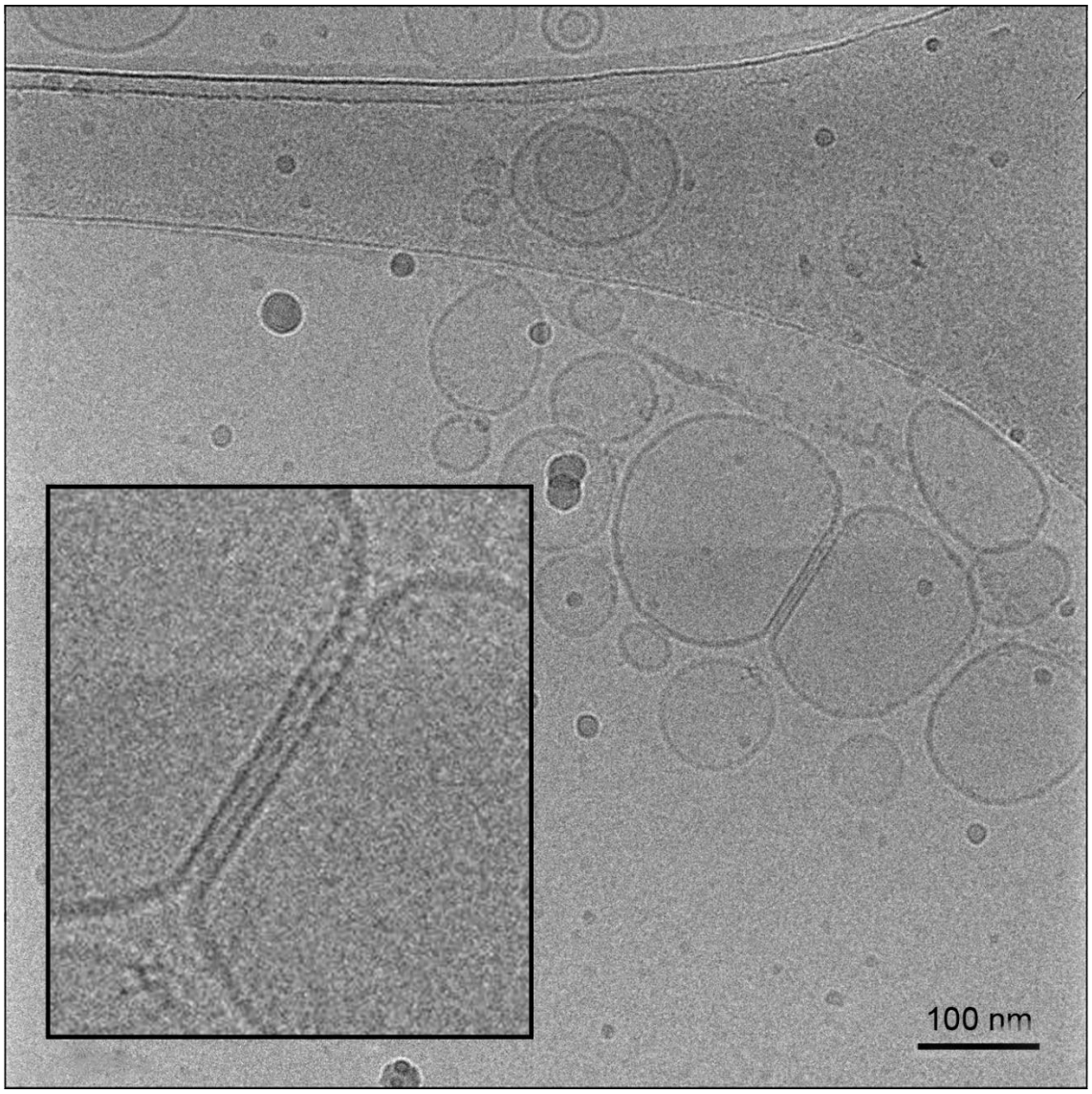

Figure 5.4 – Cryo-EM image of T3 250 pH non-responsive DNA loaded vesicles. Scale bar representing 100 nm.

The cryo image clearly displays two ~100 nm vesicles forming a dimer. The straight adhesion plaque between the vesicles (enlarged in the insert) signifies the difference between liposome adhesion and vesicles that are just in close proximity. The data gathered by cryo imaging therefore complements and supports both the DLS based technique and the hypothesis that vesicles are indeed aggregating together via DNA hybridisation.

5.2.1.2 Thermal-melt of vesicle aggregates

From the promising initial experimental data, 75 and 250 DNA/vesicle loadings were continued as the representative concentrations of DNA, to form potential size limited clusters. Due to the desired medical applications of these Janus vesicles, experiments were carried out examining whether biological temperatures affected the number of liposomes tethered within a cluster. Conditions were then later set to the extreme of 60 ^{o}C where the DNA should have melted, displaying single vesicles.

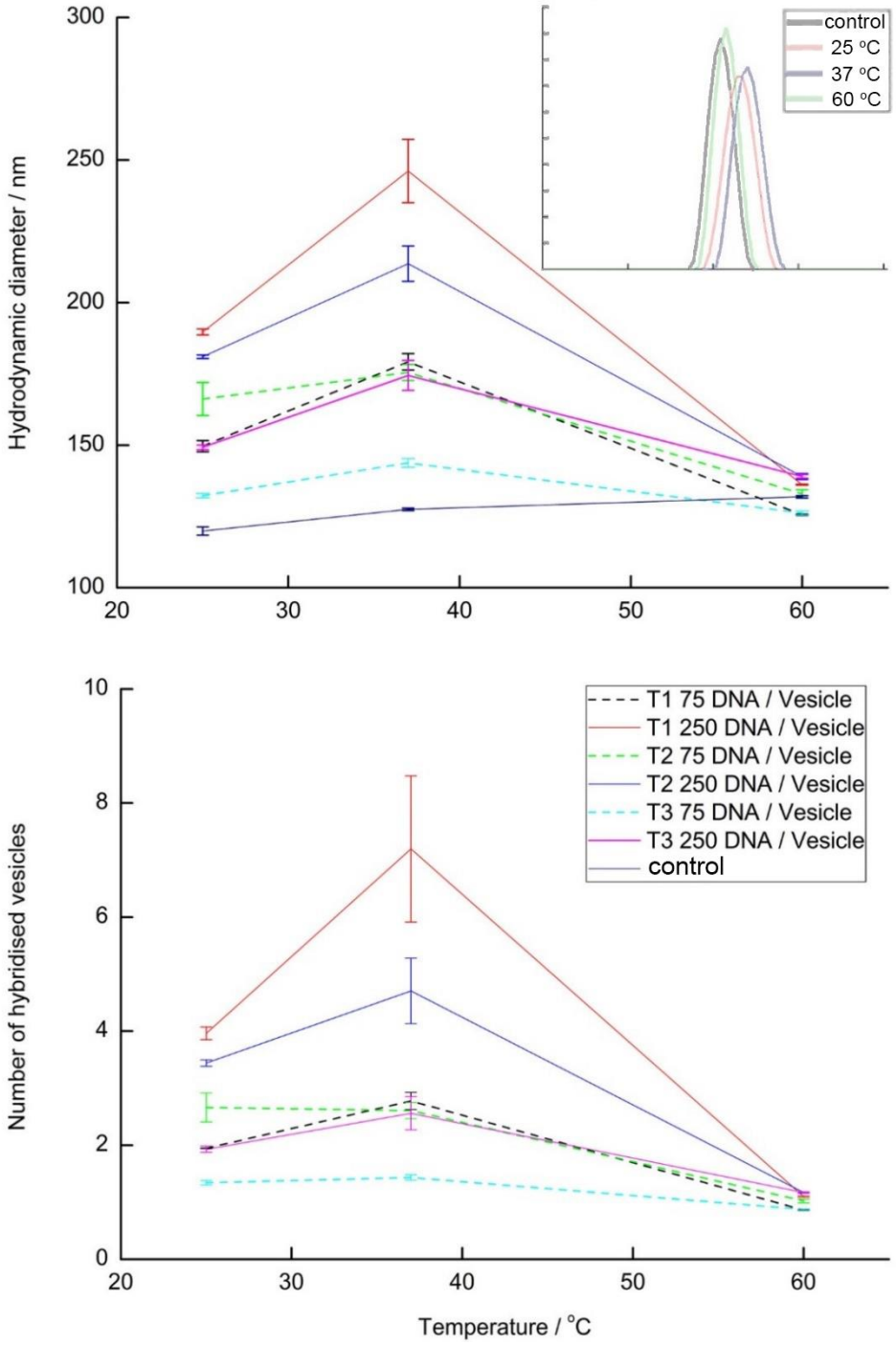

Figure 5.5 – Top insert: example of raw thermal-melt data of Janus DNA linked vesicles (T1 250 non-responsive DNA/vesicle loading). Samples were left for 30 minutes at each temperature before measurement. Top: Thermal-melt hydrodynamic diameter of Janus DNA linked liposomes across the assumed tie line, with 75 and 250 pH non-responsive DNA/vesicle loadings. Bottom: graph displaying the average number of vesicles tethered in a cluster, calculated from the hydrodynamic diameter. Lipid concentration was $1x10^{-3}$ M.

All samples within Figure 5.5 show growth when heated from 25 ^{o}C to biologically relevant 37 ^{o}C. This behaviour was expected as the recorded phase diagram at 20 ^{o}C will not be accurate to these raised temperatures. Furthermore, through heating the l_o patch will be reduced in area as the temperature nears that of the T_m of highest melting lipid (DPPC 41 ^{o}C). In other words, at 37 ^{o}C saturated lipids will begin to mix with the l_d domain. This has a profound effect on lipid-DNA partitioning. Firstly, the lipid-DNA has a saturated chain and will therefore behave similarly to DPPC and begin to partition to the l_d phase, allowing ABB tethering etc. subsequently increasing the hydrodynamic diameter of clusters. Secondly the diminished area of the l_o phase will mean that not all the lipid DNA will be able to partition to the reduced l_o phase. In both of these models the 250 DNA loading will be more significantly affected, raising the hydrodynamic diameter which is seen in the data.

60 ^{o}C has been shown to be sufficiently warm enough to melt both hybridised DNA and lipid domains, resulting in homogeneous membrane formation and DNA dehybridisation. From the data, hybridised vesicle clusters at 60 ^{o}C should form single vesicles. This hypothesis is consistent with the DLS data presented within Figure 5.5. Moreover, 60 ^{o}C heating was shown to meaningfully increase the hydrodynamic diameter of vesicles as seen with the POPC control, resulting from thermal expansion of the membranes surface.

5.2.1.3 Long term thermal stability

All the samples heated to 60 ^{o}C for thirty minutes showed little discrepancy from one another in terms of hydrodynamic diameter. This leads to the conclusion that thirty minutes should be long enough for all 60 ^{o}C samples to reach a hydrodynamic equilibrium. However, it would not be safe to assume samples held at 37 ^{o}C reach a hydrodynamic equilibrium, due to slow lipid diffusion. To account for the lipid diffusion at 37 ^{o}C, an investigation was conducted where samples were held at 37 ^{o}C for 24 hours before DLS measurement.

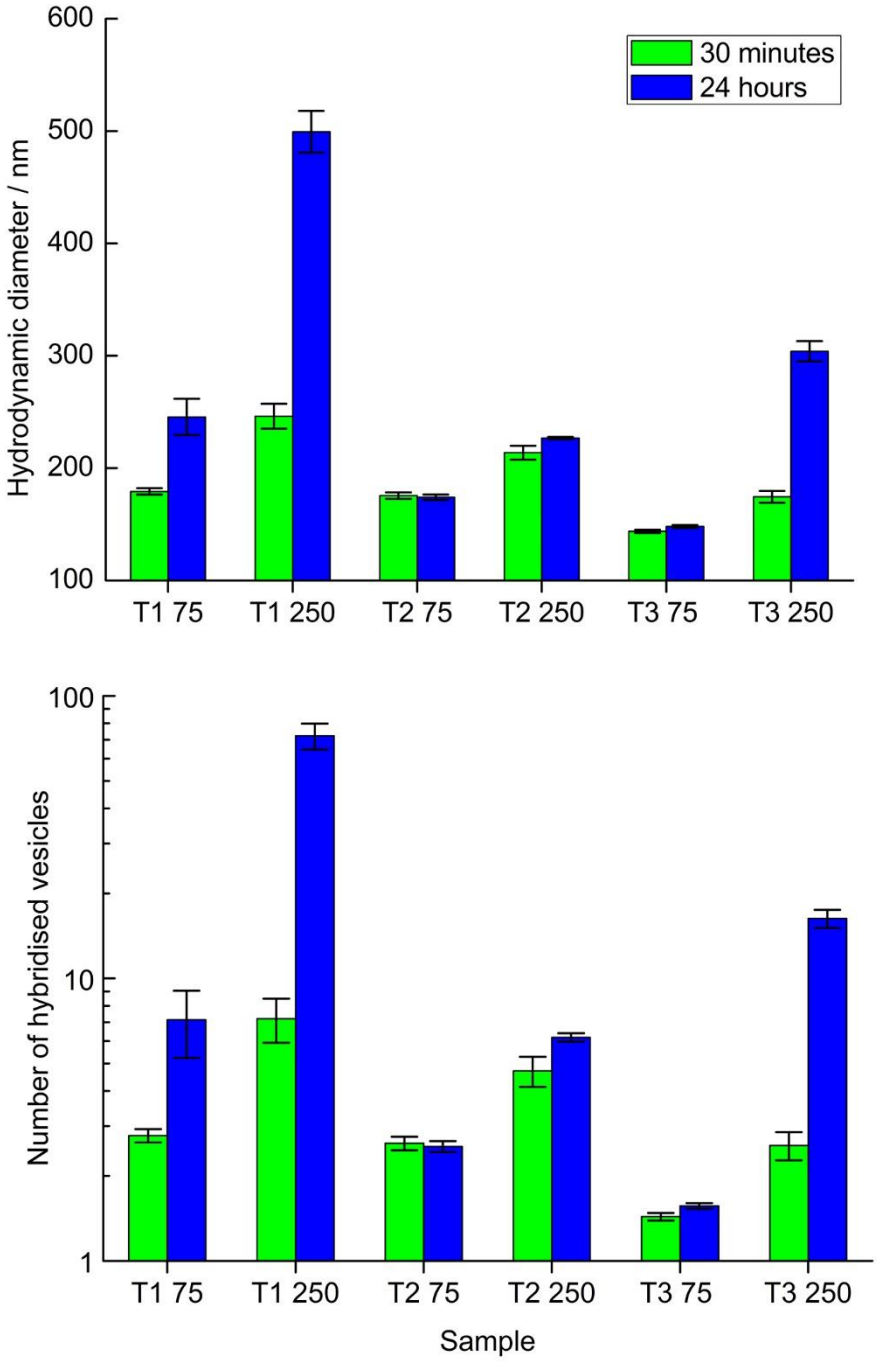

Figure 5.6 – Top: graph to show hydrodynamic diameter growth between samples held at 37 °C for 30 minutes and 24 hours. Bottom: graph to show the average number of vesicles per cluster tethered together, calculated from the hydrodynamic diameter.

Heating the samples for extended periods of time does lead to an upsurge in hydrodynamic diameter for vesicles who's l_o domain size is saturated in lipid DNA. T2 75 DNA/vesicle and T3 75 DNA/vesicle

have low DNA loadings in comparison to the area of the l_o domain, therefore when heated it is less probable for lipid-DNA to diffuse out of the l_o domain, and enable successful non-AB vesicle hybridisation.

As discussed, in medical applications it would be undesirable for a small cluster to mass aggregate through lipid-DNA surface migration, as shown in the presented data by T1 250 DNA/vesicle. However, the rate of DNA migration out of the l_o patch will have to compete with liposome sample dilution when transported around the blood stream. Explicitly, the significance of liposomes being open to mass hybridisation would be lessened by there being no available liposomes in reach, once quickly diluted in the blood stream.

5.2.1.4 Vesicle ageing stability

A liposome's period of usefulness, with regards to aging, is very variable dependent upon cargo type, cargo concentration, lipid composition, temperature and other external effects. However, this thesis only considered ageing for samples across the pseudo tie line with 75 and 250 lipid-DNA loadings. Only when in future development for specific treatments will further stability testing be required.

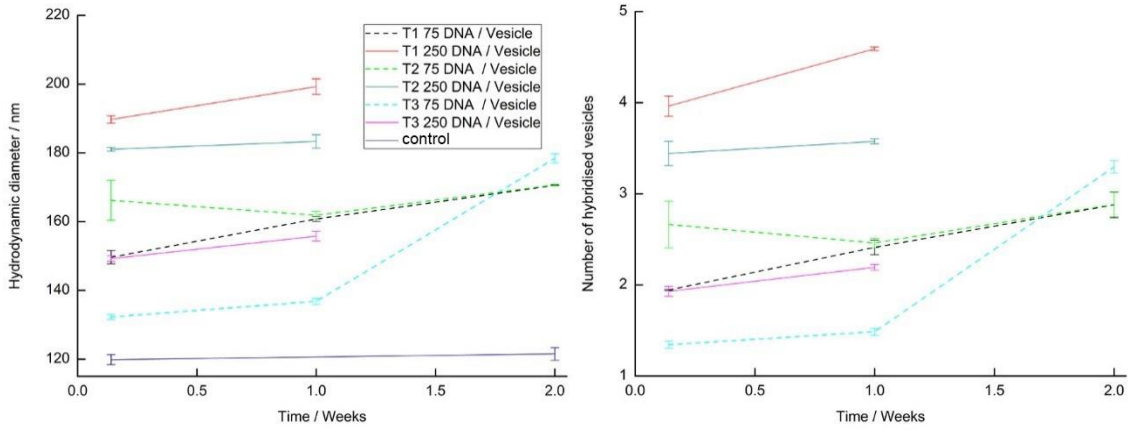

Figure 5.7 – Ageing study of Janus DNA linked liposomes across the pseudo tie line with 75 and 250 non-responsive DNA/vesicle loadings. Left: graph displaying the average hydrodynamic diameter of clustering. Right: graph displaying the number of vesicles tethered in a cluster, calculated from the hydrodynamic diameter. Reading was taken at 25 ^{o}C.

Figure 5.7 shows that clusters form stable aggregates over a week across the tie line regardless of lipid-DNA concentration. One week of cluster stability is a significant amount of time when typical

vesicle drug carrier stability is usually measured over a period of 24 hours [155]. Therefore, if small liposome clusters were to be used within medical applications, it would not be the liposome DNA bridging scaffold that would lead to a limited shelf life, it would be the drug leakage from the vesicles. Data shows longer storage would be subject to tie line position. Over a two-week period, the lower 75 DNA/vesicle loading did show signs of long term instability, specifically at T3 but conversely T2 displayed negligible cluster growth over the two weeks.

5.2.2 pH responsive DNA mediated assembly

5.2.2.1 pH switching

To maximise the number of treatments this liposome DNA mediated clustering platform could be applied to, the in-house pH responsive sequence developed by Zhou et al. was incorporated into vesicles [107]. Initially to test liposome pH switching viability, homogeneous POPC liposomes were doped with 250 lipid-DNA/vesicle and analysed through DLS. Vesicles doped with the pH non-responsive sequence were used as a control.

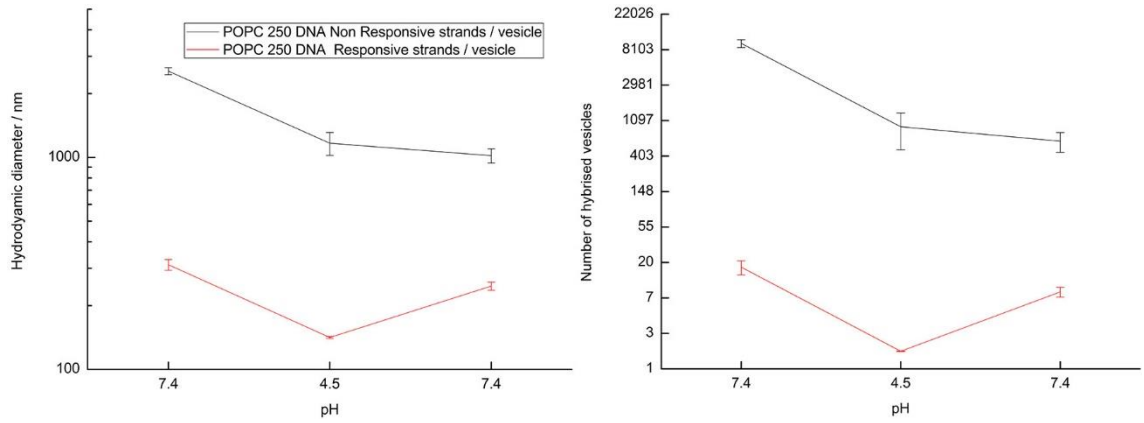

Figure 5.8 – pH switching of POPC vesicles tethered together using 250 lipid-DNA pH non-responsive strands and pH responsive sequence/vesicle respectively. Left: Graph displaying the average hydrodynamic diameter of clustering on a logarithmic scale to the base of ten. Right: graph displaying the number of vesicles tethered in a cluster calculated from the hydrodynamic diameter on a natural logarithmic scale. The left-hand side on the x axis displays the initial starting pH. Samples were incubated for an hour after pH switching before measurement. Reading was taken at 25 ^{o}C.

At the starting pH 7.4, there is disparity between the binding affinity of the pH non-responsive sequence and the pH responsive sequence even at the same DNA loading/vesicle, by an order of magnitude in hydrodynamic diameter. This discrepancy can be accounted to the stability of each of the sequences. By design, the pH responsive mismatched sequence forms less stable duplexes than the fully complementary sequences. This instability consequently reduces the number of vesicles able to successfully hybridise together in a cluster. The reduction in pH to 4.5, leads to a noteworthy reduction in hydrodynamic diameter for both sequences. Because of the pH non-responsive sequences being fully complementary, they are more stable at lower pH, hindering the release of single vesicles from clusters. On the other hand, through design the pH responsive i-motif sequence incorporates BP mismatching. By lowering the pH the duplex is destabilised, enabling the release of single vesicles. Upon increasing the pH back to 7.4 the non-responsive sequence does not increase the hydrodynamic radius, indicating that there is no increase in vesicle clustering. In reaction to these results it was hypothesised that the sequences again may have been damaged through acid depurination, greatly reducing hybridisation. The disparity between the i-motif and fully complementary sequences is illustrated in Figure 4.18 and Figure 4.19, where the non-responsive sequence is found to degrade after one hour at low pH and high temperature, in contrast to the i-motif.

In addition, the disparity in reforming clusters may also be due to the greater overall percentage of damage to the short non-responsive sequence, over the long pH response sequence. In other words, if a BP is damaged/removed, longer DNA sequences are more likely to be able to still hybridise together, due to the large number of supporting BPs as shown in Figure 5.8. Shorter sequences have less hybridising BPs; resulting in an overall larger proportion of the molecule unable to hydrogen bond with a correlating sequence, preventing duplex formation.

With both sets of sequences displaying promising results in the formation of clusters, a study examining phase separated vesicles was conducted.

5.2.2.2 Phase diagram led cluster formation

The same experimental conditions to those used in Figure 5.2 were repeated, but in place of the non-responsive DNA sequence the i-motif sequence was implemented.

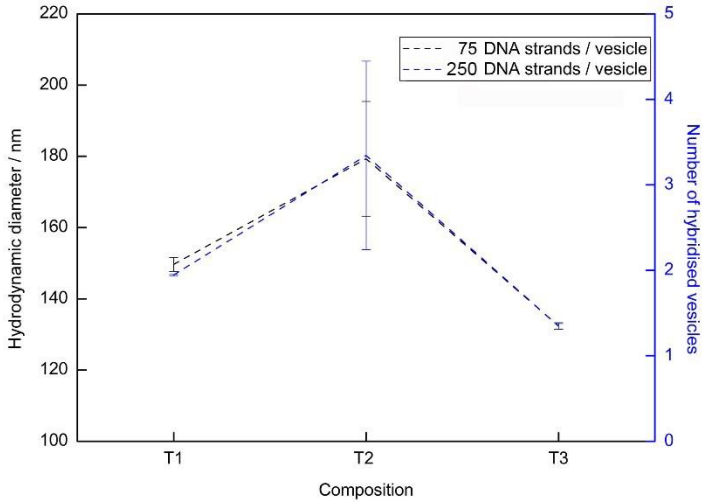

Figure 5.9 – Average hydrodynamic diameter of pH responsive DNA tethered vesicle clusters, and the resulting calculated apparent number of vesicles in said clusters, changes with positioning on the tie line of the l_d-l_o phase coexistence region. Readings were taken at 25 ^oC.

Concerns whether the i-motif sequence would provide suitable “stickiness” for small cluster formation in phase separated liposomes was put to rest by the data displayed in Figure 5.9. The data show composition T1 with a 75 DNA/vesicle loading forming size limited clusters. The results here are akin to the data presented in Figure 5.2 and the subsequent model presented in Figure 5.3. At composition T2 there is an increase in the hydrodynamic radius of clusters, equating to a larger hydrodynamic radius than previously shown for the non-responsive sequence. There may be a contribution to this from the longer sequence promoting the distance between vesicles. Between the two lipid-DNA sequences the i-motif is averaged to be 15.5 BPs longer which equates to a 5.27 nm extension, when BP separation is 0.34 nm [156]. This extension affords more space for binding vesicles enabling the potential for further hybridisation with other vesicles.

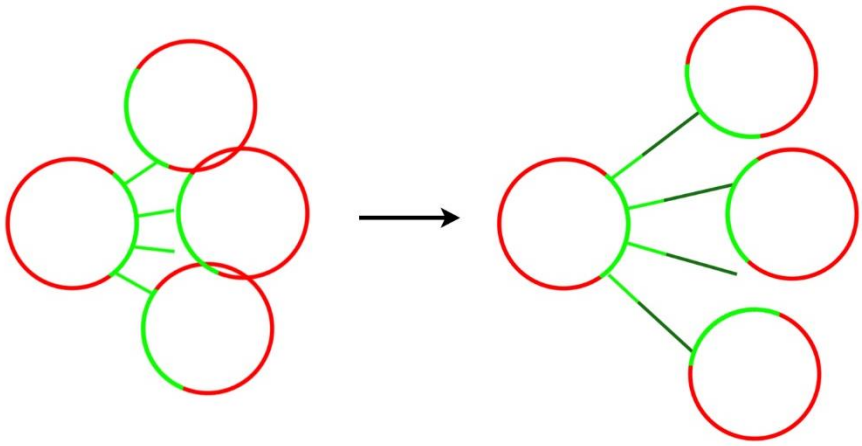

Figure 5.10 – Cartoon of a liposome cross section model displaying how DNA sequence length affects the average vesicle cluster size. Cartoon spheres representing phase separated vesicles with green highlighting the l_o domain and the red the l_d domain. On the left, the light green straight lines represent the short non-responsive 13 mer. On the right, vesicles are connected through the longer pH responsive 30 mer sequence, represented by the conjoined light and dark green line, with the dark green displaying the 5.3 nm extension. Cartoon not to scale.

The model shown within Figure 5.10 displays the shorter sequence (left hand side) providing unfavourable hybridisation of more than three vesicles, where the longer sequence (right hand side) affords potential for four vesicles to cluster tether.

Data thus far have shown that small size limited clusters can be formed through careful selection of both the lipid composition and the lipid-DNA concentration. Further experiments in this chapter are to improve upon this foundation to ensure a reliable drug delivery platform and to display further potential uses as a medical device.

5.3 Lipid-PEG addition with phase diagram led cluster formation

5.3.1 Lipid-PEG

For successful longer term intravenous circulation of vesicle clusters, it is essential that polyethylene glycol (PEG) or another non fouling polymer coating is added to the liposomes' surface. PEGylating NPs produces "stealth" NPs, preventing recognition by the body's mononuclear phagocyte system [157]. Without NPs being PEGylated vesicles display short circulation times and rapid burst release, limiting the potential effectiveness of the drug delivery platform and therefore the patient's treatment and outcomes.

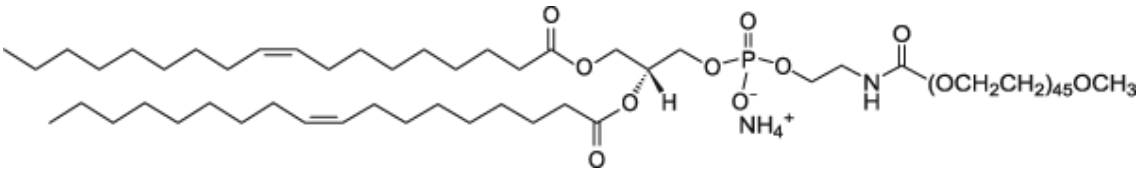

Figure 5.11 – Structure of unsaturated PEGylated lipid, 2-dioleoyl-sn-glycero-3-phosphoethanolamine-N-[methoxy(polyethylene glycol)-2000].

5.3.1.1 Lipid-PEG concentration

Initially lipid-PEG was introduced into POPC homogeneous vesicles to examine the effect PEG may have on DNA hybridisation. POPC vesicles doped with 250 and 75 strands of pH responsive and non-responsive DNA/vesicle were tested against 0-6% PEG loading, data shown in Figure 5.12.

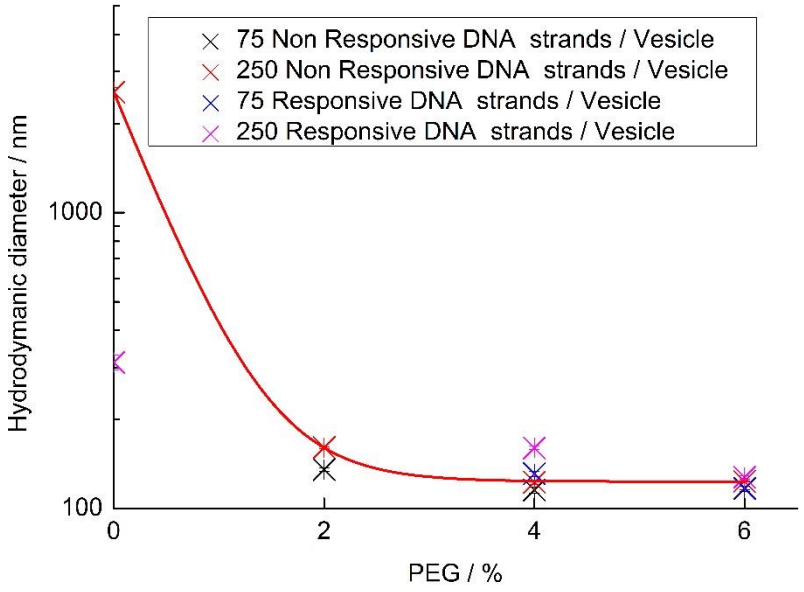

Figure 5.12 – Membrane lipid-PEG mol% showing decreasing hybridisation between vesicles in POPC doped lipid-DNA vesicles. Red line is a guide for the eye. Reading was taken at 25 ºC.

The addition of PEG results in a sizeable reduction in vesicle hybridisation, reducing clustering from the thousands to single vesicles, with a 4% lipid-PEG addition to the membrane. This was achieved through PEG chains providing an effective physical blocking action to DNA. This was likely accomplished through the length of PEG being comparable in length to that of the longest used 30 mer DNA sequence, when PEG is in a brush state. In its fully extended form PEG 2000 has been shown to equal 11.5 nm in length whereas the 30 mer DNA sequence is 10.2 nm [156]. However when PEG percentage is raised from 4% to 6%, passing through 5%, the mushroom to brush PEG transition, data show no significant difference in hybridisation between the two PEG states [158].

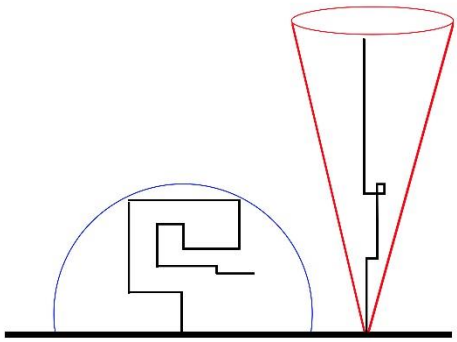

Figure 5.13 – Left: PEG concentration <5 % forming a mushroom shapeon the surface of a vesicle outlined by the blue semicircle. Right: PEG concentration >5 % presenting an extended brush shape on the surface of a vesicle outlined by the red cone [158].

While PEG randomly partitioning to the phase separated surface of the Janus vesicle could have drastic effects on size limited cluster formation, this can be controlled through the tailoring of the lipid tail. The use of an unsaturated lipid tail promotes partitioning of DNA to the l_d region in a phase separated liposome. Additionally, once vesicles are hybridised into an AB structure the l_o area with limited lipid-PEG would be concealed through membrane deformation. Thereby the exterior of the vesicle surface would be fully PEGylated as described in Figure 5.14.

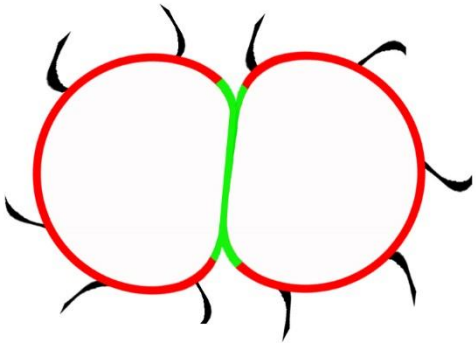

Figure 5.14 – Cross sectional cartoon of dimer phase separated vesicles tethered together using lipid-DNA partitioned to l_o phase (green), with lipid-PEGs (black) partitioned to the l_d phase.

The lipid-PEG integration to the l_d phase offers potential in further developing liposome hybridisation specificity. While CL has significantly helped to drive size limited cluster formation, significant proportions of the phase diagram, dependent upon DNA concentration, still provide unwanted nonspecific hybridisation. To prevent the nonspecific hybridisation PEG would sterically block any approaching l_d phase partitioned DNA.

Moving forward, 2% lipid-PEG loading was selected as there was no significant difference between this and a higher PEG loading. Furthermore, a higher concentration of lipid-PEG would result in the addition of another component within the phase diagram; potentially perturbing the mapped phase space plotted in chapter 3. Under these circumstances the lower 2 mol% PEG maximises hybridisation blocking with minimal phase interference.

5.3.2 pH non-responsive DNA mediated cluster assembly

5.3.2.1 Across tie line examination

To measure the effect of lipid-PEG addition has on phase separated vesicles, the first experiment conducted was to use DLS to measure the hydrodynamic diameter of lipid nanoparticles across the pseudo tie line.

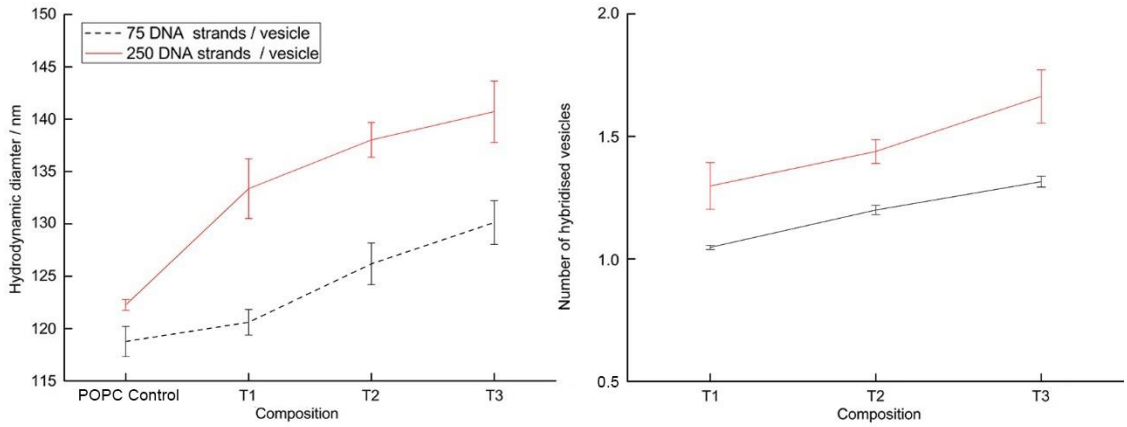

Figure 5.15 – Data to show the effect on hydrodynamic diameter (left) and calculated number of vesicles tethered together with pH non-responsive DNA (right) with the addition of 2 mol% lipid-PEG to the phase separated membrane. Reading was taken at 25 ºC.

The first striking observation is that 2 mol% lipid-PEG significantly lowers the hydrodynamic diameter across the tie line. The data show that neither of the lipid-DNA concentrations at any of the positions on the tie line led to more than average dimer formation. This significant reduction in number of bound vesicles highlights that lipid-PEG in the l_d phase, proactively prevents unwanted random tethering, while also showing some signs of preventing wanted hybridisation in order to form clusters. T1 75 DNA/vesicle loading has the same level (within error) of hybridisation as the control. Furthermore, Figure 5.15 displays the 250 DNA/vesicle loading as always having higher vesicle tethering than the 75 DNA/vesicle loading (significant when uncertainty is allowed for). This is likely contributable to the increased lipid-DNA forming a “stickier” domain; promoting tethering.

5.3.2.2 Thermal-melt of vesicle aggregates

Continuing with the lipid-PEG pH non-responsive DNA system, melting studies were performed to observe whether higher/more biologically relevant temperatures still gave rise to an elevated hydrodynamic diameter.

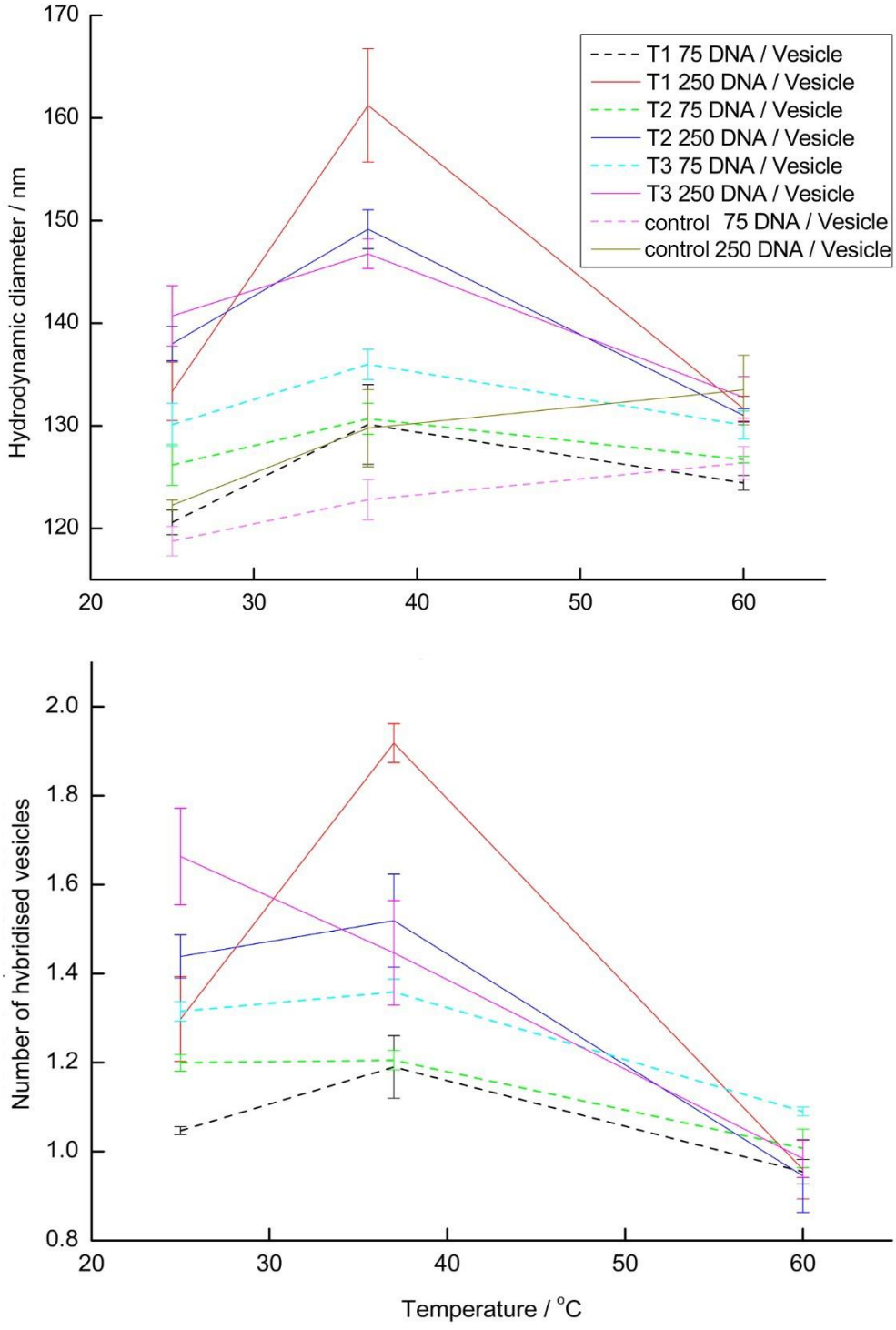

Figure 5.16 – Heating study of hybridised vesicles with 2 mol% PEG integration loaded with 75 and 250 pH non-responsive lipid-DNA/vesicle. Samples were held at respective temperatures for 30 minutes. Top: Measured hydrodynamic diameters from phase separated vesicles, Bottom: Calculated average number of hybridised phase separated vesicles in a cluster from the measured hydrodynamic diameter heating study.

Once heated to 37 ^{o}C the PEGylated pH non-responsive sequence gave a larger hydrodynamic diameter, behaving similarly to samples where PEG is not present, with the advantage of never rising above average dimer formation after being held at 37 ^{o}C for 30 minutes. Through these initial studies DNA linked Janus vesicles assure, upon injection into the patient, there would be no subsequent architectural changes with body temperature. The data again show that through further heating to 60 ^{o}C the DNA sequence melts and single vesicles are formed, demonstrating clustering is mediated by reversible lipid-DNA interactions.

Counterintuitively, data for T3 250 DNA/vesicle when heated from 25 ^{o}C to 37 ^{o}C show an increase in hydrodynamic diameter where there is a reported decrease the number of tethered vesicles in sample. This apparent discrepancy can be explained with reference to vesicle thermal expansion. The number of vesicles hybridised in a cluster is calculated from the ratio between the un-hybridised single vesicle control and the clustered vesicle sample. In the case of T3 250 DNA/vesicle the control has thermally expanded more than the clustered sample giving rise to an apparent decrease in the number of tethered vesicles. However, this is likely not the case due to a significant rise in uncertainty in the number of tethered vesicles in that particular sample.

5.3.2.3 Vesicle ageing stability

2% lipid-PEG addition has demonstrated a reduction in random l_d tethering over short periods of time for 250 and 75 DNA/vesicle loadings, across the pseudo tie line. For effective use within hospital treatments the longer the shelf life that can be afforded the better. An extended shelf life opens up avenues for new treatments to be taken outside of the hospital in the home. To measure vesicle aging stability with PEG addition, experiments were conducted where PEGylated samples were refrigerated for two weeks to examine cluster growth rates.

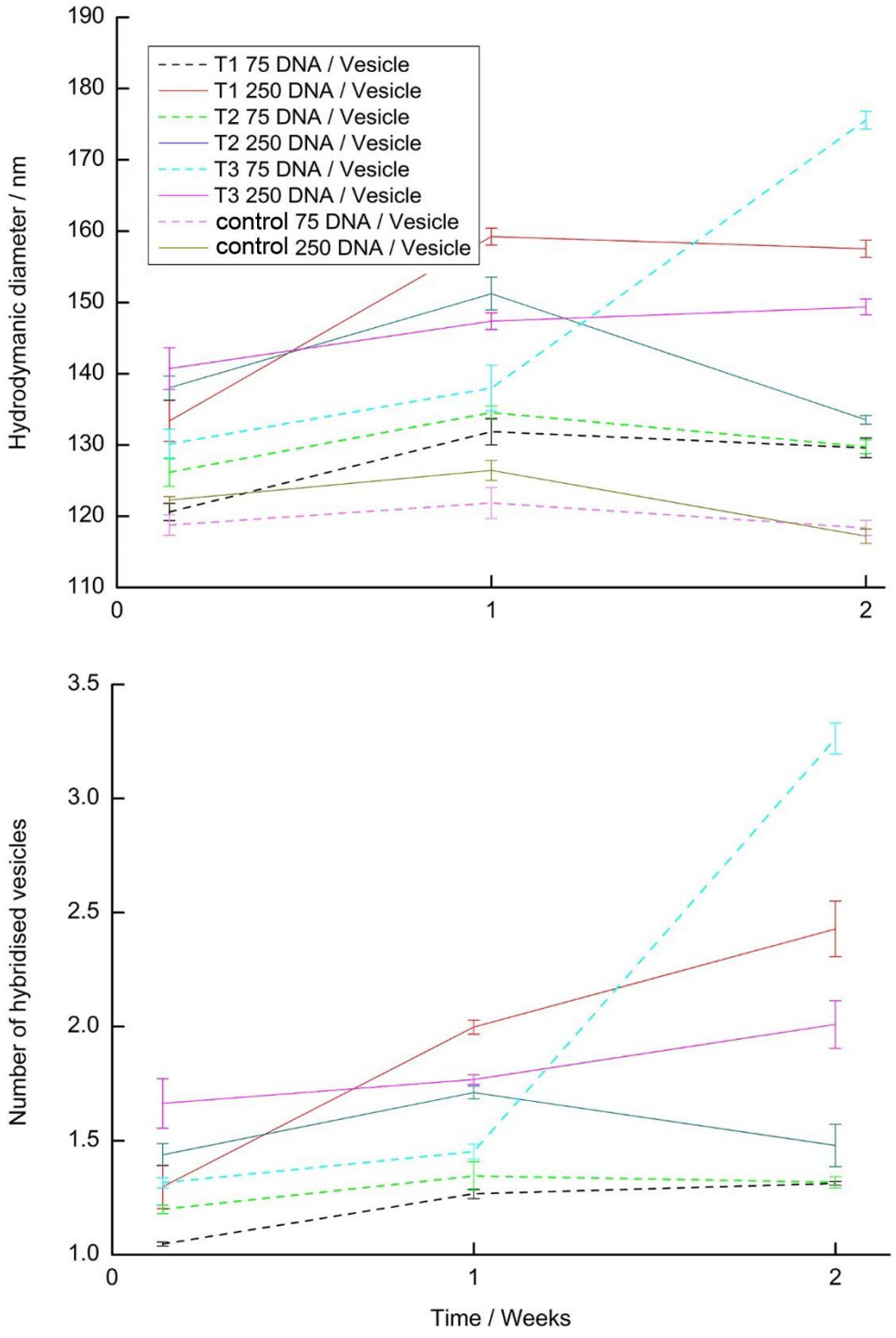

Figure 5.17 – Across tie line study for pH non-responsive DNA linked vesicles with 2 mol% lipid-PEG doping. All samples were stored in the fridge between measurements. Measurements taken at 25 °C.Top: A plot of the measured average hydrodynamic diameter. Bottom: A plot of the calculated average number of hybridised vesicles/cluster.

The first week of ageing shows unanimously across both DNA loading and tie line, that there is a small increase in hydrodynamic diameter. Again, the same rationale for sample aging that was used for samples that contain no lipid-PEG can be used here. For example, T1 250 DNA/vesicle loading as discussed has a small l_o domain and large DNA loading that cannot fully partition to the l_o patch. While initially the l_d non-specific hybridisation is blocked by PEG, over time hybridisation likelihood will grow causing the rise in hydrodynamic diameter seen experimentally in Figure 5.17.

Over the two weeks there is further aggregation of samples, specifically T3 75 DNA/vesicle loading, which was previously seen for samples without the introduction of lipid-PEG in Figure 5.7. This pattern can be attributed to the low concentration of DNA strands in the l_o domain and the resulting weak bond between vesicles. Over time the prospect of numerus weak tethering between liposomes becomes more likely. Two properties that enhance this effect are the large l_o domain enabling the space for high local concentrations of vesicles, and low concentration of DNA; prohibiting a tight zippering action between two deformable Janus particles.

Additionally, over the two weeks samples T2 and T3 250 DNA/vesicle loading displayed average dimer formations remaining largely undisturbed, making them prospective candidates for future dimer treatment development. T1 and T2 75 DNA/vesicle loading form ~50% dimers with little change over the two weeks. Over a longer ageing study these preparations may provide long term average dimer stability. However, over considerable time scales combined with the type of cargo, leakage may become significant. This would need further study when the Janus vesicle platform is applied to a specific treatment.

To maximise the drug delivery platform's potential, 2 mol% lipid-PEG was introduced to Janus liposome clusters, tethered together using pH responsive i-motif sequences.

5.3.3 pH responsive DNA mediated cluster assembly

5.3.3.1 Across tie line examination

A similar study to that done for the non-pH responsive sequences (Figure 5.15) was carried out to investigate the i-motif sequences.

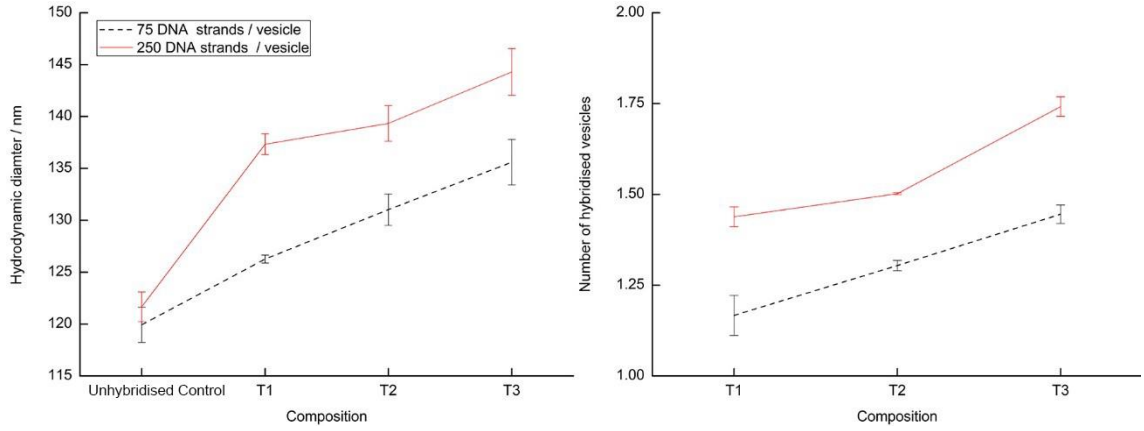

Figure 5.18 - Data to show the effect of 2 mol% lipid-PEG addition on i-motif DNA tethered vesicles. Left displays the recorded hydrodynamic diameter and right the calculated number of vesicles tethered together. Readings were taken at 25 ºC.

The data present in Figure 5.18 closely mirrors its pH non-responsive counterpart, preventing mass aggregation of samples across the tie line as shown in samples lacking lipid-PEG in Figure 5.9. PEG 2000 is therefore shown to be long enough to counteract the 30 mer sequence non-specific binding in the l_d phase.

5.3.3.2 pH switching

Vesicles across the tie line were pH switched to examine whether the PEG would interfere with the formation of single vesicles and reformation of dimers when acid and base were added, respectively.

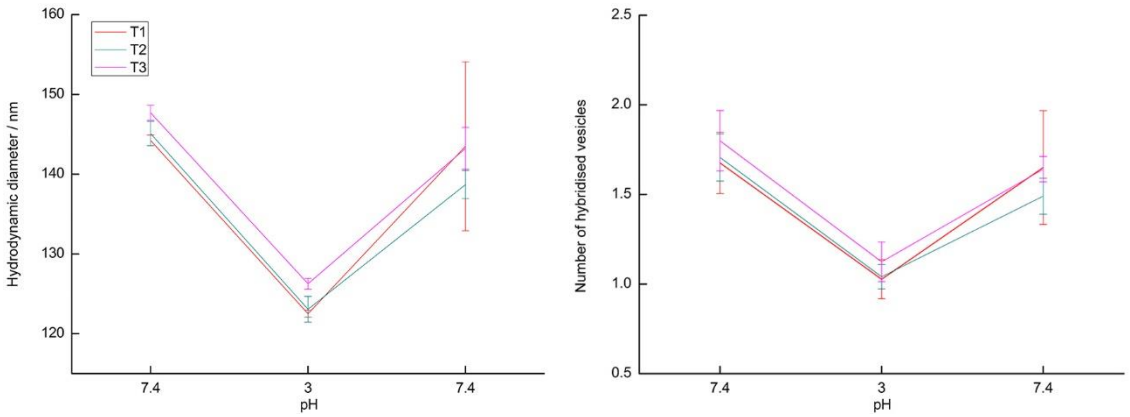

Figure 5.19 – pH switching response for 250 pH responsive DNA/vesicles across the assumed tie line in the l_d-l_o region. Readings were taken at 25 ^oC. Left hand side pH 7.4 is the starting pH.

The data shown in Figure 5.19 describe a system where the i-motif DNA sequence is suitable to link vesicles together alongside PEG stabilisation. The data denote dimer formation at pH 7.4, where a decrease in pH dehybridises linking DNA; creating single liposomes. Through the addition of 1.2 M $NaOH_{(aq)}$ base dimer clusters reform, creating a sophisticated switchable device independent from tie line position. This new highly specific pH switchable devise unlocks potential for new medical based treatments.

5.3.3.3 Thermal-melt of vesicle aggregates

Similarly, to previous work, small cluster thermal stability experiments were carried out across all tie line positions with 75 and 250 DNA/vesicle loadings.

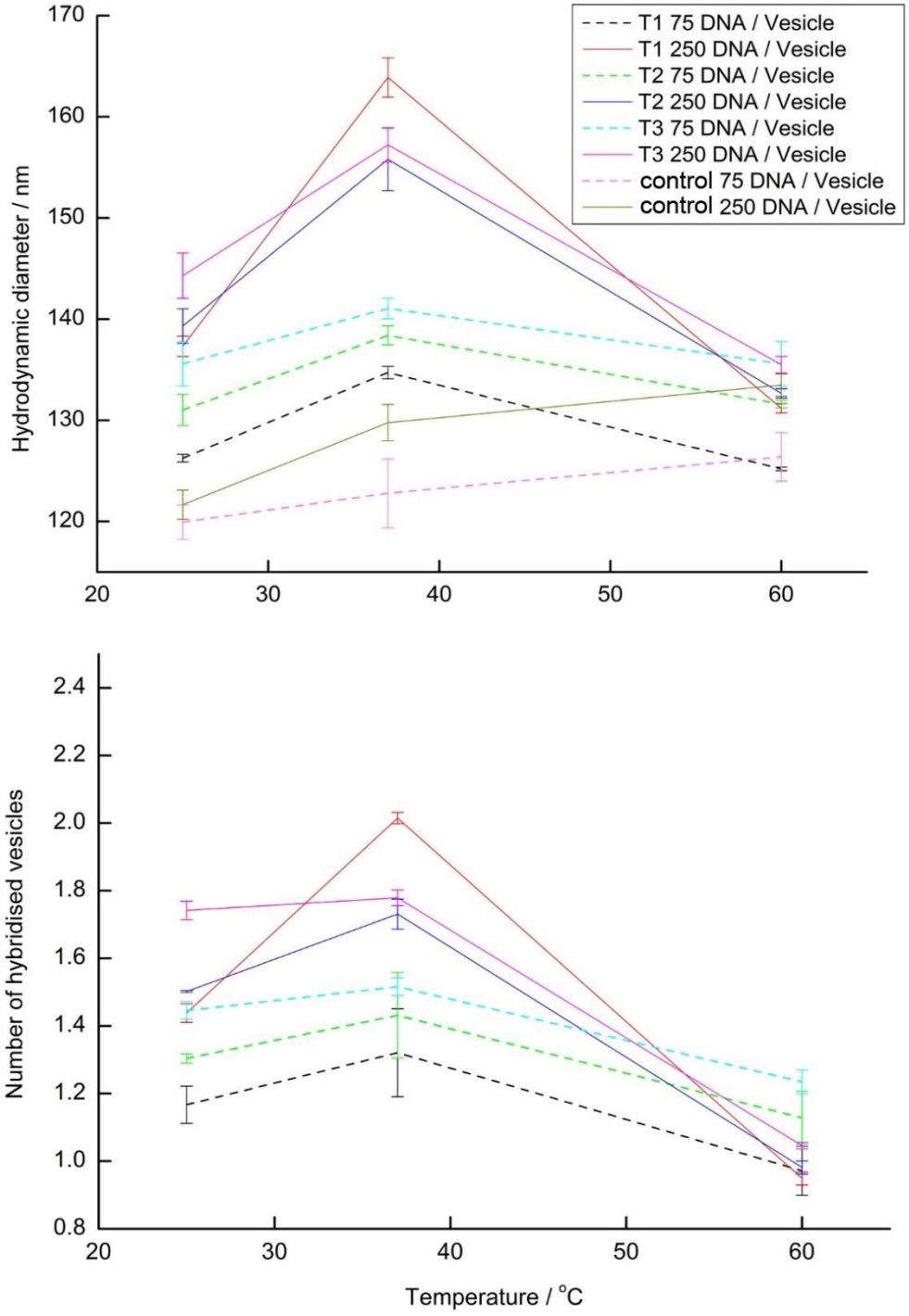

Figure 5.20 – Top: Heating study showing measured hydrodynamic diameters from phase separated vesicles with a 2 mol% PEG integration and 75 and 250 pH responsive DNA/vesicle loadings. Samples held at respective temperatures for 30 minutes. Bottom: Calculated average number of hybridised phase separated vesicles in a cluster from the measured hydrodynamic diameter heating study.

The pH responsive sequence across all tie line positions and DNA/vesicle loadings displayed good agreement with the pH non-responsive sequence, with the addition of 2 mol% lipid-PEG. The lipid-PEG acts as a positive tethering stabilising agent irrespective of the sequences tested here, opening up avenues to more sophisticated DNA sequences of a similar 30 mer length. Having longer strands of DNA that are not proportionate in length to the PEG polymer may result in a reduction in PEG effectiveness. Alternatively, a longer PEG 6000 polymer incorporated into the vesicle may allow for a longer DNA sequence while still enabling a l_d hybridisation phase block.

Again counterintuitively, data for T3 250 DNA/vesicle when heated from 25 ^oC to 37 ^oC show an increase in hydrodynamic diameter where there is only a small reported increase in the number of tethered vesicles in sample. This apparent discrepancy can be again explained with reference to vesicle thermal expansion. The number of vesicles hybridised in a cluster is calculated from the ratio between the un-hybridised single vesicle control and the clustered vesicle sample. In the case of T3 250 DNA/vesicle the control has thermally expanded more than the clustered sample giving rise to only a small increase in the number of tethered vesicles with respect to the hydrodynamic diameter.

5.3.3.4 Vesicle ageing stability

The hybridisation seen within Figure 5.20 is representative of vesicles 24 hours after preparation. The i-motif sequence has mismatching base pairs that could lead to reduced hybridisation kinetics and over time lipid-PEG may not be as effective at blocking l_d hybridisation as first suspected for the longer sequence [159].

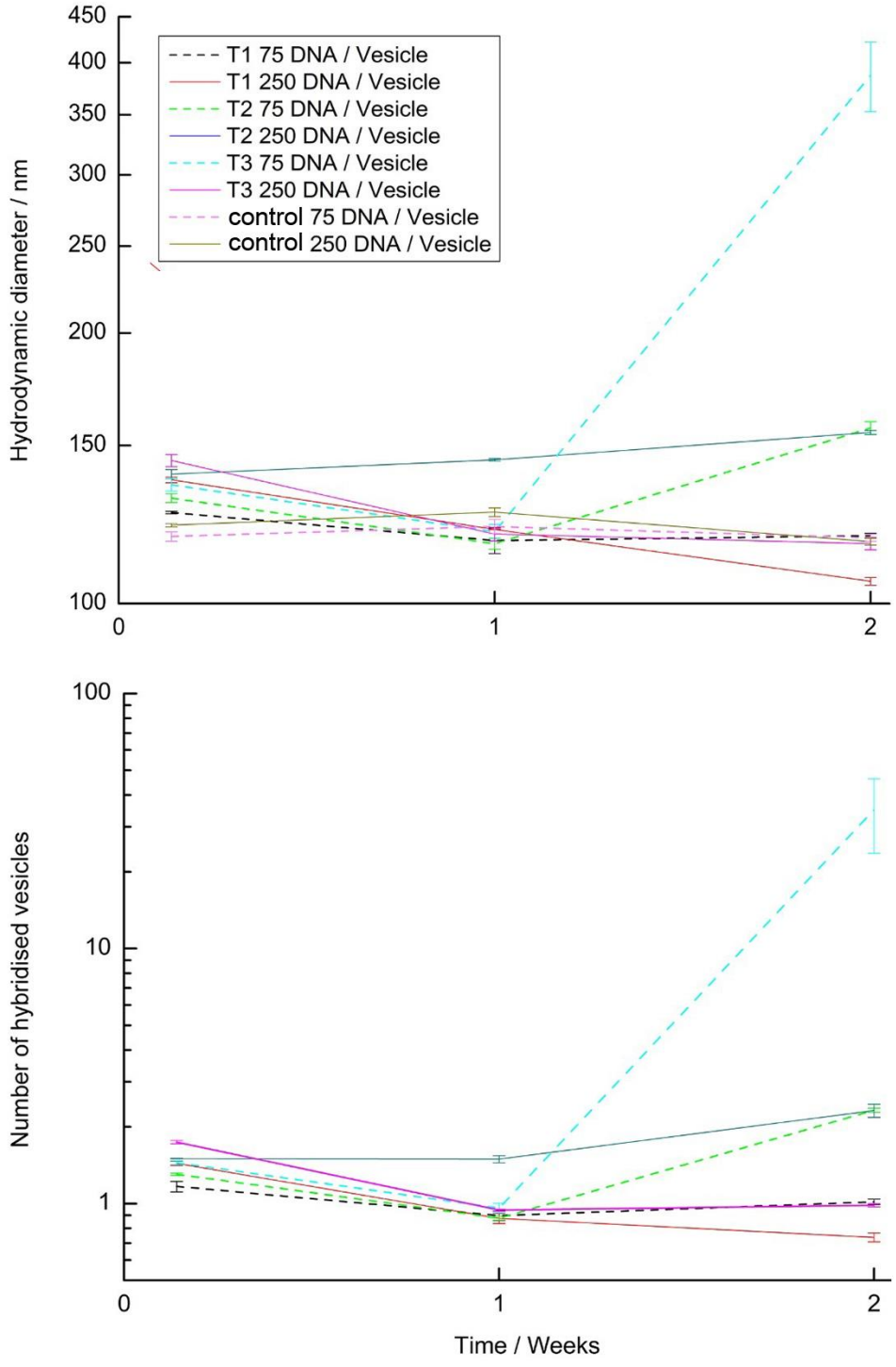

Figure 5.21 - Across tie line aging study for pH responsive DNA linked vesicles with 2 mol% lipid-PEG. All samples were stored in the fridge between measurements. Measurements read at 25 ºC. Top: Measured average hydrodynamic diameter plot. Bottom: Calculated number of hybridised vesicles per cluster plot.

Again, over the week long period, PEG provided sufficient blocking power to prevent uncontrolled l_d enabled vesicle hybridisation. However over the week, with the exception of T2 250 DNA/vesicle, clusters dehybridised releasing single vesicles. The reduction in vesicle tethering for the majority of the samples is likely due to lipid-PEG slowly partitioning into the l_o domain and disrupting the weak hybridisation. Conversely in the second week, specifically for the 75 DNA/vesicle loading, there is a trend whereby the larger the l_o domain area the more vesicles hybridise together. This growth could be attributed to three simultaneous effects accruing after the first week.

When the low levels of lipid-PEG partition to the l_o domain its disruptive forces are relative to lipid-DNA to lipid-PEG separation. In small l_o patches PEG effects will be more prominent than in larger l_o domains, T1 to T3 respectively. In turn the disruptive forces of the PEG are therefore reduced, commanding an order of magnitude difference with more vesicles being tethered together in T3 over T2, when doped with 75 i-motif/vesicle. Furthermore, as previously discussed, T3 has a very large surface area allowing for multiple tethering as described in Figure 5.3. And finally, a longer i-motif sequence affords larger vesicle aggregates as suggested in Figure 5.10.

5.3.4 Lipid-PEG doped liposome stability

5.3.4.1 Long term thermal stability

Lipid-PEG has shown that it is capable of significantly reducing nonspecific hybridisation both at room and ~body temperature. However, as previously discussed, samples were only heated at 37 ^{o}C for 30 minutes. Therefore, to test how effective PEG was against nonspecific hybridisation, at raised temperatures over extended periods, samples were prepared and placed in a water bath at 37 ^{o}C for 24 hours before DLS examination. Through examining the long term thermal stability, it could be possible to select an appropriate universal composition that could be safely used in long circulation formulations.

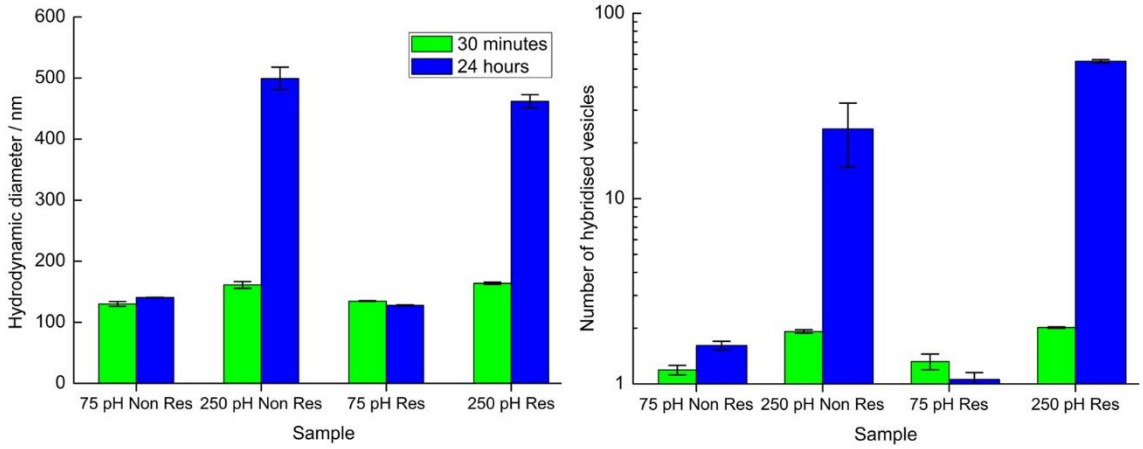

Figure 5.22 – Phase separated T1 samples with 2 mol% lipid-PEG doped with 75 and 250 pH non-responsive and pH responsive DNA/vesicle. Left: Graph displaying time held at 37 °C against hydrodynamic diameter. Right: Calculated average number of vesicles for hydrodynamic diameter. Both graphs have been presented on a log Y scale.

As expected a 250 DNA/vesicle loading, where l_o is fully saturated with lipid-DNA, leads to high levels of clustering, accentuated through an extended heating time. Over time at a raised temperature, more saturated lipids will be able to diffuse out of the l_o domain reducing l_o domain size, promoting nonspecific hybridisation. 75 DNA/vesicle loading maintains low vesicle hybridisation, with the pH responsive sequence dehybridising through extended heating. This is not to be unexpected when considering the initial low levels of successful hybridisation.

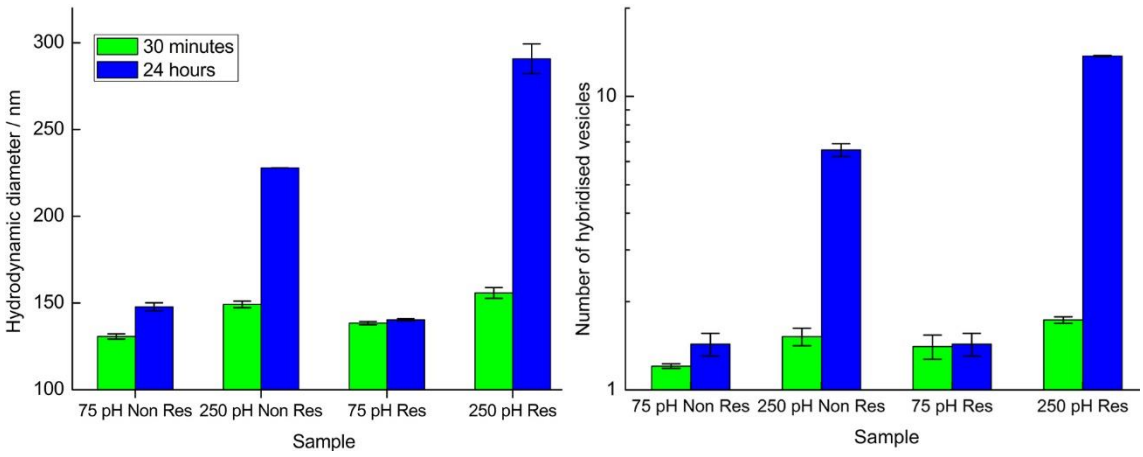

Figure 5.23 - Phase separated T2 samples with 2 mol% lipid-PEG doped with 75 and 250 pH non-responsive and pH responsive DNA/vesicle. Left: Graph displaying time held at 37 ºC against hydrodynamic diameter. Right: Calculated average number of vesicles for hydrodynamic diameter. Both graphs have been presented on a log Y scale.

The larger I_o patch in T2 affords more controlled hybridisation when the raised temperature is held for longer periods of time than T1. Nevertheless the 250 DNA/vesicle loading resulted in cluster sizes on average five times greater than dimer formation. Both 75 DNA/vesicle loadings showed potential in being able to prevent extended clustering. However, for both 75 DNA/vesicle loadings there are only low numbers of small clusters, which if introduced as a treatment would lead to poor cluster yield once single and dimer vesicles were separated.

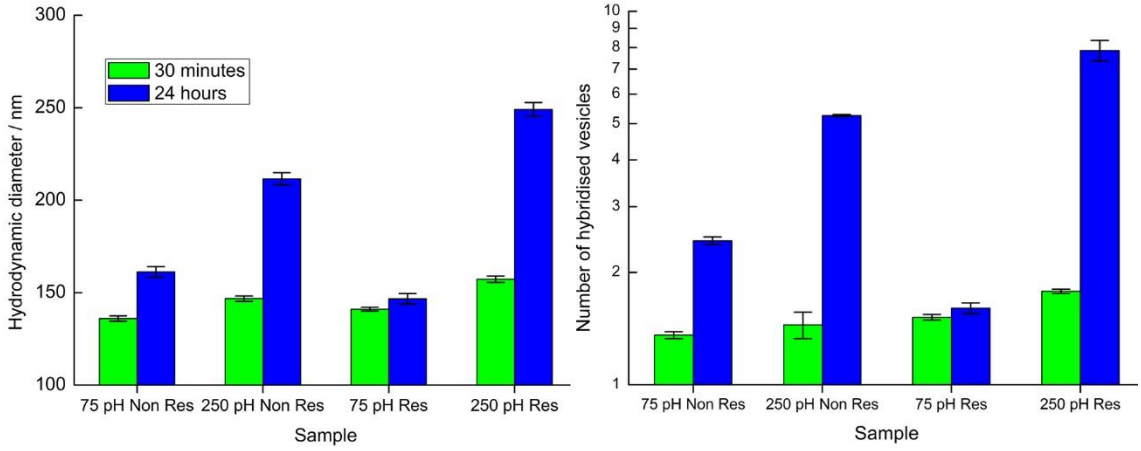

Figure 5.24 - Phase separated T3 samples with 2 mol% lipid-PEG doped with 75 and 250 pH non-responsive and pH responsive DNA/vesicle. Left: Graph displaying time held at 37 ºC against hydrodynamic diameter. Right: Calculated average number of vesicles for hydrodynamic diameter. Both graphs have been presented on a log Y scale.

Further DPPC addition improves size limited cluster formation relative to T2 and T1 compositions. 250 lipid-DNA/vesicle doping proves to be unsuitable when heated for long periods of time. However, a 75 loading of pH non-responsive DNA/vesicle is shown to improve dimer formation. This sample therefore would provide a potential drug delivery platform that would be stable in warmer environments for extended periods of time. Similarly, the 75 loading of i-motif sequence displayed high binding specificity after extended heating. These extended heating studies have exposed Janus vesicles to be a versatile concept, capable of satisfying the demands for safer, highly specific treatments.

5.3.4.2 Liposome stability after 24 hours 37 ºC heating

Heating to 37 ºC for 24 hours does raise further interesting questions. Once the system has been heated to 37 ºC if placed back in the fridge, for example 24 hours, would this render smaller vesicle clusters once again? In other words, once uncontrolled weak DNA bridges have been formed, would these fall apart once saturated lipids condense? If this was the case a more versatile, safer delivery platform could be modelled. The first DNA set of sequences examined were the complementary pH non-responsive sequence.

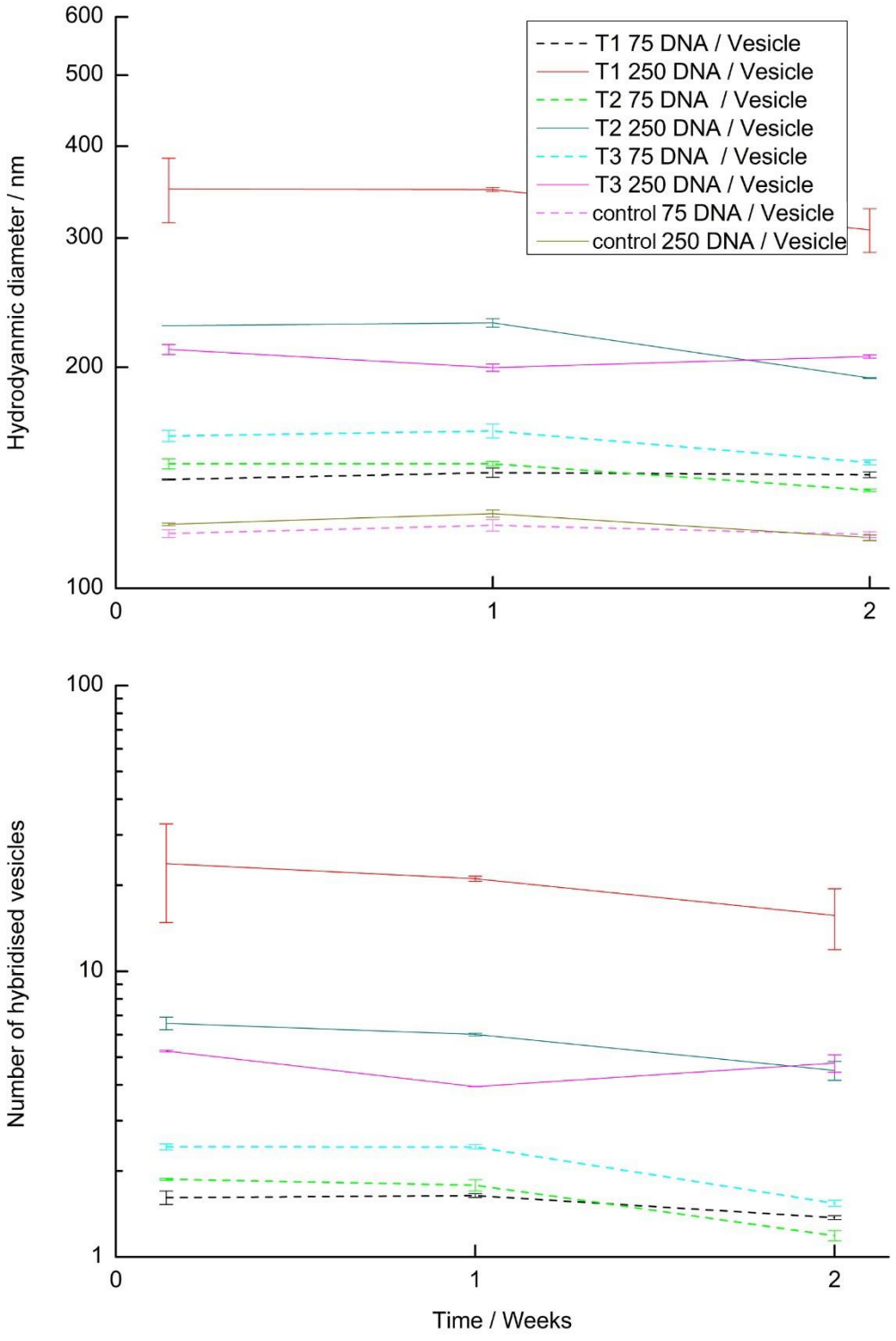

Figure 5.25 – Vesicles across assumed tie line doped with 2% PEG and pH non-responsive DNA at concentration of 75 and 250 DNA/vesicle, heated to 37 °C for 24 hours then refrigerated for two weeks. Y axes are presented on a log scale. Top: Measured hydrodynamic diameter Bottom: Calculated average number of vesicles in a single cluster. Remeasured at 25 ºC.

Over the two weeks hydrodynamic diameter remains constant for each respective sequence. Refrigeration has therefore not been shown to enable cluster reversibility once heated to 37 ^{o}C. Sample T3 75 DNA/vesicle loading has not shown the mass hybridisation that has come to be expected on the second week of ageing. This is perhaps due to a rise in lipid-PEG in the l_o domain upon heating, which still resides in the more solid l_o domain two weeks later, prohibiting aggregation. The same experiment was then carried out for the pH responsive sequence.

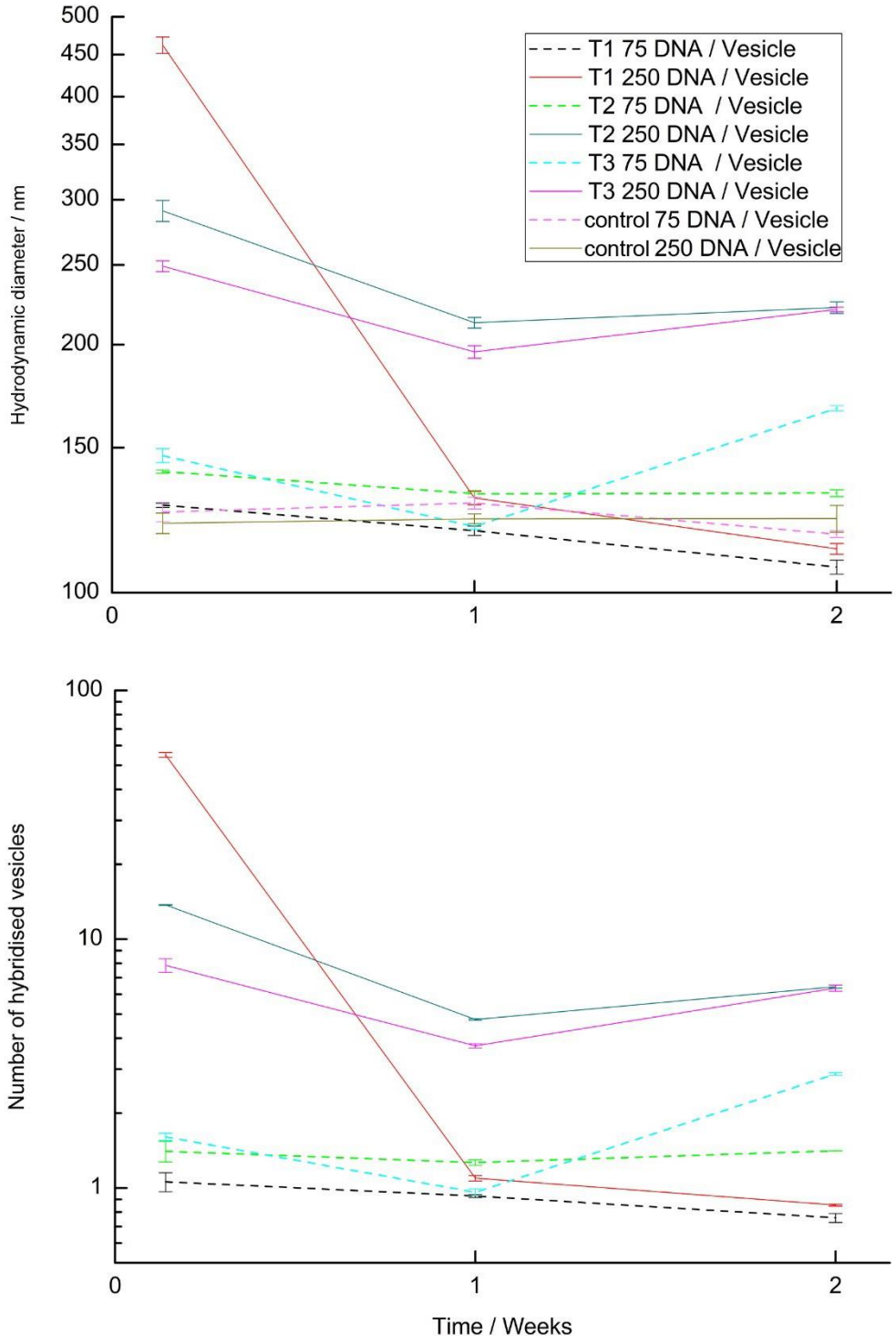

Figure 5.26 - Vesicles across tie line doped with 2% PEG and pH responsive DNA at concentration of 75 and 250 DNA/vesicle, heated to 37 °C for 24 hours then refrigerated for two weeks. Y axes are presented on a log scale Top: Measured hydrodynamic diameter Bottom: Calculated average number of vesicles in a single cluster. Remeasured at 25 ºC.

In contrast to the data presented in Figure 5.25, the data for 250 DNA/vesicle loading in Figure 5.26 do show a drop in hybridisation over a week, most notably T1 250 DNA/vesicle. It is hypothesised that the small l_o domain begins to diffuse at 37 ^oC enabling lipid-DNA to diffuse across the surface where it can weakly, non-specifically hybridise with other vesicles. Upon cooling the weak bonds are broken through stronger lipid-PEG lipid-DNA interactions significantly reducing vesicle aggregation. T2 and T3 250 DNA/vesicle loadings have larger l_o domains reducing the number of lipid-DNA strands diffusing out of the domain, resulting in aggregates more controlled in size than T1. Because hybridisation is still essentially being directed by the l_o domain there is only a small drop upon cooling and aging. 75 DNA/vesicle loading fundamentally stays consistent with ageing, but with the exception of T3 75 DNA/vesicle. This is the opposite of the trend set out by the non-responsive sequence in Figure 5.25. It is therefore hypothesised after two weeks the rise in vesicle hybridisation will be a result of the longer sequence of DNA and the larger l_o domain as previously discussed.

5.4 Summary

Throughout the chapter, vesicle clustering between lipid-DNA doped vesicles was monitored using DLS. The study found that liposome composition and DNA concentration had critical effects on vesicle aggregation, summerised in Figure 5.27.

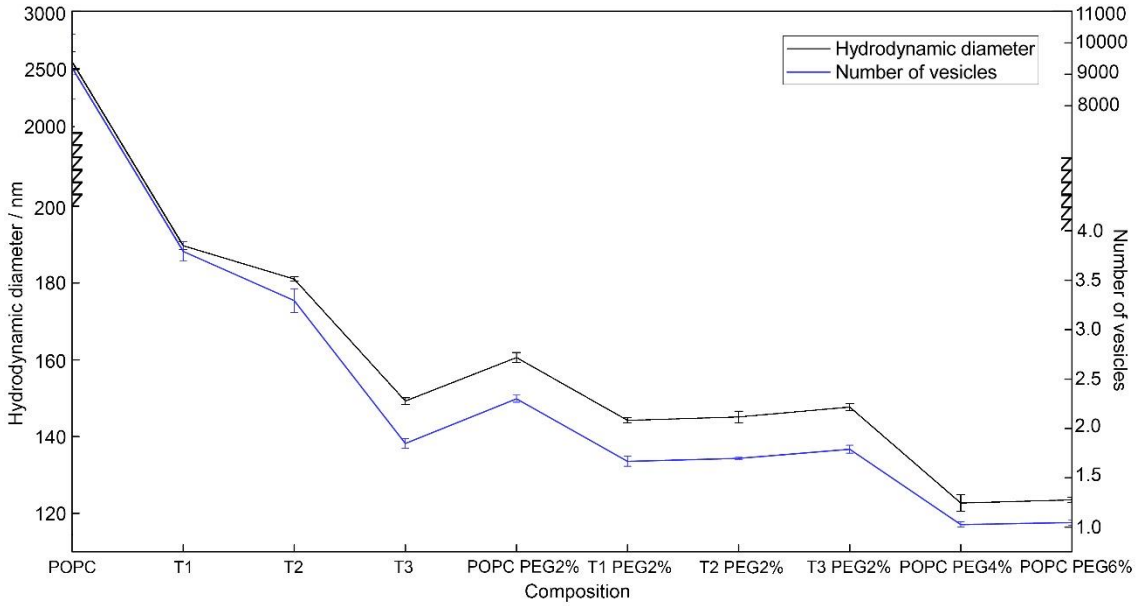

Figure 5.27 – Summary graph of how changes in liposome composition lead to a change in the hydrodynamic diameter of clusters i.e. a change in the average number of vesicles able to hybridise together using 250 DNA/vesicle pH non-responsive lipid-DNA conjugates with lipid maintained at a concentration of $1x10^{-3}$ M. All samples measured at 25 ^{o}C.

Figure 5.27 displays that the use of the developed phase diagram in chapter 3 and the introduction of low levels of PEG, as to not disturb phase behaviour, reduces random nonspecific tethering. Through these added layers of sophistication, stable size limited vesicle clusters can be modelled. Furthermore, depending on application, membrane composition can be adapted to improve thermal stability and aging capacity. The platform also enables changes in the lipid-DNA bridge to grant additional properties. Through using an i-motif sequence a pH responsive mechanism was built into the clusters. This addition to the structure affords this platform a bio-relevant stimuli responsive mechanism that could be tailored to chemotherapeutic treatments.

Chapter 6

Concluding statements

6.1 Summary

Controlled size limited assembly of Janus DNA hybridised nano vesicles was shown to be made possible through selective DOPC:DPPC:cholesterol lipid compositions and the introduction of 10 mol% cardiolipin. Where cardiolipin was found to have an affinity to significantly influence saturated lipid partitioning. Fundamentally this project added a fourth lipid component, 10 mol% CL, to the established DOPC, DPPC, cholesterol phase diagram, while maintaining vesicle diameter at ~100 nm. To measure the impact of CL in nano vesicle lipid phase behaviour, Förster Resonance Energy Transfer (FRET) was employed as the phase detection technique. From FRET heating profiles, using trace complementary FRET probes rhod PE and NBD PE, the 10 mol% CL slice through the four component phase diagram was mapped at 20 ^{o}C. From this phase diagram the l_d-l_o phase co-existence region was plotted, which was later used to modify the l_o patch size on the surface of the vesicle. Furthermore, while examining the phase behaviour of these vesicles an unexpected l_o-H_{II} phase coexistence region was demonstrated. The formation of this phase coexistence region was argued to be linked to cholesterol concentration, in line with what has previously shown in literature with DOPE. The phase diagram was then verified using complementary confocal fluorescence microscopy images of GUV samples.

Before the application of lipid-DNA to phase separated vesicles UV spectroscopy was coupled with temperature ramping, to measure vesicle bound thermal lipid-DNA bridge stability. Experiments involved examining two DNA sequences, a short fully complementary sequence and a longer pH responsive i-motif sequence. Through the measurement of DNA T_m and the generation of van't Hoff plots, thermodynamic properties of membrane bound DNA in physiological HEPES buffer were measured. This was continued to further examine DNA stability in lower pH conditions and in variable salt conditions. Results showed the DNA sequence type and concentration dictated T_m, furthermore pH reduction gave a lower T_m across all samples. Additionally, salt concentration was found to greatly affect DNA binding through screening the negative charges on the phosphate backbone. Finally, UV temperature ramp experiments were used to investigate the potential for DNA bridged vesicles to become pH switchable devices. However, it was found that temperature ramping led to the depurination of BPs on the DNA, preventing hybridisation when the pH was raised back to physiological pH. DNA depurination was then confirmed via HPLC analysis.

Once lipid-DNA bridged POPC vesicle stability was examined and they were found to be suitable, the DNA-lipids were introduced to phase separated vesicles. Three appropriate l_d-l_o phase separating compositions were selected, where the size of the l_o patch was increased from T1 to T3. From the two DNA strand types, DNA concentration and tie line position, a comprehensive study of vesicles aggregate size was made via DLS. The vesicle cluster diameters were then interpreted into coarse average number of vesicles in clusters. From the data, it was found that membrane phase separation considerably reduced aggregate size from 2500 nm to < 200 nm, enabling potential Janus DNA vesicle aggregates to take advantage of the EPR effect. Further study displayed that the position on the pseudo tie line further influenced the size of hybridised clusters. Continuing with DLS experiments, the impact of PEG addition on vesicle aggregates was monitored. Again, PEG addition was found to reduce vesicle aggregation size in homogeneous POPC liposomes and phase separated vesicles. PEG therefore provides a twofold beneficial influence to Janus DNA hybridised clusters. Firstly, PEG provides the means to form size limited clusters across the pseudo tie line. Secondly, longer circulation times are afforded to PEGylated NPs when introduced into the body due to PEG's "stealth" properties. Finally, pH responsiveness was observed across the pseudo tie line using the i-motif sequences. Through this study, it was found that vesicles hybridised in clusters could be dehybridised at pH 4 and once again self-assemble when the pH was raised back to 7.4. These data display the potential for DNA hybridised vesicles to be used in a triggered release application, whereby vesicles are released from a cluster or surface during drug delivery. This diversity widens the scope for these materials as a potential drug delivery platform, which can be tailored to form new chemotherapy treatments.

6.2 Future work

It may be suggested that effort should be made to examine the rest of the four component phase diagram. However, this would not be in line with the overall project goal of producing a drug delivery platform. While full mapping of the phase diagram would be of academic interest, it would not significantly impact the developed carrier and thus would be an unnecessary large expenditure of resources. In addition, 10 mol% CL was already found to be sufficient to direct lipid partitioning in order to produce < 200 nm clusters and dimers with and without PEG addition. However, in the short term continued work in studying Janus DNA vesicle clusters through Cryo TEM would be of value. Through this sustained research, a fuller picture of the number of vesicles hybridised in a cluster could be put together which would be more accurate than the DLS interpretation put forward here. Also, fluorescence cross-correlation spectroscopy (FCCS) could be implemented as a further complementary technique, that could be used to measure the number of vesicles in a cluster. Additionally, Cryo TEM would enable an average distance between hybridised vesicles to be measured, through the unique pattern displayed between two hybridised vesicles.

Future research more in line with the original project goals would be tailored towards studying additional DNA sequences, specifically in respect to using other i-motifs. Through the integration of further BP mismatches in the DNA i-motif sequence, it would be possible to aid the pH-triggered i-motif formation. In other words, added BP mismatches would increase inter-strand dehybridisation susceptibility to a pH trigger.

In the long term of the development cycle, effort should be made to move away from making a broad-spectrum drug delivery platform, to one which focuses on a specific application. Primarily this would entail examining Janus vesicles in terms of loading potential, drug release kinetics and monitoring the membrane's structural integrity. Each drug would have its own loading efficiency and leakage rate dependant on the individual species' structure and resulting hydrophobicity. Long term stability in regard to leakage would be dependent upon the drug's partition coefficients, both in the liposome core and across the membrane [160]. The next step would be to integrate these materials into cell culture experiments, where a comparison of single vesicles against clustered vesicles in prodrug and combinational therapies would be undertaken. However, the experiments are well beyond the scope for this first principle examination of DNA bridged Janus vesicle cluster design.

References

1. B. Haley, E. Frenkel, *Urologic Oncology: Seminars and Original Investigations*, 2008, **26**, (1), 57-64.
2. R. Samsur, V. K. Rangari, S. Jeelani, L. Zhang, Z. Y. Cheng, *Journal of Applied Physics*, 2013, **113**, (21), 214903.
3. L. Dai, S. Chen, J. Liu, Y. Gao, J. Zhou, Z. Chen, C. Cao, H. Luo, M. Kanehira, *Physical Chemistry Chemical Physics*, 2013, **15**, (28), 11723-11729.
4. A. Burton, *Environmental Health Perspectives*, 2012, **120**, (6), a229-a229.
5. http://www.cancerresearchuk.org/health-professional/cancer-statistics Accessed 10/03/2017
6. http://www.cancerresearchuk.org/about-cancer/cancers-in-general/cancer-questions/what-is-palliative-treatment-and-when-should-it-be-used Accessed 05/03/2017
7. http://www.cancerresearchuk.org/about-cancer/type/lung-cancer/about/types-of-lung-cancer Accessed 10/03/2017
8. W. H. De Jong, P. J. A. Borm, *International Journal of Nanomedicine*, 2008, **3**, (2), 133-149.
9. Y. Namiki, T. Fuchigami, N. Tada, R. Kawamura, S. Matsunuma, Y. Kitamoto, M. Nakagawa, *Accounts of Chemical Research*, 2011, **44**, (10), 1080-1093.
10. G. Bozzuto, A. Molinari, *International Journal of Nanomedicine*, 2015, **10**, 975-999.
11. V. Kumar Khanna, *ISRN Pharmacology*, 2012, **2012**, 9.
12. X. Liu, Y. Zheng, N. M. Samoshina, A. H. Franz, X. Guo, V. V. Samoshin, *Journal of Liposome Research*, 2012, **22**, (4), 319-328.
13. L. J. Wilkinson, R. J. White, J. K. Chipman, *Journal of Wound Care*, 2011, **20**, (11), 543-549.
14. P. Devaraj, P. Kumari, C. Aarti, A. Renganathan, *Journal of Nanotechnology*, 2013, **2013**, 5.
15. C. Levard, E. M. Hotze, G. V. Lowry, G. E. Brown, *Environmental Science & Technology*, 2012, **46**, (13), 6900-6914.
16. C. Bharti, U. Nagaich, A. K. Pal, N. Gulati, *International Journal of Pharmaceutical Investigation*, 2015, **5**, (3), 124-133.
17. Y. Zhao, X. Sun, G. Zhang, B. G. Trewyn, I. I. Slowing, V. S. Y. Lin, *ACS Nano*, 2011, **5**, (2), 1366-1375.
18. X. Huang, J. Zhuang, X. Teng, L. Li, D. Chen, X. Yan, F. Tang, *Biomaterials*, 2010, **31**, (24), 6142-6153.
19. C. E. Probst, P. Zrazhevskiy, V. Bagalkot, X. Gao, *Advanced Drug Delivery Reviews*, 2013, **65**, (5), 703-718.
20. M. A. Walling, J. A. Novak, J. R. E. Shepard, *International Journal of Molecular Sciences*, 2009, **10**, (2), 441-491.

21. V. Torchilin, *Handbook of Nanobiomedical Research: Fundamentals, Applications, and Recent Developments*. 2014: World Scientific Publishing Company Pte Limited.
22. L. Vigderman, E. R. Zubarev, *Advanced Drug Delivery Reviews*, (0).
23. J. D. Gibson, B. P. Khanal, E. R. Zubarev, *Journal of the American Chemical Society*, 2007, **129**, (37), 11653-11661.
24. R. Hong, G. Han, J. M. Fernández, B.-j. Kim, N. S. Forbes, V. M. Rotello, *Journal of the American Chemical Society*, 2006, **128**, (4), 1078-1079.
25. P. Ghosh, G. Han, M. De, C. K. Kim, V. M. Rotello, *Advanced Drug Delivery Reviews*, 2008, **60**, (11), 1307-1315.
26. A. Walther, A. H. E. Muller, *Soft Matter*, 2008, **4**, (4), 663-668.
27. T. Nisisako, T. Torii, *Advanced Materials*, 2007, **19**, (11), 1489-1493.
28. R. Munday, *Free Radical Biology and Medicine*, 1989, **7**, (6), 659-673.
29. M. A. Maurer-Jones, I. L. Gunsolus, C. J. Murphy, C. L. Haynes, *Analytical Chemistry*, 2013, **85**, (6), 3036-3049.
30. D. Marsh, *Biophysical Journal*, 2012, **102**, (5), 1079-1087.
31. C. Tanford, *The hydrophobic effect: formation of micelles and biological membranes*. 1973: Wiley.
32. http://avantilipids.com/index.php?option=com_content&view=article&id=216&Itemid=206&catnumber=850355 Accessed 18/12/12
33. D. Boal, *Mechanics of the Cell*. 2002: Cambridge University Press.
34. J. Zhang, X. Li, X. Li, *Progress in Polymer Science*, 2012, **37**, (8), 1130-1176.
35. D. M. Fambrough, D. J. Benos, R. Epand, *Lipid Polymorphism and Membrane Properties*. 1997: Elsevier Science.
36. C. LoPresti, M. Massignani, C. Fernyhough, A. Blanazs, A. J. Ryan, J. Madsen, N. J. Warren, S. P. Armes, A. L. Lewis, S. Chirasatitsin, A. J. Engler, G. Battaglia, *ACS Nano*, 2011, **5**, (3), 1775-1784.
37. R. Chandrawati, F. Caruso, *Langmuir*, 2012, **28**, (39), 13798-13807.
38. C. LoPresti, H. Lomas, M. Massignani, T. Smart, G. Battaglia, *Journal of Materials Chemistry*, 2009, **19**, (22), 3576-3590.
39. M. L. Immordino, F. Dosio, L. Cattel, *International Journal of Nanomedicine*, 2006, **1**, (3), 297-315.
40. M. Cuchel, D. J. Rader, *Circulation*, 2006, **113**, (21), 2548-2555.
41. T. H. Bayburt, Y. V. Grinkova, S. G. Sligar, *Nano Letters*, 2002, **2**, (8), 853-856.
42. E. Serebryany, G. A. Zhu, E. C. Y. Yan, *Biochimica et Biophysica Acta (BBA) - Biomembranes*, 2012, **1818**, (2), 225-233.
43. P. A. Beales, T. K. Vanderlick, *The Journal of Physical Chemistry A*, 2007, **111**, (49), 12372-12380.

44. B. Maherani, E. Arab-tehrany, A. Kheirolomoom, V. Reshetov, M. J. Stebe, M. Linder, *Analyst*, 2012, **137**, (3), 773-786.
45. I. A. Siddiqui, V. M. Adhami, J. Christopher, Chamcheu, H. Mukhtar, *International Journal of Nanomedicine*, 2012, **7**, 591-605.
46. V. Agrawal, P. K. Manash, M. K. Anup, *Journal of Liposome Research*, 2005, **15**, (3-4), 141-155.
47. C.-M. J. Hu, S. Aryal, L. Zhang, *Therapeutic Delivery*, 2010, **1**, (2), 323-334.
48. Z. Fan, P. P. Fu, H. Yu, P. C. Ray, *Journal of Food and Drug Analysis*, 2014, **22**, (1), 3-17.
49. K. P. McNamara, Z. Rosenzweig, *Analytical Chemistry*, 1998, **70**, (22), 4853-4859.
50. H. Takeuchi, Y. Kitagawa, *Journal of Gastrointestinal Oncology*, 2012, **3**, (2), 84-85.
51. W. Eck, G. Craig, A. Sigdel, G. Ritter, L. J. Old, L. Tang, M. F. Brennan, P. J. Allen, M. D. Mason, *ACS Nano*, 2008, **2**, (11), 2263-2272.
52. Z. Fan, M. Shelton, A. K. Singh, D. Senapati, S. A. Khan, P. C. Ray, *ACS Nano*, 2012, **6**, (2), 1065-1073.
53. J. Rautio, K. Laine, M. Gynther, J. Savolainen, *The AAPS Journal*, 2008, **10**, (1), 92-102.
54. G. van Meer, D. R. Voelker, G. W. Feigenson, *Nature reviews. Molecular cell biology*, 2008, **9**, (2), 112-124.
55. S. L. Veatch, S. L. Keller, *Physical Review Letters*, 2002, **89**, (26), 268101.
56. G. Pabst, N. Kučerka, M. P. Nieh, J. Katsaras, *Liposomes, Lipid Bilayers and Model Membranes: From Basic Research to Application*. 2014: CRC Press.
57. J. T. Buboltz, G. W. Feigenson, *Biochimica et Biophysica Acta (BBA) - Biomembranes*, 1999, **1417**, (2), 232-245.
58. D. Vind-Kezunovic, C. H. Nielsen, U. Wojewodzka, R. Gniadecki, *Biochimica et Biophysica Acta (BBA) - Biomembranes*, 2008, **1778**, (11), 2480-2486.
59. S. R. Shaikh, A. C. Dumaual, L. J. Jenski, W. Stillwell, *Biochimica et Biophysica Acta (BBA) - Biomembranes*, 2001, **1512**, (2), 317-328.
60. A. J. García-Sáez, S. Chiantia, P. Schwille, *Journal of Biological Chemistry*, 2007, **282**, (46), 33537-33544.
61. P. I. Kuzmin, S. A. Akimov, Y. A. Chizmadzhev, J. Zimmerberg, F. S. Cohen, *Biophysical Journal*, 2005, **88**, (2), 1120-1133.
62. L. J. Pike, *Journal of lipid research*, 2009, **50 Suppl**, S323-328.
63. P. W. Atkins, *Physical Chemistry Fith Edition* Oxford: Oxford University Press.
64. B. G. Tenchov, *Progress in Surface Science*, 1985, **20**, (4), 273-340.
65. J. L. Rubenstein, B. A. Smith, H. M. McConnell, *Proceedings of the National Academy of Sciences of the United States of America*, 1979, **76**, (1), 15-18.
66. A. Kessel, N. Ben-Tal, S. May, *Biophysical Journal*, 2001, **81**, (2), 643-658.
67. J. T. Buboltz, C. Bwalya, K. Williams, M. Schutzer, *Langmuir*, 2007, **23**, (24), 11968-11971.
68. S. L. Veatch, S. L. Keller, *Biophysical Journal*, 2003, **85**, (5), 3074-3083.

69. R. N. M. Weijers, *Current Diabetes Reviews*, 2012, **8**, (5), 390-400.
70. T. Baumgart, G. Hunt, E. R. Farkas, W. W. Webb, G. W. Feigenson, *Biochimica et biophysica acta*, 2007, **1768**, (9), 2182-2194.
71. Y. Z. Yoon, J. P. Hale, P. G. Petrov, P. Cicuta, *Journal of Physics: Condensed Matter*, 2010, **22**, (6), 062101.
72. J. T. Buboltz, *Physical Review E*, 2007, **76**, (2), 021903.
73. V. V. Didenko, *BioTechniques*, 2001, **31**, (5), 1106-1116, 1118, 1120-1101.
74. M. Loew, R. Springer, S. Scolari, F. Altenbrunn, O. Seitz, J. Liebscher, D. Huster, A. Herrmann, A. Arbuzova, *Journal of the American Chemical Society*, 2010, **132**, (45), 16066-16072.
75. T. M. Konyakhina, J. Wu, J. D. Mastroianni, F. A. Heberle, G. W. Feigenson, *Biochimica et Biophysica Acta (BBA) - Biomembranes*, 2013, **1828**, (9), 2204-2214.
76. P. Uppamoochikkal, S. Tristram-Nagle, J. F. Nagle, *Langmuir : the ACS journal of surfaces and colloids*, 2010, **26**, (22), 17363-17368.
77. A. K. Smith, J. H. Freed, *The Journal of Physical Chemistry B*, 2009, **113**, (12), 3957-3971.
78. S. L. Veatch, O. Soubias, S. L. Keller, K. Gawrisch, *Proceedings of the National Academy of Sciences of the United States of America*, 2007, **104**, (45), 17650-17655.
79. http://www.microscopyu.com/articles/superresolution/diffractionbarrier.html Accessed 10/03/2017
80. A. C. Brown, K. B. Towles, S. P. Wrenn, *Langmuir*, 2007, **23**, (22), 11180-11187.
81. A. C. Brown, K. B. Towles, S. P. Wrenn, *Langmuir*, 2007, **23**, (22), 11188-11196.
82. P. L. Biancaniello, J. C. Crocker, D. A. Hammer, V. T. Milam, *Langmuir*, 2007, **23**, (5), 2688-2693.
83. V. T. Milam, *Current Opinion in Colloid & Interface Science*, 2016, **26**, 75-83.
84. Y.-H. Chan, B. Lengerich, S. Boxer, *Biointerphases*, 2008, **3**, (2), FA17-FA21.
85. R. J. R. W. Peters, I. Louzao, J. C. M. van Hest, *Chemical Science*, 2012, **3**, (2), 335-342.
86. P. A. Beales, T. K. Vanderlick, *Advances in Colloid and Interface Science*, 2014, **207**, 290-305.
87. R. Zidovetzki, I. Levitan, *Biochimica et Biophysica Acta (BBA) - Biomembranes*, 2007, **1768**, (6), 1311-1324.
88. P. A. Beales, T. K. Vanderlick, *The journal of physical chemistry. B*, 2009, **113**, (42), 13678-13686.
89. J. Dai, M. Alwarawrah, J. Huang, *The journal of physical chemistry. B*, 2010, **114**, (2), 840.
90. T. A. Harroun, J. Katsaras, S. R. Wassall, *Biochemistry*, 2008, **47**, (27), 7090-7096.
91. P. A. Beales, J. Nam, T. K. Vanderlick, *Soft Matter*, 2011, **7**, (5), 1747-1755.
92. R. B. Wallace, J. Shaffer, R. F. Murphy, J. Bonner, T. Hirose, K. Itakura, *Nucleic Acids Research*, 1979, **6**, (11), 3543-3558.
93. http://www.sigmaaldrich.com/img/assets/17240/meltingtemp.pdf Accessed 10/03/2017

94. N. von Ahsen, C. T. Wittwer, E. Schütz, *Clinical Chemistry*, 2001, **47**, (11), 1956-1961.
95. S. M. Freier, R. Kierzek, J. A. Jaeger, N. Sugimoto, M. H. Caruthers, T. Neilson, D. H. Turner, *Proceedings of the National Academy of Sciences of the United States of America*, 1986, **83**, (24), 9373-9377.
96. P. A. Beales, T. K. Vanderlick, *Biophysical Journal*, 2009, **96**, (4), 1554-1565.
97. G. C. Saunders, H. C. Parkes, S. B. Primrose, L. o. t. G. Chemist, *Analytical Molecular Biology: Quality and Validation*. 1999: Royal Society of Chemistry for Laboratory of the Government Chemist.
98. R. Owczarzy, P. M. Vallone, F. J. Gallo, T. M. Paner, M. J. Lane, A. S. Benight, *Biopolymers*, 1997, **44**, (3), 217-239.
99. J. SantaLucia, *Proceedings of the National Academy of Sciences*, 1998, **95**, (4), 1460-1465.
100. J. D. Watson, F. H. C. Crick, *Nature*, 1953, **171**, (4356), 737-738.
101. J. Choi, T. Majima, *Chemical Society Reviews*, 2011, **40**, (12), 5893-5909.
102. K. Gehring, J.-L. Leroy, M. Gueron, *Nature*, 1993, **363**, (6429), 561-565.
103. J. L. Leroy, K. Gehring, A. Kettani, M. Gueron, *Biochemistry*, 1993, **32**, (23), 6019-6031.
104. M. Guéron, J.-L. Leroy, *Current Opinion in Structural Biology*, 2000, **10**, (3), 326-331.
105. S. Nonin-Lecomte, J. L. Leroy, *Journal of Molecular Biology*, 2001, **309**, (2), 491-506.
106. H. A. Day, P. Pavlou, Z. A. E. Waller, *Bioorganic & Medicinal Chemistry*, 2014, **22**, (16), 4407-4418.
107. L. Song, V. H. B. Ho, C. Chen, Z. Yang, D. Liu, R. Chen, D. Zhou, *Advanced Healthcare Materials*, 2013, **2**, (2), 275-280.
108. J. R. Griffiths, *British Journal of Cancer*, 1991, **64**, (3), 425-427.
109. A. Tong, *Sensor Review*, 2001, **21**, (3), 5.
110. http://www.pyromation.com/Downloads/Data/emfk_c.pdf Accessed 01/09/2014
111. S. P. J. Higson, *Analytical Chemistry*. 2003, New York: Oxford 434.
112. http://chemwiki.ucdavis.edu/Physical_Chemistry/Spectroscopy/Electronic_Spectroscopy/Jablonski_diagram Accessed 05/04/2013
113. https://avantilipids.com/product/810144/ Accessed 30/12/2016
114. https://avantilipids.com/product/810150/ Accessed 30/12/2016
115. D. C. Harris, *Quantitative Chemical Analysis*. 2007: W. H. Freeman.
116. http://www.labautopedia.org/mw/index.php/An_Introduction_to_Fluorescence_Resonance_Energy_Transfer_(FRET)_Technology_and_its_Application_in_Bioscience Accessed 11/01/13
117. I. Medintz, N. Hildebrandt, *FRET - Förster Resonance Energy Transfer: From Theory to Applications*. 2013: Wiley.
118. R. B. Sekar, A. Periasamy, *The Journal of Cell Biology*, 2003, **160**, (5), 629-633.
119. http://www.biotek.com/resources/articles/fluorescence-resonance-energy-transfer.html Accessed 05/04/2013

120. H. Kuhn, H. D. Försterling, D. H. Waldeck, *Principles of Physical Chemistry*. 2009: Wiley.
121. http://149.171.168.221/partcat/wp-content/uploads/Malvern-Zetasizer-LS.pdf Accessed 10/03/2017
122. http://www.horiba.com/uk/scientific/products/particle-characterization/technology/dynamic-light-scattering/ Accessed 15/04/2016
123. S. Mathiasen, S. M. Christensen, J. J. Fung, S. G. F. Rasmussen, J. F. Fay, S. K. Jorgensen, S. Veshaguri, D. L. Farrens, M. Kiskowski, B. Kobilka, D. Stamou, *Nat Meth*, 2014, **11**, (9), 931-934.
124. Y. Watanabe, M. Nakatomi, *Tetrahedron*, 1999, **55**, (32), 9743-9754.
125. Y. Xu, S. A. Lee, T. G. Kutateladze, D. Sbrissa, A. Shisheva, G. D. Prestwich, *Journal of the American Chemical Society*, 2006, **128**, (3), 885-897.
126. S. A. J. van der Meulen, G. V. Dubacheva, M. Dogterom, R. P. Richter, M. E. Leunissen, *Langmuir*, 2014, **30**, (22), 6525-6533.
127. T. Nasiru, L. Avila, M. Levine, *Journal of High School Research*, 2011, **2**, 1-5.
128. http://www.atdbio.com/content/17/Solid-phase-oligonucleotide-synthesis Accessed 21/04/2016
129. O. Kühl, *Phosphorus-31 NMR Spectroscopy: A Concise Introduction for the Synthetic Organic and Organometallic Chemist*. 2008: Springer Berlin Heidelberg.
130. D. L. Pavia, G. M. Lampman, G. S. Kriz, J. A. Vyvyan, *Introduction to Spectroscopy*. 2014: Cengage Learning.
131. https://www.chroma.com/spectra-viewer Accessed 23/10/2016
132. S. N. Pinto, F. Fernandes, A. Fedorov, A. H. Futerman, L. C. Silva, M. Prieto, *Biochimica et Biophysica Acta (BBA) - Biomembranes*, 2013, **1828**, (9), 2099-2110.
133. Y. Ishida, T. Shimada, H. Tachibana, H. Inoue, S. Takagi, *The Journal of Physical Chemistry A*, 2012, **116**, (49), 12065-12072.
134. H.-L. Wu, Y. Tong, Q. Peng, N. Li, S. Ye, *Physical Chemistry Chemical Physics*, 2016, **18**, (3), 1411-1421.
135. B. A. Lewis, D. M. Engelman, *Journal of Molecular Biology*, 1983, **166**, (2), 211-217.
136. D. K. Rana, S. Dhar, S. C. Bhattacharya, *Physical Chemistry Chemical Physics*, 2014, **16**, (13), 5933-5936.
137. R. Šachl, J. Humpolíčková, M. Štefl, Lennart B.-Å. Johansson, M. Hof, *Biophysical Journal*, 2011, **101**, (11), L60-L62.
138. B. M. Castro, R. F. M. de Almeida, A. Fedorov, M. Prieto, *Chemistry and Physics of Lipids*, 2012, **165**, (3), 311-319.
139. D. E. Laughlin, K. Hono, *Physical Metallurgy: 3-Volume Set*. 2014: Elsevier Science.
140. B. de Kruijff, A. J. Verkleij, J. Leunissen-Bijvelt, C. J. A. van Echteld, J. Hille, H. Rijnbout, *Biochimica et Biophysica Acta (BBA) - Biomembranes*, 1982, **693**, (1), 1-12.
141. G. Olofsson, E. Sparr, *PLoS ONE*, 2013, **8**, (9), e73040.

142. E. Hayakawa, M. Naganuma, K. Mukasa, T. Shimozawa, T. Araiso, *Biophysical Journal*, 1998, **74**, (2), 892-898.
143. F. S. Ariola, D. J. Mudaliar, R. P. Walvick, A. A. Heikal, *Physical Chemistry Chemical Physics*, 2006, **8**, (39), 4517-4529.
144. P. Yakovchuk, E. Protozanova, M. D. Frank-Kamenetskii, *Nucleic Acids Research*, 2006, **34**, (2), 564-574.
145. J. Huotari, A. Helenius, *The EMBO Journal*, 2011, **30**, (17), 3481-3500.
146. T. Suzuki, S. Ohsumi, K. Makino, *Nucleic Acids Research*, 1994, **22**, (23), 4997-5003.
147. K. S. Gates, *Chemical research in toxicology*, 2009, **22**, (11), 1747-1760.
148. R. An, Y. Jia, B. Wan, Y. Zhang, P. Dong, J. Li, X. Liang, *PLoS ONE*, 2014, **9**, (12), e115950.
149. Y. Mishima, *Cancer Neutron Capture Therapy*. 2013: Springer US.
150. C. Shao, T. U. H. Genetics, *Epigenetics of Tandem DNA Repeats in FSH Muscular Dystrophy, the DNMT3B-deficient ICF Syndrome, and Ovarian Epithelial Tumors*. 2007: Tulane University.
151. D. Rhodes, H. J. Lipps, *Nucleic Acids Research*, 2015.
152. A. T. Phan, J.-L. Mergny, *Nucleic Acids Research*, 2002, **30**, (21), 4618-4625.
153. E. Largy, J.-L. Mergny, *Nucleic Acids Research*, 2014, **42**, (19), e149-e149.
154. B. J. Berne, R. Pecora, *Dynamic Light Scattering: With Applications to Chemistry, Biology, and Physics*. 1976: Dover Publications.
155. A. S. Ulrich, *Bioscience Reports*, 2002, **22**, (2), 129-150.
156. S. Q. Liu, *Bioregenerative Engineering: Principles and Applications*. 2007: Wiley.
157. C. Alvarez-Lorenzo, A. Concheiro, *Smart Materials for Drug Delivery*. 2013: Royal Society of Chemistry.
158. C. Allen, N. Dos Santos, R. Gallagher, G. N. C. Chiu, Y. Shu, W. M. Li, S. A. Johnstone, A. S. Janoff, L. D. Mayer, M. S. Webb, M. B. Bally, *Bioscience Reports*, 2002, **22**, (2), 225-250.
159. H. Park, A. Germini, S. Sforza, R. Corradini, R. Marchelli, W. Knoll, *Biointerphases*, 2006, **1**, (4), 113-122.
160. B. P. Binks, P. D. I. Fletcher, A. J. Johnson, R. P. Elliott, *Physical Chemistry Chemical Physics*, 2012, **14**, (44), 15525-15538.